

Precision Measurement of the Chiral Anomaly and Improvements of the Data Acquisition System at the COMPASS Experiment at CERN

Dominik Ecker

Vollständiger Abdruck der von der TUM School of Natural Sciences der Technischen
Universität München zur Erlangung eines

Doktors der Naturwissenschaften (Dr. rer. nat.)

genehmigten Dissertation.

Vorsitz: apl. Prof. Dr. Norbert Kaiser

Prüfer*innen der Dissertation:

1. Prof. Dr. Stephan Paul
2. Prof. Dr. Lothar Oberauer

Die Dissertation wurde am 22.08.2023 bei der Technischen Universität München eingereicht
und durch die TUM School of Natural Sciences am 11.09.2023 angenommen.

Abstract

The COMPASS collaboration at CERN operated a multi-purpose fixed-target spectrometer at the Super Proton Synchrotron from 2002 to 2022 with unprecedented high-intensity and high-energy muon and hadron beams. World-leading data sets, in size and complexity, have been acquired for a better understanding of quantum chromodynamics of strong interaction. Apart from modern particle detector technology, a driving feature in achieving these goals is the data acquisition system (DAQ), allowing to combine a huge amount of detector information with the needed bandwidth. Since 2014, the DAQ has explored and employed novel approaches of event building using field-programmable gate arrays. In the first part of this thesis, I improved the reliability of the DAQ by developing and implementing a crosspoint switch and by commissioning a real-time beam monitoring tool. The information from the real-time beam monitoring tool is transmitted to accelerator and beam line operators, who use it to tune the beam properties.

In the second part, I perform a test of predictions of the chiral anomaly, a fundamental property of quantum chromodynamics. It governs processes involving an odd number pions, which are the Goldstone bosons of chiral symmetry breaking. This applies most profoundly to the coupling of three pions to a photon. The magnitude of the coupling is described the constant $F_{3\pi}$, and its value is precisely predicted by chiral perturbation theory. It can be measured in $\pi^- \gamma \rightarrow \pi^- \pi^0$ scattering.

Within this thesis, I conduct a precision analysis on $F_{3\pi}$ using data of the COMPASS experiment, where pion-photon scattering is mediated via the Primakoff effect using heavy nuclei as target. We exploit the interference of the production of the $\pi^- \pi^0$ final state via the chiral anomaly with the photo-production of the $\rho(770)$ resonance over a wide mass range up to $m_{\pi^- \pi^0} \sim 1.2 \text{ GeV}/c^2$, employing a dispersive framework that had been worked out by theory colleagues from Bonn university specifically for the purpose of our analysis. This is, beyond the increased number of events, a significant advantage compared to previous measurements restricting themselves to the threshold region only. The presented analysis allows to simultaneously extract the radiative width of the $\rho(770)$ resonance and gives a stronger handle on $F_{3\pi}$ in a unified approach, thereby minimizing systematic effects that have not been addressed previously.

Our analysis yields

$$F_{3\pi} = (9.24(\pm 0.21)_{\text{stat}}(\pm 0.83)_{\text{syst}}) \text{ GeV}^{-3},$$

which roughly agrees with theory, but is dominated by systematic uncertainties. The main source for the systematic uncertainty is the handling of background processes. Compared to previous approaches of this analysis, we developed a significantly improved model for the most important background contribution stemming from $\pi^- + \text{Ni} \rightarrow \pi^- \pi^0 \pi^0 + \text{Ni}$ events. The improved model facilitates a proper disentangling of smaller background contributions, and may hence lead to smaller systematic uncertainties in the future. Uncertainties between 2 to 4% are shown to be in reach, but could not be fully worked out within this thesis anymore.

Contents

Introduction	1
1 Theory and motivation	3
1.1 Quantum Chromodynamics — the theory of strong interaction	3
1.1.1 Confinement and the quark model	6
1.1.2 QCD in the chiral limit	7
1.2 Pion lifetime and the chiral anomaly	11
1.3 Previous tests of the chiral anomaly	14
1.3.1 Experimental tests of $F_{\gamma\gamma}$	14
1.3.2 Experimental tests of $F_{3\pi}$	16
1.4 Radiative width of the ρ meson	18
1.4.1 Motivation to study radiative decays of vector mesons	18
1.4.2 Previous measurements	19
2 Primakoff reactions	21
2.1 Introduction to scattering processes	21
2.1.1 Mandelstam variables	21
2.1.2 Coordinate systems	23
2.1.3 Strong production mechanisms of light mesons at COMPASS	24
2.2 The Primakoff effect	25
2.2.1 Henry Primakoff's idea of a photon target	26
2.2.2 Minimum momentum transfer	27
2.2.3 Weizsäcker Williams factorization	28
2.2.4 Nuclear excitations	30

2.3	Kinematics of the $\pi^- \gamma^{(*)} \rightarrow \pi^- \pi^0$ reaction	32
2.3.1	Angular distributions and partial-wave expansion	34
2.3.2	Resonant production of the $\rho(770)$ meson	35
2.3.3	Higher-order and electromagnetic corrections	37
2.4	Extracting $F_{3\pi}$ from Primakoff data	39
2.4.1	Dispersion relations	39
2.4.2	Dispersive approach for the anomalous process $\pi^- \gamma^{(*)} \rightarrow \pi^- \pi^0$	41
2.4.3	Comparison to ChPT	42
2.4.4	Extraction of $\Gamma_{\rho \rightarrow \pi\gamma}$	43
3	The COMPASS experiment	45
3.1	General physics program and spectrometer layout	45
3.2	The M2 beamline at CERN	47
3.3	Spectrometer setup in 2009 for the Primakoff program	49
3.3.1	Target region	49
3.3.2	Electromagnetic calorimeters	50
3.3.3	Trigger strategy	51
3.4	Accessible Primakoff channels at COMPASS	54
3.5	Readout electronics and Data Acquisition System	54
3.5.1	System design and topology of the iFDAQ from 2014 to 2019	55
3.5.2	Software architecture of the iFDAQ	57
4	Improving reliability and stability of the data acquisition	59
4.1	Crosspoint switch	60
4.1.1	Hardware and firmware design	61
4.1.2	Integration and application in the iFDAQ	65
4.1.3	Application at Belle II	67
4.2	Commissioning of a real-time beam monitoring system	67
5	Event reconstruction and selection	71
5.1	Event preselection	72

5.2	Reconstruction of neutral pions	76
5.2.1	Reconstruction of photons and calibration of the calorimeter	77
5.2.2	Selecting showers for π^0 reconstruction	81
5.2.3	Resolution in Q^2 and \sqrt{s} and kinematic constraints	83
5.2.4	Alignment of calorimeters	86
5.3	Event selection	87
5.3.1	Beam and final state particle identification	87
5.3.2	π^0 selection and event kinematics	91
5.3.3	Overview of event sample sizes in the Primakoff 2009 data set	94
6	Generation of pseudodata by Monte-Carlo simulation	97
6.1	Material description	98
6.2	ECAL calibration	98
6.3	ECAL resolution	100
6.4	Simulation of the beam	102
6.5	Trigger simulation	104
6.6	Q -dependencies	105
7	Determination of the integrated luminosity via free kaon decays	109
7.1	Overview of charged-kaon decays	111
7.2	Simulation of kaon decays	112
7.2.1	Kinematics of hadronic K^- -decays	112
7.2.2	Kinematics of semileptonic K^- -decays	115
7.3	Determination of the effective integrated luminosity	116
7.4	Systematic uncertainties	118
8	Extracting values for $F_{3\pi}$ and the radiative width of the $\rho(770)$	121
8.1	Considered background contributions	121
8.1.1	Kaon decays	121
8.1.2	Kaon interactions	123
8.1.3	Non- π^0 events	124

8.2	Background subtraction	125
8.2.1	Evaluation of the $\pi^- + \text{Ni} \rightarrow \pi^- \pi^0 \pi^0 + \text{Ni}$ model	127
8.2.2	Determination of the number of elastic Primakoff events	130
8.3	Correcting for experimental acceptance	133
8.4	Normalization to the photon flux	135
8.5	Fitting the dispersive model	137
8.6	Summary and open issues	138
9	Discussion of the result and outlook	141
9.1	Comparison to previous results and systematic uncertainties	141
9.2	Conclusion and outlook	144
9.3	Radiative width of the $\rho_3(1690)$	144
9.4	Analysis of $\pi^- \gamma^{(*)} \rightarrow \pi^- \pi^0 \pi^0$ cross section	145
A	Equations, transformations, and conventions	147
A.1	Gell-Mann matrices	147
A.2	Dirac matrices	148
A.3	Lorentz transformation of the electromagnetic field of a point charge	148
A.4	Derivation of angular dependencies of $\pi^- \gamma \rightarrow \pi^- \pi^0$	151
A.5	Twice subtracted dispersion relation	152
B	Kinematic distributions	153
B.1	Kinematic distributions of the selected $\pi^- + \text{Ni} \rightarrow \pi^- \pi^0 \pi^0 + \text{Ni}$ events and comparison to simulation	153
B.2	Kinematic distributions of the selected $K^- \rightarrow \pi^- \pi^0$ events and comparison to simulation	157
B.3	Kinematic distributions of the selected $K^- \rightarrow \pi^- \pi^0 \pi^0$ events and comparison to simulation	160
B.4	ϕ_{TY} distributions in selected $\pi^- \gamma^{(*)} \rightarrow \pi^- \pi^0$ events	163
C	Register description of crosspoint switch firmware	165
	Bibliography	173

Introduction

Our understanding of the subatomic world of elementary particles is formulated in a concise and self-consistent framework called the standard model (SM). The story of the SM is a story of triumph and success. Throughout the last decade, the SM did not stop to amaze scientists by the quantity and quality of its predictions, culminating in the finding of the Higgs boson in 2012. The SM has described particle physics to an extent, that scientists are hunting for effects that cannot be explained within the framework of the SM, searching for physics beyond the SM (BSM). Measurements and findings of BSM physics are however very rare. If published, they draw global attention, like the recent result on the muon magnetic moment ($g - 2$) at Fermilab [1].

Despite the global hunt for BSM physics, it is important to realize, how much room the SM still leaves for deepening the knowledge on elementary particles even within the framework. Particularly the strong interaction is only little understood when it comes to low-energies and bound states. Despite the fact that it is mainly bound states of protons and neutrons that make up most of the matter on earth. A fact, which often is forgotten in the hunt for BSM effects.

The chiral anomaly, topic of this research project, is a fundamental property of the strong interaction. Still, most of its predictions and implications are only poorly verified by experiment. One of them, the value of the $F_{3\pi}$ constant, is being tested in this thesis. For understanding the theoretical concepts, Chapter 1 gives a compact introduction to the theory of strong interaction, namely Quantum Chromodynamics, and then focuses on the chiral anomaly and its predictions. We also go through existing measurements of $F_{3\pi}$ and discuss their precision and shortcomings. Just as important is the detailed understanding of the kinematics of the reactions of interest. Only when the kinematics are fully understood, the observed distributions can be reproduced in simulation. We therefore dedicate Chapter 2 to the detailed description of the involved scattering processes and elaborate on how we can extract the wanted quantities from our measurement.

There would not be any data to analyze, if there was not the experiment, which recorded the data in 2009. We therefore describe the experimental setup in Chapter 3 and highlight important features for this measurement. Like the people who facilitated this analysis by supporting data taking in 2009, long before I took my first steps in science, I contributed to improvements of the experimental setup, in particular of the data acquisition system, in the years 2015-2018. The outcome of this work is presented in Chapter 4.

Any analysis in high-energy physics begins with identifying signal events in the enormous amount of data which are produced by modern experiments. The event selection and how the events are reconstructed is discussed in Chapter 5. The presented high-precision analysis is very sensitive to the applied event selection and to calibrations applied to the calorimeter. Some calibrations have already been developed for other analysis. Still, we study the impact of all these calibrations and go through details of all applied corrections.

Just as important as a well calibrated spectrometer, is an equally well descriptive Monte-Carlo simulation. The analysis would not have been possible without all the work, that was put into the simulation including the correct kinematics of reactions of interest, be it for diffractive three pions, electromagnetic two pions, or kaon decays. Chapter 6 focuses on the simulation and highlights necessary adjustments. Afterwards, we are prepared for physics analysis and investigate kaon decays in Chapter 7 to determine the luminosity and finally come to the result of the measurement in Chapter 8. We conclude with a short summary of the findings, and an outlook on future analysis which are facilitated by this work.

Chapter 1

Theory and motivation

The strong interaction has preserved some mysteries and challenges for scientists to this day. Despite the progress in quantum field theories, the development of Quantum Chromodynamics in the 20th century, and its very detailed experimental verification in certain areas such as perturbation QCD, many basic features of the strong interaction remain a field of ongoing research. Since this thesis is trying to shed light on some of these basic, little understood phenomena of strong interaction, the first chapter is dedicated to the theory, reveal its challenges and explain the quantities that are measured.

1.1 Quantum Chromodynamics — the theory of strong interaction

The strong interaction is the strongest of all four fundamental interactions in the Standard Model. It binds the protons and neutrons together in nuclei, being so strongly attractive at short distances that it dominates over the electromagnetic repulsion of the liked-charged protons. On an even smaller scale, protons themselves are actually bound states of strong interaction. They are composite objects of quarks. As such, they are part of a whole class of particles called "hadrons" from the Greek word for "strong" ($\alpha\delta\rho\acute{o}\sigma$).

The modern quantum field theory that describes the strong interaction in the Standard Model is Quantum Chromodynamics (QCD). It is supposed to describe all phenomena of nuclear physics. Yet, more than 50 years after the discovery of the elementary particles of QCD, quarks and gluons [2], we are just starting to understand how QCD forms the building blocks of matter, namely protons and neutrons, and how they in turn form heavier composite objects - the nuclei.

The basic degrees of freedom of QCD are the mentioned quarks and gluons. Quarks are massive point-like particles with spin 1/2 (*fermions*). They come in six different flavors $f =$ "up" (u), "down" (d), "charm" (c), "strange" (s), "top" (t), or "bottom" (b). In addition to the flavor quantum number, they carry charge of the strong interaction, the "color" charge. Shortly after the development of the quark model, the need for three colors of quarks became

apparent. For example, the Δ^{++} -resonance with spin $J_z = +3/2$, which should be explained as bound state of $|u \uparrow u \uparrow u \uparrow\rangle$, could not exist due to the Pauli exclusion principle, if the three up-quarks wouldn't differ in the color quantum number. Other experimental evidence, e.g. from measuring cross-sections of e^+e^- annihilation and comparing the cross-sections of hadronic final states to the muonic final state [3, 4]

$$R_{\text{had}} \equiv \frac{\sigma(e^+e^- \rightarrow \text{hadrons})}{\sigma(e^+e^- \rightarrow \mu^+\mu^-)} \quad (1.1)$$

also suggests that there are $N_c = 3$ different color charges in QCD: *red*, *green*, and *blue*.

The strong interaction however, does not distinguish between quarks of different colors. A theory describing the strong interaction should hence incorporate a local color symmetry. The unitary transformations which mix quarks of three different colors are generated by the elements of the $SU(3)$ Lie algebra, namely λ_a with $a = 1, \dots, 8$ that satisfy

$$[\lambda_a, \lambda_b] = i \sum_{c=1}^{N_c^2-1} f_{abc} \lambda^c. \quad (1.2)$$

The standard 3×3 matrix representation of the λ_a according to *Gell-Mann* is given in App. A.1. The f_{abc} are the structure constants of the $SU(3)$ group and are totally antisymmetric in the color labels a, b and c .

A *Dirac spinor*, describing a quark, transforms in the most general way with these generators as:

$$\psi \longrightarrow \tilde{\psi} = \exp\left(-i \frac{\lambda_a \theta_a(x)}{2}\right) \psi \quad (1.3)$$

where $(\theta_1, \theta_2, \dots, \theta_8)$ are eight real parameters. Local color symmetry, i.e. local gauge invariance, requires that the Lagrangian density is invariant under any transformation in the color space according to Eq. (1.3). In analogy to Quantum Electrodynamics (QED), this requires the introduction¹ of a covariant derivative involving a new Lorentz-vector field $G_{\mu\nu}^a$:

$$\mathcal{L}_{QCD} = \sum_{\substack{f=\{u,d, \\ c,s,t,b\}}} \sum_{i,j=1}^{N_c} \bar{\psi}_{f,j} (i\gamma^\mu D_{i,\mu}^j - m_f \delta_i^j) \psi^{f,i} - \frac{1}{4} \sum_{a=1}^{N_c^2-1} G_{\mu\nu}^a G_a^{\mu\nu} \quad (1.4)$$

with $\psi_{f,i}$ spinors of the quark fields with flavor f and color i , γ^μ Dirac matrices², m_f quark masses, and $D_{i,\mu}^j$ is the gauge covariant derivative given by

$$D_{i,\mu}^j = \delta_i^j \partial_\mu + i g_s \sum_{a=1}^{N_c^2-1} \lambda_i^{a,j} A_{a,\mu} \quad (1.5)$$

with g_s is the dimensionless coupling strength and $A_{a,\mu}$ are the gluon gauge fields. The gauge invariant gluon field-strength tensor $G_{\mu\nu}^a$ from Eq. (1.4) is given by:

$$G_{\mu\nu}^a = \partial_\mu A_\nu^a - \partial_\nu A_\mu^a - g_s \sum_{b,c=1}^{N_c^2-1} f_{abc} A_\mu^b A_\nu^c \quad (1.6)$$

¹We use natural units in this chapter, where $\hbar = c = 1$

²The standard representation of the Dirac matrices is given in App. A.2

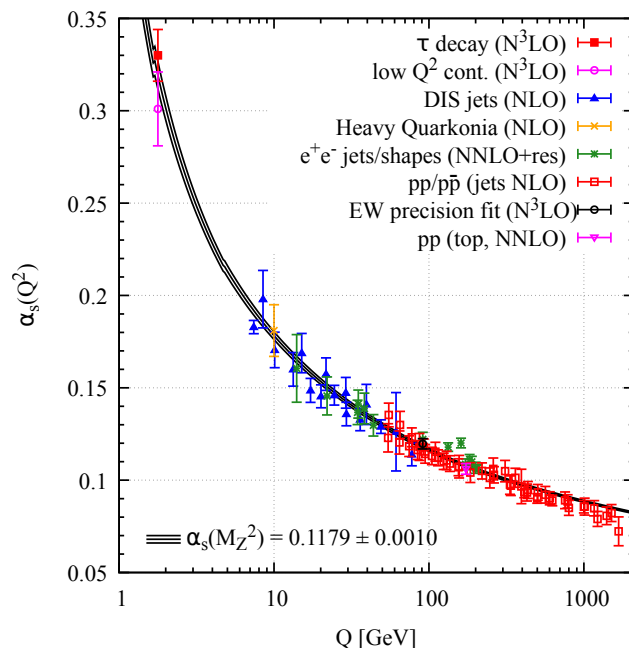


Fig. 1.1 World data on α_s as a function of the energy scale Q overlaid by the theory prediction for $\alpha_s(Q^2)$. The respective degree of QCD perturbation theory used in the extraction of α_s is indicated in brackets (NLO: next-to-leading order; NNLO: next-to-next-to-leading order; NNLO+res.: NNLO matched to a resummed calculation; N³LO: next-to-NNLO). From Ref. [6].

The Lagrangian density of QCD of Eq. (1.4) is a natural consequence of local color symmetry, and it also implies the introduction of a gauge field which is associated to the gluons. Gluons are the massless spin-1 exchange particles which mediate the strong force by coupling to the color charge of the strong interaction via the strong coupling constant α_s . Unlike the photon, exchange boson of Quantum Electrodynamics (QED) and electrically neutral, gluons carry color charge themselves and can hence couple to themselves.

The self-interaction of gluons has important consequences for the behavior of the strong interaction: as in any other quantum field theory, the coupling constant α_s depends on the momentum transfer Q of the physical process under consideration. In QCD (unlike QED), the coupling decreases with increasing energy [5] and is given by

$$\alpha_s(Q^2) \equiv \frac{g_s^2(Q^2)}{4\pi} \approx \frac{1}{\beta_0 \ln(Q^2/\Lambda_{\text{QCD}}^2)} \quad (1.7)$$

where α_s is the QCD equivalent of the fine-structure constant of the electromagnetic interaction, $\beta_0 = (33 - n_f)/(12\pi)$ depends on the number n_f of quark flavors that are considered light, i.e., for which $m_f \ll Q$, and $\Lambda_{\text{QCD}} \approx 200 \text{ MeV}$ is the QCD scale parameter.

The theory prediction for the behavior of the so-called *running coupling* of QCD is well confirmed by cross-section measurements from high-precision, deep-inelastic scattering (DIS) data as shown in Fig. 1.1. The decrease of α_s towards high Q is so strong that the single quarks behave almost as free particles in the regime of extreme energies: high center-of-mass scattering processes, high temperatures or when confined in hadrons with radii much smaller

than the size of a nucleon of about 1 fm. The fact that the coupling strength decreases towards zero at high Q is known as *asymptotic freedom* [7, 8].

Processes in this regime can be calculated analog to QED using a perturbative expansion scheme in powers of α_S . Perturbative QCD has been extensively tested and verified in high-energy accelerators such as the Large Hadron Collider (LHC) at CERN [6].

The success of this technique, however, does not remove the challenge of understanding the non-perturbative aspects of QCD. At low momenta or larger distance scales, α_S is in the order of 1 and an expansion in powers of α_S is not applicable anymore. Low-energy QCD, whose phenomena are critical for the understanding and the concepts of many observed properties of bound states of QCD, remains a challenge for theorists up this very day. To obtain theoretical predictions, different methods have to be applied, such as numerical simulations of QCD (lattice QCD) or the use of effective field theories like Chiral Perturbation Theory.

1.1.1 Confinement and the quark model

The Lagrangian of QCD is written in terms of quarks and gluons. However, at low energies these basic degrees of freedom remain hidden inside hadrons, color neutral composite objects of the strong interaction. There is clear indication of *confinement* not only from experiments but also from lattice QCD [5, 9]. As a consequence, free quarks have not been observed in nature, but they form a rich spectrum of observable hadrons.

Heisenberg's observation of isospin symmetry [10] was the first formal attempt to find regularities in the observed spectrum of particles. In a more modern quark picture, his discovery can be traced back to the similarity of u - and d -quark masses which forms a $SU(2)$ flavor symmetry. This symmetry leads to isospin multiplets with almost identical mass (e.g. the proton/neutron doublet or the pion triplet).

In the early 1960ies, when most of the hadron spectrum was discovered, Murray Gell-Mann [11] and Yuval Ne'eman [12] independently of each other extended the isospin formalism by the third flavor, the strangeness. Mathematically, the famous "eightfold way" forms a $SU(3)$ flavor symmetry with equally mass-degenerate hadron multiplets. Soon after, it was discovered that all newly discovered particles of the "particle zoo" at that time could be described, ordered, and classified according to the "eightfold way" if they were composite objects of only very few different constituents. Gell-Mann named these constituents "quarks". The hadron spectrum could then be subdivided into two classes: mesons with integer spin which are a bound state of quark with color charge and anti-quark with respective anti-color $|q\bar{q}\rangle$; and baryons with half-integer spin which are a bound state of three quarks all with different color charge (color singlet) $|qqq\rangle$.

In the so-called quark model, the quantum numbers of a hadron are fully determined by the quantum numbers of its constituent quarks. For mesons, which are the subject of research of this thesis, the most important quantum numbers are the spin J , the parity eigenvalue P of their wave function, their isospin I , and the third component of the isospin I_z . Another interesting quantum number is the charge conjugation C . For neutral mesons and for charged

mesons without strangeness, the charge conjugation operator \hat{C} can be generalized to the G -parity operator \hat{G} with

$$\hat{G} = \hat{C} e^{i\pi I_y} \quad (1.8)$$

The G -parity is the combination of charge conjugation and a rotation by 180° around the y -axis in isospin space. Such a rotation corresponds to a sign flip of I_z , which in turn is equivalent to a sign flip of the electrical charge and hence compensates for the action of the \hat{C} -operator. The members of an isospin triplet, e.g. (π^-, π^0, π^+) , are eigenstates of the \hat{G} -operator:

$$\hat{G}|\pi\rangle = G|\pi\rangle = (-1)^I \cdot |\pi\rangle \quad (1.9)$$

with

$$G = C(-1)^I \quad (1.10)$$

The G -parity describes the characteristic of the strong interaction which does not see the electric charge of a resonance and hence cannot distinguish between differently charged states. Processes of the strong interaction do therefore conserve G -parity.

1.1.2 QCD in the chiral limit

Following the introduction of the constituent quark model in the early 1960s, every hadron was regarded as an ordinary quantum mechanical bound state of constituent-quarks and/or constituent-antiquarks. In that approach, however, a fine-tuned potential is needed to explain the masses of the light pseudoscalar mesons. For illustration, consider the mass of a neutron $m_N = 940 \text{ MeV}$: in the constituent quark model, the mass of a single quark (m_Q) would be roughly $1/3$ of that of a neutron with a quark content of $|udd\rangle$:

$$m_Q \approx m_N/3 \approx 310 \text{ MeV} \quad (1.11)$$

This result from baryons is consistent with the approximate result from the heavier mesons, e.g. the ρ -meson which consists of a quark and an antiquark: $m_Q = m_{\bar{Q}} \approx m_\rho/2 \approx 390 \text{ MeV}$. However, if one of the eight light pseudoscalar mesons is regarded, e.g. the pion, a quark mass of

$$m_Q = m_{\bar{Q}} \approx m_\pi/2 \approx 70 \text{ MeV} \quad (1.12)$$

is obtained. Compared to the result from Eq. (1.11), this is a completely different scale. The pion and the other light mesons (K, η) appear to be unnaturally light. In the early 1960ies $m_\pi/m_N \approx 0.15$ was regarded as an empirical fact that needed an explanation [13].

A mechanism, in which Nature produces unnaturally light, namely massless, spinless bosons, is when a symmetry is spontaneously or dynamically broken in the underlying theory [14, 15]. The symmetry that is broken in the context of generating the eight pseudoscalar mesons is called *chiral symmetry* and shall be briefly explained here.

Since the masses of the quarks enter the QCD Lagrangian of Eq. (1.4) as free parameters of the theory, the Lagrangian offers various possibilities for symmetries. It is therefore worthwhile

to look at the mass term of the QCD Lagrangian of Eq. (1.4) in more detail (omitting the summation over color indices from now on for simplicity):

$$\mathcal{L}_{\text{mass}} = \sum_{\substack{f,k=\{u,d, \\ c,s,t,b\}}} -\bar{\psi}_f \mathcal{M}_k^f \psi^k \quad (1.13)$$

with the quark mass matrix $\mathcal{M}_k^f = \text{diag}(m_u, m_d, m_c, m_s, m_t, m_b)$. The flavor symmetry of the QCD Lagrangian is only broken by this quark mass term. The quark masses of the different flavors are [16]:

$$\begin{aligned} m_u &= (2.16 \pm 0.49) \text{ MeV} & m_d &= (4.67 \pm 0.48) \text{ MeV} & m_s &= (93 \pm 11) \text{ MeV} \\ m_c &= (1.27 \pm 0.02) \text{ GeV} & m_b &= (4.18 \pm 0.03) \text{ GeV} & m_t &\approx 170 \text{ GeV} \end{aligned} \quad (1.14)$$

Apparently, the masses of the u -, d -, and s -quarks are very small compared to the remaining three flavors and also very small compared to characteristic hadronic scales such as the proton mass ($m_p \approx 938 \text{ MeV}$). On the other hand, the c -, b -, and t -quarks are very heavy. It is hence meaningful to look at the so-called *chiral limit* in which the light quarks are regarded as massless $m_u = m_d = m_s = 0$ and the heavy quarks are regarded as infinitely heavy, which means that they disappear from the Lagrangian as active degrees of freedom.

In the chiral limit, the QCD Lagrangian features an additional, more complex symmetry related to the conserved right- or left-handedness (chirality) of zero mass spin-1/2 particles. Right- and left-handed quark fields are projected out from the general quark fields via

$$\psi_{R,L}^f = \frac{1}{2} (1 \pm \gamma_5) \psi^f \quad (1.15)$$

As for any other field of massless fermions, right- and left-handed quark fields do not “communicate” and decouple from each other. The Lagrangian does therefore provide a flavor symmetry among the three light flavors for left- and right-handed quarks separately: the *chiral* $SU(3)_R \times SU(3)_L$ symmetry. Mathematically, transformations of the form

$$\psi_R^f \longrightarrow \sum_{k=u,d,s} \exp\left(i\theta_R^a \frac{\lambda_{k,a}^f}{2}\right) \psi_R^k, \quad \psi_L^f \longrightarrow \sum_{k=u,d,s} \exp\left(i\theta_L^a \frac{\lambda_{k,a}^f}{2}\right) \psi_L^k \quad (1.16)$$

leave the QCD Lagrangian with $\mathcal{L}_{\text{mass}} = 0$ invariant. Chiral symmetry implies two times eight conserved Noether currents

$$J_{R,a}^\mu = \sum_{f,k=u,d,s} \bar{\psi}_{f,R} \gamma^\mu \frac{\lambda_{k,a}^f}{2} \psi_R^k, \quad J_{L,a}^\mu = \sum_{f,k=u,d,s} \bar{\psi}_{f,L} \gamma^\mu \frac{\lambda_{k,a}^f}{2} \psi_L^k \quad (1.17)$$

with $\partial_\mu J_{R,a}^\mu = \partial_\mu J_{L,a}^\mu = 0$. For convenience, it is common to give a linear combination of these right- and left-handed currents which behave like vector, respectively axialvector currents under parity transformations:

$$\begin{aligned} V_a^\mu &= J_{R,a}^\mu + J_{L,a}^\mu = \sum_{f,k=u,d,s} \bar{\psi}_f \gamma^\mu \frac{\lambda_{k,a}^f}{2} \psi^k \\ A_a^\mu &= J_{R,a}^\mu - J_{L,a}^\mu = \sum_{f,k=u,d,s} \bar{\psi}_f \gamma^\mu \gamma_5 \frac{\lambda_{k,a}^f}{2} \psi^k \end{aligned} \quad (1.18)$$

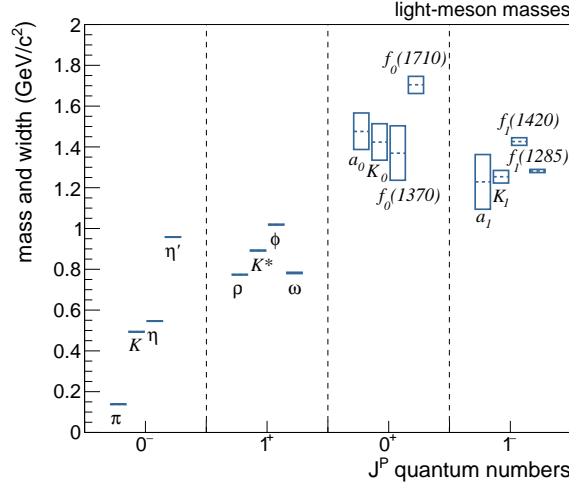


Fig. 1.2 Masses and widths of the light mesons grouped by their quantum numbers J^P . Only the mesons which have a suspected $|q\bar{q}\rangle$ quark model assigned are shown. The assignment is tentative, since not for all mesons the structure is already clarified. In particular for the scalar mesons (0^+), many states that are often considered to be four-quark states are omitted from the figure ($a_0(980)$, $f_0(980)$, $f_0(500)$). The tentative assignment is taken from ref. [17], masses and widths from ref. [18]. Clearly, the chiral symmetry, which should result in parity doublets with the same mass, doesn't seem to be manifested in the spectrum.

with corresponding charges:

$$Q_a^V = \int d^3x \sum_{f,k=u,d,s} \psi_f^\dagger(x) \frac{\lambda_{k,a}^f}{2} \psi^k(x), \quad Q_a^A = \int d^3x \sum_{f,k=u,d,s} \psi_f^\dagger(x) \gamma_5 \frac{\lambda_{k,a}^f}{2} \psi^k(x) \quad (1.19)$$

Now, if chiral symmetry was intact, both vector and axial charge operators would annihilate the vacuum:

$$Q_a^V|0\rangle = Q_a^A|0\rangle = 0 \quad (1.20)$$

Since Q^A and Q^V have opposite parity assignments, one would expect a close similarity of the spectra of positive and negative parity states, in analogy to the intact isospin symmetry which features corresponding mass-degenerate isospin multiplets. However, chiral symmetry does not seem to be manifested in the spectrum of the light mesons. This can be seen in Fig. 1.2 when looking for example at the mass of the ρ -meson with $m_\rho = 0.775$ GeV and its chiral partner the a_1 -meson with $m_{a_1} = 1.23$ GeV. Even more striking is the discrepancy in the case of the pseudoscalar mesons ($J^P = 0^-$). In particular, in the u - and d -quark sector, where one naively would expect the best approximate symmetry due to the fact that in this generation, the quark masses are smallest, one observes the biggest symmetry breaking: the $a_0(1450)$ with $m_{a_0} = 1.47$ GeV and the pion with $m_{\pi^0} \approx 0.135$ GeV. The question arises, why isospin symmetry is such a good symmetry, the eightfold way is still reasonable, but chiral symmetry is not manifested at all in the spectrum. One must conclude that chiral symmetry is spontaneously or dynamically broken. In addition to the experimental evidence manifested in the spectrum of the light mesons, there is also theoretical indication from lattice QCD calculations, see [19].

Following the Nambu-Goldstone mechanism, one of the two vacuum expectation values of Eq. (1.20) should be non-trivial. The approximate symmetry of the three flavors u , d , and

s , $SU(3)_V$, is a subgroup of the chiral group, it is intact, and it is of vectorial character. This suggests that

$$Q_a^V |0\rangle = 0 \quad Q_a^A |0\rangle \neq 0 \quad (1.21)$$

which means that the chiral $SU(3)_R \times SU(3)_L$ symmetry is spontaneously broken down to the flavor group $SU(3)_V$. According to Goldstone's theorem [15], there should be a spinless particle of zero mass for each of the eight broken axial charges with

$$Q_a^A |0\rangle = |\phi_a\rangle \quad (1.22)$$

Since the Q_a^A are axial charges, the Goldstone states of *dynamic chiral symmetry breaking* (DCSB) must have negative parity. The eight light pseudoscalar mesons (π^\pm , π^0 , K^\pm , K^0 , \bar{K}^0 , η) could then be explained as the Nambu-Goldstone bosons which arise as a consequence of the breakdown of chiral symmetry from $SU(3)_R \times SU(3)_L$ to the flavor group $SU(3)_V$. Following this mechanism, the emergent bosons should be massless. However, chiral symmetry is not exact. It holds true only in the case of massless quarks, the *chiral limit*. In reality, the symmetry is explicitly broken by the small masses of the u -, d -, and s -quarks and consequently, also the Nambu-Goldstone bosons acquire masses. But their very special role remains clearly visible in the hadronic mass spectrum. All other baryons and almost all mesons are well separated from the ground state $|0\rangle$ by a characteristic gap of ≈ 1 GeV.

The approach to exploit the chiral symmetry in the chiral limit and treat the small masses of the quarks (u , d , and possibly s) as perturbation was pioneered by S. Weinberg [20] in the late 60ies and during the 70ies. He used an effective Lagrangian which is written in terms of the observable fields of QCD at low energies, i.e. the Goldstone bosons, photon fields, and other matter fields, instead of the basic degrees of freedom of QCD - quarks and gluons:

$$\mathcal{L}_{\text{eff}} = \mathcal{L}(\partial_\mu U(\phi), \mathcal{M}, F, N, \dots) \quad (1.23)$$

with ϕ being the Goldstone bosons of chiral symmetry breaking, \mathcal{M} the quark mass matrix, F the photon field, and N other matter fields. The effective Lagrangian is constructed in a way that it also exhibits chiral symmetry, and it is thereby uniquely determined [20]. Weinberg's first success in calculating correct π - π scattering lengths [21] has triggered subsequent work by Gasser and Leutwyler leading to the development of Chiral Perturbation Theory (ChPT) [22, 23, 24].

By now, many other verified predictions of ChPT (some of which will be explained in later sections of this thesis) have confirmed the standard mechanism of DCSB. Since it allows discussing physics in a manner consistent with the fundamental theory, ChPT came to be well-established as theoretical method in the low-energy regime where the energies are smaller than a typical strong interaction scale $\sim m_p$ [5]. In particular, so-called *low-energy theorems*, which can be derived from ChPT, are an exact result of QCD in the chiral limit. They are a strict consequence of QCD depending only on some parameters that have to be determined phenomenologically, the *low-energy constants* (LEC) [25].

1.2 Pion lifetime and the chiral anomaly

The two main characteristics of QCD, confinement and the appearance of nearly massless pseudoscalar mesons, emergent from the dynamic breaking of chiral symmetry, are non-perturbative phenomena. Both of these phenomena are greatly expressed in the pion. Its dual nature - "on the one hand Goldstone boson of DCSB and on the other hand a superposition of highly relativistic bound states of quark-antiquark pairs in quantum field theory - is conceptually understood and generally accepted" [5].

The pion features another characteristic of QCD, which became apparent with the first measurements of the neutral-pion lifetime.

The first definitive measurements started in the 60ies along with improvements of accelerator technology and hence higher energies so that there exists a large Lorentz boost. In 1963, the 18GeV beam of the proton synchrotron at CERN was used to measure a π^0 -lifetime of $\tau(\pi^0) = (9.5 \pm 1.5) \cdot 10^{-17}$ s [26]³. This value came as a surprise as it differed significantly from the theoretical prediction. Theoreticians at that time used the framework of *Partially Conserved Axial Current* (PCAC) to obtain: $\tau_{\text{PCAC}}(\pi^0) \approx 10^{-13}$ s. This prediction is three orders of magnitudes larger than the measurements suggested.

The solution to this problem was found only in 1969, when at CERN Bell and Jackiw [27] looked at the π^0 -decay and Adler [28] at the Institute for Advanced Study examined spinor field theory. Independent of each other, they were able to determine the correct partial width of the pion as a function of only few constants: the elementary charge e , the number of colors $N_c = 3$, and a LEC - the pion decay constant [29]

$$F_\pi = (92.21 \pm 0.14) \text{ MeV} \quad (1.24)$$

The pion decay constant is proportional to the transition of the one π final state to the vacuum. It can be thought of as the "wavefunction" overlap of the quark and the antiquark that make up the pion. that can be determined from leptonic decays of the charged pion ($\pi^\pm \rightarrow \mu^\pm + \nu$).

With the mentioned constants the partial width of the neutral pion is:

$$\Gamma^{\text{anom}}(\pi^0 \rightarrow \gamma\gamma) = F_{\gamma\gamma}^2 \cdot \frac{m_{\pi^0}^3}{64\pi} = \left(\frac{e^2 N_c}{12\pi^2 F_\pi} \right)^2 \frac{m_{\pi^0}^3}{64\pi} = 7.75 \text{ eV} \quad (1.25)$$

$$\begin{aligned} \tau(\pi^0) &= \text{BR}(\pi^0 \rightarrow \gamma\gamma) \cdot \frac{\hbar}{\Gamma^{\text{anom}}(\pi^0 \rightarrow \gamma\gamma)} \\ &= 8.38 \cdot 10^{-17} \text{ s} \end{aligned} \quad (1.26)$$

where $\text{BR}(\pi^0 \rightarrow \gamma\gamma) = (98.823 \pm 0.034) \%$ [18] is the branching ratio of the neutral-pion decay into two photons and Γ^{anom} its partial decay width as calculated by Adler, Bell, and Jackiw. Their result is based on the (anomalous) non-vanishing value for

$$F_{\gamma\gamma} = \frac{e^2 N_c}{12\pi^2 F_\pi} \quad (1.27)$$

³This is the corrected value that was presented after a reanalysis in 1985

in the chiral limit. The discovery of the anomaly finally explained the experimental values for the lifetime of the neutral pion.

To understand their discovery, we go back to modern QCD. In addition to the chiral $SU(3)_R \times SU(3)_L$ symmetry, the QCD Lagrangian is also invariant under global axial $U(1)$ transformations in the chiral limit:

$$\psi^f(x) \rightarrow e^{i\theta\gamma_5}\psi^f(x) \quad (1.28)$$

Applying Noether's theorem should result in a ninth conserved axial current, the flavor singlet current:

$$\begin{aligned} A_0^\mu &= \sum_{f=u,d,s} \bar{\psi}_f \gamma^\mu \gamma_5 \psi^f \\ &= \bar{\psi}_u \gamma^\mu \gamma_5 \psi^u + \bar{\psi}_d \gamma^\mu \gamma_5 \psi^d + \bar{\psi}_s \gamma^\mu \gamma_5 \psi^s \end{aligned} \quad (1.29)$$

with $\partial_\mu A_0^\mu = 0$. Being a quantum theory, one has to carry through a renormalization procedure for the axial current during which one has renormalization choices. E.g. one can choose to renormalize in such a way that

$$\partial_\mu A_0^\mu = \sum_{f=u,d,s} i2m_f \bar{\psi}_f \gamma_5 \psi^f \quad (1.30)$$

which indeed vanishes in the chiral limit where $m_f = 0$ with $f = u, d, s$. However, it turns out that such a renormalization violates QCD's first principle of local color symmetry and hence is not acceptable. When normalizing in a way that gauge invariance is preserved, an additional term appears in Eq. (1.30) which leads to non-conservation of the axial current even for massless quarks. Although the exact form of this term is not of specific interest for this experimental work, it shall briefly be given for completeness:

$$\partial_\mu A_0^\mu = \frac{\alpha_S}{4\pi} N_f \epsilon_{\mu\nu\rho\sigma} G^{\mu\nu} G^{\rho\sigma} + \sum_{f=u,d,s} i2m_f \bar{\psi}_f \gamma_5 \psi^f \quad (1.31)$$

with N_f the number of considered quark flavors and $\epsilon_{\mu\nu\rho\sigma}$ the fully antisymmetric Levi-Civita tensor. The appearance of the Levi-Civita tensor is characteristic for processes driven by the chiral anomaly and can be made plausible by parity considerations: both, the strong and the electromagnetic interaction conserve parity. To describe interactions with an odd number of pseudoscalars ($P = -1$), an additional minus sign, which is provided by the fully antisymmetric tensor, is needed.

What Adler discovered for the example of QED, where the anomaly exists as well, and Bell and Jackiw discovered for the example of the π^0 -decay was that preserving both, the axial current and gauge invariance, is not possible. One can say that the $U(1)_A$ symmetry of the classical Lagrangian is broken at quantum level. Such symmetry breaking is called anomalous and one refers to anomalies as symmetries of classical Lagrangians which do not lead to conserved Noether currents. The chiral anomaly is sometimes also called ABJ-anomaly for Adler-Bell-Jackiw.

In QCD, the chiral anomaly is responsible for the comparatively high mass of the η' -meson of $m_{\eta'} = 958 \text{ MeV}$. This value is significantly larger than the masses of all other pseudoscalar

$SU(2)$ flavor	$SU(3)$ flavor
$\pi^0 \rightarrow \gamma\gamma$	$K^+ K^- \rightarrow \pi^+ \pi^- \pi^0$
$\gamma\pi^- \rightarrow \pi^- \pi^0$	$\eta \rightarrow \pi^+ \pi^- \gamma$
$\pi^+ \rightarrow e^+ \nu_e \gamma$	$K^+ \rightarrow \pi^+ \pi^- e^+ \nu_e$
etc.	etc.

Table 1.1 Examples of anomalous processes as described by the WZW term

mesons (see Fig. 1.2). Without the chiral anomaly, the $U(1)_A$ -symmetry would lead to a ninth conserved Noether current which should result in nine instead of eight (almost) massless pseudoscalar mesons.

The discovery of the chiral anomaly was put on even more profound theoretical basis in the subsequent years by Wess and Zumino in 1971 [30] and by Witten in 1983 [31]. Wess and Zumino showed that as consequence of the chiral anomaly in an effective theory also other processes with odd number of pseudoscalar mesons appear. And Witten, with the framework of ChPT at hand, observed that the conventional Lagrangian of ChPT according to Gasser and Leutwyler, which contains only interactions with an even number of Goldstone mesons involved, features a hidden additional symmetry which is not a symmetry of the QCD Lagrangian. This symmetry can only be broken by an additional term involving the Levi-Civita tensor. Witten could connect the simplest possible form of such a term to the chiral anomaly and identify it with the effective action of Wess and Zumino. Since then, the additional term connected to the chiral anomaly in the effective Lagrangian of ChPT is called Wess-Zumino-Witten (WZW) term.

The presence of the Levi-Civita tensor means that processes described by the WZW term are of a different character than those of the conventional ChPT Lagrangian. As already mentioned, the anomalous WZW term describes interactions involving an odd number of pseudoscalar mesons or the coupling of one or two photons to one, three, five, etc. pseudoscalars. The existence of the chiral anomaly then, in addition to predicting the decay amplitude for $\pi^0 \rightarrow \gamma\gamma$, also makes parameter-free predictions for other processes [32], some of which are shown in Table 1.1.

As can be seen from the table, the WZW term does not only describe the triangle diagram of the pion decay, as shown in Fig. 1.3a, but also other anomalous box, pentagon, etc. diagrams.

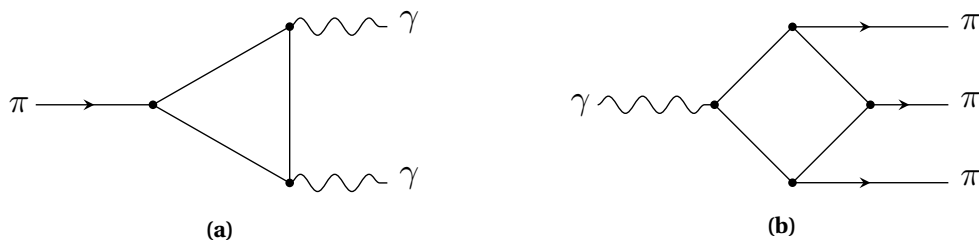


Fig. 1.3 Tree-level diagrams of anomalous processes which proceed dominantly via the Wess-Zumino-Witten term: (a) the decay/coupling of the neutral pion to two photons ($F_{\gamma\gamma}$) and (b) the coupling of one photon to three pions ($F_{3\pi}$)

The most important one for this thesis is shown in Fig. 1.3b: the coupling of one photon to three pions.

The low-energy theorems for the two processes of Fig. 1.3 determine the form factor of the respective process. They can be derived from leading order calculations of ChPT and they are fully governed by the WZW term. For the $\pi^0 \rightarrow \gamma\gamma$ amplitude, the form factor is given by

$$F_{\gamma\gamma} = \frac{e^2 N_c}{12\pi^2 F_\pi} = (2.519 \pm 0.004) \cdot 10^{-2} \text{GeV}^{-1} \quad (1.32)$$

which we know already from Eq. (1.25). Similar calculations for the $\gamma 3\pi$ vertex lead to the following form factor:

$$F_{3\pi} = \frac{e N_c}{12\pi^2 F_\pi^3} = (9.78 \pm 0.04) \text{GeV}^{-3} \quad (1.33)$$

It is noteworthy that both low-energy theorems depend on the number of colors N_c . This can be seen in the diagrams of Fig. 1.3: the triangle and the box represent quark loops and additional freedom in the color charge of the quarks should ultimately increase the amplitude of the interaction. Agreement between theoretical and experimental values therefore seems to be a proof that $N_c = 3$. However, as pointed out by Bär and Wiese [33], a change of N_c would imply a change of quark charges in a way that N_c directly cancels in the leading order terms of most of the anomalous processes. In particular, it cancels in all processes involving only pions and photons, such as the decay of the neutral pion. To justify the chosen notation of the low-energy theorems in which the quark charges do not appear as free parameter anymore, one might argue that these charges are known already from other processes. Hence, the anomalous processes lend additional, yet excellent, experimental support to $N_c = 3$ supplementary to the R-ratio of Eq. (1.1). As a final remark, it should be noted that there are anomalous processes, e.g. the decay $\eta \rightarrow \pi^+ \pi^- \gamma$ whose width is proportional to N_c^2 . Agreement between experiment and theory for this decay would be the ultimate proof for $N_c = 3$ [33].

1.3 Previous tests of the chiral anomaly

Considering the fundamental nature of the existence of the chiral anomaly and the high accuracy of theory predictions of anomalous processes, it is important for experiments to verify the predictions at the same level of precision. There are existing measurements for the verification of $F_{\gamma\gamma}$ and $F_{3\pi}$.

1.3.1 Experimental tests of $F_{\gamma\gamma}$

The π^0 decay offers the most sensitive test of the phenomenon of anomalous symmetry breaking. It is also the most accessible one and—as previously discussed—the process due to which the phenomenon of the chiral anomaly was discovered. The *Particle Data Group* (PDG) lists five measurements that are considered for their average value for the π^0 lifetime which can be seen in Fig. 1.4.

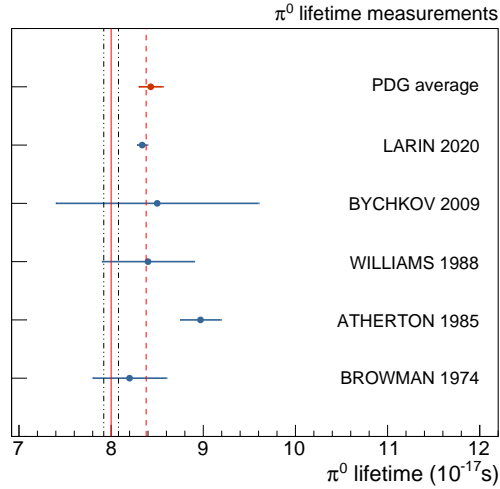


Fig. 1.4 $\tau(\pi^0)$, the mean π^0 -lifetime in units of 10^{-17} s. The experimental results that are shown are: Larin *et al.* (2020) combining data from PrimEx-II and PrimEx-I [34], Bychkov *et al.* (2009) [35], Williams *et al.* (1988) with data from the Crystal Ball detector [36], Atherton *et al.* (1985) [26], Browman *et al.* (1974) [37], and the PDG average value compiled of these five measurements [18]. The right, red, dashed line is the leading-order prediction of the chiral anomaly as first obtained in 1969 by Adler [28], Bell, and Jackiw [27]. The left, red, solid line is the most recent higher-order chiral prediction with its estimated 1% error (black lines) by Moussalam and Kampf (2009) [38].

Despite the fact that π^0 decays appear in huge abundance in many high-energy particle physics experiments, a direct measurement of the π^0 lifetime proves to be difficult due to its small value of $\tau(\pi^0) \approx 10^{-16}$ s. The only possibility for a direct measurement is to determine the propagation distance of a π^0 at high Lorentz-boosts before it decays. The already mentioned first definitive measurement of the π^0 lifetime in 1963 is such a direct measurement. The value of a reanalysis in 1985 [26] is the only direct measurement that is considered for the PDG average.

Another class of measurements made use of the Primakoff effect—see Chapter 2 for an explanation—to determine the coupling strength of a pion to two photons. In the decade from 1965 to 1974, several Primakoff experiments were performed all over the world. Most of them are neglected for the PDG average since they suffer from using the same calculation framework based on a couple of accuracy-limiting approximations [32]. The only Primakoff experiment from this decade contributing to the PDG value is the Browman measurement [37]. This experiment had the advantages of higher beam energies and also utilized an improved calculation framework. The most recent and most precise experimental determination of the lifetime is a Primakoff experiment as well: at JLAB, the PrimEx collaboration conducted two high-precision measurements in the years 2004 and 2010. The combined analysis, which is used for the PDG value, was published in 2020 [34] and reached a 1.5% precision—similar to theory.

The 1988 measurement by the Crystal Ball collaboration [36] is to some extent a generalization of the Primakoff approach. At DESY, they used the e^+e^- collider to investigate the reaction $e^+e^- \rightarrow e^+e^-\gamma^{(*)}\gamma^{(*)} \rightarrow e^+e^-P \rightarrow e^+e^-\gamma\gamma$ with $P = \pi, \eta, \eta'$. In contrast to Primakoff experiments which use nuclear targets, the crystal ball result is based on purely electromagnetic

physics.

The last measurement contributing to the PDG average used data recorded with the PIBETA detector [35]. Bychkov *et al.* investigated the radiative pion decay $\pi^+ \rightarrow e^+ \nu \gamma$ whose form factor is related by an isospin rotation to the amplitude of $\pi^0 \rightarrow \gamma \gamma$.

As can be seen from Fig. 1.4 all measurements, except for the direct measurement, agree well with the leading order prediction of the anomalous triangle diagram of Fig. 1.3 (a). The agreement is even remarkably good and so far it is the strongest proof for the concept of the chiral anomaly. However, the situation is not completely satisfying since the prediction should be valid only in the non-physical chiral limit with vanishing quark masses. Corrections due to explicit chiral symmetry breaking should modify this value. The most recent calculation including such “real world” corrections as well as NNLO corrections of ChPT was calculated by Kampf and Moussallam in 2009 [38]. It is drawn in Fig. 1.4 as solid red line with its 1% error. The two most precise measurements do not agree with this prediction within their errors. To which extent the chiral anomaly is correctly described by the WZW term of ChPT and how its predictions in the chiral limit are correctly extrapolated to the physical quark masses is hence not yet satisfactorily clarified.

1.3.2 Experimental tests of $F_{3\pi}$

A high-precision verification of the hypothesis of the chiral anomaly in other processes governed by the WZW term is certainly of interest. In the case of the $\gamma 3\pi$ vertex, as sketched in Fig. 1.3 (b), there exists a measurement that was performed in 1987 by Antipov *et al.* [39]. The experiment was carried out at the 40 GeV negative-pion beam of the IHEP accelerator (Serpukhov, Russia) with the SIGMA spectrometer. The vertex of interest can be accessed in reactions

$$\pi^- \gamma^{(*)} \rightarrow \pi^- \pi^0 \quad (1.34)$$

where the incoming negative pion is the beam particle and the photon is provided by the Primakoff effect. For details about Primakoff reactions, please refer to Chapter 2.

To extract the value of $F_{3\pi}$, Antipov *et al.* were facing the challenge that the prediction of the form factor according to Eq. (1.33) is only valid at the non-physical point of $s = t = u = 0$ (s , t , and u being the *Mandelstam* variables see Sec. 2.1.1) which can only be accessed in the chiral limit with vanishing quark masses and hence massless pions. In real world, a center-of-mass energy of at least $\sqrt{s} > 2m_\pi$ is necessary to produce the two pions in the final state. For details about the kinematics, refer to Sec. 2.3.

Antipov *et al.* measured the number of identified $\pi^- \gamma^{(*)} \rightarrow \pi^- \pi^0$ events just above the kinematic threshold for $2m_\pi < \sqrt{s} < 4m_\pi$ as shown in Fig. 1.5. They assumed a constant average amplitude for the form factor $\overline{F}_{3\pi}$ over the experimentally covered range in s and in t and normalized the amount of expected events to the atomic number Z of their target materials and selected range for the photon momentum $q^2 < 2 \cdot 10^{-3} \text{ GeV}^2$. Finally, they fitted the theory prediction folded with their acceptance to the data as indicated by the red line in Fig. 1.5 and

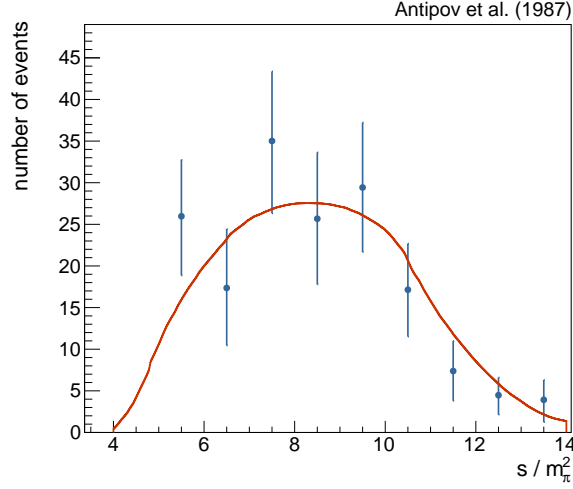


Fig. 1.5 Distribution of the events in reaction (1.34) over s as measured by Antipov *et al.* [39]. The line is the theoretical cross-section with account for the acceptance normalized for the number of events from reaction (1.34) in the range $q^2 < 2 \cdot 10^{-3} \text{ GeV}^2$.

obtained:

$$F_{3\pi}^{\text{Antipov}} = (12.9 \pm 0.9 \pm 0.5) \text{ GeV}^{-3} \quad (1.35)$$

This result suggests some tension with the low-energy theorem of Eq. (1.33) when it is directly compared. However, in 2001 Ametller *et al.* [40] showed that “resort to theory is necessary in order to bridge the gap between $F_{3\pi}(0, 0, 0)$ and the measured amplitude $\bar{F}_{3\pi}(s, t, u)$ ”. Close to the threshold region where the Mandelstam variables are small compared to the typical hadronic scale set by the ρ meson mass, they constructed a systematic expansion within the framework of ChPT. If isospin symmetry is preserved, the tree-level term of the chiral expansion does not feature any dependence on the Mandelstam variables: $F_{3\pi}^{\text{LO}}(s, t, u) = F_{3\pi}$. But with one- and two-loop contributions having become available [41, 42], Ametller *et al.* obtained a different value from the Serpukhov data:

$$F_{3\pi}^{\text{NNLO}} = (11.4 \pm 1.3) \text{ GeV}^{-3} \quad (1.36)$$

which is lower than the result from Eq. (1.35) but still 1.3σ from the theory prediction.

In a second step, they took isospin breaking effects into account and realized that there is a significant electromagnetic correction to the leading-order term. For details about the corrections, please refer to Sec. 2.3.3. They calculated the correction and obtained:

$$F_{3\pi}^{\text{Ametller}} = (10.7 \pm 1.2) \text{ GeV}^{-3} \quad (1.37)$$

finally removing the tension of the experiment with the low-energy theorem.

In 2005, an experimental value for $F_{3\pi}$ was extracted from $\pi^- e^- \rightarrow \pi^- e^- \pi^0$ reactions [43]. This extraction was based on cross section measurements for the given process that was published already in 1985 by the NA7 experiment at CERN: Amendolia *et al.* [44] reported 36 identified events sitting on a dominant background of elastically scattered $\pi^- e^-$. Although

the experimental background was described, comparisons of experimental and theoretical distributions in different kinematic variables have not been published and this data is lost. It is hence impossible to verify the treatment of the background. The 36 identified $\pi^- e^- \rightarrow \pi^- e^- \pi^0$ events correspond to a cross section of (2.11 ± 0.47) nb [44]. I. Giller *et al.* went ahead and extracted a value for $F_{3\pi}$ from this data and obtained [43]:

$$F_{3\pi}^{\text{NA7}} = (9.6 \pm 1.1) \text{GeV}^{-3} \quad (1.38)$$

Both results are in agreement with the theory prediction. However, they are only tested at the 10% level. In particular for the NA7 result, there are technical inconsistencies and questions about the correct handling of the data arise. It would clearly be desirable to improve the accuracy of experimental verification to the same level as theory ($\mathcal{O}(1\%)$) and confront the low-energy theorem with more modern data and refined analysis approaches. The COMPASS experiment at CERN recorded data with a negative pion beam impinging on nuclear targets in 2009 and 2012. Together with a calorimetric trigger on neutrals in the final state, this data set contains $\pi^- \gamma^{(*)} \rightarrow \pi^- \pi^0$ events as already shown in [45] and [46]. This thesis will pave the way for a state-of-the-art extraction of a value for $F_{3\pi}$ based on the COMPASS 2009 Primakoff data set.

1.4 Radiative width of the ρ meson

The measurement of $F_{3\pi}$ is strongly connected to a measurement of the radiative width of the $\rho(770)$ meson, $\Gamma(\rho^\pm \rightarrow \pi^\pm \gamma)$. For details, refer to Section 2.3.2. The ρ is an isospin triplet whose three states are ρ^+ , ρ^0 , and ρ^- . The ρ mesons are the lightest vector mesons ($J^P = 1^-$) with a mass of $m_\rho = (775.26 \pm 0.25)$ MeV [18] and hence take a special place in the spectrum of light mesons. This section will illustrate the importance of measuring the radiative width of the ρ and discuss previous experimental determinations.

1.4.1 Motivation to study radiative decays of vector mesons

Radiative decays of the low-lying vector mesons are very interesting for tests of the quark model, SU(3), and the Vector Dominance Model. An overview of early publications during the 70ies after the development of the quark model can be found in [47]. In analogy to the hydrogen atom, the radiative decay of a vector meson to a pseudoscalar meson can be viewed as a transition from a 3S_1 to a 1S_0 state of the quark-antiquark system in the constituent quark model. Simple quark model calculations for the radiative width of the ρ that can be seen as

$$|\rho^-\rangle = d \uparrow \bar{u} \uparrow \quad (1.39)$$

vary

$$\Gamma(\rho^- \rightarrow \pi^- \gamma)_{\text{qm}} = \begin{cases} 120 \text{ keV} & \text{in 1965 [48]} \\ (67 \pm 7) \text{ keV} & \text{in 1980 [47]} \\ 45.8 \text{ keV} & \text{in 1992 [49]} \end{cases} \quad (1.40)$$

and spark interest in a modern, solid experimental determination. More recent lattice calculations [50, 51] approach the physical pion mass and are now in a position to be tested quantitatively. The updated value from lattice calculations for the physical pion mass is [52]

$$\Gamma(\rho^- \rightarrow \pi^- \gamma)_{\text{lattice}} = (168 \pm 13 \pm 8) \text{keV} \quad (1.41)$$

which suggests tension with the experimental values.

Interest in the radiative width of the ρ has also been triggered by a recent determination of the anomalous magnetic moment of the muon [53], which suggested some tension with the SM. The magnetic moments of electron and muon, defined as

$$\vec{\mu}_\ell = g_\ell \left(\frac{q}{2m_\ell} \right) \vec{s} \quad (1.42)$$

with the Landé g -factor

$$g_\ell = 2(1 + a_\ell) \quad (1.43)$$

($\ell = e, \mu$) have played an important role in the development of the SM. Following the prediction of the Dirac equation, the g -factor for both, electron and muon, should be $g_\ell = 2$. Deviations from this value, collected in a_ℓ , the anomalous magnetic moment, arise within the SM from virtual effects including electromagnetic, strong, and weak interactions. For a high-precision measurement of the anomalous magnetic moment of the muon a_μ , the international theory community calculated the contributions to a_μ from the SM [54]. Different contributions add to a_μ . The one with the biggest relative uncertainty is hadronic light-by-light scattering (HLbL). Data-driven calculations of HLbL contributions rely on experimental input [54], in particular for the electromagnetic form factors of the light vector mesons. A precise experimental determination of the radiative width of the $\rho(770)$ will help to reduce the uncertainties on the determination of $(g-2)_\mu$.

1.4.2 Previous measurements

Direct measurements of vector meson decays V to a pseudoscalar meson $P + \gamma$ are not feasible due to the small partial rates of these processes. The inverse reaction can be studied by photo-producing the vector meson through the exchange of a virtual pseudoscalar meson between a nuclear target and an incident photon: $\gamma_{\text{beam}} + P \rightarrow V$. However, several hadronic exchanges can lead to the same final state and determinations of the radiative width become model-dependent.

Reversing the role of beam and target is advantageous: An incident pseudoscalar can then absorb a photon from the Coulomb field of the target nucleus (Primakoff process) and form the vector meson: $P_{\text{beam}} + \gamma \rightarrow V$. For details on Primakoff processes, see Chapter 2. But even then, there will be hadronic exchanges contributing. However, as will be explained in Sec. 2.1.3, Coulomb production is well understood and dominates over hadronic production mechanisms at high beam energies, which allows for a less model-dependent extraction of radiative widths. Previous measurements of the radiative width of the ρ^\pm all used the Primakoff effect in the reaction $\pi^\pm A \rightarrow \pi^\pm \pi^0 A$. The three measurements contributing to the PDG

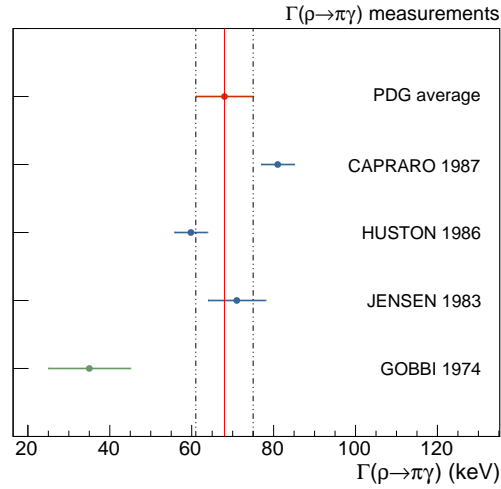


Fig. 1.6 $\Gamma(\rho^\pm \rightarrow \pi^\pm \gamma)$, the radiative width of the ρ (770). The experimental results that are shown are: The PDG average value [18] in red compiled of the three values in blue, Capraro *et al.* (1987) [55], Huston *et al.* (1986) [56], Jensen *et al.* (1983) [57], and the for the PDG average neglected value of Gobbi *et al.* (1974) [58] in green.

average value and the first definitive measurement of the radiative width are summarized in Fig. 1.6.

The first definitive measurement by Gobbi *et al.* [58] in 1974 was conducted at Brookhaven National Laboratory. They used a pion beam of $p_{\text{beam}} = 22.6 \text{ GeV}$. At such comparatively low beam energies, hadronic exchanges still contribute significantly. It is essential to reliably separate Coulomb and strong parts. In particular, a_2 exchange effects may have been neglected in early extractions [47]. This is probably the reason accounting for the discrepancy between the first extractions and later measurements.

All three experiments that are considered by the PDG for the average value have been performed at higher beam energies. Jensen *et al.* (1983) [57] used the π^- beam at Fermilab at incident beam momenta of 156 GeV and 260 GeV where Coulomb production is expected to dominate the coherent cross section. To be able to study possible hadronic contributions, they measured at two different beam energies. Later in 1986, Huston *et al.* [56] conducted a similar experiment at Fermilab, this time with a π^+ beam at 200 GeV to test isospin symmetry at the same time. The last measurement contributing to the PDG averaged value is an experiment at CERN: Capraro *et al.* extracted the ρ radiative width from data obtained with a π^- beam at 200 GeV. Compared to the previous measurements, they employed an improved background subtraction based on Monte-Carlo simulation of the dominant $\pi^- \pi^0 \pi^0$ background.

All the mentioned measurements used a Breit-Wigner fit to extract the partial decay width of the ρ . As it will become clear in Sec. 2.3.2 of this thesis, the shape of the ρ can not accurately be described by a Breit-Wigner function. Moreover, none of the above mentioned experiments considered chiral production of $\pi^- \pi^0$ as possible source of background. We will see in the following, that the measurement of $F_{3\pi}$ and $\Gamma(\rho \rightarrow \pi^- \gamma)$ are connected, form potential background to each other, and are best measured in a combined approach.

Chapter 2

Primakoff reactions

Various different kinds of reactions may occur in a scattering process, each with characteristic dependencies on kinematic variables. The reaction of interest for the determination of $F_{3\pi}$ is a so-called Primakoff reaction. Still, the understanding of other processes is important, since they potentially form background contributions to our desired reaction. This chapter will therefore start with a very brief introduction to scattering processes in general, and subsequently focus on Primakoff reactions. In particular, the kinematics of the $\pi^- \gamma^{(*)} \rightarrow \pi^- \pi^0$ reaction will be discussed in greater detail, since it is the process which gives access to the $\gamma 3\pi$ vertex.

2.1 Introduction to scattering processes

In a typical scattering experiment, a beam particle 1 hits a target particle 2. The target particle may be at rest (fixed-target setup) or accelerated (collider setup). The interaction of the two particles potentially results in the production of several (N_f) new particles in the final state:

$$1 + 2 \rightarrow 3 + 4 + \dots + (N_f + 2) \quad (2.1)$$

Some of the new particles might be short-lived and will only be detected by its decay products in the final state. Such a short-lived particle is called a resonance (X) and it can occur in the scattering process in the following ways:

$$1 + 2 \rightarrow X \rightarrow 3 + 4 + \dots + (N_f + 2) \quad (2.2)$$

or

$$1 + 2 \rightarrow 3 + X \rightarrow 3 + (4 + \dots + (N_f + 2)) \quad (2.3)$$

2.1.1 Mandelstam variables

Since any decay of a resonance X into a multi-particle final state can be modeled as a sequence of two-body decays, the two-body process plays a distinguished role. We will therefore

restrict ourselves to two-body kinematics $1 + 2 \rightarrow 3 + 4$ in the following.

Consider two incoming particles with momenta \vec{p}_1 and \vec{p}_2 and masses m_1 and m_2 and two outgoing \vec{p}_3 and \vec{p}_4 . The four-momenta are defined as $p_i^\mu = (E_i, \vec{p}_i)$ with $E_i^2 = m_i^2 + \vec{p}_i^2$. The Lorentz-invariant Mandelstam variables are then defined as:

$$\begin{aligned} s &= (p_1^\mu + p_2^\mu)^2 = (p_3^\mu + p_4^\mu)^2 = m_1^2 + m_2^2 + 2(E_1 E_2 - \vec{p}_1 \cdot \vec{p}_2) \\ t &= (p_1^\mu - p_3^\mu)^2 = (p_2^\mu - p_4^\mu)^2 = m_1^2 + m_3^2 - 2(E_1 E_3 - \vec{p}_1 \cdot \vec{p}_3) \\ u &= (p_1^\mu - p_4^\mu)^2 = (p_2^\mu - p_3^\mu)^2 = m_1^2 + m_4^2 - 2(E_1 E_4 - \vec{p}_1 \cdot \vec{p}_4) \end{aligned} \quad (2.4)$$

and they satisfy

$$s + t + u = \sum_{i=1}^4 m_i^2 \quad (2.5)$$

which means that there are only two independent variables to fully characterize a two-body scattering process for given masses m_i . In the center-of-momentum (*cm*) frame, we have $\vec{p}_1 = -\vec{p}_2$ and $\vec{p}_3 = -\vec{p}_4$ and thus:

$$\begin{aligned} s &= (E_1 + E_2)^2 = (E_3 + E_4)^2 \\ t &= m_1^2 + m_3^2 - 2(E_1 E_3 - |\vec{p}_1| |\vec{p}_3| \cos \theta_{\text{cm}}) \\ u &= m_1^2 + m_4^2 - 2(E_1 E_4 - |\vec{p}_1| |\vec{p}_4| \cos \theta_{\text{cm}}) \end{aligned} \quad (2.6)$$

introducing the scattering angle θ_{cm} between particle 1 and 3 in the *s*-channel center-of-momentum frame. The physically allowed phase-space region for the *s*-channel process is defined by two independent variables s and θ_{cm} and features a threshold in s :

$$s \geq (m_1 + m_2)^2 \text{ and } -1 \leq \theta_{\text{cm}} \leq +1 \quad (2.7)$$

The differential cross-section for any inelastic scattering process according to equation (2.1) is given by:

$$d\sigma = \frac{1}{F} |\mathcal{M}_{fi}|^2 d\phi_{N_f}(p_1^\mu + p_2^\mu; p_3^\mu, \dots, p_{N_f+2}^\mu) \quad (2.8)$$

with the flux factor F , which for a collinear collision of two particles is generally given by

$$F = 4((p_{1\mu} p_2^\mu)^2 - m_1^2 m_2^2)^{1/2}, \quad (2.9)$$

the Lorentz-invariant N_f -body phase-space element $d\phi_{N_f}$, and the *matrix element* (or amplitude) for the transition from initial state $|i\rangle$ to final state $|f\rangle$ \mathcal{M}_{fi} . Again looking at the two-body reaction in the center-of-momentum frame, we have $\sqrt{s} = E_1 + E_2 = E_3 + E_4$, $|\vec{p}_1| = |\vec{p}_2| =: p$, and $|\vec{p}_3| = |\vec{p}_4| =: p'$. The flux factor in Eq. (2.9) and the phase-space element in Eq. (2.8) become in this case

$$F = 4p\sqrt{s} \quad (2.10)$$

and

$$d\phi_2 = \frac{1}{4\pi} \frac{p'}{\sqrt{s}} \frac{d\Omega}{4\pi} \quad (2.11)$$

with $d\Omega = d\cos\theta_{\text{cm}} d\phi$ is the solid angle element around the scattering angle $\theta_{\text{cm}} = \angle(\vec{p}_1, \vec{p}_2)$.

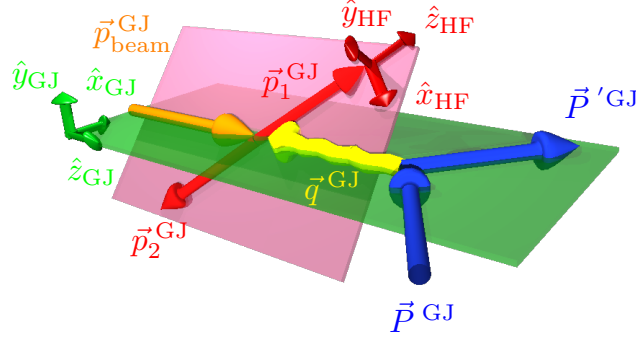


Fig. 2.1 Definition of the Gottfried-Jackson (GJ) and helicity (HF) reference frames. The target (\vec{p}^{GJ}) and the recoil (\vec{p}'^{GJ}) span the production plane in green. The two particles in the final state (\vec{p}_1 and \vec{p}_2) go back-to-back and form the red plane with the beam particle.

2.1.2 Coordinate systems

The angular distributions of a physics process are studied in the *cm*-frame of the interaction or the decay. It is common to introduce the Gottfried-Jackson (GJ) reference frame. In this frame, the direction of the beam particle defines the z_{GJ} axis. This suffices to define the polar scattering angle θ_{GJ} , the angle in the red plane between an outgoing particle and the beam direction. However, specific angular distributions from conservation of angular momentum of parent and daughter particles including their spin, would result in modulations of the azimuthal angle. The reference plane for azimuthal distributions is given by the so-called production plane, which is the plane that is spanned by target, recoil, and beam momenta. The y_{GJ} axis is defined as the normal of the production plane:

$$\hat{y}_{\text{GJ}} = \frac{\vec{p}_{\text{recoil}}^{\text{GJ}} \times \vec{p}_{\text{beam}}^{\text{GJ}}}{|\vec{p}_{\text{recoil}}^{\text{GJ}} \times \vec{p}_{\text{beam}}^{\text{GJ}}|} = \frac{\vec{p}_{\text{beam}}^{\text{lab}} \times \vec{p}_X^{\text{lab}}}{|\vec{p}_{\text{beam}}^{\text{lab}} \times \vec{p}_X^{\text{lab}}|} \quad (2.12)$$

with ϑ and φ being the angle between recoil and beam momentum in the GJ-frame and beam and final state momentum in the laboratory frame. Circumflexes indicate unit vectors. As suggested in Eq. (2.12), \hat{y}_{GJ} can be calculated in the lab frame from the measured directions of the beam and the final state vector. Fig. 2.1 illustrates the definition of the Gottfried-Jackson frame. The angular distributions can be described by the polar angle θ_{GJ} and the azimuthal angle ϕ_{GJ} (the angle between the red and green plane). The azimuthal angle in the GJ frame is also called Treiman-Young angle ϕ_{TY} .

Since in the GJ frame X is at rest, the momenta of the two particles forming X are back-to-back. If one of these particles is unstable and decays further, e.g. particle 1 in Fig. 2.1, its decay is described in the helicity frame (HF). The HF is constructed by boosting into the rest frame of the unstable particle. The z_{HF} axis points into the original direction of motion of the unstable particle in the GJ frame, \vec{p}_1^{GJ} in Fig. 2.1. The y axis of the HF frame is defined as $\hat{y}_{\text{HF}} = \hat{z}_{\text{GJ}} \times \hat{z}_{\text{HF}} / |\hat{z}_{\text{GJ}} \times \hat{z}_{\text{HF}}|$ and the \hat{x}_{HF} is defined to form a right-handed coordinate system. Again, the daughter particles of the decaying particle are emitted back-to-back in the helicity frame and angular distributions can be given by θ_{HF} and ϕ_{HF} .

2.1.3 Strong production mechanisms of light mesons at COMPASS

Interactions of our beam pion with the target can be of strong and electromagnetic character, see Fig. 2.2. Since the strong production of $\pi^- \pi^0$ and $\pi^- \pi^0 \pi^0$ final states constitutes the potential background for $\pi^- \gamma^{(*)} \rightarrow \pi^- \pi^0$ reactions (indeed the biggest component is the strong production of $\pi^- \pi^0 \pi^0$), we will focus in this section on the strong production mechanisms of light mesons at COMPASS and summarize their dependencies on relevant kinematic variables.

At high beam energies, as it is the case for the COMPASS experiment, momentum is transferred to target nuclei mostly in the t -channel [59] (see Fig. 2.2). The four-momentum carried by the exchange particle is called q^μ by convention. It should be noted that the exchange particle is a space-like virtual particle and hence $q^2 < 0$. To work with positive values, one commonly defines Q^2 in the following way:

$$q^2 = q_\mu q^\mu =: -Q^2 \quad (2.13)$$

The longest-range component of the strong force between our beam particle and the target nucleon/nucleus is provided by the exchange of the lightest color-singlet bosons. The exchange of heavier particles will lead to contributions at shorter ranges. Regge theory [60, 61, 62] provides a successful tool to sum up contributions of the different exchange particles. Ordinary Regge exchange particles are for example the π , the ρ , ω , or f_2 . These quasi-particles are called Reggeons (\mathbb{R}). Experimentally, it is known that the differential cross section falls approximately exponentially with Q^2 for small Q^2 :

$$\frac{d\sigma}{dQ^2} \propto g(Q^2) \cdot e^{-bQ^2} \quad (2.14)$$

with b being a positive number that is characteristic for the target material, the Reggeon scatters off, and $g(Q^2)$ a coupling constant [59], whose Q^2 -dependence is given by the quantum numbers of the considered Reggeon.

At high energies however, strong hadron scattering processes are not mediated by ordinary Regge exchange particles, but mainly by *Pomeron* exchange. Such processes are called *diffractive*. They completely dominate the cross section at high center-of-mass energies and feature

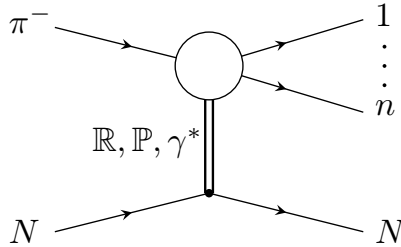


Fig. 2.2 Production of an n -body final state X via diffraction or photon exchange of a pion beam on a target nucleon/nucleus N .

Table 2.1 Dependencies of the total cross section on selected experimental parameters for different scattering processes. The shown Q^2 dependencies are valid for small Q^2 .

	Primakoff	\mathbb{P} (strong)	\mathbb{R} (strong)
$\sigma(E_{\text{beam}})$	$\propto \ln(\sqrt{E})$	$\propto \text{const.}$	$\propto 1/\sqrt{E}$
$\sigma(A_{\text{target}})$	$\propto \text{const.}$	$\propto A^{2/3}$	$\propto A^{2/3}$
$\sigma(Z_{\text{target}})$	$\propto Z^2$	$\propto \text{const.}$	$\propto \text{const.}$
$\sigma(Q^2)$	$\propto \frac{Q^2 - Q_{\text{min}}^2}{Q^4}$	$\propto (Q^2)^M e^{-bQ^2}$	$\propto g(Q^2) \cdot e^{-bQ^2}$

a characteristic Q^2 -dependence

$$\frac{d\sigma}{dQ^2} \propto (Q^2 - Q_{\text{min}}^2)^M e^{-b(Q^2 - Q_{\text{min}}^2)} \quad (2.15)$$

with M being the spin projection, i.e. the spin of the outgoing system projected on the beam axis. The $\pi^- + \text{Ni} \rightarrow \pi^- \pi^0 \pi^0 + \text{Ni}$ reactions, which are the reactions of interest in this thesis in terms of the diffractive contribution, are dominated at small masses of $m_{3\pi}$ by $M = 0$ [63]. The Q^2 -dependence has to be multiplied with the (strong) form factor of the target nucleus with a characteristic series of diffractive minima and maxima in Q^2 .

For Pomeron exchange, the produced intermediate or final state X has the same isospin, strangeness, C -, and G -parity as the beam particle. For a pion beam in particular, this means that in diffractive reactions only states with $I^G = 1^-$ can be produced and hence according to Eq. (1.9), only final states with an odd number of pions are possible:

$$G(|\pi\rangle) = -1 \neq G(|\pi\pi\rangle) = +1 \quad (2.16)$$

In addition to the above mentioned strong processes, also electromagnetic interaction between the beam particle and the nucleus can occur. These electromagnetic interactions between an ultra-relativistic beam particle and a nucleus are called *Primakoff* reactions and will be the main focus of this work. The next sections are dedicated to explain the dependencies of Primakoff reactions on the kinematic variables.

Table 2.1 summarizes the dependencies of \mathbb{R} - and \mathbb{P} -exchange and also lists the dependencies of Primakoff reactions, as discussed below, for comparison. In terms of relative cross section among the three presented reactions, diffractive processes dominate at beam energies of interest. However, in final states with an even number of pions, \mathbb{P} -exchange is forbidden due to G -parity conservation of the strong interaction, and Primakoff reactions dominate over possibly allowed other \mathbb{R} -exchanges (e.g. π and ω). At last, it should be noted that multi-Regge exchange processes like *central-production* or *Deck-like* effects [64] also contribute and modify the observed \hat{t} -distributions.

2.2 The Primakoff effect

In the following, I will explain and motivate Primakoff reactions and the relevant kinematic quantities. These quantities span five orders of magnitude from tiny momentum transfers

$|q| = \mathcal{O}(10^{-3} \text{ GeV}/c)$ to the required beam momenta $|p_{\text{beam}}| = \mathcal{O}(10^2 \text{ GeV}/c)$. The large scale variation imposes great experimental challenges which will be covered in Chapter 3. The topic of this chapter are the more formal algebraic and numerical challenges that also arise from dealing with this large scale difference [45].

It is essential to understand the kinematics of Primakoff reactions for two reasons: first, Primakoff reactions may differ in certain kinematic variables from other processes and it is therefore possible to select and distinguish them from background processes, and second a profound knowledge of the kinematics is needed to determine the acceptance of the spectrometer via Monte Carlo simulation. This section will cover kinematic quantities of Primakoff reactions in general. The particular kinematics of the $\pi^- \gamma^{(*)} \rightarrow \pi^- \pi^0$ reaction will be covered in Section 2.3.

2.2.1 Henry Primakoff's idea of a photon target

When beam particles interact electromagnetically in the Coulomb field of a target nucleus, the interaction is mediated by photons. Henry Primakoff proposed in 1951 to make use of the electromagnetic interaction and measure the π^0 production cross section in the collision of a beam photon and a photon stemming from the Coulomb field of a nucleus [65] as depicted in Fig. 2.3. We know this reaction already from Sec. 1.3: the up-to-now most precise determination of the π^0 -lifetime [34] follows the original approach of Henry Primakoff and utilizes the Primakoff effect to measure the production cross section of π^0 -mesons.

Primakoff's idea of a "photon" target exploits the similarity between the electromagnetic fields of a relativistically moving particle and the fields of a pulse of radiation. A comprehensive treatise of the Lorentz-transformations of the electromagnetic field of a relativistic particle can be found in Ref. [66] and is shortly summarized in Appendix A.3. It motivates why the interaction of an ultra-relativistic particle with the Coulomb-field of a nucleus can be approximated by the exchange of a single photon—an approximation that von Weizsäcker and Williams had already formalized in the 1930ies (see Section 2.2.3). Henry Primakoff was the first to propose to exploit this fact to study photon-photon interactions. Extending the original idea, one considers *Primakoff reactions* or the *Primakoff effect* as scattering of any ultra-relativistic particle, not only photons, on Coulomb-field quanta, i.e. quasi-real photons, of a nucleus.

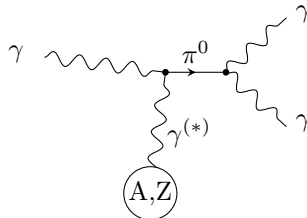


Fig. 2.3 Photo-production of a π^0 : an incident photon interacts electromagnetically with a target nucleus with atomic number A and charge number Z . The interaction, which takes place in the Coulomb field of the nucleus, is mediated by photon exchange. The two photons can form a π^0 -meson.

2.2.2 Minimum momentum transfer

One of the most important quantities by which Primakoff reactions are characterized, is the transferred momentum q to the nucleus. As we will see in this chapter, there is a minimum momentum transfer Q_{\min} due to four-momentum conservation. Equations for Q_{\min} have already been established in Refs. [45, 67] neglecting the small recoil energy of the nucleus. However, for the specific Primakoff channel of interest for this thesis $\pi^-\gamma^{(*)} \rightarrow \pi^-\pi^0$ it turned out to be necessary to include the recoil particle into the considerations.

To develop the necessary equation, we will start with the kinetic energy which is transferred to the nucleus. Fig. 2.4 shows the typical kinematic in the laboratory frame and the chosen naming convention for the involved momenta when a beam particle with four-momentum p_{beam} scatters off a fixed target with mass M . Since for a fixed-target setup, the target nucleus before the collision p_{target} is at rest and after the collision p_{recoil} , it has gained the energy E_{kin} and three-momentum \vec{q} , we have:

$$q = p_{\text{target}} - p_{\text{recoil}} = \begin{pmatrix} M \\ \vec{0} \end{pmatrix} - \begin{pmatrix} M + E_{\text{kin}} \\ -\vec{q} \end{pmatrix} = \begin{pmatrix} -E_{\text{kin}} \\ \vec{q} \end{pmatrix} \quad (2.17)$$

The squared four-momentum of the target is Lorentz-invariant and we can say:

$$\begin{aligned} p_{\text{target}}^2 &= p_{\text{recoil}}^2 \\ M^2 &= M^2 + 2ME_{\text{kin}} + E_{\text{kin}}^2 - \vec{q}^2 \\ \Rightarrow E_{\text{kin}} &= \frac{Q^2}{2M} \end{aligned} \quad (2.18)$$

where we have used that $E_{\text{kin}}^2 - \vec{q}^2 = q^2 = -Q^2$. The minimum kinetic energy $(E_{\text{kin}})_{\min}$, which the nucleus gains in the collision is given by $(E_{\text{kin}})_{\min} = Q_{\min}^2/2M$.

Before we derive expressions for Q_{\min} , we have to define p_X : it is the sum of the four-momenta

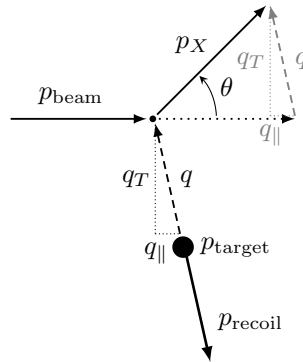


Fig. 2.4 Kinematics for a fixed-target Primakoff process into final state X in the laboratory frame: the target nucleus with mass M is at rest before the collision ($p_{\text{target}} = (M, \vec{0})$) and has four-momentum $p_{\text{recoil}} = (M + E_{\text{kin}}, -\vec{q})$ after the collision. The three-momentum of the final state ($\vec{p}_X = \sum_{i=\text{out}} \vec{p}_i$) has an angle θ w.r.t. the incoming beam particle. The momentum transfer q can be split into two parts, one pointing parallel to the beam q_{\parallel} , and one perpendicular to beam direction q_T .

of all outgoing particles and its square gives the Mandelstam s of the beam- X - γ vertex:

$$(p_{\text{beam}}^\mu + q^\mu)^2 = p_X^2 = \left(\sum_{i=\text{out}} p_i^\mu \right)^2 =: s \quad (2.19)$$

The minimum momentum transfer appears in exact longitudinal kinematics [45], meaning that $\vec{p}_{\text{beam}} \parallel \vec{q} \parallel \vec{p}_X$. To arrive at an expression for Q_{min} , we start to derive general expressions for q :

$$\begin{aligned} q^2 &= (p_X^\mu - p_{\text{beam}}^\mu)^2 = s + m_{\text{beam}}^2 - 2E_{\text{beam}}E_X + 2\vec{p}_{\text{beam}} \cdot \vec{p}_X \\ &= s + m_{\text{beam}}^2 - 2E_{\text{beam}}E_X + 2|\vec{p}_{\text{beam}}||\vec{p}_X| \cos \theta \\ &= s + m_{\text{beam}}^2 - 2E_{\text{beam}}(E_{\text{beam}} - E_{\text{kin}}) + 2|\vec{p}_{\text{beam}}|(|\vec{p}_{\text{beam}}| - q_{\parallel}) \\ &= s - m_{\text{beam}}^2 + 2E_{\text{beam}}E_{\text{kin}} - 2p_{\text{beam}}q_{\parallel} \end{aligned} \quad (2.20)$$

where we have used that $E_X = E_{\text{beam}} - E_{\text{kin}}$ and $q_{\parallel} = |\vec{p}_{\text{beam}}| - |\vec{p}_X| \cos \theta$. Eq. (2.20) yields for q_{\parallel} :

$$q_{\parallel} = \frac{s - m_{\pi}^2 + 2E_{\text{beam}}E_{\text{kin}} + Q^2}{2p_{\text{beam}}} \quad (2.21)$$

and finally, we obtain for exact longitudinal kinematics, i.e. $Q = q_{\parallel} = Q_{\text{min}}$:

$$Q_{\text{min}}(s) = \underbrace{\frac{s - m_{\pi}^2}{2p_{\text{beam}}}}_{Q_{\text{min}}^0} + \frac{Q_{\text{min}}^2(s) + 2E_{\text{beam}}(E_{\text{kin}})_{\text{min}}}{2p_{\text{beam}}} \quad (2.22)$$

Considering the scale difference in p_{beam} and Q_{min} , the best way to solve this quadratic equation numerically is to start with $Q_{\text{min}}(s) = Q_{\text{min}}^0$ and iterate according to Eq. (2.22). Convergence to double precision is achieved within a single step in the kinematics relevant in this work [45].

2.2.3 Weizsäcker Williams factorization

In the 1930's von Weizsäcker and Williams calculated QED processes, specifically so-called *bremsstrahlung* events [68, 69]. They used the method of virtual quanta which correlates the effects of a collision of a highly-relativistic, charged particle with a nucleus to a single collision of this particle with a quasi-real photon representing the Coulomb field of the nucleus. The *equivalent photon approximation* (EPA) is justified since the electromagnetic field of a relativistic charge resembles a pulse of plane polarized radiation (see App. A.3).

Working out the quantum-mechanical equations, they discovered that the cross section for scattering of any charged particle (in our case a pion) in the Coulomb-field of a nucleus decouples for very small momentum transfer into two factors: one factor describing a real-photon cross section $d\sigma_{\pi\gamma \rightarrow X}/d\phi_n$ with its n -dimensional phase space ϕ_n , the other one a density of almost real, small-momentum photons surrounding the nucleus. Since these surrounding

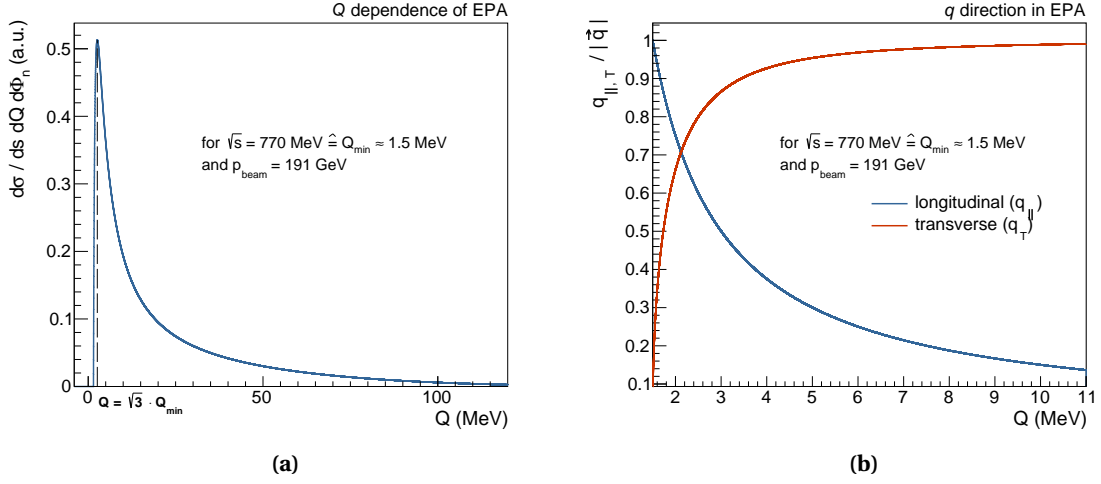


Fig. 2.5 Shown in (a): Q dependence of the cross section $\frac{d\sigma}{ds dQ d\phi_n}$ in the Weizsäcker-Williams equivalent photon approximation for a fixed $\sqrt{s} = 770$ MeV. The distribution features a characteristic peak at tiny momentum transfers of $Q = \sqrt{3}Q_{\min}$. Shown in (b): direction of the momentum transfer (longitudinal or transverse) in comparison to $|\vec{q}|$. As can be seen already slightly above the threshold Q_{\min} , most of the momentum is transferred in transverse direction with respect to the beam.

photons represent the Coulomb field of the nucleus, the density of the quasi-real photons increases with higher atomic number Z :

$$\frac{d\sigma^{\text{EPA}}}{ds dQ^2 d\phi_n} = \underbrace{\frac{Z^2 \alpha}{\pi(s - m_\pi^2)} F^2(Q^2)}_{\text{flux of quasi-real photons}} \frac{Q^2 - Q_{\min}^2}{Q^4} \cdot \frac{d\sigma_{\pi\gamma \rightarrow X}}{d\phi_n} \quad (2.23)$$

with $F(Q^2)$ being the electromagnetic form factor of the nucleus, and s the corresponding Mandelstam variable in the process $\pi + \gamma \rightarrow X$ according to Eq. (2.19) and displayed in Fig. 2.6.

The electromagnetic, elastic form factor $F(Q^2)$ is related to the charge distribution of the nucleus. In the limit of very small momentum transfer, where the cross section of Primakoff reactions peak, the nucleus can be approximated by a homogeneous sphere with sharp radius R :

$$\rho(R) = \begin{cases} 3/(4\pi R^3) & \text{for } r \leq R \\ 0 & \text{for } r > R \end{cases} \quad (2.24)$$

The elastic form factor for a sphere with sharp radius is given by [70]:

$$F_{\text{el}}(Q^2) = \frac{3}{(QR)^3} (\sin(QR) - QR \cos(QR)) \quad (2.25)$$

The charge radius of the nucleus can be approximated by

$$R \approx R_0 A^{\frac{1}{3}} \quad (2.26)$$

with $R_0 \approx 1.2$ fm and A the mass number of the nucleus ($A = 58$ for nickel).

We see in which sense Q_{\min} is an important quantity: it rules the Q^2 dependence of the differential cross section $d\sigma^{\text{EPA}}/ds dQ^2 d\phi_n$, leading to the characteristic Weizsäcker-Williams

dependence. Since the distribution features a sharp peak at low Q^2 , it is convenient to show the cross section

$$\frac{d\sigma^{\text{EPA}}}{ds dQ d\phi_n} = 2Q \cdot \frac{d\sigma^{\text{EPA}}}{ds dQ^2 d\phi_n} \quad (2.27)$$

as function of Q instead of Q^2 to optimize visibility of the features at low Q . This is done exemplarily in Fig. 2.5a for a fixed $\sqrt{s} = 770 \text{ MeV}$: starting at $Q = Q_{\text{min}}$, the cross section $\frac{d\sigma^{\text{EPA}}}{ds \cdot dQ \cdot d\phi_n}$ rises steeply to its maximum at $Q = \sqrt{3} \cdot Q_{\text{min}}$ followed by a strong drop with increasing momentum transfer Q . This Q dependence of the cross section is usually referred to as Primakoff peak, which appears at tiny momentum transfers of $Q \sim \mathcal{O}(1 \text{ MeV})$. To identify Primakoff events, it is hence of great importance to have a good Q -resolution and select events at these tiny momentum transfers.

Concerning the direction of \vec{q} , the laboratory components of \vec{q} are given by Eq. (2.21) and in transverse direction by:

$$q_T = \sqrt{\vec{q}^2 - q_{\parallel}^2} = \sqrt{Q^2 + E_{\text{kin}}^2 - q_{\parallel}^2} \quad (2.28)$$

Looking at the distributions for q_T and q_{\parallel} as shown in Fig. 2.5b, we see that for most of the events the momentum is mainly transferred perpendicular to the beam direction. Typical values for E_{kin} do not exceed 50 keV and are for the majority of the shown distribution in Fig. 2.5a three orders of magnitude smaller than Q . We see therefore from Eq. (2.28) that $q_T \approx Q$. This is an important observation since typically experiments measure only q_T due to insufficient longitudinal resolution in terms of q_{\parallel} .

Another consequence of the relatively small values of E_{kin} is that Primakoff events are *exclusive* reactions, meaning that the energy balance is given by

$$\Delta E = E_X - E_{\text{beam}} \approx 0 \quad (2.29)$$

To identify, select, and distinguish Primakoff events from background processes, one has to look for events with $\Delta E = 0$ at very small q_T . This exploits the sharpness of the Primakoff peak compared to the relatively shallow Q^2 distributions of the strong interaction (see tab.2.1) and distinguishes Primakoff events from other reactions.

2.2.4 Nuclear excitations

The scattering process does not necessarily have to be elastic. The exchanged photon may excite the nucleus. In this case, the photon has to transfer additional excitation energy. In general, we have for Primakoff reactions $\pi^-(p_1)A \rightarrow A^*\pi^-(p_2)\pi^0(q_{\pi^0})$ on a nucleus with mass number A and recoiling (eventually excited) nucleus A^* ,

$$\pi^-(p_1)\gamma^*(q) \rightarrow \pi^-(p_2)\pi^0(p_0) \quad (2.30)$$

The incoming beam four-vector has energy-momentum components $p_1 = (E_b, \vec{p}_b)$. The direction of \vec{p}_b fixes the direction of \hat{z} . The four-vector q shall have the energy component \tilde{q}_E which is composed of

$$\tilde{q}_E = -(E_{\text{kin}} + \Delta E) \quad (2.31)$$

the kinetic energy E_{kin} of the recoiling A^* and its excitation energy ΔE in the laboratory frame, in which the incoming nucleus A is at rest. From this definition follows that \tilde{q}_E is always a negative quantity. With $p_{A^*} = (E_{A^*}, -\vec{q})$ it follows that

$$\begin{aligned} p_{A^*}^2 &= M_{A^*}^2 = E_{A^*}^2 - \vec{q}^2 \\ &= (M_A + \Delta E)^2 = (M_A + \Delta E + E_{\text{kin}})^2 - \vec{q}^2 \end{aligned} \quad (2.32)$$

so

$$2(M_A + \Delta E)E_{\text{kin}} + E_{\text{kin}}^2 = \vec{q}^2 \quad (2.33)$$

and

$$E_{\text{kin}} = \frac{\vec{q}^2 - E_{\text{kin}}^2}{2(M_A + \Delta E)} \quad (2.34)$$

may be viewed as a recursive determining equation for E_{kin} for any given \vec{q}^2 and ΔE , which always converges starting with $E_{\text{kin}}^{(1)} = 0$.

The three-momentum components of q are decomposed into longitudinal and transverse parts with respect to the incoming beam direction, $\vec{q} = \vec{q}_{\parallel} + \vec{q}_T$. The parallel component lies by definition in \hat{z} direction and $\vec{q}_T \cdot \hat{z} = 0$. For the case of the incoming particles (the pion and the nucleus) being spin-zero particles, there is no given reference transverse axis, and it may be chosen such that \hat{x} and \hat{z} span the plane in which the vector of the recoiling nucleus lies, $\vec{q}_T \cdot \hat{y} = 0$. This is unique for all cases except the limiting case in which $q_T = |\vec{q}_T| \rightarrow 0$ (with vanishing phase space). From

$$s = (p_1 + q)^2 = m_{\pi}^2 + 2p_1 \cdot q + q^2 = m_{\pi}^2 + 2E_b \tilde{q}_E - 2\vec{p}_b \cdot \vec{q}_{\parallel} + q^2 \quad (2.35)$$

it follows that

$$q_{\parallel} = |\vec{q}_{\parallel}| = \frac{s - m_{\pi}^2 + 2E_b q_E + Q^2}{2p_b} \quad (2.36)$$

where $p_b q_{\parallel} = -\vec{p}_b \cdot \vec{q}_{\parallel}$ has been taken into account and the positive quantities

$$q_E = -\tilde{q}_E = E_{\text{kin}} + \Delta E > 0 \quad (2.37)$$

$$Q^2 = -q^2 > 0 \quad (2.38)$$

are used.

For the case of the nickel nucleus being excited into the giant dipole resonance, $\Delta E \approx 18$ MeV and the term $2E_b q_E \approx 3.42$ GeV² dominates in Eq. (2.36). Consequently,

$$9 \cdot 10^{-3} \text{ GeV} < q_{\parallel}^{\Delta E=18 \text{ MeV}} \approx \frac{s - m_{\pi}^2 + 2E_b q_E}{2p_b} < 1.3 \cdot 10^{-2} \text{ GeV} \quad (2.39)$$

For the further dynamics and the cross sections, the most relevant quantity is Q^2 . It is determined by ΔE , which can not be directly observed or reconstructed in high-energy kinematics,

and by the observable q_T via

$$\begin{aligned}
 Q^2 &= -q_E^2 + q_{\parallel}^2 + q_{\perp}^2 \\
 &= -q_E^2 + \left(\frac{2E_b q_E + s - m_{\pi}^2 + Q^2}{2p_b} \right)^2 + q_{\perp}^2 \\
 &= \frac{m_{\pi}^2}{p_b^2} q_E^2 + \frac{(4E_b q_E + s - m_{\pi}^2 + Q^2)(s - m_{\pi}^2 + Q^2)}{4p_b^2} + q_{\perp}^2
 \end{aligned} \tag{2.40}$$

Inelastic scattering processes, also require adapting the form factor in Eq. (2.23). For E1 resonances, e.g. the giant dipole resonance, the inelastic form factor can be described according to the Goldhaber-Teller model [71]:

$$F_{\text{GT}} = \frac{Q \cdot b_{\text{collective}}}{\sqrt{8}} F_{\text{el}}(Q) \tag{2.41}$$

with $b_{\text{collective}}$ being the oscillator length, which for the purpose of this thesis does not need to be quantified.

2.3 Kinematics of the $\pi^- \gamma^{(*)} \rightarrow \pi^- \pi^0$ reaction

The goal of this thesis is to extract an experimental value for the fundamental physical constant $F_{3\pi}$ of Eq. (1.33). The necessary $\gamma 3\pi$ vertex can be accessed in Primakoff reactions according to Eq. (1.34) where the photon is provided by the Coulomb field of a nucleus. To be able to extract a value for $F_{3\pi}$, it is important to fully understand the kinematics of this reaction. We consider the collision of a (real) photon with a beam pion and for our purposes detach this process from the target nucleus following the idea of the EPA. We assign the four-momentum vectors to the corresponding particles:

$$\pi^-(p_1) \gamma(\epsilon, q) \rightarrow \pi^-(p_2) \pi^0(p_0) \tag{2.42}$$

with ϵ being the polarization vector of the photon. Fig. 2.6 illustrates the process with the chosen naming for the momenta in the cm-frame. The Lorentz-invariant Mandelstam variables for this process are:

$$\begin{aligned}
 s &= (q^{\mu} + p_1^{\mu})^2 = (p_2^{\mu} + p_0^{\mu})^2 = 4(m_{\pi}^2 + p'^2) \\
 t &= (p_1^{\mu} - p_2^{\mu})^2 \\
 u &= (p_1^{\mu} - p_0^{\mu})^2
 \end{aligned} \tag{2.43}$$

with $p' = |\vec{p}_0| = |\vec{p}_2|$ and working in the isospin limit with

$$m_{\pi^0} = m_{\pi^{\pm}} \equiv m_{\pi} \approx 138 \text{ MeV} \tag{2.44}$$

. Assuming that the involved particles are real (and thus neglecting the small virtuality of the $\gamma^{(*)}$), the Mandelstam variables satisfy according to Eq. (2.5):

$$s + t + u = 3m_{\pi}^2. \tag{2.45}$$

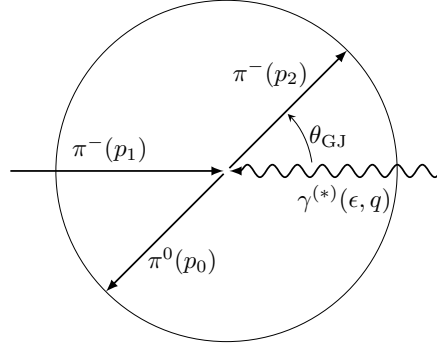


Fig. 2.6 Kinematics of reaction $\pi^-\gamma^{(*)} \rightarrow \pi^-\pi^0$ in the center-of-momentum frame. Since for the incoming photon $q^2 < 0$, the momenta of the outgoing particles are smaller than those of the incoming particles. Figure adapted from [45].

We are left with only two independent variables s and t (respectively $\cos \theta_{\text{GJ}}$). Apparently, the distribution in s has a kinematic threshold of $s > 2m_\pi$. Following the argumentation in Section 2.1.1 and neglecting for now dependencies in the azimuthal angle, t and u can be expressed in terms of the scattering angle in the cm frame/polar angle in the GJ frame according to Eq. (2.6) via:

$$\begin{aligned} t &= \frac{3m_\pi^2 - s}{2} + \frac{s - m_\pi^2}{2} \sqrt{1 - \frac{4m_\pi^2}{s}} \cos \theta_{\text{GJ}} \\ u &= \frac{3m_\pi^2 - s}{2} - \frac{s - m_\pi^2}{2} \sqrt{1 - \frac{4m_\pi^2}{s}} \cos \theta_{\text{GJ}} \end{aligned} \quad (2.46)$$

To calculate the cross section as a function of s according to Eq. (2.8), we need the flux factor F and the matrix element $\mathcal{M}(s, t, u)$. The former is calculated according to Eq. (2.9) and is given by:

$$F = 2(s - m_\pi^2) \quad (2.47)$$

The matrix element for the process is obtained by the WZW term of the chiral Lagrangian and is given by [72, 73]

$$\mathcal{M}(s, t, u) = i\epsilon_{\mu\nu\alpha\beta} \epsilon^\mu p_1^\nu p_2^\alpha p_0^\beta \mathcal{F}(s, t, u) \quad (2.48)$$

characteristically involving the fully antisymmetric Levi-Civita tensor $\epsilon_{\mu\nu\alpha\beta}$ and $\mathcal{F}(s, t, u)$ being a scalar function, the form factor of the process. The matrix element enters the total cross section modulus-squared.

We start to review the derivation of the cross section for a real photon in the process, since this form is commonly used for theory calculations. In Section 2.3.1, we will see that the total cross section for a virtual photon is the same despite different dependencies on the azimuthal angle ϕ_{TY} . For contracting the Lorentz indices, we average over the two transverse photon polarizations. For a real photon travelling along the inverse z -axis, the two transverse polarizations four-vectors are $\epsilon_\mu^1 = (0, \hat{x}_{\text{GJ}})$ and $\epsilon_\mu^2 = (0, \hat{y}_{\text{GJ}})$ which limits the number of non-zero permutations of $\mu\nu\alpha\beta$. After contracting the Lorentz indices as it is explicitly carried out in

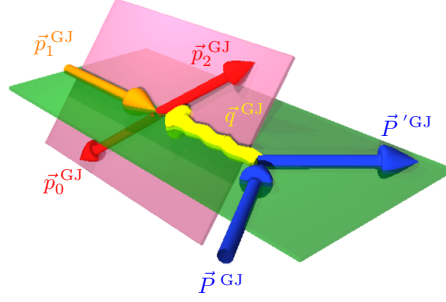


Fig. 2.7 Kinematics of reaction $\pi^- + \text{Ni} \rightarrow \pi^- \pi^0 + \text{Ni}$ in the center-of-momentum frame depicted in a three-dimensional view. To understand the dependence of the cross section on the azimuthal angle, the reaction of Eq. (2.42) needs to be embedded into the whole Primakoff process.

App. A.4, one obtains for the polarization averaged squared amplitude:

$$\frac{1}{2} \sum_{\text{pol}} |\mathcal{M}(s, t, u)|^2 = \frac{1}{32} (s - 4m_\pi^2)(s - m_\pi^2)^2 (1 - \cos^2 \theta_{\text{GJ}}) |\mathcal{F}(s, t, u)|^2 \quad (2.49)$$

From the two-body phase-space element from Eq. (2.11), we get a factor of

$$\begin{aligned} \int d\phi_2 &= \int_{-\pi}^{\pi} \int_{-1}^1 \frac{1}{4\pi} \frac{\sqrt{s - 4m_\pi^2}}{2\sqrt{s}} \frac{1}{4\pi} d\cos \theta_{\text{GJ}} d\phi_{\text{TY}} \\ &= \int_{-1}^1 \frac{1}{16\pi} \frac{\sqrt{s - 4m_\pi^2}}{\sqrt{s}} d\cos \theta_{\text{GJ}} \end{aligned} \quad (2.50)$$

after integration over the azimuthal angle ϕ and using Eq. (2.43) to express p' in terms of s . Again, we assume for this step that the photon in the interaction is real and not polarized implying that there is no dependence of the cross section on the azimuthal angle.

Combining Eqs. (2.47), (2.49) and (2.50) according to Eq. (2.8), we finally have the total cross section σ_{tot} as a function of s :

$$\sigma_{\text{tot}}(s) = \frac{(s - 4m_\pi^2)^{3/2} (s - m_\pi^2)}{1024\pi\sqrt{s}} \int_{-1}^1 dz (1 - z^2) |\mathcal{F}(s, t, u)|^2 \quad (2.51)$$

with $z = \cos \theta_{\text{GJ}}$. Evaluating the scalar form factor of the process in the chiral limit ($s = 0, t = 0, u = 0$) will give us, by definition, the wanted value for $F_{3\pi}$. We therefore rename:

$$\mathcal{F}(s, t, u) =: F_{3\pi}(s, t, u) \quad (2.52)$$

2.3.1 Angular distributions and partial-wave expansion

It is important to know the correct angular distributions of $\pi^- \gamma^{(*)} \rightarrow \pi^- \pi^0$ events to generate a realistic set of pseudodata and to distinguish the signal from background events. We start with

the azimuthal dependencies in the Gottfried-Jackson rest frame ϕ_{TY} . According to Eq. (2.51), there is no ϕ_{TY} -dependence. However, we detached the scattering of the pion with the photon completely from the underlying Primakoff process such that we can rotate the plane in which the scattering takes place (see Fig. 2.6 and the red plane in Fig. 2.7) arbitrarily around the z -axis without loss of generality. Embedding the scattering into the Primakoff process yields a reference plane, namely the production plane, as indicated by the green plane in Fig. 2.7.

We have to consider the argumentation in App. A.3 which tells us that the information of the direction of the production plane is mediated by the polarization of the photon. In the GJ-frame, where the y -axis is perpendicular to the production plane and the x -axis lies within the production plane, the polarization vector will be in x -direction. Carrying out the calculation in App. A.4 for a polarized photon, we are left with

$$\frac{d\sigma}{d\phi_{\text{TY}}} \propto \sin^2 \phi_{\text{TY}} \quad (2.53)$$

The integration over ϕ_{TY} , however, yields the same factor of π no matter whether one averages over the two transverse polarization vectors and hence loses the ϕ_{TY} -dependence or one integrates over $\sin^2 \phi_{\text{TY}}$. Eq. (2.51) remains unchanged.

The dependence on the polar angle of the GJ-frame is given in Eq. (2.51) as

$$\frac{d\sigma}{d\cos\theta_{\text{GJ}}} \propto (1 - \cos^2\theta_{\text{GJ}}) F_{3\pi}(s, t, u) = (1 - \cos^2\theta_{\text{GJ}}) F_{3\pi}(s, t(s, z)) \quad (2.54)$$

where parts of the angular dependence and the energy dependence is hidden in $F_{3\pi}(s, t(s, z))$. We can factorize the angular and the energy dependence by expanding $F_{3\pi}$ in a partial-wave series [42, 72]

$$F_{3\pi}(s, t(s, z)) = \sum_{\text{odd } l} f_l(s) P_l'(z) \quad (2.55)$$

where l is the orbital angular momentum quantum number, $f_l(s)$ an analytic function containing all dependencies on s , and $P_l'(z)$ denotes the derivative of the Legendre polynomials. The partial-wave expansion contains only odd l because the pions in the final state have the total isospin $I = 1$ [42]. Hannah could show that at low energies ($\sqrt{s} \lesssim 1 \text{ GeV}/c^2$) partial waves with $l \geq 3$ are negligible. Following this argumentation and using $P_1(z) = z$ yields

$$\frac{d\sigma}{d\cos\theta_{\text{GJ}}} \propto \sin^2\theta_{\text{GJ}} \quad (2.56)$$

This is coherent with the conservation of angular momentum: considering that we have a spin-1 particle, the photon, and a spin-0 particle, the pion, in the initial state and two spin-0 particles in the final state, the final-state pions have to be produced at least in a relative P -wave. Up to around $\sqrt{s} \approx 1 \text{ GeV}$ no other orbital angular momenta contribute to the total cross section.

2.3.2 Resonant production of the $\rho(770)$ meson

After pions and kaons, the ρ -mesons are the lightest hadrons. They can be interpreted as a $|q\bar{q}\rangle$ -state of u - and d -quarks. The ρ is an isospin triplet, whose three states are denoted

2.3. KINEMATICS OF THE $\pi^- \gamma^{(*)} \rightarrow \pi^- \pi^0$ REACTION

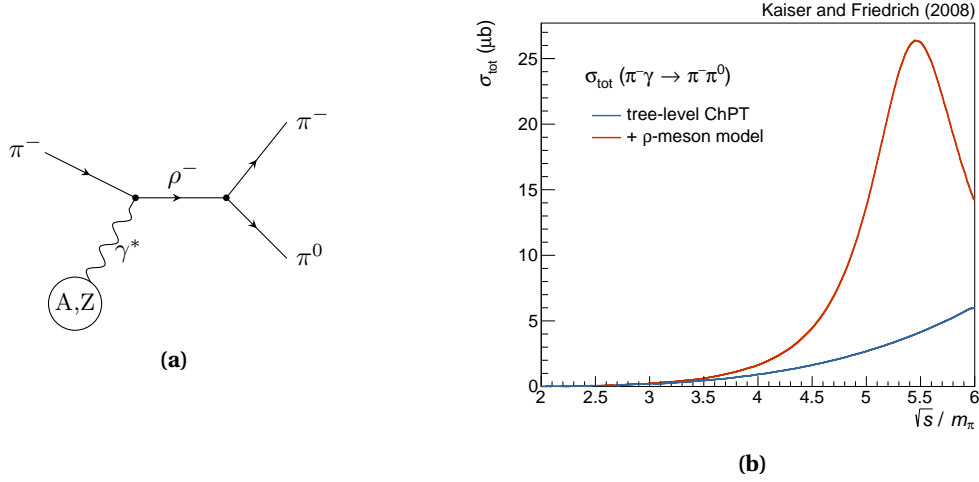


Fig. 2.8 In (a): tree-level diagram for coherent $\rho(770)$ -production. In (b): total cross sections for the reaction $\pi\gamma \rightarrow \pi^-\pi^0$ as a function of the center-of-mass energy \sqrt{s} calculated by Kaiser and Friedrich in [67]. The blue line shows the prediction by the chiral anomaly on tree-level. The red line includes additionally a ρ -meson model.

ρ^+ , ρ^- , and ρ^0 , which have all approximately the same mass of $m_\rho \approx 775 \text{ MeV}/c^2$. Its spin is $J = 1$ meaning that, in contrast to the pion, the spins of the two constituent quarks are aligned. The ρ couples and hence decays with almost 100% branching fraction to two pions [18]. As a matter of fact, theorists postulated the existence of the ρ as a $\pi\pi$ resonance in the late 1950ies.

Despite the overwhelming coupling to two pions, the $\rho(770)$ resonance couples also to $\pi\gamma$ with a branching fraction of $\Gamma_i/\Gamma = (4.5 \pm 0.5) \cdot 10^{-4}$ [18]. It can therefore be resonantly produced in the s -channel in $\pi\gamma$ scattering:

$$\pi^- \gamma \rightarrow \rho^- \rightarrow \pi^- \pi^0 \quad (2.57)$$

The tree-level diagram of this process is depicted in Fig. 2.8 (a). The total cross section for the reaction $\pi^- \gamma \rightarrow \pi^- \pi^0$ shows hence a contribution by the resonant production of the $\rho(770)$ -meson. The resonant ρ production is a fully coherent background to the direct coupling of a photon to three pions, meaning that it coincides in all quantum numbers and shows the same angular distributions. The two processes interfere. They only differ in their \sqrt{s} -dependence, since the resonant production peaks at the mass of the ρ -meson of $m_\rho \approx 775 \text{ MeV}$.

Fig. 2.8 (b) shows a prediction for the total cross section as a function of \sqrt{s} : in blue, a calculation from ChPT and in red, the same calculation added to a model for the ρ -resonance according to [67]. The low-mass tail, close to the kinematic threshold of $\sqrt{s}_{\text{thr}} = 2m_\pi$, is mainly driven by the chiral anomaly. Previous extractions of $F_{3\pi}$ by Antipov *et al.* [39] and by Giller *et al.* [43] used this fact and investigated only the low-mass tail of the spectrum as can be seen in Fig. 1.5.

Above center-of-mass energies of $\sqrt{s} \simeq 4m_\pi$, the effects of the ρ -resonance are dominant. The cross-section for resonant ρ -production quickly increases and peaks at $m_\rho = 775 \text{ MeV} \approx 5.6m_\pi$. Beyond this mass, it decreases again. At the same time, also the cross-section for chiral production of $\pi^- \pi^0$ increases. The two processes have different phases and interfere.

The shape of the total cross section for $\pi^- \gamma \rightarrow \pi^- \pi^0$ is hence an elaborate result of the interference between resonant ρ -production and chiral production of the $\pi^- \pi^0$ final state. Especially slightly above the ρ peak, where resonant production and chiral production are comparatively strong, we can gain a lot of additional information from the shape of the cross section. An extraction of $\Gamma_{\rho \rightarrow \gamma \pi}$ based on fitting only a Breit-Wigner distribution to the shown spectrum in Fig. 2.8 (b) neglects the chiral contribution. The previous measurements [55, 56, 57] (for details see Section 1.4.2) contributing to the PDG average value hence neglect the chiral contribution to the overall cross-section.

For this thesis, we will use a combined approach based on dispersion theory [72] to extract a value for $F_{3\pi}$ and $\Gamma_{\rho \rightarrow \pi \gamma}$ at the same time. In this way, we consider the contributions of each process in the whole \sqrt{s} -range and are able to include all events up to $\sqrt{s} = 1.2 \text{ GeV} \approx 7 m_\pi$. The dispersive approach will be discussed in Section 2.4.

2.3.3 Higher-order and electromagnetic corrections

In [42], Hannah constructed a systematic expansion for the amplitude of the anomalous process $\gamma \pi \rightarrow \pi \pi$ within the framework of ChPT:

$$F_{3\pi}(s, t, u) = F_{3\pi} \left(f^{(0)}(s, t, u) + f^{(1)}(s, t, u) + f^{(2)}(s, t, u) + \dots \right) \quad (2.58)$$

with the $f^{(i)}$ being the i th-order corrections and being obtained by the WZW term. Hannah evaluated the expansion up to two loops by means of a dispersive method. Disregarding isospin breaking effects, the leading order term amounts to one $f^{(0)}(s, t, u) = 1$. The next-to-leading order corrections (NLO) have become available in Ref. [41] and account to

$$\begin{aligned} f^{(1)}(s, t, u) = & -\frac{64\pi^2}{3e} \cdot C_2^r \cdot (s+t+u) - \frac{s+t+u}{96\pi^2 F_\pi^2} \left(1 + \log \frac{m_\pi^2}{m_\rho^2} \right) \\ & + \frac{1}{\pi} \int_{4m_\pi^2}^{\infty} \frac{ds'}{s'^2} \left(\frac{s^2}{s'-s} + \frac{t^2}{s'-t} + \frac{u^2}{s'-u} \right) \text{Im} f_1^{(1)}(s') \end{aligned} \quad (2.59)$$

The expression converges to the chiral anomaly $F_{3\pi}$ in the chiral limit and is given in terms of $f_1(s)$ from the partial wave expansion Eq. (2.55) and C_2^r , a low-energy constant (LEC) from the 2nd order anomalous chiral Lagrangian. C_2^r is to be determined from experiment, but the authors of Ref. [41] were able to estimate a theoretical prediction for it:

$$C_2^r = -\frac{3e}{128\pi^2 m_\rho^2} = -0.00120 \text{ GeV}^{-2} \quad (2.60)$$

The exact form of two-loop correction term $f^{(2)}(s, t, u)$ shall be omitted here. Important is only that in the two-loop term, two more LECs, \bar{c}_2 and \bar{d}_2 , appear. Again, Hannah was able to estimate them from theory and in this way determined $f^{(2)}(s, t, u)$.

$f^{(1)}(s, t, u)$ and $f^{(2)}(s, t, u)$ feature a non-negligible s and t dependence. In this way, Hannah reduced the disagreement between ChPT prediction and the Serpukhov result (which did not assume any dependence on s).

2.3. KINEMATICS OF THE $\pi^- \gamma^{(*)} \rightarrow \pi^- \pi^0$ REACTION

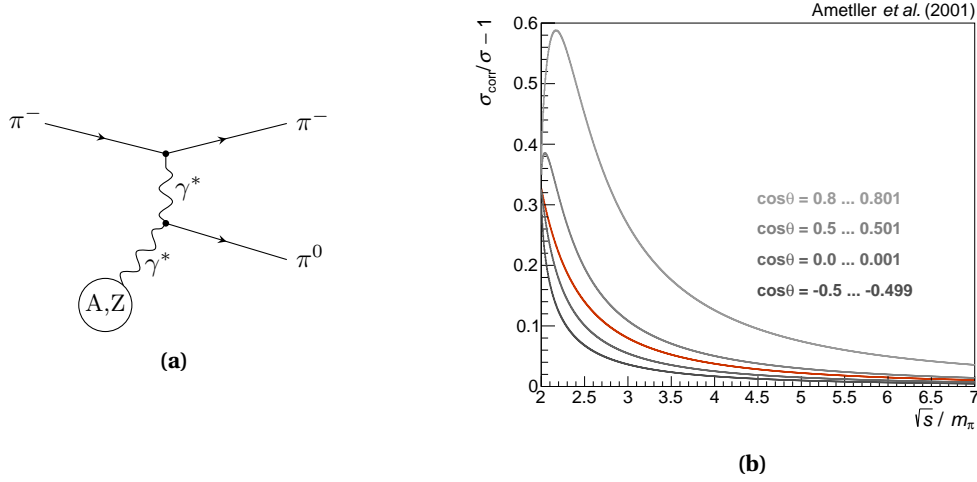


Fig. 2.9 In (a): tree-level graph for the dominant contribution to electromagnetic corrections to $\pi^- \gamma \rightarrow \pi^- \pi^0$: t -channel exchange of a virtual photon as it was discovered in [40]. In (b): relative increase $frac{\sigma_{\text{corr}}}{\sigma} - 1$ of the cross section including radiative corrections as a function of s for various values of θ_{GJ} . The red curve shows the corresponding relative increase in the cross-section σ integrated over $\cos \theta_{\text{GJ}}$ (adapted from [40]).

Finally, Ametller *et al.* have evaluated the ChPT expansion in the situation where virtual photons are present [40]. Differentiating between charged and neutral pions, i.e. taking isospin breaking effects into account, they have shown that there is a significant contribution to the total cross-section of the process $\pi^\pm \gamma \rightarrow \pi^\pm \pi^0$ due to t -channel exchange of a virtual photon. The diagram, as it is calculated by Ametller *et al.*, is shown in Fig. 2.9a. It represents an electromagnetic correction to the tree-level term $f^{(0)}(s, \cos \theta_{\text{GJ}})$ in the chiral expansion of Eq. (2.58):

$$f^{(0)}(s, \cos \theta_{\text{GJ}}) = 1 - 2e^2 \frac{F_\pi^2}{t} \quad (2.61)$$

with

$$t = 2m_{\pi^\pm}^2 - \frac{(s + m_{\pi^\pm}^2)(s + m_{\pi^\pm}^2 - m_{\pi^0}^2)}{2s} + \frac{(s - m_{\pi^\pm}^2)\lambda^{1/2}(s, m_{\pi^\pm}^2, m_{\pi^0}^2)}{2s} \cos \theta_{\text{GJ}} \quad (2.62)$$

being the isospin-breaking generalization of Eq. (2.46) with $\lambda(s, m_{\pi^\pm}^2, m_{\pi^0}^2)$ being the Källén function defined as

$$\lambda(x, y, z) = x^2 + y^2 + z^2 - 2xy - 2yz - 2xz \quad (2.63)$$

Fig. 2.9b shows the value of $f^{(0)}(s, \cos \theta_{\text{GJ}})$ including the corrections for different values of $\cos \theta_{\text{GJ}}$ in the range of s as covered by the Serpukhov experiment. At the threshold, its value is $f^{(0)}(4m_\pi^2, \cos \theta_{\text{GJ}}) = 1.16$ as compared to the constant value $f^{(0)}(s, \cos \theta_{\text{GJ}}) = 1$ without the corrections. Since the form factor of the process enters the cross-section of Eq. (2.51) quadratically, this leads to a $\approx 35\%$ increase of the cross-section σ . The relative increase of the cross-section can be seen in Fig. 2.9b as dashed line. The electromagnetic corrections are most significant in the threshold region $s/m_\pi^2 \approx 4$.

Higher-order electromagnetic corrections in $f^{(1)}(s, \cos \theta_{\text{GJ}})$ via photon loops are calculated as well in Ref. [40]. However, it is shown that these higher-order corrections are small ($\sim 1\%$).

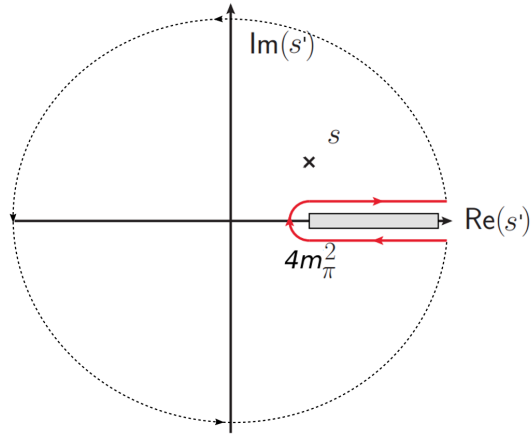


Fig. 2.10 Contours for the Cauchy integral formula for the calculation of $f(s)$.

2.4 Extracting $F_{3\pi}$ from Primakoff data

In this section, I motivate the most crucial steps which are needed to understand the model that we are going to use to extract a value for $F_{3\pi}$ and $\Gamma_{\rho \rightarrow \pi\gamma}$. However, this section represents only a short summary, more details can be found in Refs. [42, 59, 72, 74].

2.4.1 Dispersion relations

Cauchy's integral formula states that one can reconstruct the full amplitude of a complex-valued analytic function at any point inside a disk by its values on the boundary of the disk:

$$f(s) = \frac{1}{2\pi i} \oint_C ds' \frac{f(s')}{s' - s} \quad (2.64)$$

with $f(s')$ being an analytic function inside and on the closed contour C , and s any point inside the contour C . Let's assume that $f(s')$ has a branch point at $s' = s_{\text{thr}}$ and a corresponding branch cut from s_{thr} to ∞ . Then, we can deform the contour in a way that its radius goes to infinity and that it excludes the branch cut, as indicated in Fig. 2.10. If $f(s')$ vanishes faster than $1/s'$ for $|s| \rightarrow \infty$, the integral along the circular dashed lines in Fig. 2.10 does not contribute:

$$f(s) = \frac{1}{2\pi i} \int_{s_{\text{thr}}}^{\infty} ds' \frac{\text{disc } f(s')}{s' - s} \quad (2.65)$$

Using the Schwarz reflection principle, we can rewrite the discontinuity as

$$\text{disc } f(s) = f(s' + i\epsilon) - f^*(s' + i\epsilon) = 2i \text{Im} f(s) \quad (2.66)$$

Plugging this back into Eq. (2.65), we obtain

$$f(s) = \frac{1}{\pi} \int_{s_{\text{thr}}}^{\infty} \frac{\text{Im}f(s')}{s' - s} ds' \quad (2.67)$$

which is an example of an unsubtracted dispersion relation. For our example at hand, the amplitude for $\pi^- \gamma^{(*)} \rightarrow \pi^- \pi^0$ develops a branch cut from $s_{\text{thr}} = 4m_{\pi}^2$. The virtue of Eqs. (2.65) and (2.67) is that we can reconstruct the full function everywhere in the complex plane by knowing its discontinuity or the integral over its imaginary part by means of dispersion relations.

As we have seen, the integral along the circular dashed lines in Fig. 2.10 only vanishes, when $f(s')$ vanishes faster than $1/s'$ for $|s| \rightarrow \infty$. In case that $f(s')$ does not approach zero sufficiently fast, we can introduce subtractions by inserting the identity

$$\begin{aligned} \frac{1}{s' - s} &= \frac{1}{s' - s} - \frac{1}{s' - s_0} + \frac{1}{s' - s_0} \\ &= \frac{s' - s_0}{(s' - s)(s' - s_0)} - \frac{s' - s}{(s' - s_0)(s' - s)} + \frac{1}{s' - s_0} \\ &= \frac{1}{s' - s_0} + \frac{s - s_0}{(s' - s)(s' - s_0)} \end{aligned} \quad (2.68)$$

into Eq. (2.67) where we have chosen an arbitrary subtraction point s_0 . This improves the convergence for $|s| \rightarrow \infty$ by increasing the power of s' in the denominator:

$$f(s) = \underbrace{\frac{1}{\pi} \int_{s_{\text{thr}}}^{\infty} \frac{\text{Im}f(s')}{s' - s_0} ds'}_{C_1} + \frac{s - s_0}{\pi} \int_{s_{\text{thr}}}^{\infty} \frac{\text{Im}f(s')}{(s' - s)(s' - s_0)} ds' \quad (2.69)$$

The first term is independent of s . It is called a *subtraction constant*, we will denote as C_1 for the once-subtracted integral. The subtraction constant is unknown and has to be determined by external input, e.g. from data. The subtraction improves convergence of the dispersion integral at the expense of introducing a new subtraction constant.

There is no restriction on how often one introduces a subtraction, such that we can construct an N -times subtracted dispersion relation by

$$f(s) = P_{N-1}(s) + \frac{(s - s_0) \dots (s - s_N)}{\pi} \int_{s_{\text{thr}}}^{\infty} \frac{\text{Im}f(s')}{(s' - s)(s' - s_0) \dots (s' - s_N)} ds' \quad (2.70)$$

with $P_{N-1}(s)$ being the subtraction polynomial of order $N - 1$

$$P_{N-1}(s) = C_N^{(1)} + C_N^{(2)} s + C_N^{(3)} s^2 + \dots + C_N^{(N)} s^{N-1} \quad (2.71)$$

with N different subtraction constants $C_N^{(1)} \dots C_N^{(N)}$. Since later on, we are interested in twice-subtracted dispersion relations, the explicit case is carried out in Appendix A.5.

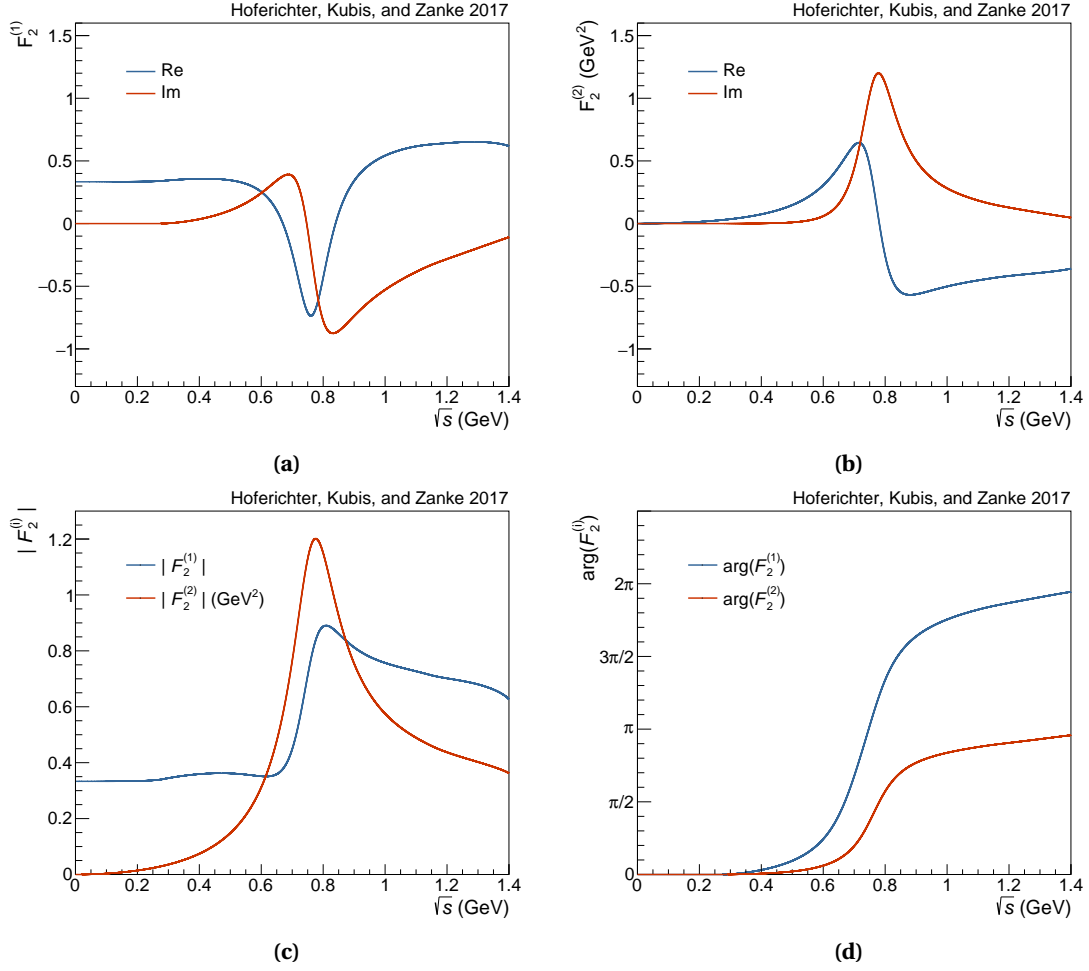


Fig. 2.11 Basis functions $\mathcal{F}_2^{(i)}$ for $\gamma\pi \rightarrow \pi\pi$. The real (blue) and imaginary (red) parts for $\mathcal{F}_2^{(1)}$ are shown in (a) and for $\mathcal{F}_2^{(2)}$ in (b). (c) shows the amplitude and (d) the phases of the functions. The basis functions can be found in Ref. [76] and have been provided to the author of this thesis as look-up table [77].

2.4.2 Dispersive approach for the anomalous process $\pi^- \gamma^{(*)} \rightarrow \pi^- \pi^0$

Hoferichter *et al.* provided a dispersive approach to deduce a value for $F_{3\pi}$ from cross section data as a function of s in Ref. [72]. From Eq. (2.51) we see, that the process $\pi^- \gamma^{(*)} \rightarrow \pi^- \pi^0$ is described by the scalar function $F_{3\pi}(s, t, u)$. At low energies, neglecting partial waves with angular momentum $l \geq 3$, the amplitude $F_{3\pi}(s, t, u)$ may be decomposed as [75]

$$F_{3\pi}(s, t, u) = F_{3\pi}(s) + F_{3\pi}(t) + F_{3\pi}(u) \quad (2.72)$$

In Ref. [76], Hoferichter *et al.* showed that the solution of the twice-subtracted dispersion relation for $F_{3\pi}(s)$ can be represented in the form

$$F_{3\pi}^{\text{DR}}(s) = \frac{1}{3} \left(C_2^{(1)} + C_2^{(2)} s \right) + \frac{1}{\pi} \int_{4m_\pi^2}^{\infty} \frac{ds'}{s'^2} \frac{s^2}{s' - s} \times \left(C_2^{(1)} \text{Im} \mathcal{F}_2^{(1)}(s') + C_2^{(2)} \text{Im} \mathcal{F}_2^{(2)}(s') \right) \quad (2.73)$$

with $C_2^{(i)}$ being the subtraction constants in the twice-subtracted dispersion relation. The $C_2^{(i)}$ are free parameters and have to be determined from a fit to data. In contrast to the basis functions $\mathcal{F}_2^{(i)}$, which can be calculated "once and for all" [76] from the twice-subtracted dispersion relations for a given input of the $\pi\pi$ phase shift. Fig. 2.11 shows the real and imaginary parts of the two basis functions as well as their polar representation, magnitude and phases, as determined in Ref. [76]. The numerical values for the $\mathcal{F}_2^{(i)}$ s, on which Fig. 2.11 is based, can be found in Ref. [78]. To generate Fig. 2.11, I interpolated the numerical values linearly.

The dispersion relations have been solved in Ref. [72] using so-called *Omnès* functions. From the representation with Omnès functions and cumbersome calculations, one can observe that the dispersion relations are linear in the subtraction constants, which significantly simplifies the expression:

$$F_{3\pi}^{\text{DR}}(s) = C_2^{(1)} \mathcal{F}_2^{(1)}(s) + C_2^{(2)} \mathcal{F}_2^{(2)}(s) \quad (2.74)$$

The subtraction constants serve as multiplicative constants over the whole energy range and combine linearly the basis functions displayed in Fig. 2.11. This yields a strong impact of the ρ resonance region on the extraction of $F_{3\pi}$.

Combining Eqs. (2.72) and (2.74), we can determine the whole amplitude by

$$\begin{aligned} F_{3\pi}(s, t, u) = & C_2^{(1)} \left(\mathcal{F}_2^{(1)}(s) + \mathcal{F}_2^{(1)}(t) + \mathcal{F}_2^{(1)}(u) \right) \\ & + C_2^{(2)} \left(\mathcal{F}_2^{(2)}(s) + \mathcal{F}_2^{(2)}(t) + \mathcal{F}_2^{(2)}(u) \right) - \frac{2e^2 F_\pi^2 F_{3\pi}}{t} \end{aligned} \quad (2.75)$$

where in the kinematic region relevant for the cross section only the s -channel develops an imaginary part. The imaginary parts for t - and u -channel can be dropped from the start. The last term accounts for the dominant electromagnetic corrections according to Eq. (2.61). Eq. (2.75) is a convenient fit function of the dispersive model to the actual cross section data to obtain $C_2^{(1)}$ and $C_2^{(2)}$.

2.4.3 Comparison to ChPT

The chiral anomaly $F_{3\pi}$ is defined as the value of $F_{3\pi}(s, t, u)$ in the chiral limit where $s = t = u = 0$. In Section 2.3.3, we have sketched the chiral expansion and we have seen that the s -dependence of the higher-order corrections significantly alter the value of $F_{3\pi}(s, t, u)$ when crossing the gap from the chiral limit to the experimental s . The dispersion relations have been derived using on-shell kinematics and hence cannot be used to extrapolate to the chiral limit. We have to refer to the chiral expansion.

The chiral expansion of Eq. (2.58) up to NLO can be expressed with Eq. (2.59) as:

$$\begin{aligned} F_{3\pi}^{\text{NLO}}(s, t, u) = & \frac{1}{\pi} \int_{4m_\pi^2}^{\infty} \frac{ds'}{s'^2} \left(\frac{s^2}{s'-s} + \frac{t^2}{s'-t} + \frac{u^2}{s'-u} \right) \times \text{Im} f_1^{(1)}(s') \\ & + F_{3\pi} \left[1 - \frac{64\pi^2}{3e} C_2^r \cdot 3m_\pi^2 - \frac{3m_\pi^2}{96\pi^2 F_\pi^2} \left(1 + \log \frac{m_\pi^2}{m_\rho^2} \right) \right] \end{aligned} \quad (2.76)$$

which exhibits some similarity with the dispersion relation of Eq. (2.73). To be able to compare the two expressions, we need to express Eq. (2.73) in terms of the partial wave $f_1(s)$. The partial wave follows from

$$f_1(s) = \frac{3}{4} \int_{-1}^1 dz (1-z^2) F_{3\pi}(s, t, u) \quad (2.77)$$

which yields following representation of the dispersion equations [72, 76]:

$$F_{3\pi}^{\text{DR}}(s, t, u) = \left(C_2^{(1)} + C_2^{(2)} m_\pi^2 \right) + \frac{1}{\pi} \int_{4m_\pi^2}^{\infty} \frac{ds'}{s'^2} \left(\frac{s^2}{s'-s} + \frac{t^2}{s'-t} + \frac{u^2}{s'-u} \right) \times \text{Im} f_1(s') \quad (2.78)$$

Now, we can compare the chiral expansion up to NLO with the dispersion relation

$$F_{3\pi}^{\text{DR}}(s, t, u) = F_{3\pi}^{\text{NLO}}(s, t, u) + \mathcal{O}(\text{NNLO} + \dots) \quad (2.79)$$

We find that $\left(C_2^{(1)} + C_2^{(2)} m_\pi^2 \right)$ is related to $F_{3\pi}$ via

$$\begin{aligned} \left(C_2^{(1)} + C_2^{(2)} m_\pi^2 \right) &= F_{3\pi} \left[1 + 3m_\pi^2 \left(-\frac{64\pi^2}{3e} C_2^r - \frac{1}{96\pi^2 F_\pi^2} \left(1 + \log \frac{m_\pi^2}{m_\rho^2} \right) \right) \right] \\ &=: F_{3\pi} (1 + 3m_\pi^2 \bar{C}) =: \bar{F}_{3\pi} \end{aligned} \quad (2.80)$$

with $\bar{C} = -\frac{64\pi^2}{3e} C_2^r - \frac{1}{96\pi^2 F_\pi^2} \left(1 + \log \frac{m_\pi^2}{m_\rho^2} \right)$. Eq. (2.80) gives an instruction how to extract a value for $F_{3\pi}$ from the subtraction constants, which in turn have to be determined by a fit to cross section data. We see that the two subtraction constants are directly linked to $F_{3\pi}$ via an additional renormalization term $3m_\pi \bar{C}$, which stems from the chiral expansion. It has been estimated in Ref. [41] and accounts for $3m_\pi^2 \bar{C} = 6.6\% \bar{F}_{3\pi}$.

To account for the second order chiral corrections, the dispersive representation should be compared to two-loop chiral expansion. The additional LECs, that appear in the NNLO correction, prevent an unambiguous extraction of $F_{3\pi}$. Since these LECs have been estimated in Ref. [42] by ‘‘order-of-magnitude arguments’’ [72], matching at two-loop level may prove valuable to check for systematic uncertainties.

2.4.4 Extraction of $\Gamma_{\rho \rightarrow \pi\gamma}$

The properties of a resonance are encoded in the pole position and residues of the S-matrix in a model independent way. For a comprehensive introduction into the S-matrix formalism, see e.g. Ref. [59]. The mass of a resonance determines the real part of the corresponding pole, whereas the width gives its imaginary part. The $\rho(770)$ pole position in the complex s -plane reads then

$$s_\rho = \left(m_\rho - i \frac{\Gamma_{\text{tot}}}{2} \right)^2 \quad (2.81)$$

The residue of the pole is proportional to the amplitude of a process (in a narrow-width approximation) and can be interpreted as the coupling constant of the process. The narrow-width approximation relates the residue of our pole $g_{\rho\pi\gamma}$ to the radiative width of the ρ via [76]

$$\Gamma_{\rho \rightarrow \pi\gamma} = \frac{e^2 g_{\rho\pi\gamma}^2}{96\pi m_\rho^3} (m_\rho^2 - m_\pi^2)^3 \quad (2.82)$$

The goal is hence to determine $g_{\rho\pi\gamma}$ from our dispersive model. The necessary calculations are involved. Its details can be followed in Ref. [76]. It proceeds by means of the unitarity relation which ultimately connects $g_{\rho\pi\gamma}$ with $g_{\rho\pi\pi}$ and $f_1(s)$:

$$\frac{e g_{\rho\pi\gamma}}{g_{\rho\pi\pi}} = -i \frac{s_\rho \sigma_\pi^2(s_\rho)}{48\pi} f_1(s_\rho) \quad (2.83)$$

with

$$\sigma_\pi(s) = \sqrt{1 - \frac{4m_\pi^2}{s}} \quad (2.84)$$

$f_1(s_\rho)$ can be calculated from Eq. (2.77) and was determined in Ref. [76]:

$$f_1(s_\rho) = C_2^{(1)}(0.588 + 0.193i) - C_2^{(2)}(0.071 + 0.570i) \text{ GeV}^2 \quad (2.85)$$

All that is needed to determine $g_{\rho\pi\gamma}$ from Eq. (2.83) is a realistic value for $g_{\rho\pi\pi}$, which can be taken from Ref. [79]: $|g_{\rho\pi\pi}| = 6.01_{-0.07}^{+0.04}$.

Chapter 3

The COMPASS experiment

Both major parts of the thesis, the analysis of the Primakoff data (see Chapters 5 to 8) and the hardware work (see Chapter 4), were carried at the COMPASS experiment. The presented analysis is based on the Primakoff data set recorded in the year 2009, whereas the hardware development improved the stability of the data taking campaigns in the years 2016 to 2022. This chapter briefly introduces the experimental setup in a general way before focusing on the particular spectrometer and trigger setup for 2009 and the FPGA-based data acquisition system, which has been put into operation only in 2014.

COMPASS (COMmon Muon Proton Apparatus for Structure and Spectroscopy) is a versatile experiment designed to study QCD in the low-energy regime. It is a fixed-target experiment located at the M2 beamline at CERN, which offers high-intensity, high-energy muon and hadron beams. Its magnetic spectrometer is able to perform high-resolution measurements of charged and neutral final states. The capability of the beamline to provide a high-energy (up to 250 GeV) negative pion beam combined with the flexible setup of the COMPASS spectrometer, in particular the adaptability of target material and trigger setup, offers a suitable opportunity to study low-energy QCD in Primakoff reactions.

3.1 General physics program and spectrometer layout

The COMPASS collaboration unites two different fields of high-energy particle physics: nuclear structure functions and hadron spectroscopy. The physics program of COMPASS I and COMPASS II [80, 81] covers campaigns using muon beams dedicated to measure parton distribution functions in e.g. Deeply Virtual Compton Scattering (DVCS), Semi-Inclusive Deep Inelastic Scattering (SIDIS), or Drell-Yan processes. Campaigns for meson spectroscopy, which require a pion beam, took place in the years 2004, 2008, 2009, and 2012. In these years, spectroscopy data are taken with a liquid-hydrogen and lead target. In the years 2009 and 2012, dedicated Primakoff campaigns were performed with nickel and tungsten targets and trigger setups for neutral particles in the final state.

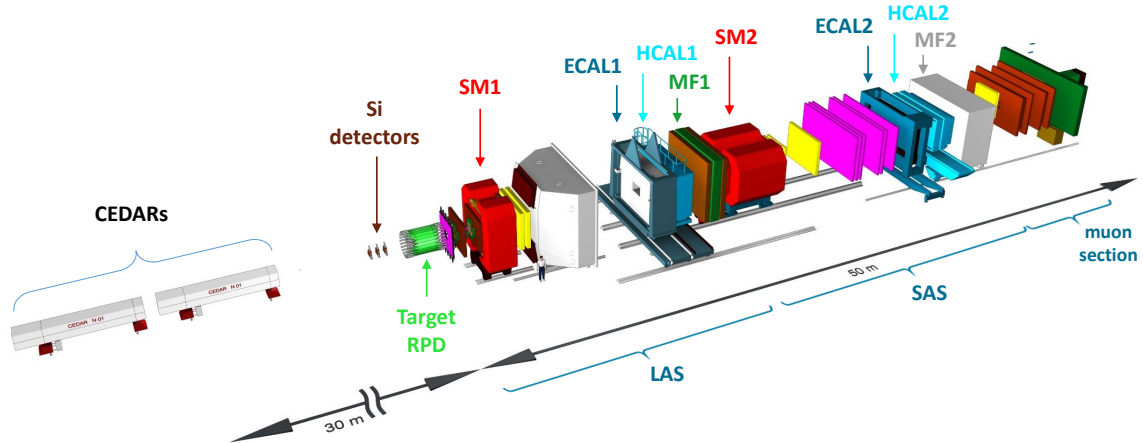


Fig. 3.1 Schematic view of the COMPASS setup for measurements with hadron beams. The beam enters the target region surrounded by the recoil proton detector (green) from the left side. The final-state particles are measured with the COMPASS Large-Angle (LAS) and Small-Angle (SAS) magnetic spectrometer. The figure was adapted from Ref. [82].

Merging the two initially independent initiatives, to measure structure functions and to perform hadron spectroscopy, into a single collaboration resulted in a highly flexible and versatile spectrometer setup [80]. The magnetic spectrometer was designed to offer high-rate capability, excellent particle identification, and a wide angular and momentum acceptance. To increase the covered angular and momentum range, the spectrometer is designed as a two-stage spectrometer. Directly downstream of the target is the so-called large-angle spectrometer (LAS), followed by the small-angle spectrometer (SAS). Each of the two stages is built around a dipole magnet. The magnet of the LAS, called SM1, has a bending power of 1.0 Tm, the one of the SAS, SM2, a bending power of 5.5 Tm. Charged particles with momentum higher than $\sim 15 \text{ GeV}/c$ are able to enter the second stage. The magnets are preceded and followed by telescopes of tracking detectors. Each stage features a hadronic and electromagnetic calorimeter and a muon filter station for high energy muon identification. The LAS contains a ring-imaging Cherenkov detector (RICH) for hadron identification. The overall layout covers an opening angle of $\pm 180 \text{ mrad}$ [80]. SAS and LAS together span over 50 m in length. The general spectrometer layout can be seen in Fig. 3.1 for the setup with hadron beams [82].

Different detector technologies are used in each tracking telescope at different distances from the beam axis to match the requirements in rate capability, space and time resolution, and active surface to be covered. Along the beam axis and close to the target, detectors must provide high-rate capability and excellent spatial resolution of $\sim 10 \mu\text{m}$. Far from the beam axis, the requirements on rate capability are less strict, but larger areas need to be covered. Details on the different tracking detectors can be found in Refs. [80, 81, 82]. The hadronic and electromagnetic calorimeter as well as the muon filter of the LAS feature a central hole matching the angular acceptance of the SAS.

The target region is equipped with high-resolution silicon detectors. Three stations upstream of the target measure beam trajectories and form the beam telescope. Two stations downstream of the target ensure precise vertex reconstruction around the target position.

3.2 The M2 beamline at CERN

The M2 beamline provides high-intensity, high-energy muon and hadron beams, both positively and negatively charged. Protons from the Super Proton Synchrotron (SPS) with a momentum of around 400 GeV impinge on a Beryllium production target leading to showers of secondary hadrons, mainly pions, kaons, and protons, downstream of the production target. Particles of the desired momentum range are selected by a series of quadrupole and dipole magnets and collimators. The almost 1 km long M2 beamline allows collected pions to decay to muons. By filtering for muons with a hadron absorber upstream of the experiment, the beamline can offer a tertiary muon beam.

For the Primakoff campaign, a secondary, ~ 190 GeV, negative hadron beam was chosen. This beam features a high intensity of $5 \cdot 10^6 \text{ s}^{-1}$ and a low momentum spread on percent-level. The negative hadron beam used in 2009 is mainly composed of pions (94.3%), kaons (2.55%), and antiprotons (1%). According to the high-precision determination of the beam composition in Ref. [83], taking into account a possible muon contribution in the beam, the kaon-to-pion ratio in the beam was found to be:

$$R_{\text{beam}} := \frac{n_{K^-}}{n_{\pi^-}} = 0.02785 \left(\begin{smallmatrix} +0.00048 \\ -0.00063 \end{smallmatrix} \right)_{\text{stat}} (+0.0003)_{\text{sys}} \quad (3.1)$$

For beam particle identification, two Cherenkov detectors, so-called CEDAR detectors [84] (Cherenkov differential counter with achromatic ring focus), are placed ~ 30 m upstream of the COMPASS target. Beam particles traverse the 6 m long vessel filled with pressurized helium gas centered the beam axis indicated in Fig. 3.2 by the gray dashed line. They move faster than the speed of light in helium gas and emit Cherenkov light in a characteristic angle depending on the velocity of the particle. Since the momentum of the particle is defined by the beam optics and is the same for all particles, different species with different masses have different velocities and radiate Cherenkov photons in slightly different angles indicated by the green and red lines in Fig. 3.2. The emitted Cherenkov cone is focused by a parabolic mirror

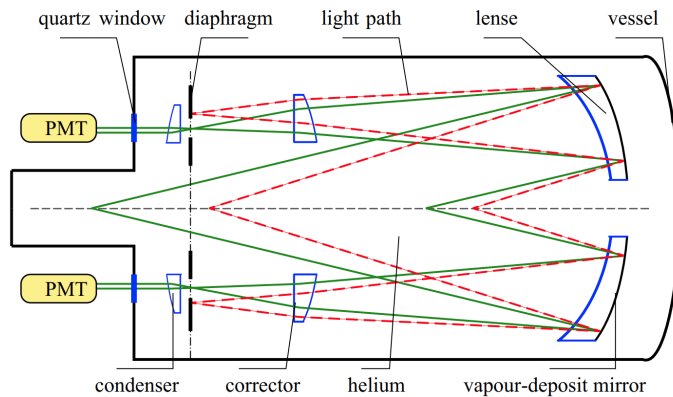


Fig. 3.2 The basic principle of the CEDAR detector. Two particles with the same momentum but with different masses (green and red lines) radiate Cherenkov photons at different angles. Using mirrors, the light cones are focused to rings with different radii. A diaphragm selects the rings from the desired particle type. Figure taken from [82].

and lenses to a ring. A diaphragm selects Cherenkov light that was emitted under an angle of $\sim 25.8\text{mrad}$ [84]. By adjusting the gas pressure inside the main vessel, the refractive index of each CEDAR can be adjusted to be sensitive to a particular particle species. In 2009 for the negative hadron beam, both CEDARs were adjusted to identify kaons to maximize kaon detection efficiency.

The projected Cherenkov ring is detected by eight photo multiplier tubes (PMTs) which are equidistantly positioned around the ring of the diaphragm. A simple approach to identify a particle is the so-called majority method, which requires a signal in at least six of the eight PMTs, allowing for inefficiencies of the tubes. The majority method however reaches only an efficiency of less than 50% [82] due to the small difference in the Cherenkov angles θ of pions and kaons compared to the large inclination spread of beam trajectories:

$$\Delta\theta = \theta_K - \theta_\pi \approx 120\ \mu\text{rad} \quad (3.2)$$

where we have used $\cos\theta = 1/(n\beta)$ with $n \approx 1.00034$ estimated from the required detection angle 25.8mrad . $\Delta\theta$ is in the same order of magnitude as the spread in inclination of beam trajectories of about $200\ \mu\text{rad}$ (see Fig. 5.2b).

To improve the efficiency for tagging beam kaons, we use a likelihood approach developed in Ref. [85] and optimized for the 2009 Primakoff data taking campaign. This approach is based on evaluating the CEDAR response on clean kaon (from $K^- \rightarrow \pi^- \pi^0$) and pion (from $\pi^- + N \rightarrow \pi^- \pi^0 + N$) samples and extrapolating their trajectory, which is measured by the beam telescope, back to the CEDAR location using the knowledge of the beam optics. The likelihood approach increases the CEDAR efficiencies to correctly tag kaons and pions to

$$\begin{aligned} \epsilon_\pi &= 0.934(\pm 0.003)_{\text{stat}}(\pm 0.009)_{\text{sys}} \\ \epsilon_K &= 0.825(\pm 0.004)_{\text{stat}}(\pm 0.001)_{\text{sys}} \end{aligned} \quad (3.3)$$

where the statistical and systematic uncertainties are not explicitly given in Ref. [85], but estimated from the number of events in the study and by the difference between the two approaches presented in the note.

As already mentioned, the M2 beamline provides muon and hadron beams with a momentum spread of about 3% from 188.5 GeV to 194.5 GeV [86]. In case of data taking with muon beam, the exact beam momentum can be determined by using the beam momentum station (BMS) consisting of six tracking planes up- and downstream of one of the last bending magnet in the M2 beamline. For data taking with hadron beam, the BMS is removed to minimize the material budget along the beam path.

Since the beam line optics incorporate correlations between beam momentum and beam position/inclination, one can constrain the energy of the incoming beam particle based on the four-dimensional space $(x, y, \frac{p_x}{p_z}, \frac{p_y}{p_z})$ with the beam axis in z -direction. We use the polynomial described in Ref. [86], which correlates beam energy and the parameters of the beam trajectory at the position $z_0 = -72.5\text{cm}$:

$$E_{\text{beam}} = \sum_{i,m=0}^5 \sum_{j,n=0}^{5-i} B_{mn}^{ij} x_{ij} a^{mn} \quad (3.4)$$

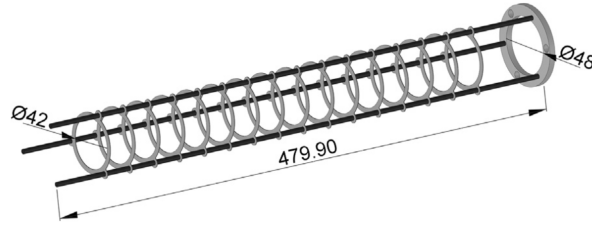


Fig. 3.3 Schematic view of the target holder used for measurements with nuclear targets [82], the dimensions are in mm.

with B_{mn}^{ij} being a rank four tensor holding parameters which encode the beam optics. The parameters for the 2009 and 2012 hadron beamline setup are given in [86]. The matrices $x_{ij} = x^i \cdot y^j$ and $a_{mn} = \left(\frac{p_x}{p_z}\right)^m \cdot \left(\frac{p_y}{p_z}\right)^n$ have the dimension 6×6 and contain all powers of the beam trajectory position and inclination in x - and y -direction.

3.3 Spectrometer setup in 2009 for the Primakoff program

Details about the COMPASS setup with hadron beams can be found in Ref. [82]. We will summarize only the most important and specific features of the setup for the Primakoff measurement in the following. We introduce the COMPASS main coordinate system as it is used in the reconstruction of events:

The origin of the reference system is in the target region. The z -axis points along the beam axis. x and y are the transverse coordinates with the y -axis pointing upwards. The x -axis is defined horizontally to get a right-handed coordinate system. The spectrometer magnets bend negatively charged particles in positive x -direction.

3.3.1 Target region

The target region comprises the target itself, the *recoil proton detector* (RPD) surrounding the target, the Sandwich veto detector, and the silicon detectors. For measurements with nuclear targets, as it is the case for the Primakoff program, a light-weight target holder made of carbon fiber rods and thin frames of fiberglass reinforced epoxy was engineered as can be seen in Fig. 3.3. It can house up to 16 target disks glued to the frames.

The set of target disks for the Primakoff run consists of one 4.2mm nickel disk the main target and two thin disks of tungsten. The additional tungsten targets provide the possibility to verify and cross-check the Z -dependence of the Weizsäcker-Williams approximation (see Eq. (2.23)). Table 3.1 summarizes the different target disks and their properties.

The target thicknesses were chosen mainly to limit the conversion of photons and minimize the effect of multiple scattering on the resolution of charged-particle trajectories. Since the tungsten targets are located more downstream, they are thinner to minimize the impact on

3.3. SPECTROMETER SETUP IN 2009 FOR THE PRIMAKOFF PROGRAM

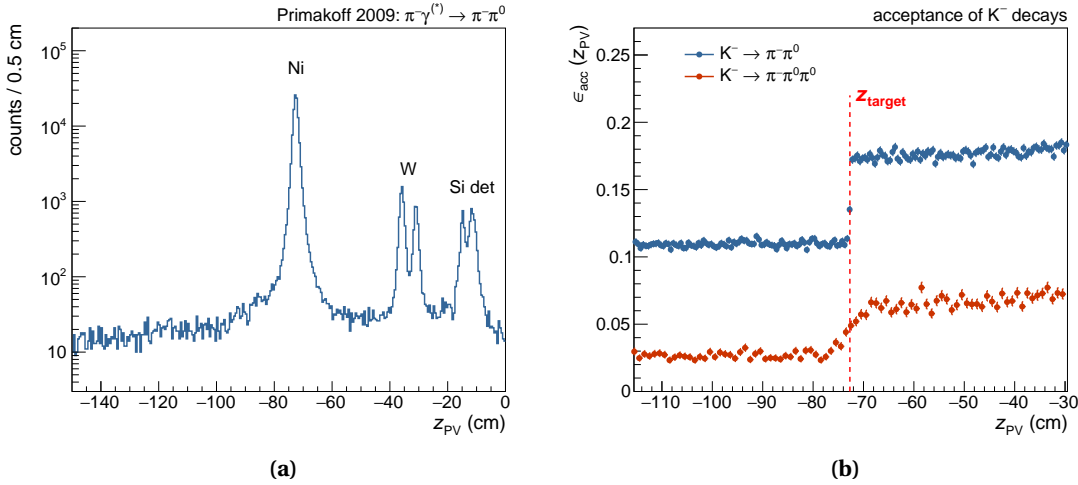


Fig. 3.4 In (a): Distribution of primary vertices along the z -axis for selected $\pi^-\gamma^{(*)} \rightarrow \pi^-\pi^0$ events in the target area. In (b): acceptance for $K^- \rightarrow \pi^-\pi^0$ (blue) and $K^- \rightarrow \pi^-\pi^0\pi^0$ (red) decays over the Ni target disk.

events originating at the main target. At the same time, this setup limits the luminosity on the tungsten targets. Fig. 3.4a shows the distribution of reconstructed primary vertices of selected $\pi^-\gamma^{(*)} \rightarrow \pi^-\pi^0$ events. We can identify areas, where denser material is placed along the beam axis: the nickel and tungsten targets, and parts of the first silicon tracking detector (entrance window and first plane).

The 4.2 mm thickness of the Ni target is also a compromise of maximizing luminosity and minimizing photon conversion rate to retain a reasonable sensitivity for events originating upstream of the target, in particular for kaon decays. As will become clear in Chapter 7, sensitivity for kaon decays is essential for the analysis. Fig. 3.4b shows the gradient of the probability to detect a kaon decay, the so-called *acceptance* $\epsilon_{\text{acc}}(z)$, along the z -axis.

3.3.2 Electromagnetic calorimeters

The processes of interest (see Eq. (5.1)) for the presented analysis contain all either one or two neutral pions. The electromagnetic calorimeters are hence of major importance. A good energy and spatial resolution of the calorimeters is essential to be capable to reconstruct and resolve the tiny momentum transfer $\mathcal{O}(\text{MeV})$ which characterizes Primakoff events. The spectrometer setup of 2009 comprises two electromagnetic calorimeters: ECAL1 in the LAS

Table 3.1 Overview of target disks used during the Primakoff run 2009.

Material	z -position (cm)	Thickness		
		(mm)	(X_0) (%)	(g/cm^2)
Ni	-72.6	4.2	29.5	3.74
W	-36.0	0.050	1.43	0.092
W	-31.1	0.025	0.71	0.048

and ECAL2 in the SAS. ECAL1 covers the angular ranges 37–136 mrad in x and 21–98 mrad in y for photons originating in the target region. ECAL2 covers the angular ranges up to 39 mrad in x -direction and up to 29 mrad in y with a hole in the acceptance for the beam spot. For the Primakoff run 2009, more than 99% of reconstructed electromagnetic showers are detected in ECAL2 [63]. ECAL2 also offers superior spatial and energy resolution to ECAL1. The energy resolution can be studied through the width of the reconstructed π^0 peak and is given as $8.85 \text{ MeV}/c^2$ for ECAL1 and $3.88 \text{ MeV}/c^2$ for ECAL2 [87]. For these reasons, we will consider only ECAL2 for the analysis presented in this thesis and neglect the kinematic region where one of the photons of the final state is detected by ECAL1.

The ECAL2 modules are arranged in a 64×48 matrix as shown in Fig. 3.5. There are three different types of modules each with identical transverse size of $3.83 \times 3.83 \text{ cm}^2$. The outermost and the intermediate parts are equipped with similar, homogeneous lead glass blocks of slightly different materials. The material used for the intermediate part is radiation hardened by being enriched with cerium [82]. The innermost part of ECAL2 is equipped with Shashlik type modules, which are composed of ~ 300 alternating layers of lead and scintillator plates. The photons from the scintillator plates are collected by 16 wavelength-shifting fibers and guided to a photomultiplier at the back of the module. The Shashlik modules provide higher stopping power and even higher radiation hardness compared to the lead glass modules. For the Primakoff data taking, there is a hole of 2×2 cells at the nominal beam position in ECAL2.

3.3.3 Trigger strategy

The COMPASS Primakoff trigger in 2009 is designed to select events with neutral particles in the final state. The limited buffer capability of the detector readout electronics requires a fast trigger decision within $3 \mu\text{s}$, which limits the complexity of the trigger. The Primakoff trigger

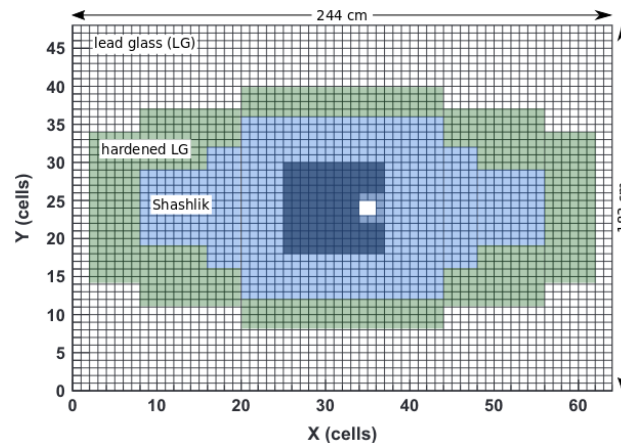


Fig. 3.5 Structure of ECAL2: the calorimeter is composed of lead glass, radiation-hardened lead glass, and Shashlik modules. The active area of the ECAL2 trigger (shown in dark blue) lies in the center within the Shashlik area. The cells around the beam hole (white spot), that are shown in lighter blue, are explicitly excluded from contributing to the trigger due to high rates. The lead glass and Shashlik areas are corrected w.r.t. Ref. [82].

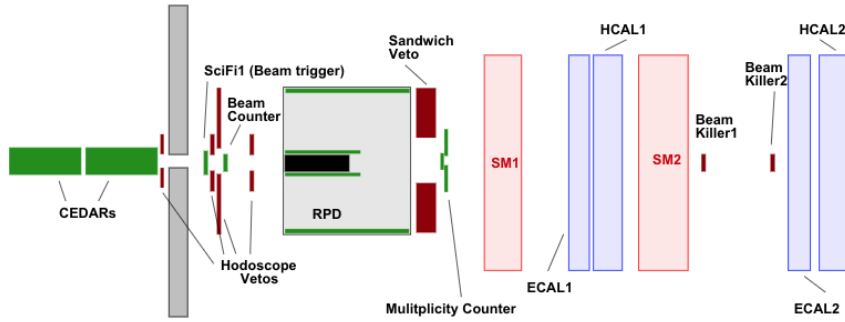


Fig. 3.6 Arrangement of trigger elements in the spectrometer (schematic side view, not to scale). Taken from Ref. [82].

consists of three subsystems: "beam-defining elements to select beam particles crossing the target, veto detectors to reject events containing particles produced outside the target or outside the spectrometer acceptance," [82] and, specific for the Primakoff trigger, a minimum energy deposit in the calorimeters to require neutral particles in the final state. Fig. 3.6 shows schematically the location of the different trigger elements in the spectrometer.

The first trigger subsystem, the beam trigger, selects incoming beam particles. It consists of two fast-responding detectors and sets the reference time for an event. It is triggered on a coincident signal in a scintillating fiber detector (SciFi1) located ~ 7 m upstream of the target region and in a beam counter. The beam counter is a scintillating disk of similar shape (3.2 cm diameter) as the target disks and hence "reduces the geometric acceptance of the beam in the transverse plane to match the target geometry" [82].

The second trigger subsystem, the veto, consists of two scintillation counters ("beam killers"), a Sandwich veto detector and a hodoscope veto system. The beam killers have a diameter of 3.5 cm and are placed along the beam axis. A coincident signal in both beam killers inhibits a false trigger signal caused by non-interacting beam particles. The hodoscope veto removes events with beam particles far from the beam axis. Details can be found in Refs. [80, 88]. The active area of the sandwich veto detector covers exactly the angular acceptance gap of RPD and spectrometer. It is sensitive to charged and neutral particles.

The calorimetric trigger selects high-energy photons in forward direction detected by some of the most central 12×12 cells of ECAL2. The trigger implements the sum of time-correlated energies in the selected region of cells. The active cells contributing to the sum are given by:

$$\delta_{XY} = \begin{cases} 1 & \text{if } (24 < \mathbf{X} < 37 \wedge 17 < \mathbf{Y} < 30) \bar{\wedge} (\mathbf{X} > 33 \wedge 21 < \mathbf{Y} < 26) \\ 0 & \text{else} \end{cases} \quad (3.5)$$

with \mathbf{X} and \mathbf{Y} being the indices of the column respectively row of cells in ECAL2. The condition of Eq. (3.5) is visualized in Fig. 3.5. In addition, each cell has an individual threshold of around 700 MeV which is applied on the level of the front-end electronics, given in ADC channels, and—due to individual calibration constants per cell—differs for each cell.

The sum of the energies of cells of the selected region is compared to a programmable threshold. For the run 2009, there were two different Primakoff triggers implemented. The Pri-

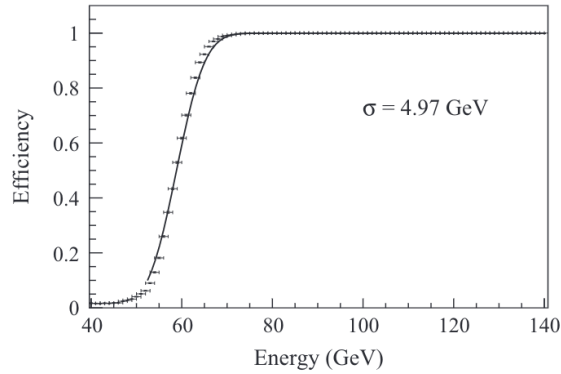


Fig. 3.7 Efficiency of the ECAL2 trigger as a function of the energy. The solid line is an error function fitted to the data. Taken from Ref. [82].

Table 3.2 Overview of trigger (sub-)systems and vetos used during the Primakoff run 2009. For the physics triggers, the number of recorded events in the 2009 Primakoff data set is given.

Trigger/Vetos	Logical composition	Recorded events
Beam trigger (BT)	SciFi1 \wedge beam counter	14.40 M
Beam killer veto	beam killer 1 \wedge beam killer 2	—
Veto	Sandwich \vee veto hodoscopes \vee beam killer	—
Calorimeter trigger (CT)	$\sum_{12 \times 12}$ cell amplitude $>$ threshold	—
Primakoff trigger Prim1	BT \wedge CT ($>$ 40 GeV) $\bar{\Lambda}$ veto	158.2 M
Primakoff trigger Prim2	BT \wedge CT ($>$ 60 GeV) $\bar{\Lambda}$ veto	199.8 M

makoff trigger “Prim2” used a threshold of $E_{\text{Prim2}} \gtrsim 60 \text{ GeV}$, “Prim1” a threshold of $E_{\text{Prim1}} \gtrsim 40 \text{ GeV}$. “Prim1” is prescaled with a factor of two and used to monitor the behavior of “Prim2”. In this way, the efficiency of “Prim2” can be observed as shown in Fig. 3.7. Table 3.2 shows, how the physics triggers are composed of the individual subsystems.

The per-cell thresholds are difficult to replicate in simulation. To circumvent a delicate description of the calibration, we apply a threshold of 1.2 GeV to each cell. The threshold is chosen sufficiently high, such that it supercedes the internal hardware threshold of each of the contributing cells:

$$E_{\text{XY}}^{\text{thr}} = \begin{cases} E_{\text{XY}} & \text{if } E_{\text{XY}} > 1.2 \text{ GeV} \\ 0 & \text{else} \end{cases} \quad (3.6)$$

In the following of this thesis, the deposited energy in the active area of the calorimetric trigger is calculated via:

$$E_{\text{trig}} = \sum_{\text{XY}} E_{\text{XY}}^{\text{thr}} \cdot \delta_{\text{XY}} \quad (3.7)$$

The final composite triggers are summarized in Table 3.2. For the physics triggers, which actually triggered the data acquisition, the table lists the number of corresponding events/triggers in the 2009 Primakoff data set.

3.4 Accessible Primakoff channels at COMPASS

The setup of the COMPASS spectrometer and the premises of the M2 beamline give access to following Primakoff reactions with the beam impinging on nuclear targets:

$$\pi^- + \gamma^{(*)} \rightarrow \begin{cases} \pi^- \gamma & \text{Compton reaction, pion polarizability [89]} \\ \pi^- \pi^0 & \text{chiral anomaly, radiative width of } \rho \\ \pi^- \pi^0 \pi^0 & \text{chiral tree and chiral loop} \\ \pi^- \pi^+ \pi^- & \text{resonances, exotics [90]} \end{cases} \quad (3.8)$$

In 2004, the negative hadron beam was impinging on lead targets and the setup comprised a trigger sensitive for $\pi^- \pi^- \pi^+$ events. Using partial-wave analysis techniques, Primakoff events were identified and the dependence of their scattering intensity on the 3π -invariant mass was compared to predictions of ChPT in Ref. [90].

With the setup in 2009 and 2012, final states with neutral particles were recorded. The trigger setup in 2012 was similar to the one described above. It was tuned mainly for the Primakoff Compton reaction $\pi^- \gamma^{(*)} \rightarrow \pi^- \gamma$. The corresponding analysis has already been carried out and a value for the pion polarizability was published in Refs. [89, 91] based on the 2009 data set.

The 2009 and 2012 data sets contain also $\pi^- \pi^0$ and $\pi^- \pi^0 \pi^0$ final states. Extensive preparatory work for the analysis of the two final states has been done in Refs. [46, 63].

3.5 Readout electronics and Data Acquisition System

The COMPASS experiment is taking data since 2002. Since then, the amount of collected data is increasing year by year, mainly due to an increase of accelerator luminosity and trigger rates, and a growing number of detector channels. A trend stimulated by ever developing storage and processing power, which can be seen in (almost) all high-energy physics experiments. Data acquisition and event building, i.e. the collection of event fragments of the different subdetectors in the short amount of time between two triggers, is a common challenge in all high-energy physics experiments and has become more and more complex. Dedicated Data-Acquisition systems (DAQ) unite the tasks of digitization, event-building, and saving the data to disk. The potential need of higher-level triggers, which ideally consider already the full detector data, requires inevitably an online event building mechanism. Most current DAQ systems use an Ethernet-based network of distributed online computers for this purpose. Concurrent developments in the technology of Field-Programmable Gate Arrays (FPGA), such as increased I/O bandwidth ($> 3 \text{ Gb/s}$) and support for high-performance SDRAM, make also FPGAs suitable for event building purposes. Over the years, the electronics of the COMPASS experiment on the detectors (front-end) as well as on the event-builder side were upgraded continuously to be capable of handling the increasing amount of data from $\mathcal{O}(100 \text{ MB/s})$ in 2002 to $\mathcal{O}(1 \text{ GB/s})$ in 2012.

Triggered by the need of a versatile, scalable, and highly reliable DAQ, the COMPASS collaboration decided to develop a new DAQ from scratch exploiting the application-specific technology of FPGAs. COMPASS commissioned its so-called intelligent, FPGA-based DAQ (iFDAQ) during the shutdown of the SPS in the years 2013 and 2014. In the following years, the system was debugged and extended.

3.5.1 System design and topology of the iFDAQ from 2014 to 2019

The core of the iFDAQ is its hardware event builder based on FPGAs. Traditional, software-based approaches rely on distributed online computers interconnected via an Ethernet Gigabit network. Compared to more traditional event builders, the iFDAQ event builder reduces costs and provides higher reliability, increased compactness and less maintenance efforts.

The hardware event builder consists of custom designed DAQ units, called Data Handling Cards (DHC) shown in Fig. 3.8. The heart of the DHCs is a XC6VLX130T FPGA of the Virtex6 family by Xilinx. Moreover, it is equipped with 4 GB DDR3 SDRAM which is used to buffer data on the module. It follows the μ TCA/AMC standard [92] and is mounted on a VME carrier card which provides the necessary ports for the different interfaces: 16 optical high-speed links, Ethernet, and TCS (trigger control system) interface. There are two different operation modes of the DHCs: they can either be used with a firmware configuring them as a 15:1 multiplexer (DHCmx) or as 8×8 switch (DHCsw). For a detailed description of the firmware designs, refer to Ref. [93].

Fig. 3.9 shows the setup of the iFDAQ exemplarily for the run 2017. The frontend electronics digitize the signals of the roughly 300k detector channels and transmit data to the data concentrator modules. Selected channels are fed to the trigger system, which takes a trigger decision based on these signals. The trigger decision is distributed via the TCS to all nodes of the iFDAQ. On a trigger, the data concentrator modules assemble a data package encapsulating the data of the connected channels and transmit it to the DHC modules of the hardware event builder via optical links using the S-Link protocol developed at CERN [94]. An optional intermediate multiplexing stage allows merging data streams of concentrator modules with low rates for an efficient usage of the S-Link bandwidth. The intermediate multiplexing stage consists of either DHCmx (15:1) or S-Link multiplexer (4:1) modules. Another layer of maximum eight DHCmx modules ensures that the maximum number of input links to the DHCsw



Fig. 3.8 Data Handling Card (DHC) mounted on a VME carrier card. The carrier card provides the necessary interconnection ports for the different interfaces.

3.5. READOUT ELECTRONICS AND DATA ACQUISITION SYSTEM

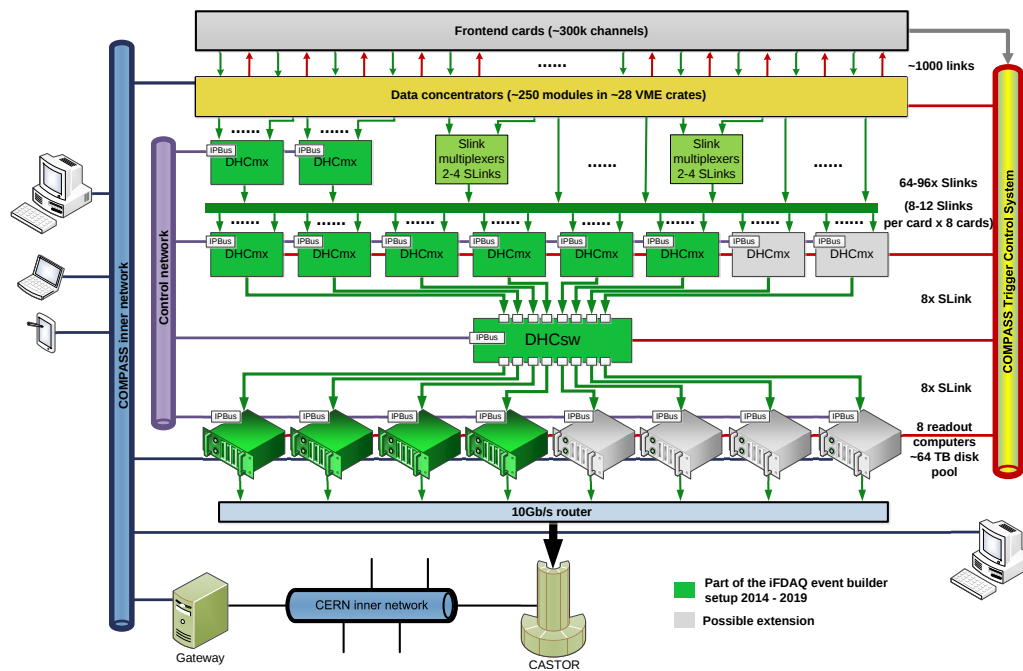


Fig. 3.9 Setup and network topology of the iFDAQ in the years 2014 to 2019.

module is not exceeded. In a round-robin, the DHCsw module distributes fully assembled events to the spillbuffer cards plugged into the readout engines. The spillbuffer cards are off-the-shelf FPGA modules, which provide a PCI-E interface to transmit the data into the buffer memory of the readout computers.

Since all data has to go through the DHCsw module, the DHCsw is the bottleneck of the system, making high data throughput the main requirement. The throughput of the DHCsw module depends on the event size. Its upper limit is 3 GB/s and for typical average event sizes, it is ≥ 1.5 GB/s [95]. The peak on-spill data rate, which is generated by the frontend electronics is around 8 GB/s. The system exploits the spill-structure of the SPS duty cycle, in which a spill period of around 5 s is followed by an off-spill period without beam of at least the same amount of time, often longer in the range 20 to 40 s. By buffering the data on all levels of the system, the on-spill data rate can be averaged over the whole accelerator duty cycle. Hence, the final four readout computers work independently of the instantaneous rate at a sustained rate of up to 500 MB/s.

The system uses three independent interfaces. For synchronization and distribution of event information, the already mentioned Trigger Control System (TCS) is used [96]. The data flow and thus the event building follows the S-Link specifications, which is a point-to-point connection. For configuration, monitoring, and control of the hardware nodes of the iFDAQ, a network protocol, the so-called IPBus [97], over Ethernet is used. The functional division simplifies diagnostic capabilities and offers efficient usage of the data bandwidth.

The requirements for the event builder such as maximum and average event size, trigger rate, and number of incoming optical links, change from program to program depending on the

spectrometer setup. The iFDAQ provides the needed flexibility and scalability to cope with the changing setups by adding or reducing the amount of DHCmx modules and/or readout engines.

The iFDAQ was designed to be a highly automated system. Intelligent and automated features increase the user-friendliness and turned out to be commonly used and appreciated by scientific staff on shift. Following intelligence elements have been deployed until 2018:

- Self-synchronized event building data flow: initiating the data flow through the event builder and maintaining a synchronous processing of data by all involved hardware nodes is achieved by distributing trigger and spill cycle information to all nodes via the Trigger Control System (TCS) and applying reset commands and timeouts. In this way, an asynchronous working node recovers usually at the latest on the next spill.
- Automatic resynchronization of front-end modules: the TCS information is also distributed to the data concentrator modules, which allows for similar automatic resynchronization. Moreover, data from a concentrator module can be excluded or included at the time during the run.
- Continuous front-end error diagnostic, automatic error handling and recovery: during the development of the iFDAQ, great emphasis was put on the ability to recover and handle errors in the data stream emerging from front-end electronics and on the capability to identify their origin. On each level of the event builder, data consistency checks are performed.

3.5.2 Software architecture of the iFDAQ

The support software for the iFDAQ provides six main functions: configuration, monitoring, and remote control of the hardware nodes, logging of information and error messages, brows-

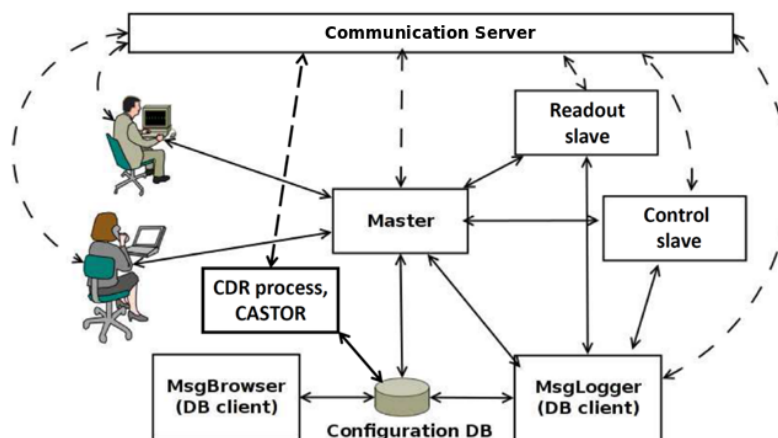


Fig. 3.10 Communication diagram of the different processes which form the support software of the iFDAQ. Adapted from Ref. [98].

ing of the messages, and readout of the fully assembled events that the hardware event builder buffered in the RAM of the readout engines.

To fulfill all these functions, the support software is a multilayer system centered around a master process, as illustrated in Fig. 3.10. Exactly one master process is automatically started on one of the iFDAQ computers. It acts as a middleman between Graphical User Interfaces (GUIs), the database server (DB), and all other processes. The GUIs display the overall status of the iFDAQ to the user and allow the shift crew to control the iFDAQ, e.g. start data taking. The support software incorporates only one real-time process, the readout slave, which is responsible for transferring the fully assembled events from SDRAM to the machine-internal hard disk. To monitor, configure, and control the hardware nodes, the master process starts one control slave per node. The message logger collects all messages from the master process and all slave processes and stores them in the DB. The message browser provides an interface for users to see new messages when they pop-up, access older messages, and offers filtering possibilities. The CDR process transfers the buffered data to CERN's Central Data Recording (CDR) facility. For inter-process communication, each process subscribes to a communication server on start-up [99].

The iFDAQ can be in four different states:

1. Turned off: only the master process is existing. It is hibernating, waiting for a command to become active.
2. Slaves started: during the transition, the master process spawns one monitoring slave process for each FPGA hardware node in the selected iFDAQ setup and starts readout slaves on each readout computer.
3. Configured: During the transition, each slave process looks up the needed information about registers on their corresponding hardware node in the database and configures the hardware node accordingly via the IPBus network. While being in the state, the monitoring slave continuously monitors the node.
4. Run/Dry run: Data flow and the necessary synchronization is established. Monitoring slaves continuously monitor their corresponding hardware node. Readout slaves move data from RAM to disk.

Chapter 4

Improving reliability and stability of the data acquisition

Data acquisition and event building are crucial tasks in any high-energy physics experiment. Like almost nothing else, downtime and reliability of the DAQ influence the efficient usage of expensive beam times. It is therefore of high importance, to minimize DAQ downtimes and improve reliability and stability of the data taking.

At COMPASS, inefficiencies during the data taking campaign arise mainly for two reasons: first, errors in the frontend electronics, which subsequently propagate through the data acquisition chain and cause a loss of synchronization of the hardware nodes until all buffers are reset on the next spill. And second, buffer overflow or hardware failure later in the data acquisition chain on one of the hardware nodes.

These two effects have different reasons. The frontend electronics, in particular the analog part, is very sensitive to properties of the beam. They are operated at COMPASS close to their maximum event and data rate capability. Any intensity spike in the beam may therefore lead to failure of the frontend electronics. The reliability can hence be improved by providing a monitoring tool for beam properties, which will allow SPS and beamline operators to tune their machines. We will discuss the implementation of a real-time beam monitoring system in Section 4.2. The system was developed by C. Michalski [100]. The final implementation and support was done in the scope of this work.

In contrast to the frontend electronics, the event building nodes work independent of the immediate beam rate shielded by several levels of buffers. Still, high load on the nodes also increases probability of failure. Dynamic load balancing between the hardware nodes is hence a mean to increase the reliability of the event builder. In particular during the commissioning phase of the spectrometer at the beginning of a data taking campaign, the average event rate of each detector is not yet known and frequent intervention is necessary. In Section 4.1 we will describe the design and implementation of a crosspoint switch, which allows rerouting point-to-point interconnections without manually plugging cables.

4.1 Crosspoint switch

Event building describes the combination of logically connected, because they can be attributed to the same trigger, but physically split data fragments. In high-energy physics, the event fragments are physically split, due to the typical size of the experiments, up to 100 m and the various kinds of detectors which make up the whole experiment.

Fig. 4.1a shows the traditional approach to tackle the task of event building, as it used also by many LHC experiments [101, 102]. Soon after digitization, the event fragments are stored in buffer PCs. A control unit distributes a message to which event builder PC the fragments of one event should be forwarded. The builder collects the different data fragments, combines them, and sends them to a central data recording (CDR) facility for off-line storage. The transmission from buffer to builder unit is carried out via a standard IP-based network protocol and off-the-shelf Ethernet network switch. Buffer units and event builder units can be replicated over a number of computers to fulfill performance needs and application scenarios. Benefits of the traditional approach are the simple integration of redundancy elements and the usage of mass-produced components. Traffic shaping in the event building network can be done on-the-fly by the control unit based on the constantly monitored load on builder nodes. A major drawback of this approach is that the throughput of the system is limited by the event building network switch. In addition, the network bandwidth is inefficiently used. Standard IP-based addressing protocols are not suited for the required communication pattern in event building networks. Data packages from many senders, which have to be routed to a single receiver, lead to network congestion. Additionally, the data overhead due to addressing and protocol standards can become significant for small data packages. All this leads to an inefficient usage of the available bandwidth and hence higher costs for high-performance hardware.

A different approach to event building was taken by the COMPASS collaboration in 2014 with the deployment of the iFDAQ. The event building is carried out by hardware nodes in FPGAs exploiting their parallel processing capabilities and pipeline architecture. The necessary

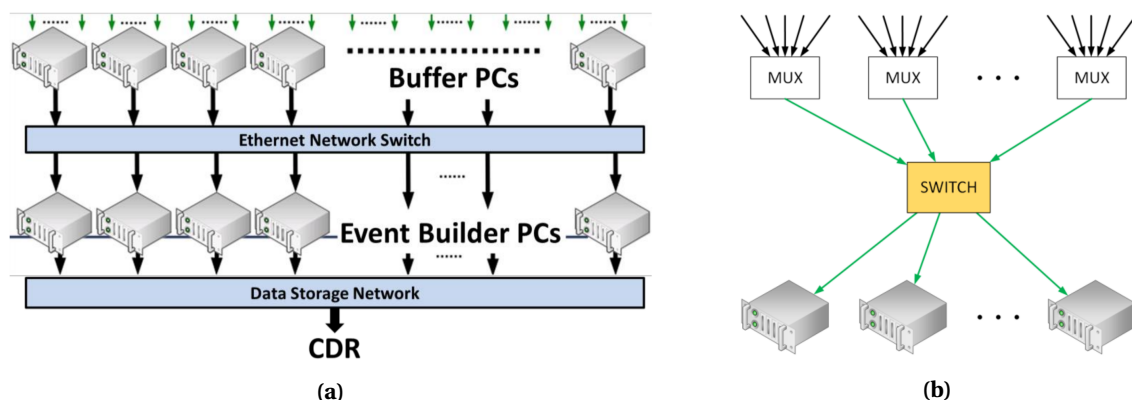


Fig. 4.1 Event builder architectures. In (a): conventional approach with PCs interconnected via Ethernet network fulfilling the event building task. In (b): pipeline architecture exploiting the properties of FPGAs. The FPGAs are interconnected with point-to-point high-speed links.

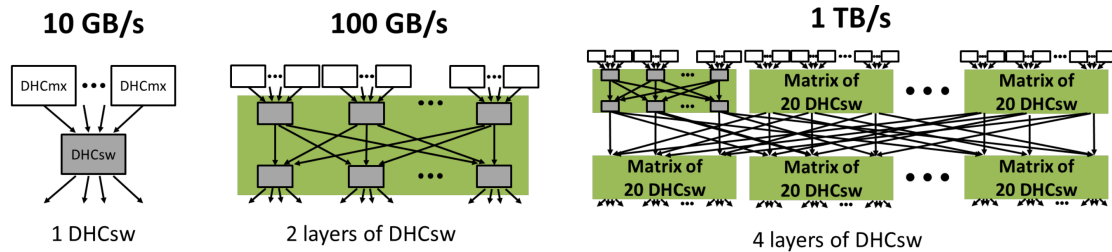


Fig. 4.2 Possibility to scale data throughput of a hardware event builder. The scenario exemplarily assumes a 10×10 switch module with a throughput of 10 GB/s for a single module.

high-speed links are point-to-point connections avoiding the overhead for addressing and enabling efficient usage of the link bandwidth. The bottleneck in this approach is the DHCsw module, by which all data have to be processed. It is, however, possible to scale the throughput by replacing the single DHCsw module with a matrix of DHCsw modules as indicated in Fig. 4.2. A hardware event builder provides a cost-efficient, highly reliable alternative to the traditional approaches. The remaining drawbacks are a strong dependence on single nodes in the hardware event builder and the lack of dynamic load balancing.

Both drawbacks arise due to the lack of simple and fast rerouting capabilities. In case of failure of one hardware node, rerouting to a redundant node allows compensating for the broken module. At the same time rerouting capabilities provide a fully customizable network topology, which can quickly be adapted to distribute the load equally on event building nodes. A programmable crosspoint switch, which can connect any data output to any data input, can provide reroutable point-to-point interconnections between nodes of the event builder.

4.1.1 Hardware and firmware design

There are several commercial manufacturers of crosspoint switches. We chose the Vitesse VSC3144 which comes as a $45 \text{ mm} \times 45 \text{ mm}$ 1072-pin BGA (ball grid array) chip for deployment on a PCB (printed circuit board). It provides 144×144 strictly non-blocking ports at a maximum bandwidth of 6.5 Gb/s per port. Since there are no registers used in the internal data path, i.e. it is fully asynchronous, the chip does not impose any restrictions on the phase, frequency, or signal pattern on any input. It can be used independent of communication protocols.

The high density of high-speed lines requires an elaborate PCB design with twelve layers and usage of low-footprint fiber connectors. The multi-fiber push on (MPO) connector comprises multiple optical fibers in a single ferrule. Their typical application is in large-scale data centers as plug and play backbone cables between switches. We used the 24 fiber version, which comprises 24 high-speed optical fibers in a single connector, as shown in Fig. 4.3a. The MPO standard provides so-called harness cables to interface with the lucent connectors (LC) used so far for hardware nodes of the iFDAQ.

To interface with the MPO connectors, twelve CXP cages are required, which can be equipped with MPO-transceivers. To keep the design suitable for standard 19" racks, we placed six CXP

4.1. CROSSPOINT SWITCH

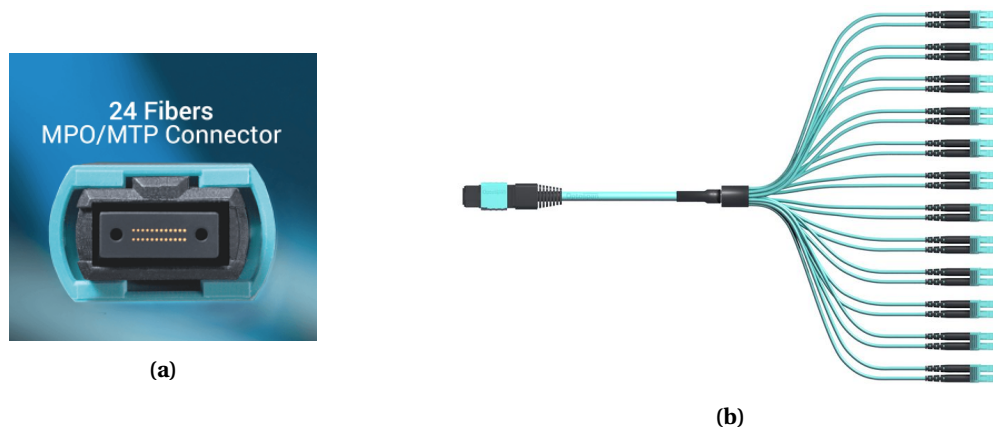


Fig. 4.3 Multi-fiber push on (MPO) standard. In (a): MPO connector providing 24 optical connections, which can be used for twelve bidirectional optical links. In (b): MPO harness cable to interface with the already existing hardware nodes, which use LC (lucent connector) standard. Figures taken from Ref. [103].

cages on the front- and the remaining six on the backside of the PCB. For control and programming of the crosspoint switch, we placed a small-sized FPGA of the Xilinx Artix-7 family on the PCB. It interfaces with the switch via a 90 MHz, 11-bit parallel data bus. Necessary high-speed links for slow-control or possible synchronization of the FPGA are provided by an SFP-cage. Apart from the already mentioned interfaces, we have an additional programming and debug interface to the FPGA using JTAG (joint test action group) standard. Fig. 4.4 shows the PCB layout.

Fig. 4.5 shows the aluminum housing of the PCB, which is designed as standard 19'' rack

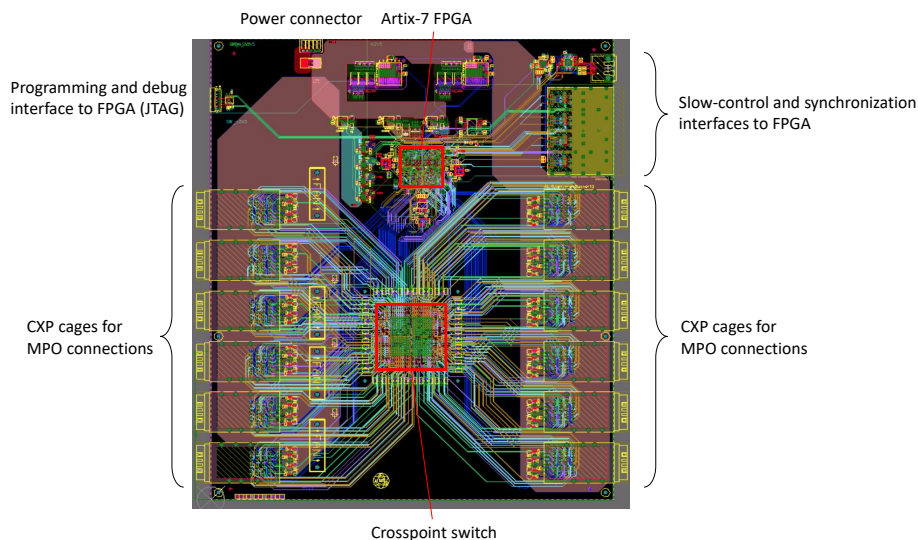


Fig. 4.4 Design view of layout of the custom-designed PCB for the crosspoint switch. The view shows different layers of the PCB in different colors. The CXP cages, six on the left and six on the right, are connected with high-speed differential lanes to the crosspoint switch located in the center. The upper third of the PCB housed power supplies, an Artix-7 FPGA, and the necessary interfaces for it.

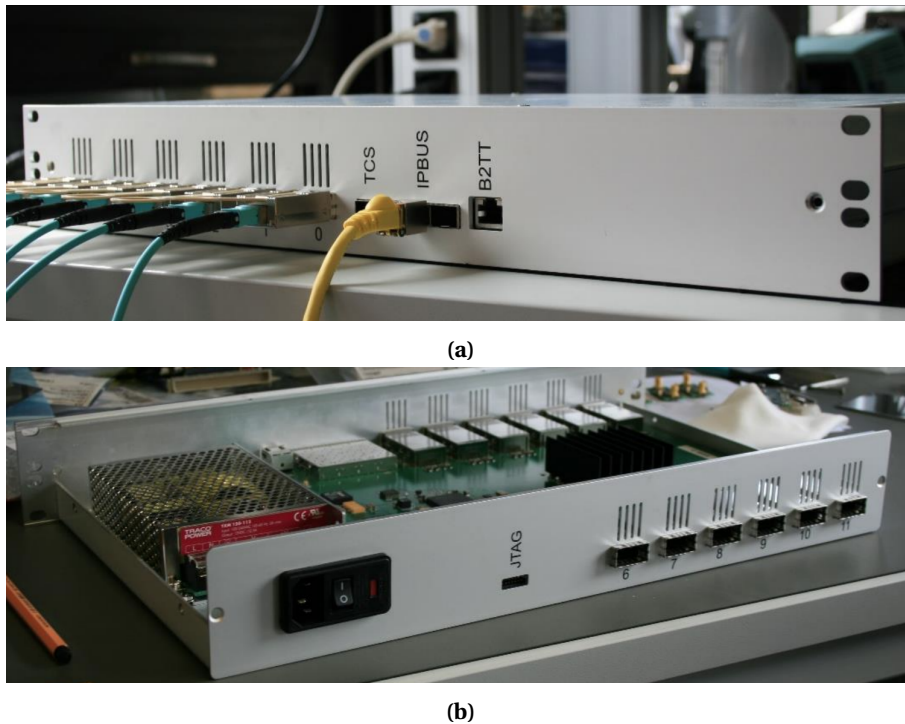


Fig. 4.5 Front view (a) and back view (b) of the chassis for the crosspoint switch. The front view is shown fully equipped and plugged for usage at COMPASS. The back view shows the open chassis, such that the power supply is visible on the left side.

chassis and provides all standard attachment holes. It also houses an AC/DC converter (on the left side in Fig. 4.5b) for maximizing user-friendliness. The correct voltages are created internally. The user only has to plug the power inlet on the backside to socket and push the power button.

Cooling is achieved by four fans pulling air from the back and pushing it to the front side. The fan holder closes the chassis to the top to prevent internal air circulation and enforcing constant airflow through slits directly above the CXP cages. The temperature of the crosspoint switch itself, which is attached to a cooling body, is constantly monitored by the FPGA.

The functionality of the crosspoint switch is illustrated in a block diagram in Fig. 4.6. The switch core can be programmed either on port-by-port basis or all port assignments can be queued and issued simultaneously with very low latency of few ns. Since the switching capability is implemented in the core of the VSC3144 chip, the FPGA only has to fulfill the programming and monitoring of the crosspoint switch via the proprietary interface of the VSC3144. The firmware is correspondingly simple. Besides the module for communication with the crosspoint switch, the firmware provides three different registers for transmitting data to the switch, which can be accessed via the IPBus protocol on the slow-control network. All registers are summarized and described in Appendix C. The three registers for transmitting information to the switch are treated with different priority. The “config” register, which can issue the simultaneous programming of queued port assignments, is treated with highest priority to ensure low latency and allow time-critical reconfiguration of the switch core. The

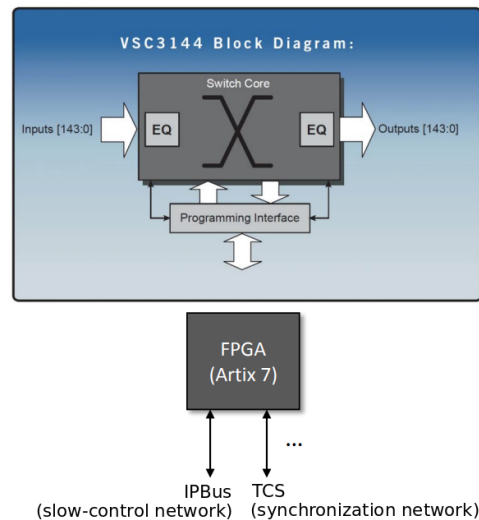


Fig. 4.6 Block diagram of the functionality of the crosspoint switch. The switching capability is provided by the core of the VSC3144 chip. Any of the 144 output can be connected to any of the 144 inputs. Even fan-out topologies can be realized. The switch core provides signal equalizing cores on each of the in- and outputs. It can be programmed by the Artix-7 FPGA via the proprietary serial or parallel programming interface.

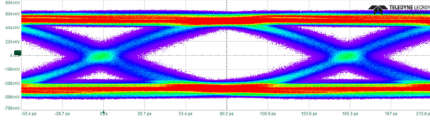
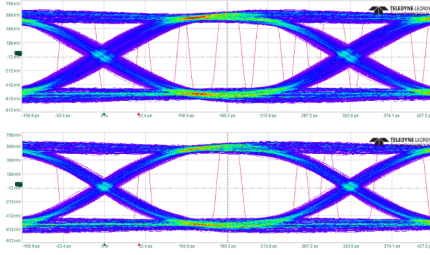
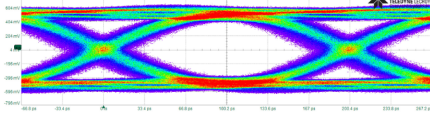
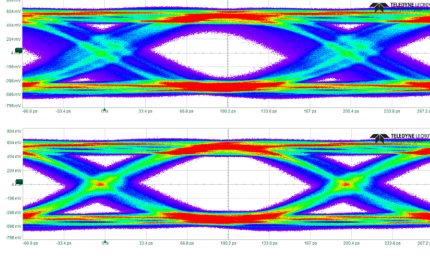
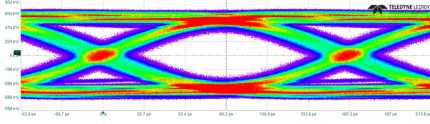
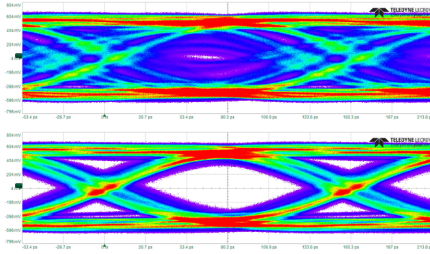
“ctrl” register has second highest priority since it also transmit operation-critical information to the switch. All other request, such as port assignments, are treated with the lowest priority and stored in a buffer, until they can be transmitted. Via the TCS interface, the FPGA could receive precise timing and reconfigure the switch core on-the-fly in between two spills. A functionality which is foreseen but not used.

The firmware also communicates with each CXP cage via a I2C interface. The deployed CXP cages provide information about the light yield, which they register on their receivers. A useful tool to identify malfunctioning transmitters. The FPGA acquires continuously this information from every CXP cage and makes it accessible on IPBus registers.

The implementation of the crosspoint switch introduces an additional component in the high-speed transmission of a sender node to a receiver node. Since the bit-error rate (BER) in high-speed transmissions is very sensitive to signal distortions, it is essential to eliminate signal degradation due to the switch. The signal quality can be assessed in eye-diagrams. This graph is generated by overlaying multiple instances of the transmitted signal on top of each other, aligning them with respect to their clock timing. The wider and the higher the opening of the eye, the better the signal quality.

Table 4.1 shows the eye diagram at the receiving side at different transmission speeds with and without the crosspoint switch in the line. Not using the signal equalizing functionality leads to a significant distortion of the signal. While the distortion is still acceptable at low speeds, it leads to almost fully closed eye at speed above 6 GB/s. Table 4.1 also shows the eye diagram using the best setting for the signal equalizing core of the switch: the signal quality can be almost restored to the same level as without switch. Only at highest transmission speeds, some remains are still visible.

Table 4.1 Eye diagrams for signal transmission at different line speeds from ~ 3 GB/s to ~ 6 GB/s. The table compares eye diagrams of transmission without crosspoint switch and with crosspoint switch. The switch provides signal equalization, which leads to significant improvements in signal quality.

data rate	signal before switch	signal after switch	no EQ signal EQ
3.13 Gb/s			
5.00 Gb/s			
6.25 Gb/s			

These observations are confirmed in long-term BER measurements. Without using the signal equalization core, the BER at 6.25 GB/s is $\sim 10^{-8}$. Using the signal equalization, it reduces to $\sim 3 \cdot 10^{-13}$ at the highest measured transmission speed. It should be noted that the VSC3144 chip is, according to the datasheet, suited for line speeds up to 6.5 Gb/s. For lower speeds, the BER was found to be below 10^{-15} when optimizing the signal equalization. Current applications of the crosspoint switch in COMPASS/AMBER and Belle II operate at line speeds between 1.5 Gb/s (Belle II) and 2 Gb/s (COMPASS), for which we can safely assume that the switch does not increase the BER.

4.1.2 Integration and application in the iFDAQ

The overall goal during the implementation of the switch into the COMPASS iFDAQ was to minimize apparent changes for shifters. In the ideal case, the implementation of the switch should stay unnoticed to protect users from unnecessary complexity, and maximize user-friendliness. Following the approach of the software design of the iFDAQ, as explained in

4.1. CROSSPOINT SWITCH

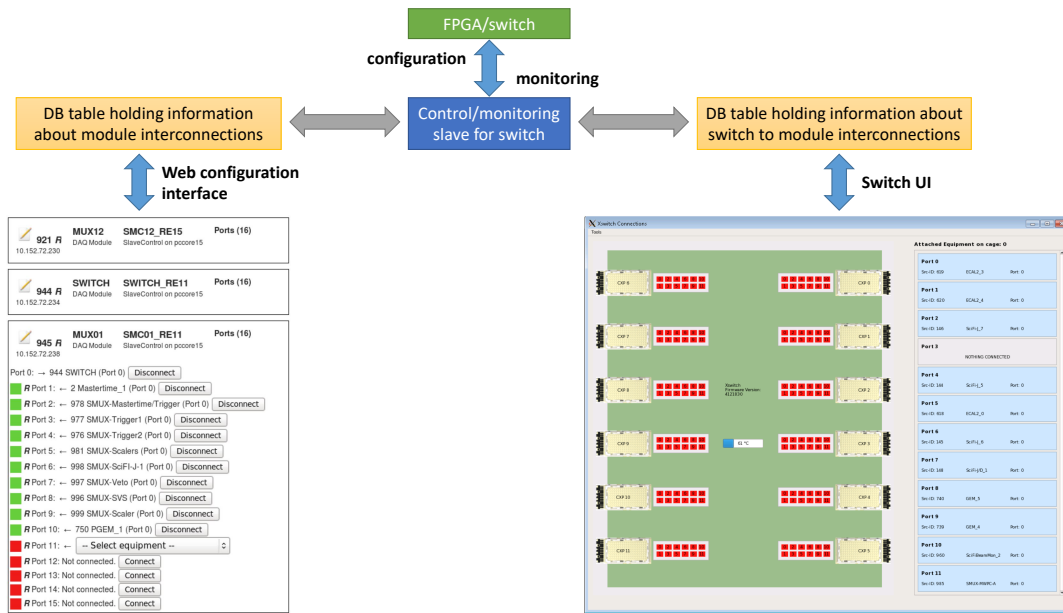


Fig. 4.7 Configuration tools and graphical user interfaces for editing the involved database tables. The control and monitoring process accesses both tables to correctly configure the crosspoint switch.

Section 3.5.2, we treated the switch like any other hardware node, which requires monitoring. A corresponding entry has to be prepared in the database and the IPBus registers have to be defined. This causes the master process to spawn a monitoring slave on the transition from “turned-off” state to “slaves started”. At the same time, it powers the switch and executes the necessary reset procedure.

During the transition from “slaves started” to “configured” state, the crosspoint switch needs to be configured. To do so, the software needs information from two different database tables. One holding the information about the connections between hardware nodes in the event builder. A freshly introduced table stores the information to which port the corresponding equipment is attached. To edit this table, we developed a graphical user interface (GUI), which interactively displays the attached equipment, see Fig. 4.7. The web configuration interface can be used to change the iFDAQ topology and corresponding reconfiguration of the crosspoint switch will automatically implement the changes. Topologies can be stored and easily recalled without physical human intervention. The working principle, how the support software has to configure the crosspoint switch is displayed in Fig. 4.8.

Another feature of the crosspoint switch is its fan-out capability. One input can be mapped to many outputs. This allows to split a data stream and send it to multiple receivers. A functionality, which is in particular useful for on-line debugging of detectors. The detector can remain included in the main data stream of the DAQ, while at the same time, the data of the specific subdetector can be forwarded to a debugging node. All this can be done during physics data taking without intervention.

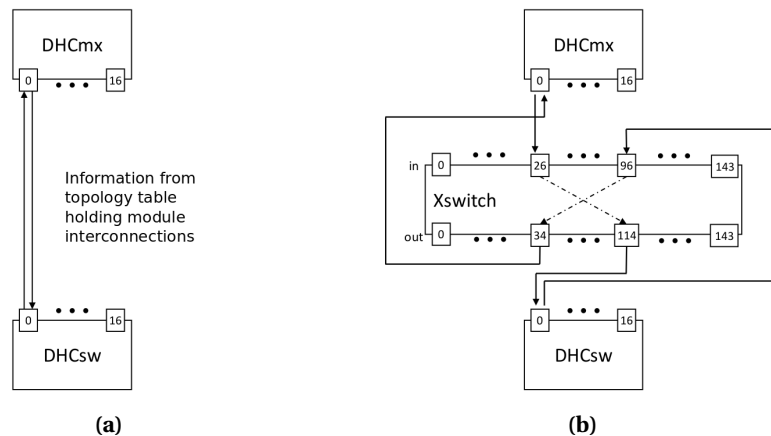


Fig. 4.8 The information about interconnections between modules in the hardware event builder as shown in (a) is held by the iFDAQ configuration table. This table can be edited via the web configuration interface. Using the information, to which port on the crosspoint switch the involved equipment is attached, corresponding port assignments can be transmitted to the switch as indicated in (b). The latter table can be edited via the newly developed GUI.

4.1.3 Application at Belle II

After completion of the development, an initially unforeseen application of the crosspoint switch at the Belle II experiment arose. Due to the collider setup, the routing of the cabling from the innermost silicon tracking detector is dictated by the very limited space in the center of the detector. However, for filtering and processing of the data, the cables need to be arranged according to their detector number. This could easily be achieved by the installation of two crosspoint switches, each handling 80×80 high-speed links.

The crosspoint switch proved to be a very useful tool also in the commissioning phase of the Belle II central vertex detector. Making use of the fan-out functionality, the data of one detector can be transmitted to all attached data processing cards. They should hence all receive exactly the same data, which drastically facilitates commissioning, debugging, and verification of the whole readout chain under real running conditions.

The light yield detection of the switch allows diagnosing bad optical links, which might lead to bit-errors during transmission and consequently a drop of performance. To ensure correct data transmission, a minimum threshold on the detected light intensity is imposed by means of the crosspoint switch.

4.2 Commissioning of a real-time beam monitoring system

The author of Ref. [100] developed a fully automated monitoring system for beam properties in real-time. The system was developed for employment on one of the scintillating fiber detectors upstream of the target. These detectors consist of planes of 96 fibers readout by photomultiplier tubes. The fiber detectors serve as tracking detectors for beam particles and

are very fast without significant dead times. They are well suited detectors for real-time beam monitoring.

The beam rate is of special interest for our application. For rate measurements, a scaler with dead-time free readout for each of the 96 channels is needed. This can be achieved with the concept of a counter and an adder. The counter was implemented as a Johnson ring counter which, due to its simple logic, requires very little computation time to determine the next state for a signal edge and provides a Hamming distance of 1 for asynchronous readout. The adder is clocked at 38.88 MHz and adds the difference between two readout states to a current count.

The physics data taking requires timing information from the fibers generated by a time-to-digital converter (TDC). The principle is to combine scaler, which is needed for the beam monitoring tool, and a TDC on the same readout board. The firmware, which was developed in Ref. [100], implemented scaler and TDC on a so-called GANDALF board [104]. GANDALF is a 6U-VME64x/VXS [105] carrier board centered around a Virtex-5 FPGA. Since the real-time beam monitoring should work independent of the iFDAQ, two different readout possibilities are required. The data for the beam monitoring is read out via the VME64x-bus to the VME CPU, whereas the data for the physics data taking is sent via high-speed interfaces to nodes of the hardware event builder. To be fully independent of the iFDAQ, artificial begin-of-spill and end-of-spill signals are generated internally based on the hit rate. Likewise, internally generated pseudo-random trigger provoke the acquisition of events for the beam monitoring. Data acquisition for the beam monitoring is hence completely decoupled from the main DAQ and does not use information about triggers or the spill structure.

For each spill, a process on the VME CPU acquires the pseudo-random data by accessing memory on the GANDALF board via the backplane of the VME crate. Data of one spill is saved in one file on the network file storage of COMPASS. An instance of the GUI, checks for new files at the defined location, decodes the information, performs the needed analysis, like a Fourier transformation of the rate, and displays the results to the user. Fig. 4.9 shows the graphical display of the information. The graphs are updated after each spill. The information is also published on the COMPASS website and used by SPS operators to tune debunching and extraction of the beam. Using the beam monitoring tool, a 50 Hz oscillation in the beam intensity could be detected.

A common problem are spikes at the start of a spill. These spikes may lead to desynchronization of certain frontend electronics which are operated at the maximum of their rate capability. Since synchronization is reestablished only on the next start-of-spill trigger, the data of corresponding detectors are lost for almost an entire spill. The real-time beam monitoring tool enables shifters to find the origin of the problem, take action, and therefore improve the quality of data taking.

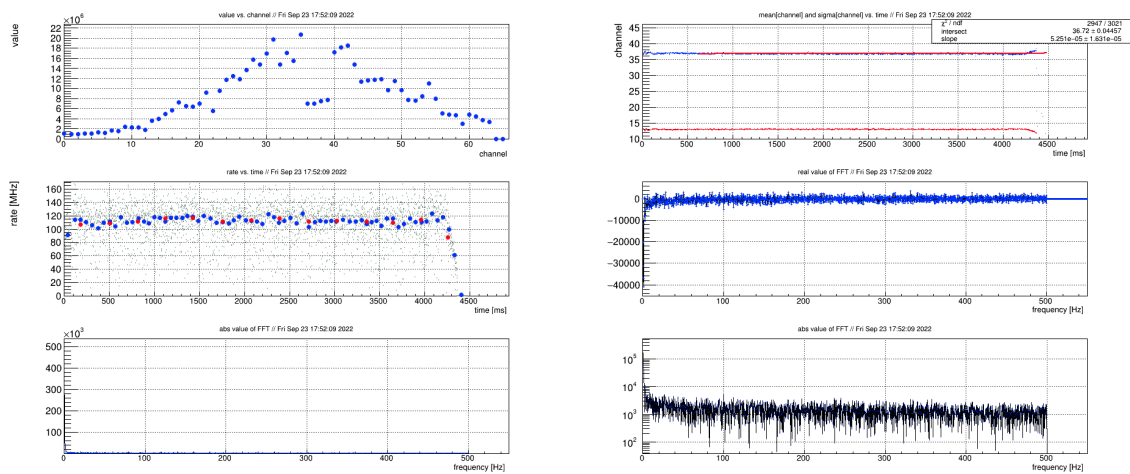


Fig. 4.9 Distributions provided by the GUI of the beam monitoring. The upper left distribution shows the number of hits for each channel integrated over the whole spill. It is dominantly determined by the beam profile in the plane. On the upper right plot, we calculate the mean channel, which the beam hit in time slices over a spill. In case the beam position is not constant over a spill, the mean hit channel varies over the spill. The distribution is linearly fitted and the slope parameter is sent to a database, such that automatic alarms can make shifters aware of a beam drift. The central left plot shows the beam rate over the time of a spill. For a good spill extraction from the SPS accelerator, the beam intensity is constant over the entire spill. Often, spikes at start and end of a spill occur, which lead to problems in the frontend electronics. With the help of the beam monitor, shifters can identify the cause of the problems and inform SPS operators. The remaining three distributions show the fourier transform of the rate. Sometimes, remains of the 50 Hz AC frequency of the common line voltage can be seen in the intensity of the SPS beam.

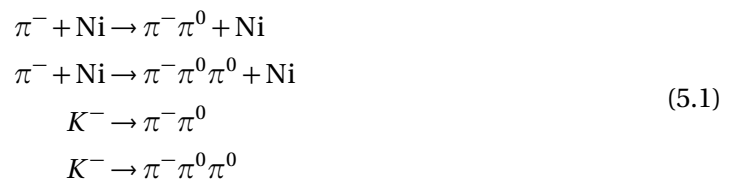
Chapter 5

Event reconstruction and selection

For each trigger decision, the detector response is read out and saved on disk. The data belonging to one trigger decision is called an event. An event includes hits in tracking detectors and energy depositions in calorimeter cells. The energy deposition is determined by measuring the created light in the scintillator with photomultiplier tubes attached to the back of each cell.

The event reconstruction is performed off-line using the saved raw data from the detectors. The COMPASS collaboration has developed a dedicated software package for the event reconstruction called CORAL (COmpass Reconstruction and AnaLysis software package) [106]. It offers track finding, vertex reconstruction, and clustering algorithms specifically adapted to the geometry and detectors of the COMPASS spectrometer layout. Since the various physics programs demand different spectrometer layouts and impose specific requirements on the reconstruction, CORAL offers numerous setting options. The following event selection and the analysis is based on a particular reconstruction of the raw data, called the $t70$ production. For the $t70$ production, special emphasis was put on a correct energy calibration of showers in ECAL2 and on the vertex reconstruction. Calibrations, which are applied either in the reconstruction process by CORAL (pre-production) or during the analysis (post-production) are explained in Section 5.2.1. To be sensitive to Primakoff reactions, which characteristically feature small momentum transfers and hence favor small scattering angles, the vertex reconstruction algorithm was optimized for high efficiency at small scattering angles partly with limited spatial vertex resolution.

COMPASS collected data of various reactions during the Primakoff data taking campaign in 2009. The main goal of the event selection and reconstruction discussed in this chapter is to extract a clean sample of the desired reactions:



A common property of all the reactions in Eq. (5.1) is their vertex: it has to be reconstructed by the beam particle (either pion or kaon) which is tracked in the beam telescope and a single ionizing, negatively charged pion in the final state. The additional π^0 s decay almost instantly into two photons, which will not be seen by the tracking detectors and can not contribute to the vertex reconstruction. It makes hence sense, to split the event selection into two parts. First, the preselection, selecting all events with primary vertices with one negatively charged outgoing pion trajectory. We will suppress background from multiple scattering events and require certain quality conditions on the vertex, the charged scattered track, and the beam track. The preselection will be described in Section 5.1. In a second step, we reconstruct the neutral pions via their decay photons and apply a specific event selection for each of the reactions of Eq. (5.1) based on kinematic quantities. The specific event selections for the different processes are described in Section 5.3. Additional details about the event selections can be found in Refs. [107, 108].

5.1 Event preselection

The goal of the preselection is to match the common conditions of the reactions in Eq. (5.1) in order to reduce the amount of data in a way that they can be analyzed efficiently for each of the processes. Following selection criteria, called cuts, are applied in the preselection:

- Existence of at least one primary vertex **and** (“Prim2” trigger bit **or** $p_{\text{scat}} < 140 \text{ GeV}/c$)

The $t70$ data set contains events for which CORAL did not reconstruct a primary vertex at all or not within the target region of COMPASS. Since events of such kind do not contain any usable information, the very first cut requires at least one reconstructed primary vertex (PV) in the target region $-350 \text{ cm} < z_{\text{PV}} < 50 \text{ cm}$. Due to the special vertex reconstruction setting allowing for small scattering angles, multiple-elastically scattered tracks cause the reconstruction of a primary vertex. We therefore require additional evidence for an (interesting) interaction: either the Primakoff2 trigger bit is set or one of the primary vertices has at least one outgoing track with less than $140 \text{ GeV}/c$ momentum.

- No pile-up events (exactly one incoming beam track)

In addition to the true interacting particle, which triggered the data acquisition for the event, accidentally coincident beam particles may enter the spectrometer. They may give rise to other primary vertices, either in the target region or further downstream in the detector. Since there is an increased probability for misreconstruction in these events, we disregard all events with more than one track in the beam telescope. Such beam tracks are identified by their first measured hit $z_{\text{first}} < -75 \text{ cm}$. Pile-up effects are the same for kaons and pions. They are taken into account in exactly the same way in the generation of pseudodata of kaon decays and pion interactions. This is important later on, since cancellation of the effects will depend on equal treatment of pions and kaons.

- The primary vertex has been reconstructed using the beam particle trajectory and exactly one outgoing/scattered trajectory
- Negative charge of scattered particle and meaningful reconstruction of its momentum

The charge and momentum of an ionizing particle traversing the spectrometer is determined by the deflection of its trajectory in the dipole magnets. Negatively charged particles are bent in positive x -direction. For each particle, the straight track segments up- and downstream of the dipole magnets can be extrapolated to intersect within the magnet. Combinatorial background may lead to a wrong determination of the charge and of the momentum of a particle. We accept only events for which the trajectory of the scattered particle was successfully “bridged” over at least the first dipole magnet, the trajectory was bent in positive x , and the momentum measurement returned meaningful values of $1 \text{ GeV}/c < p_{\text{scat}} < 200 \text{ GeV}/c$.

- Meaningful reconstruction of the beam energy

For specific parameters of the beam trajectory (position and inclination), in particular when they are far from the nominal beam parameters, the beam energy determination via the polynomial describing the beam optics (cf. Eq. (3.4)) gives unphysical results. We require, that the determined beam energy E_{beam} is close to the nominal beam energy of $E_{\text{nom}} \approx 190 \text{ GeV}$: $170 \text{ GeV} < E_{\text{beam}} < 210 \text{ GeV}$

- Event not in list of identified bad spills

In Ref. [91], a list of bad spills was compiled based on logbook entries, error messages of the readout electronics, and beam properties. We neglect events that were recorded in one of the identified bad spills.

- Primakoff2 trigger bit is set for the event.
- Number of crossed radiation lengths by the scattered charged particle $X/X_0 < 15$

The main decay mode of charged pions is the leptonic decay to muon and neutrino. To exclude contamination with events, for which either the beam particle or the scattered particle has decayed to a muon, we have to reject muons in the final state. Since muons do not interact strongly, unlike pions, they can traverse large amounts of material. We require that the scattered particle passed less than 15 radiation lengths along its trajectory. The COMPASS spectrometer is equipped with two muon identification systems [82], one in the LAS called Muon Filter 1 (MF1) and one in the SAS called Muon Filter 2 (MF2). They consist of drift tube detectors combined with absorber walls made of iron (MF1) or concrete (MF2). When a particle creates a hit in the drift tube trackers behind the walls, it has passed more than 15 radiation lengths in the absorber material and is identified as muon.

- No hits in outer muon hodoscope (HO04) which can be associated with the scattered track

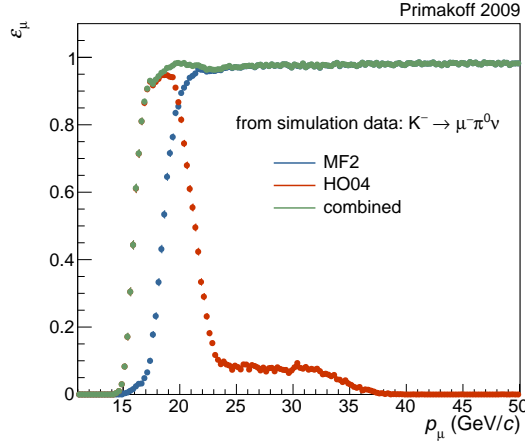


Fig. 5.1 Efficiency of the muon identification system illustrated with simulated data of the $K^- \rightarrow \mu^- \pi^0 \nu$ decay.

MF1 covers the low-momentum range up to $\approx 6 \text{ GeV}/c$. The trajectories of particles with higher momenta are bent less by SM1. They will traverse the hole in the center of MF1 and enter the SAS. The efficiency of the muon rejection of MF2 in the SAS, ε_μ , can be visualized with simulated data. Fig. 5.1 shows the efficiency obtained from simulated $K^- \rightarrow \mu^- \pi^0 \nu$ decays. Particles with momenta less than $20 \text{ GeV}/c$ will be bent by SM2, such that they are outside the geometrical acceptance of MF2. Hence, the momentum acceptance of MF2 drops for momenta below $20 \text{ GeV}/c$. Hits in the hodoscopes of the muon section behind MF2 were not considered for tracking in the $t70$ -production. Since hodoscope outer 4 (HO04) is placed far from the beam axis in bending direction of SM2, one can extend the covered momentum range by checking for corresponding hits in HO04: we extrapolate the trajectory of the scattered particle to $z_{\text{HO04}} = 39.6 \text{ m}$ and check for hits in the corresponding slabs of HO04 that are within a $-8 \text{ ns} < t_{\text{track}} < 15 \text{ ns}$ time window. The effect of considering hits in HO04 can be seen in Fig. 5.1: the minimum momentum for which muons can efficiently be rejected is lowered to $\approx 17 \text{ GeV}/c$. However, a small gap in the covered momentum range between MF1 and MF2 persists.

- $E_{\text{trig}} > 68 \text{ GeV}$

To avoid a difficult and error-prone description of trigger inefficiencies in simulation, we accept only events which have an energy deposit in the trigger region E_{trig} that is significantly higher than the trigger threshold of $E_{\text{thr}} \approx 60 \text{ GeV}$ (see Fig. 3.7). E_{trig} is calculated via Eq. (3.7).

- Transverse momentum of the charged pion $p_T > 45 \text{ MeV}/c$

A charged particle traversing material is deflected by many small-angle scatters of which most are due to Coulomb scattering. “For many small-angle scatters the net scattering [...] distributions are Gaussian via the central limit theorem” [109]. For a single-charged particle, the rms of the Gaussian distribution can be calculated via

$$\theta^{\text{rms}} = \frac{13.6 \text{ MeV}}{\beta c p} \sqrt{X/X_0} \left[1 + 0.038 \ln \left(\frac{X}{X_0 \beta^2} \right) \right] \quad (5.2)$$

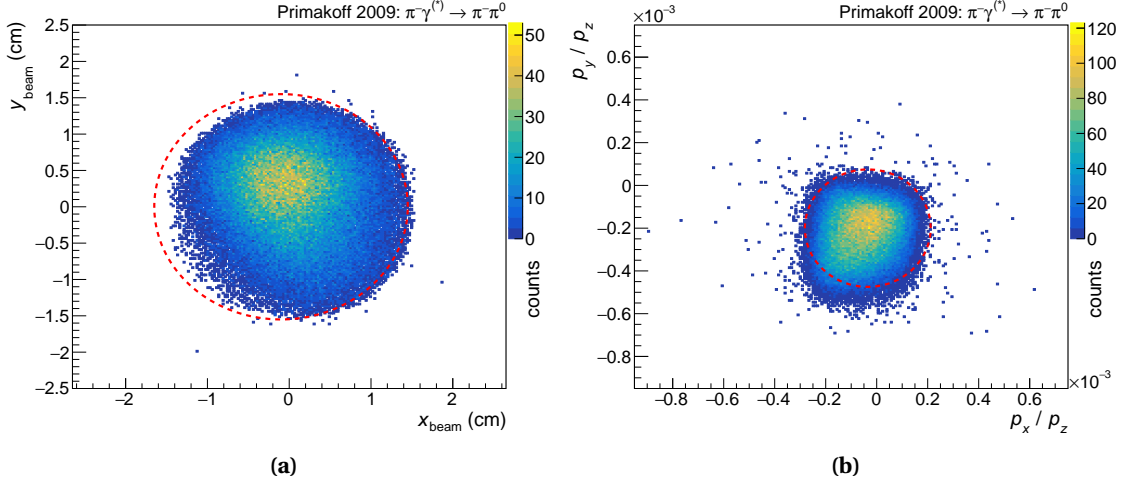


Fig. 5.2 Position (a) and inclination (b) of the beam for selected $\pi^- \gamma^{(*)} \rightarrow \pi^- \pi^0$ events. All other selection criteria of the $\pi^- \gamma^{(*)} \rightarrow \pi^- \pi^0$ event selection (see Section 5.3) except from the shown quantities are applied. The cuts on beam position and inclination are indicated as dashed ellipses.

with p the momentum and βc the velocity of the incident particle, and X/X_0 the thickness of the scattering medium in radiation lengths. The scattering angle depends on the momentum of the particle. Since the particles have a momentum distribution, it is beneficial to cut on the perpendicular momentum p_T w.r.t. the beam in order to effectively reduce multiple-scattering events in the data set. For the 4 mm Ni target ($\sim 0.3 \cdot X_0$) at ultra-relativistic speeds ($\beta = 1$) the rms of the p_T -distribution amounts to:

$$p_T^{\text{rms}} = p \cdot \theta^{\text{rms}} \approx 7.1 \text{ MeV}/c \quad (5.3)$$

The requirement of $p_T > 45 \text{ MeV}/c$ corresponds to more than $6 \cdot p_T^{\text{rms}}$ of multiple scattering.

- Position and inclination of beam trajectory

The beam energy reconstruction via the polynomial of Eq. (3.4) depends on the position and the inclination of the beam trajectory in the x/y -plane at $z_0 = -72.5 \text{ cm}$. Since the area of verification of the polynomial is not given in Refs. [86, 63], there is a risk to accept events that are outside its verified region and hence extrapolate the polynomial. For a consistent determination of the luminosity and for the generation of a corresponding set of pseudodata via Monte-Carlo simulation, it is important to have a well-defined space of beam parameters. We apply an elliptic cut on the parameters of beam position and inclination

$$\left(\frac{x - \mu_x}{a_x} \right)^2 + \left(\frac{y - \mu_y}{a_y} \right)^2 < 1 \quad (5.4)$$

with the parameters given in Table 5.1. The cuts are indicated in Fig. 5.2 by dashed lines for the example of selected $\pi^- \gamma^{(*)} \rightarrow \pi^- \pi^0$ events.

Fig. 5.3 shows the number of selected events after each cut of the preselection. From the 2.4 billion events in the Primakoff data set, we preselected 28 million generic events with one charged final-state particle.

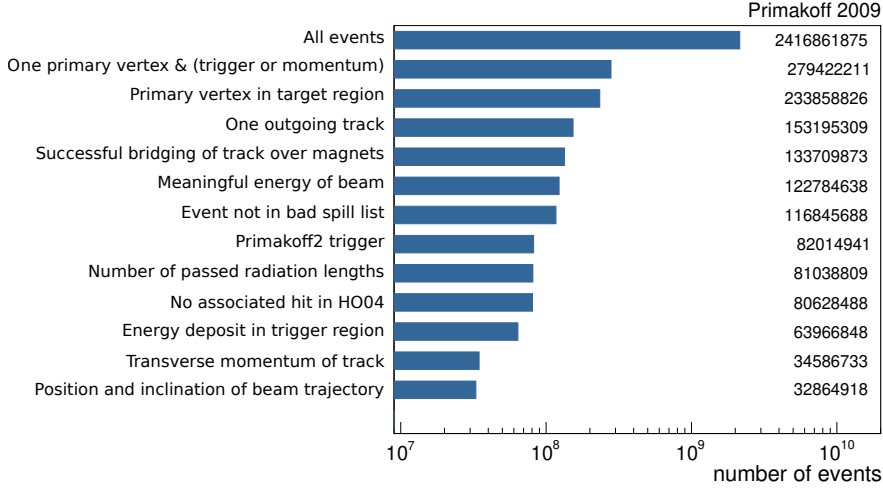


Fig. 5.3 Number of selected events after applying each cut of the preselection. The details of each cut are explained in the text.

Table 5.1 Parameters of the cut on beam position and inclination.

	μ_x	μ_y	a_x	a_y
position	-0.1 cm	0.0 cm	1.55 cm	1.55 cm
inclination	$-3.5 \cdot 10^{-5}$	$-2.0 \cdot 10^{-4}$	$2.4667 \cdot 10^{-4}$	$2.747 \cdot 10^{-4}$

5.2 Reconstruction of neutral pions

The neutral pion decays predominantly into two photons:

$$\pi^0 \rightarrow \begin{cases} \gamma\gamma & (98.823 \pm 0.034)\% \\ e^+e^-\gamma & (1.174 \pm 0.035)\% \\ \text{others} & < 10^{-5} \end{cases} \quad (5.5)$$

A π^0 is therefore reconstructed by the two photons originating at its decay vertex. $c\tau_{\pi^0} = 25.5$ nm is sufficiently small to assume for the kinematical reconstruction of the π^0 that the decay photons originate at the primary vertex. For two photons with four-momenta p_1^μ , p_2^μ and $p_i^0 = E_i = |\vec{p}_i|$, we have

$$\begin{aligned} m_{\gamma\gamma}^2 &= |p_1^\mu + p_2^\mu|^2 \\ &= (E_1 + E_2)^2 - (\vec{p}_1 + \vec{p}_2)^2 = 2E_1E_2 - 2\vec{p}_1 \cdot \vec{p}_2 \\ &= 2E_1E_2 - 2|\vec{p}_1||\vec{p}_2|\cos\vartheta \\ &= 4E_1E_2 \sin^2 \frac{\vartheta}{2} \stackrel{!}{=} m_{\pi^0}^2 \end{aligned} \quad (5.6)$$

with ϑ being the angle between the two photons. Hard photons can be measured in the COMPASS spectrometer by detecting their energy deposit in the electromagnetic calorimeters. As discussed in Section 3.3.2, we consider only photons reconstructed in ECAL2. ECAL2

is located $\Delta z = z_{\text{ECAL2}} - z_{\text{target}} \approx 34 \text{ m}$ downstream of the target, which results in small values for the angle $\vartheta \approx d_{\gamma\gamma}/\Delta z$ with $d_{\gamma\gamma}$ being the distance between the two photons when they hit ECAL2. From Eq. (5.6), we see that we have a minimum distance for the two photons of:

$$d_{\gamma\gamma}^{\text{min}} = \frac{m_{\pi^0} \cdot \Delta z}{\sqrt{E_1 E_2}} = \frac{2m_{\pi^0} \cdot \Delta z}{E_{\pi^0}} \approx 5 \text{ cm} \quad (5.7)$$

where we have used that the product of the two photon energies $E_1 E_2$ is maximum when the energy of the neutral pion, $E_{\pi^0} = E_1 + E_2$, is split equally among the photons, i.e. $E_1 = E_2 = \frac{E_{\pi^0}}{2}$. The numerical value of Eq. (5.7) is obtained for $E_{\pi^0} = 190 \text{ GeV}$, meaning that the entire available energy is carried by a single π^0 . Fig. 5.4a shows the distributions of distances between two photons when they hit ECAL2 for simulated $\pi^- + \text{Ni} \rightarrow \pi^- \pi^0 \pi^0 + \text{Ni}$ events. $\pi^- + \text{Ni} \rightarrow \pi^- \pi^0 \pi^0 + \text{Ni}$ events are the dominant events in the $t70$ data set, since they can be produced diffractively. Clearly, distances below 5 cm are rare and can only occur, when combinatorically two photons, which do not stem from the same π^0 , end up close to each other in ECAL2.

As explained in Section 2.3, the momentum transfer to the nucleus is in the order of MeV for Primakoff events. At the same time, the energy of the hadron beam is approximately 190 GeV. To be able to resolve the tiny momentum transfer, a precise measurement of the final state is necessary. For final states with neutrals, the resolution is limited by the calorimetric measurement of the photons. We will discuss in the following, how photons are reconstructed and what calibration steps are taken to reconstruct photons in ECAL2 as precisely as possible.

5.2.1 Reconstruction of photons and calibration of the calorimeter

When a photon hits a module of ECAL2, it initiates an electromagnetic shower. Depending on the energy and the position of the incident particle, the transverse dimension of the shower exceeds the dimension of a single module and spreads to neighboring modules. Typical shower sizes range from a single module for the lowest energetic photons to 6×6 modules for highest energetic photons. To reconstruct the energy of a single particle, a clustering is performed by the reconstruction software. Blocks with a signal correlated in time are assigned to the same cluster, when they are direct neighbors. The center of gravity provides an efficient estimate on position and energy of the cluster:

$$\begin{aligned} \vec{x}_\gamma &= \sum_{i=1}^{N_{\text{cells}}} E_i \cdot \vec{x}_i \bigg/ \sum_{i=1}^{N_{\text{cells}}} E_i \\ E_\gamma &= \sum_{i=1}^{N_{\text{cells}}} E_i \end{aligned} \quad (5.8)$$

with N_{cells} being the number of modules in the cluster, the \vec{x}_i and E_i the individual positions and energy measurements of the modules.

The simple clustering procedure fails, when two photons hit the calorimeter close to each other and the showers overlap. This is in particular the case, when the photons are decay

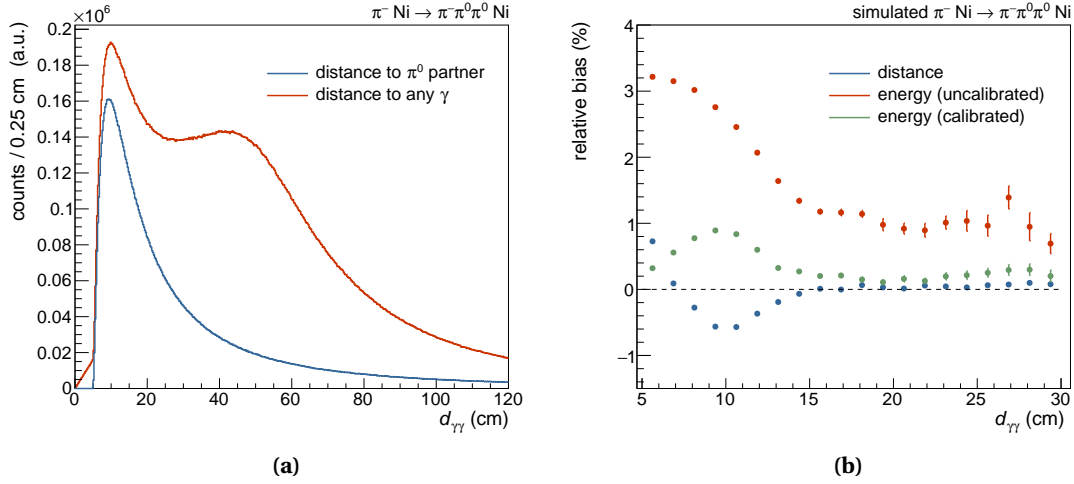


Fig. 5.4 Distances of photons hitting ECAL2 and their reconstruction biases. In (a): distributions of distances of photons to its π^0 partner ($\pi^0 \rightarrow \gamma\gamma$) in blue and to any other photon of the $\pi^- + \text{Ni} \rightarrow \pi^- \pi^0 \pi^0 + \text{Ni}$ reaction in red. Two photons of a π^0 -decay have a minimum distance to each other of ~ 5 cm. In (b): Relative bias of the reconstructed distance of two photons $(d'_{\gamma\gamma} - d_{\gamma\gamma})/d_{\gamma\gamma}$ in blue and of the reconstructed energy $1/2 \cdot \sum_{i=1}^2 (E'_i - E_i)/E_i$ before (red) and after (green) applying the energy calibration to the π^0 mass. For overlapping showers ($d_{\gamma\gamma} < 16$ cm), there are systematic effects visible which partially compensate each other. The shown dependencies are obtained from simulated $\pi^- + \text{Ni} \rightarrow \pi^- \pi^0 \pi^0 + \text{Ni}$ events.

products of high-energy π^0 s: as can be seen in Fig. 5.4a, typical distances for photons stemming from a π^0 are below 15 cm or less than four ECAL modules and hence the induced showers have a significant probability to overlap.

The algorithm developed in Refs. [87, 110, 111] allows separating overlapping showers by fitting transverse shower profiles to the observed energy distribution in a cluster. During the procedure, the energy distribution in the modules is fitted with an increasing amount of showers with the restriction that the effective mass of two closest showers must be at least $40 \text{ MeV}/c^2$ to avoid artificial splitting. When a fit with $n + 1$ showers returns a worse reduced χ^2 than the fit with n showers, the procedure is stopped. The fit increases the ability to separate showers with lower distance, that would otherwise appear to be a single cluster and by that increases the acceptance for processes with π^0 s in the final state. If a fit does not converge or does not fulfill certain quality criteria, the reconstruction software falls back to the center of gravity method of Eq. (5.8).

The procedure has limitations: if a hit pattern in a cluster of modules stems from e.g. three (or even four) particles, it is not given that the fit with two (or three) showers gives a better reduced χ^2 than the fit with one (or two) showers. If the fit returns a worse χ^2 , the procedure is stopped not finding the correct amount of photons, maybe not even fulfilling the quality criteria. Another limitation is that for overlapping showers, the reconstructed positions are systematically too close to each other. Fig. 5.4b shows the relative bias of the reconstructed distance of the two photons $(d'_{\gamma\gamma} - d_{\gamma\gamma})/d_{\gamma\gamma}$ in blue. For distances between 6 and 15 cm, the range in which many of the photons hit ECAL2, the reconstructed distance $d'_{\gamma\gamma}$ is too small. At the same time, too much of the deposited energy in the cluster is attributed to the lower-energetic photon, which leads to the observed increase in the relative bias of the

reconstructed energies $1/2 \cdot \sum_{i=1}^2 (E'_i - E_i)/E_i$ shown in red in Fig. 5.4b.

Investigations on possible improvements of photon reconstruction in ECAL2 by applying machine learning techniques were started [112] during this thesis and may lead to better results in future data productions.

During the reconstruction process, we apply several steps of calibrations and corrections to increase the energy and spatial resolution of ECAL2. We shortly summarize the applied procedures:

1. At least once for each measurement campaign, we calibrate each module individually by exposing it to a 40 GeV electron beam. After a few iterations, an individual calibration constant for each module is found.
2. We continuously monitor the time stability of each module by means of an LED-based monitoring system. The system makes use of the time between two spills of the accelerator to inject light into the modules and checks for variations in the response of the photomultipliers. The LED calibration provides an additional calibration constant per module and per spill.
3. Another calibration taken into account by CORAL is based on the measurement of the π^0 mass. $m_{\gamma\gamma}$ is calculated from the whole data set in an iterative procedure for each cell individually [113]: an energy-dependent calibration constant for each cell is determined, which shifts the peak of the $m_{\gamma\gamma}$ distribution to the nominal π^0 mass of $m_{\pi^0} = 135 \text{ MeV}/c^2$. The effect of this calibration can be seen in Fig. 5.4b in the green curve. In the center of ECAL, where most of the overlapping showers appear, the calibration according to the π^0 mass compensates for the too close spatial reconstruction of the photons by balancing it with a too high relative energy reconstruction, such that the peak of the $m_{\gamma\gamma}$ distribution is still at the nominal π^0 mass. It is hence important to apply the same procedure also on pseudodata to replicate the same effects.
4. The last corrections that are applied in the $t70$ production concern the shower positions. The positions of the reconstructed showers exhibit a dependence on the cell structure of ECAL2 as an artifact of the discrete cell structure. In an attempt to correct the effect, the positions were shifted with a cubic polynomial [87]:

$$\begin{aligned} x' &= x + a(E) \cdot x^3 + b(E) \cdot x^2 + c(E) \cdot x \\ y' &= y + a(E) \cdot y^3 + b(E) \cdot y^2 + c(E) \cdot y \end{aligned} \tag{5.9}$$

with $a(E)$, $b(E)$, and $c(E)$ being energy-dependent parameters given in Table 5.2, and x and y being the distance of the shower position to the center of the main cell or the distance of the center of gravity to the center of the most energetic cell, depending on whether the shower fit was successful or failed. The latter distance has an increased probability to be greater than half a cell size, which leads to potentially big corrections. The applied corrections have a great impact on the position resolution and introduce an energy-dependent bias due to the quadratic term. However, they increase the sharpness of the Primakoff peak in the Q^2 distribution. In this thesis, we use the applied

5.2. RECONSTRUCTION OF NEUTRAL PIONS

Table 5.2 Parameters of cubic cell response function as used for the $t70$ -production. The values are corrected w.r.t Ref. [63]. The parameters that were used for the generation of pseudodata via Monte-Carlo simulation (MC) throughout the thesis are given here as well.

coord.	data set	a (mm ⁻²)	b (mm ⁻¹)	c	shower energy (GeV)
x	$t70$	$-7.335 \cdot 10^{-4}$	$-2.991 \cdot 10^{-3}$	$2.490 \cdot 10^{-1}$	$0 \leq E < 20$
	MC	$-4.954 \cdot 10^{-4}$	$8.792 \cdot 10^{-3}$	$1.626 \cdot 10^{-1}$	
	$t70$	0	0	0	$20 \leq E < 35$
	MC	0	0	0	
	$t70$	$7.313 \cdot 10^{-4}$	$2.484 \cdot 10^{-4}$	$-2.460 \cdot 10^{-1}$	$35 \leq E$
	MC	$8.088 \cdot 10^{-4}$	$-1.473 \cdot 10^{-3}$	$-2.833 \cdot 10^{-1}$	
y	$t70$	$8.568 \cdot 10^{-4}$	$4.176 \cdot 10^{-4}$	$-2.971 \cdot 10^{-1}$	$0 \leq E$
	MC	$8.752 \cdot 10^{-4}$	$9.822 \cdot 10^{-5}$	$-3.060 \cdot 10^{-1}$	

position corrections in the $t70$ production and in the pseudodata. For the future, we should revert the corrections of Eq. (5.9) and apply newly developed ones.

- The authors of Refs. [91, 114] developed an additional calibration, which is to be applied on the reconstructed showers of the $t70$ production. The calibration is based on the shower position within a Shashlik-module. It corrects for the internal structure of the Shashlik blocks which features wave-length shifting light-guides and iron rods to hold mechanically the stack of layers. When a photon hits directly the light-guides, the created amount of scintillation light is greater than when it hits the rod. The intra-cell position calibration is energy-dependent and was evaluated in the scope of the analysis of the pion polarizability in energy ranges down to $E_\gamma = 40$ GeV. Within a student project [115], we tried to extend this calibration to lower energies. The chosen approach was analog to the already mentioned π^0 calibration. Unfortunately, no consistent cal-

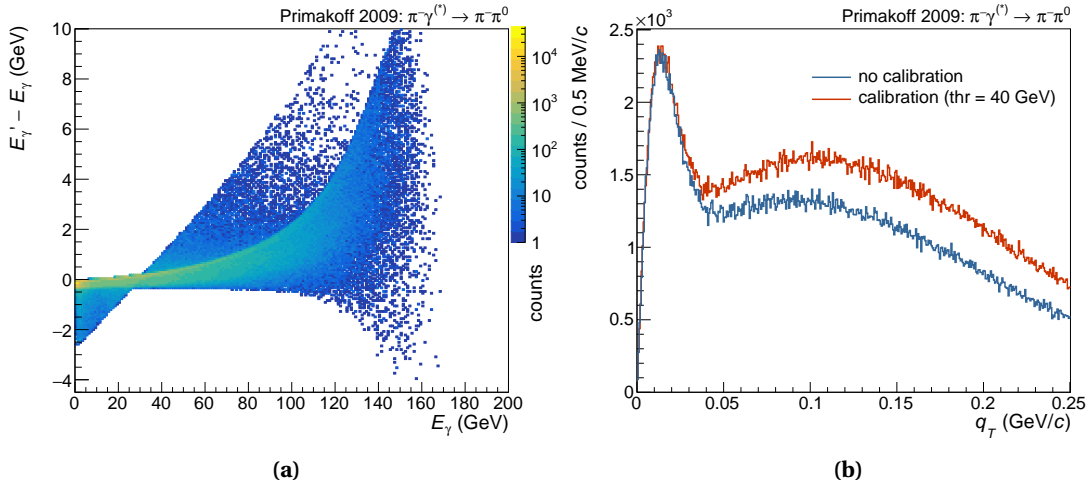


Fig. 5.5 Applying the intra-cell position dependent calibration for the Shashlik modules. In (a): the difference of the calibrated photon energy E'_γ to the uncalibrated energy E_γ as a function of E_γ . The behavior changes clearly below the verified region of $E_\gamma < 40$ GeV. For very small photon energies, the calibrated values can become negative. In (b): impact of the calibration on the q_γ -distribution of selected $\pi^-\gamma^{(*)} \rightarrow \pi^-\pi^0$ events for different thresholds.

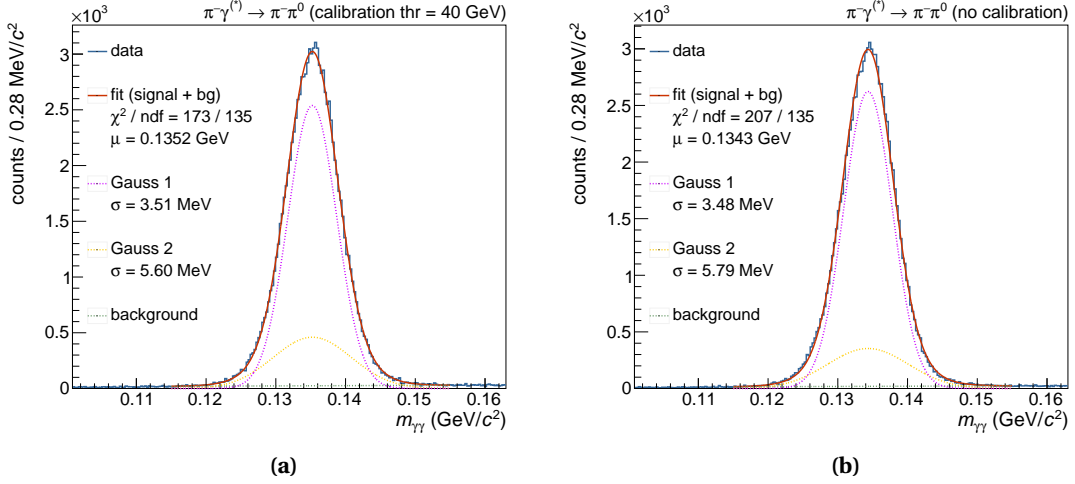


Fig. 5.6 Position and width of the reconstructed π^0 -mass peak with (a) and without (b) the intra-cell position dependent calibration for selected $\pi^-\gamma^{(*)} \rightarrow \pi^-\pi^0$ events. The distributions are fitted with a double gaussian and a 2nd order polynomial to extract the mean.

ibration below 40 GeV was found. Fig. 5.5a shows the difference of the reconstructed photon energy E'_γ after applying the intra-cell position dependent calibration. Below 30 GeV, the behavior of the calibration changes significantly and for very low-energetic photons, even negative values for the calibrated energy appear indicating that the correction is not applicable in this form. In Fig. 5.5b, we see the impact of the calibration on the q_T distribution of selected $\pi^-\gamma^{(*)} \rightarrow \pi^-\pi^0$ events. Applying the calibration hardly enhances the Primakoff peak, but has great impact on the main background contribution, whose proper shape is unknown. To evaluate the usefulness of the calibration, we fitted the $m_{\gamma\gamma}$ distribution around $m_{\pi^0} = 134.9$ MeV/c² from $m_{\min} = 115$ MeV/c² to $m_{\max} = 155$ MeV/c² with two Gaussian distributions and a second-order polynomial, see Fig. 5.6. The calibration shifts the peak slightly closer to the nominal π^0 mass. We chose to apply the calibration from 40 GeV upwards to be consistent with Ref. [108] and to avoid extrapolating the polynomial.

5.2.2 Selecting showers for π^0 reconstruction

Possible candidates of showers created by photons are selected by following criteria:

- They are within a time window of ± 8 ns with respect to the beam track, which sets the reference time for an event. The time distribution of clusters with respect to the beam particle can be seen in Fig. 5.7a.
- They lie above an energy threshold of $E_{\text{thr}} = 2$ GeV to exclude noise clusters and achieve agreement between simulated pseudodata and reconstructed showers in the $t70$ production. As can be seen in Fig. 5.7b, the distributions of showers in the $t70$ production at very low energies differs systematically from the distribution in the simulated pseudodata set of $\pi^- + \text{Ni} \rightarrow \pi^- \pi^0 \pi^0 + \text{Ni}$ events.

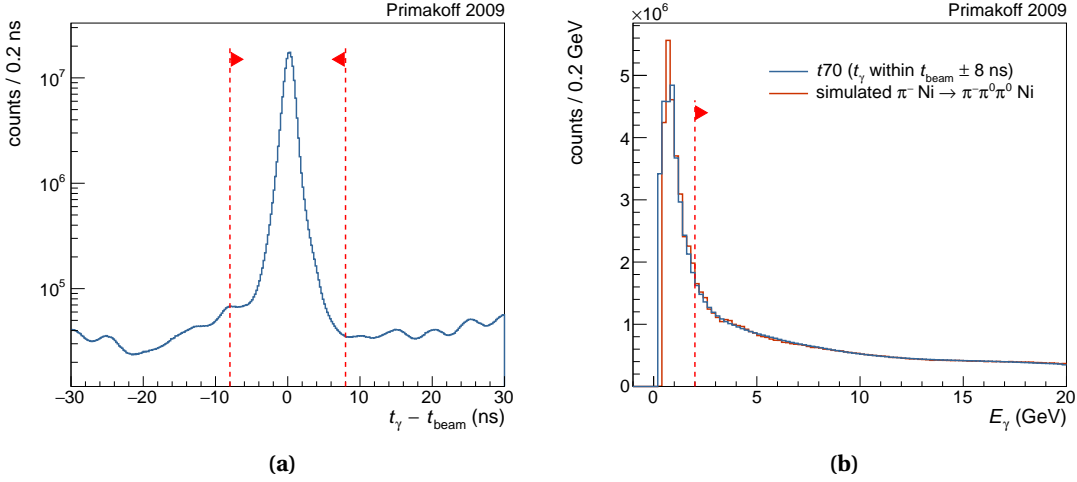


Fig. 5.7 Time and energy distribution of reconstructed photons. In (a): shower time with respect to the beam time. In (b): shower energy for simulated $\pi^- + \text{Ni} \rightarrow \pi^- \pi^0 \pi^0 + \text{Ni}$ events and for the $t70$ production. The pseudodata set is normalized to the integral of $E_\gamma > 8 \text{ GeV}$. All distributions were obtained after applying the preselection cuts. The required conditions are indicated with red lines.

- They do not lie in the vicinity of the reconstructed impact point of the scattered track on ECAL2. The charged tracks enter the calorimeter under bigger angles since they are deviated by SM2. The shower fitting algorithm based on Ref. [111] is not able to account for the ovality of showers with higher angles. The shower at the impact point of the charged track is therefore likely artificially split. In addition, the scattered particle is a charged pion for the final states of interest of this analysis. The shower profile in calorimeters produced by a hadron is different from a pure electromagnetic shower. As can be seen in Fig. 5.8a, a lot of rather low-energetic additional clusters seem to be created in the vicinity of the spot where the charged particle hits the electromagnetic calorimeter. The

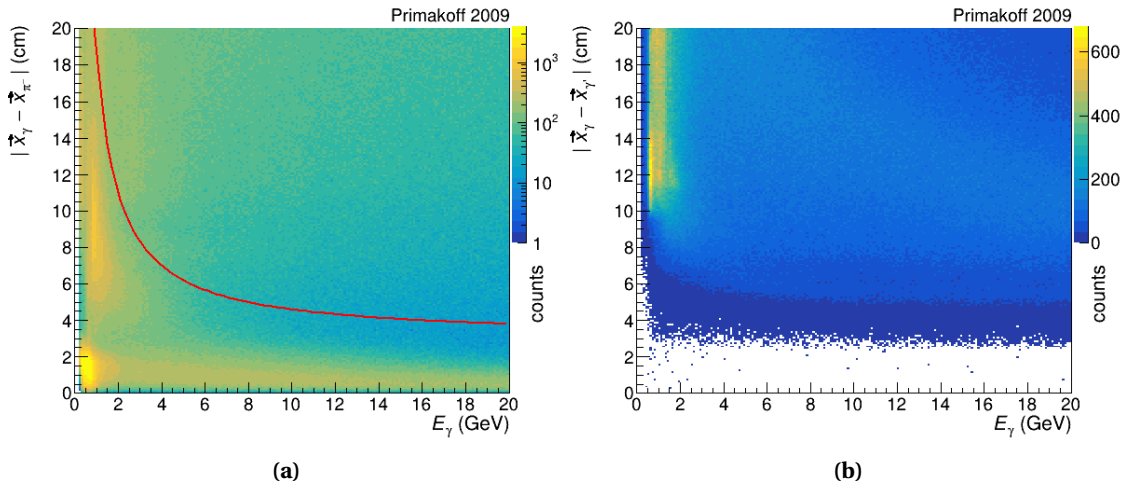


Fig. 5.8 Distance of reconstructed showers in the x/y-plane of ECAL2 \vec{x}_γ to (a) the scattered pion \vec{x}_{π^-} and (b) to other showers \vec{x}_γ vs shower energy E_γ . All preselection cuts are applied. The red line indicates the requirement of Eq. (5.10).

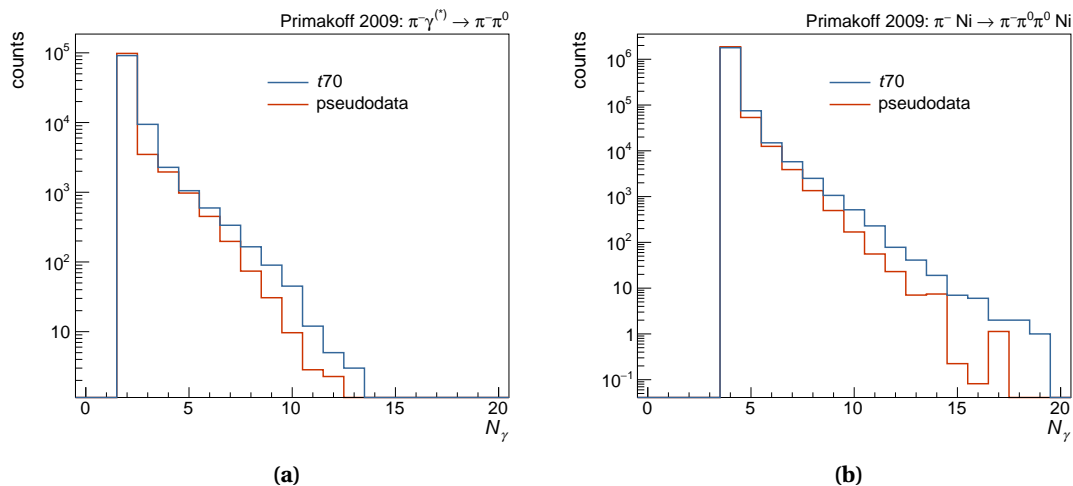


Fig. 5.9 Number of reconstructed photons for (a) $\pi^- \gamma^{(*)} \rightarrow \pi^- \pi^0$ and (b) $\pi^- + \text{Ni} \rightarrow \pi^- \pi^0 \pi^0 + \text{Ni}$ events. The plots show the distribution of the $t70$ data set in blue and the pseudodata set obtained by Monte-Carlo simulation in red. The pseudodata distributions are scaled to have the same integral as the $t70$ distributions.

structure at low energies and close distances can not be seen in Fig. 5.8b. According to Ref. [91], we associate all reconstructed showers within a radius of

$$r_{\max} = 3 \text{ cm} + \frac{16 \text{ cm} \cdot \text{GeV}}{E_{\text{clus}}} \quad (5.10)$$

to the impact of the charged track. The condition of Eq. (5.10) is indicated in Fig. 5.8a as red line.

After identifying the possible photon shower candidates, they are to be considered for the reconstruction of the π^0 . Here, a cut on the exact number of photons (two for $\pi^- \pi^0$ and four for $\pi^- \pi^0 \pi^0$ final states) is not a good choice since the number of showers is not correctly reproduced in simulation. Fig. 5.9 shows the differences for final states with one or two π^0 s. Radiative events are not included in the simulation. They certainly contribute to the surplus of reconstructed photons in the $t70$ data set. But also noise and potential background processes from pile-up events play a role.

We hence do not cut on the exact number of needed photons to ensure not to introduce a bias w.r.t. simulated data. Our chosen approach is to always combine the most energetic showers: the most energetic two in $\pi^- \pi^0$ final states and the most energetic four in the best possible way in $\pi^- \pi^0 \pi^0$ final states, meaning that the quadratic difference to the nominal π^0 mass

$$\left(m_{\gamma\gamma}^{(1)} - m_{\pi^0}\right)^2 + \left(m_{\gamma\gamma}^{(2)} - m_{\pi^0}\right)^2 = \Delta m_{\min}^2 \quad (5.11)$$

becomes minimal.

5.2.3 Resolution in Q^2 and \sqrt{s} and kinematic constraints

The resolution of the spectrometer for our desired final states of $\pi^- \pi^0$ and $\pi^- \pi^0 \pi^0$ is an important quantity for the measurement. It is dominated by the calorimetric measurement

of the π^0 decay photons. It is common practice to subject the measured parameters of a photon, i.e. position and energy, to a kinematic fit to improve the resolution of the measured kinematic quantities. *Kinematic fitting* is a procedure in which one uses the physical laws governing a particle interaction to improve the measurement of the process. For our example, the $\pi^-\gamma^{(*)} \rightarrow \pi^-\pi^0$ scattering, we can impose the π^0 mass and exclusivity of the reaction. Such constraints are generally implemented through a least-squares procedure: we can vary the photon parameters according to their measurement uncertainties to meet the given constraints and by that improve the accuracy of the measured reaction. The author of Ref. [116] developed a procedure together with code for applying kinematic constraints to a fit in COMPASS data.

The procedure of kinematic fitting assumes that the set of measured values carries Gaussian errors. This is clearly not the case for the uncertainties on the photon parameters: the photon positions have been corrected with a cubic polynomial and the photon positions as well as the energies feature a systematic bias for overlapping clusters (see Section 5.2.1). The kinematic fit with the uncertainties taken from the shower fit does therefore not improve the resolution. Instead, we follow an effective, empirical ansatz to constrain the π^0 parameters in $\pi^-\gamma^{(*)} \rightarrow \pi^-\pi^0$ events. We learned in Eq. (2.28), that momentum is mainly transferred in transverse direction. We scale the π^0 energy and the magnitude of its three-vector in a way, that q_{\parallel} practically vanishes by implying exclusivity of the reaction and the π^0 mass:

$$p_{\pi^0}^{\prime\mu} = \begin{pmatrix} E'_{\pi^0} = E_{\text{beam}} - E_{\pi^-} \\ c \cdot p_x \\ c \cdot p_y \\ c \cdot p_z \end{pmatrix} \quad (5.12)$$

with $c = \sqrt{E_{\pi^0}^{\prime 2} - m_{\pi^0}^2} / |\vec{p}_{\pi^0}|$ and $|\vec{p}_{\pi^0}| = \sqrt{p_x^2 + p_y^2 + p_z^2}$. This ansatz leaves the direction of the constrained π^0 four-vector $p_{\pi^0}^{\prime\mu}$ untouched.

$\pi^- + \text{Ni} \rightarrow \pi^-\pi^0\pi^0 + \text{Ni}$ events are more complex to constrain. M. Krämer developed a proce-

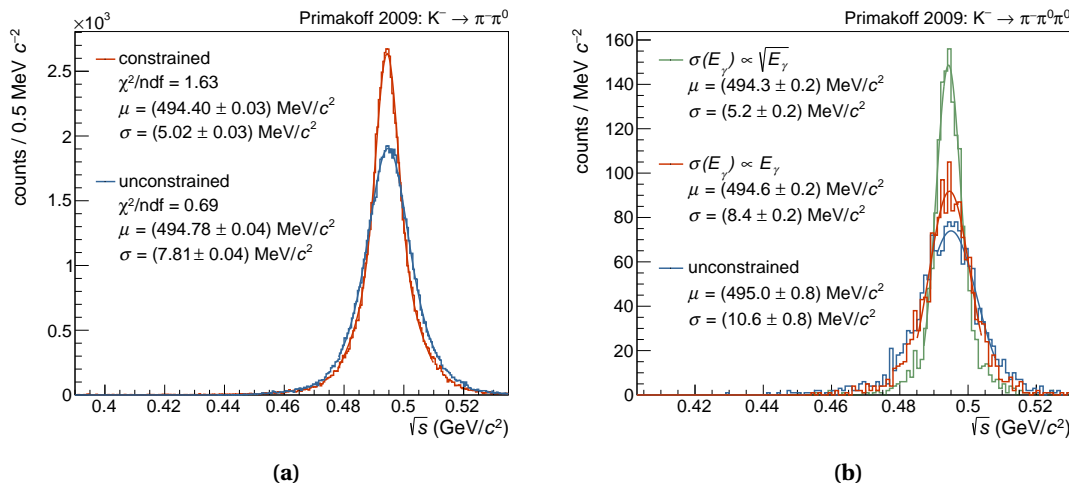


Fig. 5.10 Applying kinematic constraints: comparison of resolution in \sqrt{s} between constrained and unconstrained data for $K^- \rightarrow \pi^-\pi^0$ decays in (a) and $K^- \rightarrow \pi^-\pi^0\pi^0$ decays in (b).

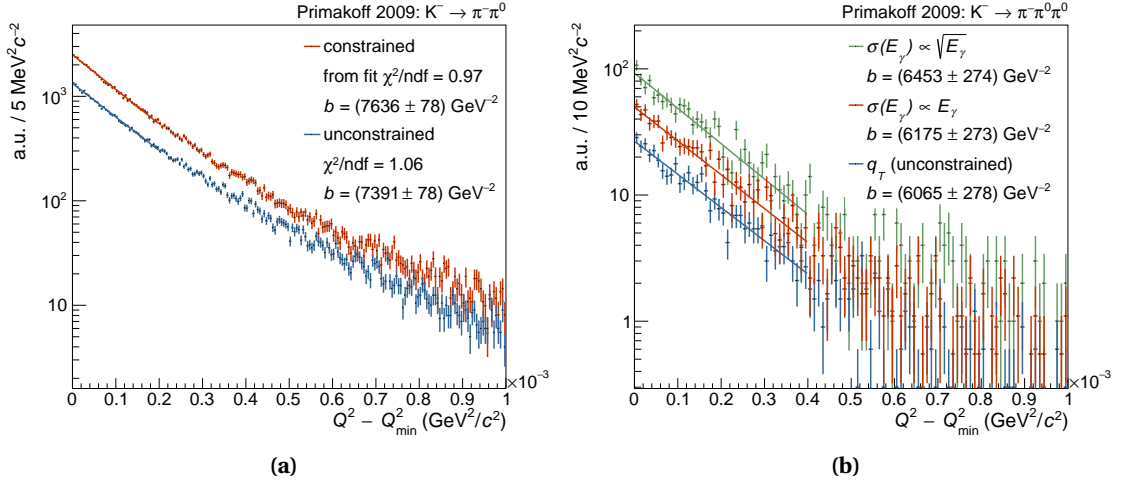


Fig. 5.11 Applying kinematic constraints: comparison of resolution in Q^2 between constrained and unconstrained data for $K^- \rightarrow \pi^- \pi^0$ decays in (a) and $K^- \rightarrow \pi^- \pi^0 \pi^0$ decays in (b). The distributions were scaled arbitrarily, such that they do not overlap.

ture in Ref. [63]. He obtains the constrained photon energies E'_γ by scaling all reconstructed photon energies E_γ by a common factor ν :

$$E'_\gamma = \nu \cdot E_\gamma \quad (5.13)$$

with

$$\nu = \frac{E_{\text{beam}} - E_{\pi^-}}{\sum_{i=1}^4 E_{\gamma,i}} \quad (5.14)$$

such that the exclusivity condition is fulfilled:

$$\sum_{i=1}^4 E'_{\gamma,i} = E_{\text{beam}} - E_{\pi^-} \quad (5.15)$$

The approach assumes, that the uncertainty on measured photon energies $\sigma(E_\gamma)$ increases linearly with energy $\sigma(E_\gamma) \propto E_\gamma$. However, simulated pseudodata suggests, that this assumption is not true.

We investigated a different approach motivated by pseudodata and experience from other experiments [117] assuming a linear combination of different dependencies:

$$\sigma^2(E_\gamma) = c_1^2 \cdot E_\gamma + c_2^2 \cdot E_\gamma^2 \quad (5.16)$$

We varied the parameters c_1 and c_2 and empirically achieved the best performance with

$$\begin{aligned} c_1 &= 0.07 \text{ GeV}^{1/2} \\ c_2 &= 0 \end{aligned} \quad (5.17)$$

To determine the spectrometer resolution and to evaluate the performance of the mentioned kinematic constraints, we investigated kaon decays: the K^- decays into both, $\pi^- \pi^0$ and $\pi^- \pi^0 \pi^0$

5.2. RECONSTRUCTION OF NEUTRAL PIONS

Table 5.3 Resolutions in \sqrt{s} and t' for $\pi^-\pi^0$ and $\pi^-\pi^0\pi^0$ final states for different π^0 constraining procedures.

decay channel	constraining procedure	$\sigma(\sqrt{s})$ (MeV/ c^2)	b (GeV $^{-2}c^2$)
$K_{2\pi}$	none	7.81 ± 0.04	7391 ± 78
	m_{π^0} and ΔE	5.02 ± 0.03	7636 ± 78
$K_{3\pi}$	none	10.6 ± 0.8	6065 ± 278
	$\sigma(E_\gamma) \propto E_\gamma$	8.4 ± 0.2	6175 ± 273
	$\sigma(E_\gamma) = 0.07 \text{ GeV}^{1/2} \cdot \sqrt{E_\gamma}$	5.2 ± 0.2	6453 ± 274

final state and appears at the exact kaon mass of $m_{K^-} = 493.68 \text{ MeV}/c^2$ [18] (the width of the kaon is negligible) and at zero momentum transfer Q^2 only smeared by resolution effects. They are hence ideal to evaluate the resolution and achieved improvements in \sqrt{s} and Q^2 . To quantify the results, we fitted the \sqrt{s} -distributions with the sum of two Gaussian distributions, as can be seen in Fig. 5.10, and the Q^2 -spectrum with an exponential $Ae^{-b(Q^2-Q_{\min})}$, as indicated in Fig. 5.11. The results of the exercise are summarized in Table 5.3. By applying suitable constraints, we can improve the \sqrt{s} -resolution by a factor of two in the 3π final state and by a factor of 1.6 in the 2π final state. The b -slope is sharpened by 4.3% and 6.4% in the 2π , respectively 3π final state. For the exercises, that lead to the results in Table 5.3, I already applied the ECAL alignment described in the next section.

A full kinematic fit with uncertainties estimated from pseudodata instead of taken the uncertainties from the shower fit, might yield slightly better results at the cost of CPU processing time [117]. In the following, we stay with the approach of Eq. (5.12) and Eqs. (5.16) and (5.17).

5.2.4 Alignment of calorimeters

The position of the calorimeters is geometrically surveyed before the run by means of a laser system. Although the precision of the geometrical survey should be comparable or even better than the spatial resolution of the calorimeter, we evaluated the position of ECAL2 by minimizing the b -slope in $K^- \rightarrow \pi^-\pi^0$ decays for different ECAL positions in x and in y .

Fig. 5.12 shows the value for the b -slope determined from a fit to the $Q^2 - Q_{\min}^2$ -distribution up to $Q^2 - Q_{\min}^2 = 2 \cdot 10^{-4} \text{ GeV}^2/c^2$. In Fig. 5.12a, we varied the x -position of ECAL2

$$x' = x_{\text{nom}} + x_{\text{shift}} \quad (5.18)$$

within $x_{\text{shift}} = (-0.3, +0.1) \text{ cm}$ while keeping a constant y -position of $y_{\text{shift}} = 0.0 \text{ cm}$. In Fig. 5.12b, we varied the y -position while keeping a constant value for x of $x_{\text{shift}} = -0.159 \text{ cm}$. The figure illustrates the sensitivity of the spectrometer to the sharpness of the Q^2 -distribution: a misalignment of the calorimeter in the order 1 mm smears the distribution already significantly.

To determine the x_{shift} - and y_{shift} -values, for which the resolution effects are minimal, i.e. the exponential slope is highest, we fitted the b -dependence on the ECAL2 position with a parabola around its maximum, as can be seen in Fig. 5.12. The obtained values $x_{\text{shift}}^{\text{max}} = (-0.160 \pm 0.002) \text{ cm}$ and $y_{\text{shift}}^{\text{max}} = (-0.002 \pm 0.002) \text{ cm}$ agree with the values of Ref. [108] within

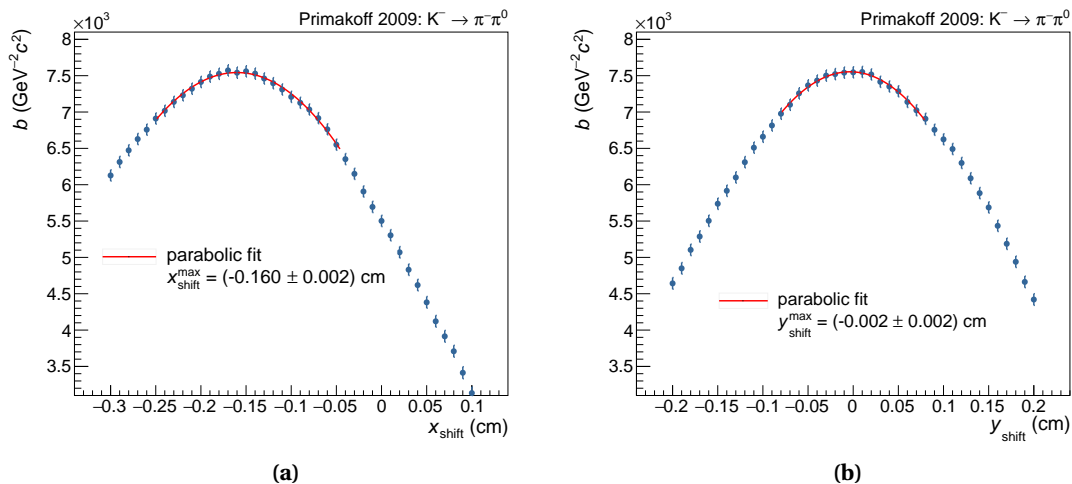


Fig. 5.12 Slope of t' -distribution for different x -positions (a) and y -positions (b) of ECAL2.

their uncertainties. In the following, we stay with the values of Ref. [108] for consistency:

$$\begin{aligned} x_{\text{shift}} &= -0.159 \text{ cm} \\ y_{\text{shift}} &= 0.000 \text{ cm} \end{aligned} \tag{5.19}$$

5.3 Event selection

With the calorimeter calibrated and the treatment of the showers explained, we are in the position to reconstruct our desired final states of Eq. (5.1).

5.3.1 Beam and final state particle identification

The CEDAR detectors (see Section 3.2) allow us to identify the species of incoming beam particles. As already mentioned, we use the likelihood approach developed in Ref. [84] to distinguish kaons from pions. Beam muons, are identified in the final state by the muon rejection as described in Section 5.1. Other contributions in the beam, e.g. antiprotons or electrons, are supposed to be small and will be neglected in the following discussion. But we should keep in mind, that potential additional background may be a result of other beam particles such as antiprotons.

For incoming beam pion, we are interested in interactions inside the target disk. This is in contrast to free decays of beam kaons, which expected to appear uniformly along the beam axis. In the hadronic two-body decay, $K^- \rightarrow \pi^- \pi^0$, the decays appear in a specific range from $\theta_{\min} \approx 1.5 \text{ mrad}$ to $\theta_{\max} \approx 4.0 \text{ mrad}$ in the scattering angle θ . The well-defined kinematics of the two-body decay mean, that the decay products go back-to-back in the cm-frame with the exact break-up momentum of $p_{K_{2\pi}} = 205 \text{ MeV}/c$ [18]. When boosted into the laboratory

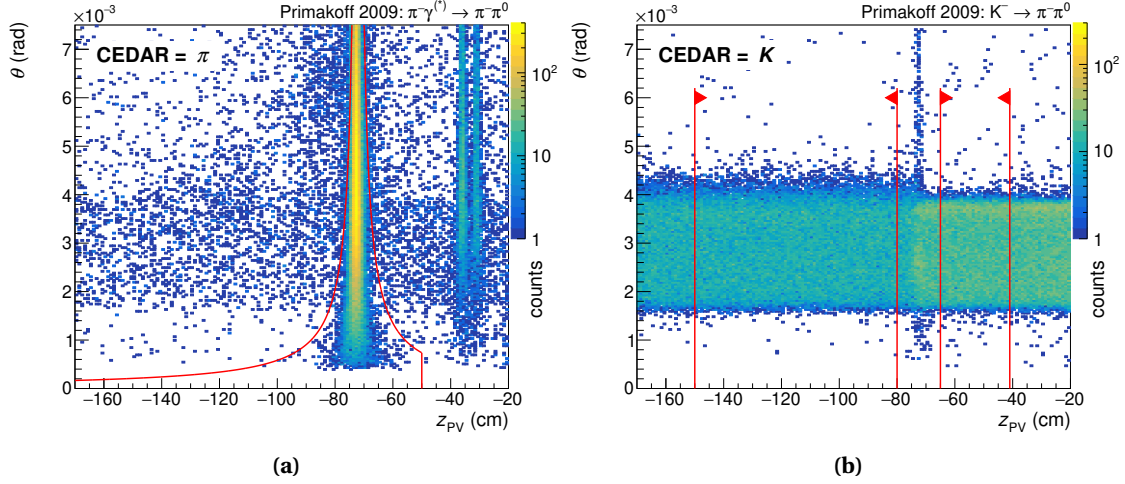


Fig. 5.13 Distribution of events along the beam axis (z_{PV}) versus the scattering angle θ . In (a): selected $\pi^-\gamma^{(*)} \rightarrow \pi^-\pi^0$ events. In (b): selected $K^- \rightarrow \pi^-\pi^0$ decays. The main difference between the two event selections is the beam particle identification by means of the CEDAR detectors — pions for (a) and kaons for (b).

frame with $p_{\text{beam}} = 190 \text{ GeV}/c$, and requiring that the π^0 energy is greater than 68 GeV such that it can trigger the acquisition for the event, the events will occur in this specific angular range.

Fig. 5.13 shows the distribution of event vertices along the beam axis versus the scattering angle for events with $\pi^-\pi^0$ final states. Filtering on beam pions shows clearly the familiar structures of our target setup: the nickel disk at $z_{\text{target}} = -73.3 \text{ cm}$ and the two tungsten disks more downstream. Since we are interested in pion interactions inside the nickel target and the resolution of the z -position of the vertex depends on the scattering angle θ , we apply the empirical selection developed in Ref. [91]

$$|z_{PV} - z_{\text{target}}| \leq 2.5 \cdot \left(0.5 \text{ cm} + \frac{6.5 \text{ cm} \cdot \text{mrad}}{\theta} \right) \quad (5.20)$$

which is indicated in Fig. 5.13a by the red lines. At very low angles, the resolution does not allow distinguishing events in the nickel disk from those in the tungsten disks. We therefore apply an additional cut $z_{PV} \leq 50 \text{ cm}$. We can clearly see the impurities of the beam particle identification by the CEDAR detectors, since the kaon decays remain visible in Fig. 5.13a. They are however much suppressed compared to Fig. 5.13b.

To select free kaon decays in the data set, we filter for beam kaons by means of the CEDARs and require the decay vertex to be within

$$\begin{aligned} -150 \text{ cm} < z_{PV} < -80 \text{ cm} \\ \text{or} \\ -65 \text{ cm} < z_{PV} < -42 \text{ cm} \end{aligned} \quad (5.21)$$

The cross section for kaons to interact in the nickel target to a final state with one π^0 is small compared to the free kaon decay, as can be guessed from Fig. 5.13b. By means of the CEDAR

beam particle identification, these events are even further suppressed in the pion data set. For the given choice of vertex selection, we can do without particle identification in the final state. The final state particle identification with the Ring Imaging Cherenkov detector (RICH) would come at the expense of a drastic cut in the accepted phase space [118]. In Section 8.1.2, we check that we are really free of background from kaon interactions.

The selection of $K^- \rightarrow \pi^- \pi^0$ ($K_{2\pi}$) decays features potential background of $K^- \rightarrow e^- \pi^0 \bar{\nu}_e$ (K_{e3}) decays, which have a branching ratio in the same order of magnitude, see Table 8.1. When the neutrino is low-energetic, the K_{e3} decays are not distinguishable from $K_{2\pi}$ decays, if we do not identify the electron as such in the final state. For this reason, we implement a final-state particle identification for electrons, which we apply in the selection of $K_{2\pi}$ decays.

This particle identification is based on information of ECAL2. While electrons are completely stopped in the electromagnetic calorimeter and deposit all their energy, pions traverse it depositing only a fraction of their energy. We can use this fact and study how much of their energy (measured by deflection in the spectrometer magnets) is deposited in ECAL2. Following the argumentation in Section 5.2.2, we associate all showers above 2 GeV, within a time window of ± 8 ns w.r.t. the beam time, and which fulfill the condition of Eq. (5.10) with the impact of the charged particle. Fig. 5.14 shows the deposited energy E_{depo} , which is the sum of all mentioned showers, versus the particle's momentum for simulated K_{e3} and $K_{2\pi}$ decays. We see that the particle needs a minimum momentum of $p_{\text{min}} = 18 \text{ GeV}/c$ to reach ECAL2 despite the deflection by SM2. In the range $18 \text{ GeV}/c < p_{\text{track}} < 30 \text{ GeV}/c$, the particles hit ECAL2 close to the edge, such that during the evolution of the shower, some energy might be lost. Only above $p_{\text{crit}} = 30 \text{ GeV}/c$, electrons reliably deposit all their energy into ECAL2.

From the simulated pseudodata, we can find a suited discrimination condition: to select $K_{2\pi}$

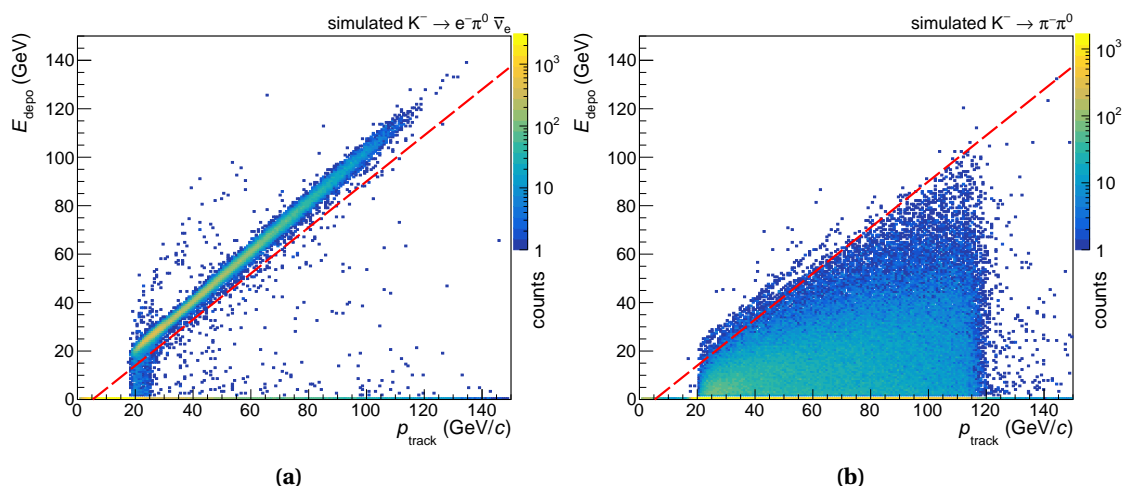


Fig. 5.14 Deposited energy E_{depo} of the charged track in ECAL2 vs its momentum measured via deflection in the spectrometer magnets in simulated $K^- \rightarrow e^- \pi^0 \bar{\nu}_e$ (a) and $K^- \rightarrow \pi^- \pi^0$ (b) decays. The dashed red line illustrates the condition of Eq. (5.22). For the displayed figures, we applied all cuts of the preselection plus the z_{PV} -cut of Eq. (5.21) for kaons.

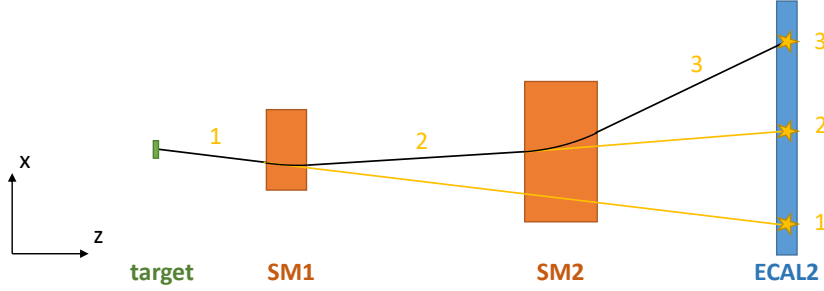


Fig. 5.15 Top view of the COMPASS spectrometer with the two dipole magnets SM1 and SM2 and the electromagnetic calorimeter ECAL2. The path of charged particles through the spectrometer is characterized by three straight segments outside the magnetic fields of the spectrometer magnets. When they pass material in these sections, there is a probability to create bremsstrahlung photons, which will be detected in ECAL2. The probability for bremsstrahlung photons depends on the particle mass and is in particular high for electrons.

decays, we require that the charged particle deposits less than

$$E_{\text{crit}} = 0.95c \cdot p_{\text{track}} - 5 \text{ GeV} \quad (5.22)$$

in ECAL2 and accept only decays with $p_{\pi^-} > 30 \text{ GeV}/c$. This condition is indicated in Fig. 5.14 as red dashed line.

We see however, that some electrons do not deposit any energy despite having enough momentum to reach ECAL2. This happens, when the electrons interact significantly before reaching ECAL2, which happens mainly in bremsstrahlung events. In such a case, their track can not be reconstructed downstream of the scattering point. We can improve the electron identification even for such events by considering the kinematics of bremsstrahlung: as indicated in Fig. 5.15, the path of a charged particle, such as an electron, through the COMPASS spectrometer is characterized by three straight segments. Due to their small mass, electrons are likely to create bremsstrahlung photons when they traverse material. The bremsstrahlung photons are radiated approximately in direction of movement. This leads to two regions in ECAL2 (numbered 1 and 2 in Fig. 5.15) with increased probability for detection of bremsstrahlung photons: region 1 is in straight extrapolation of the first track segment. The distance of region 2 to this extrapolation depends on the deflection on SM1 and hence on the momentum of the particle.

Indeed, we can identify the three regions of Fig. 5.15 in the recorded Primakoff data set, when we neglect the two showers that are used for the π^0 reconstruction and look only at showers which are correlated in the non-bending plane and in time with the charged track, as it is done in Fig. 5.16a: we observe an accumulation of photons in direct extrapolation of the charged particle track (region 1: $x_\gamma - x_1 = 0 \text{ cm}$) and we can also identify the two other regions, whose distance to the straight extrapolation depend on the track momentum. The accumulations in region 1 and 2 can only be explained by bremsstrahlung photons. We establish a criterion to identify bremsstrahlung photons

$$\frac{p_{\text{track}} \cdot (x_\gamma - x_1)}{\text{GeV} \cdot \text{cm}} \in (-50, 75) \vee (780, 980) \quad (5.23)$$

as it is illustrated in Fig. 5.16b. When we observe a bremsstrahlung photon in a kaon decay, we reject the event, since it is likely a K_{e3} event. Studies with simulated pseudodata suggest, that

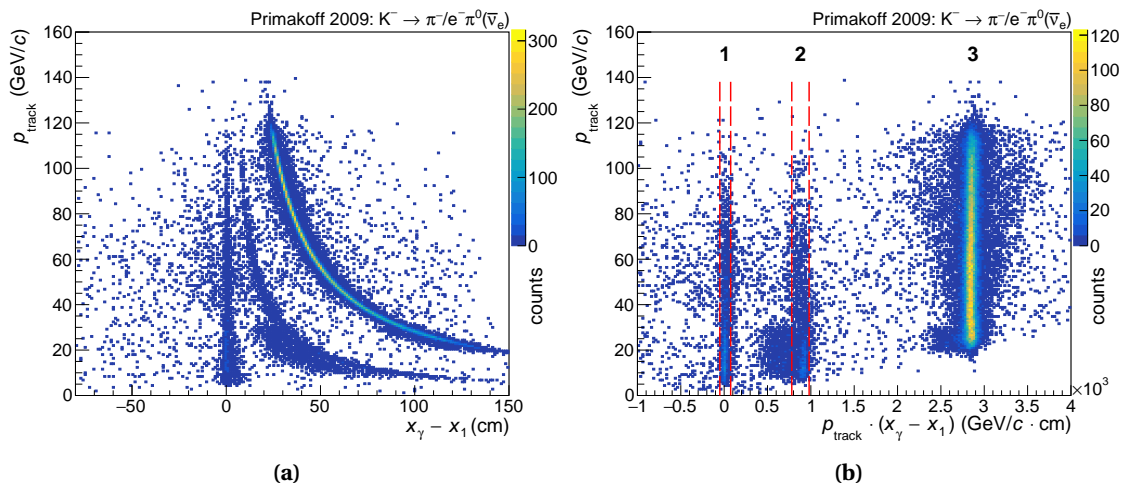


Fig. 5.16 Position of showers x_γ w.r.t. the straight extrapolation x_1 of the charged track in the bending plane of the magnets versus the momentum of the charged track. Clearly, we can identify three regions with increased probability of showers. For the plots, we considered all showers, which are not used for the π^0 reconstruction, which are within 3 cm distance to the straight extrapolation in the y -plane, within a ± 8 ns time window around the beam time, and above 2 GeV. The dashed red lines in (b) illustrate the condition of Eq. (5.23). We required all conditions of the preselection, the CEDAR kaon tag, the kaon vertex condition, and the reconstruction of a π^0 .

combining the E/p criterion of Eq. (5.22) with the identification of bremsstrahlung effectively removes all K_{e3} decays in the $K_{2\pi}$ event sample.

5.3.2 π^0 selection and event kinematics

To make sure that the two photons stem from a π^0 -decay, we cut on the invariant mass distribution of the $\gamma\gamma$ -subsystem. We require that the invariant mass is sufficiently close to the nominal π^0 -mass $m_{\pi^0}^0 \approx 135 \text{ MeV}/c^2$ by

$$120 \text{ MeV}/c^2 \leq m_{\gamma\gamma} \leq 150 \text{ MeV}/c^2 \quad (5.24)$$

for final states with one π^0 and by

$$\left(m_{\gamma\gamma}^{(1)} - m_{\pi^0}\right)^2 + \left(m_{\gamma\gamma}^{(2)} - m_{\pi^0}\right)^2 \leq r_{\max}^2 \quad (5.25)$$

for final states with two π^0 s where we set $r_{\max} = 30 \text{ MeV}/c^2$. The corresponding distributions and cuts are illustrated in Fig. 5.17. The width of the cut of $15 \text{ MeV}/c^2$ of Eq. (5.24) corresponds to 4σ as can be seen in Fig. 5.17a. In the two π^0 case, we open the cut to $r_{\max} = 30 \text{ MeV}/c^2$ intentionally, because the purpose of $\pi^- + \text{Ni} \rightarrow \pi^- \pi^0 \pi^0 + \text{Ni}$ event selection is to determine background for $\pi^- \gamma^{(*)} \rightarrow \pi^- \pi^0$ events (see Section 8.2.2). In this case, we want to be as least biased as possible by slightly inaccurate descriptions of simulated pseudodata. Since the π^0 -peak is shifted and a little narrower in simulation (see Chapter 6), we open the cut to an extent, that these small differences do not matter.

To further enrich our selected event samples with the desired events, we also set requirements to certain kinematic variables. E.g. all desired events are exclusive reactions: the energy of

5.3. EVENT SELECTION

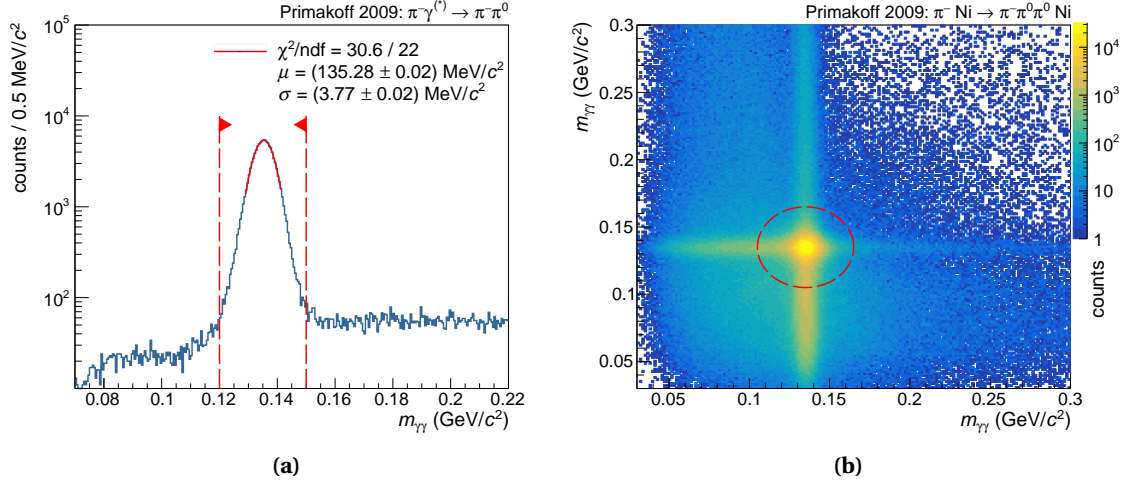


Fig. 5.17 The invariant mass spectrum of the $\gamma\gamma$ subsystem for (a) $\pi^-\gamma^{(*)} \rightarrow \pi^-\pi^0$, as an example for $\pi^-\pi^0$ final states and for (b) $\pi^- + \text{Ni} \rightarrow \pi^-\pi^0\pi^0 + \text{Ni}$ as an example for $\pi^-\pi^0\pi^0$ final states. The dashed red lines indicate the selected ranges.

the recoil is small compared to the resolution and can hence be neglected (see Section 2.2). The events fulfill Eq. (2.29) and appear at $\Delta E = E_X - E_{\text{beam}} \approx 0 \text{ GeV}$. The distributions are shown in Fig. 5.18. The width of the distributions, whether two π^0 s or just one, is very similar around $\sigma_{\Delta E} \approx 2.5 \text{ GeV}$. This hints to the fact, that the width is mainly determined by the reconstruction and uncertainty of the beam energy. To suppress background in particular in the $\pi^-\gamma^{(*)} \rightarrow \pi^-\pi^0$ distribution, we require that the events are within a 3σ interval:

$$-7.5 \text{ GeV} \leq \Delta E \leq +7.5 \text{ GeV} \quad (5.26)$$

The most relevant kinematic quantity to be investigated and cut cut on, is the momentum

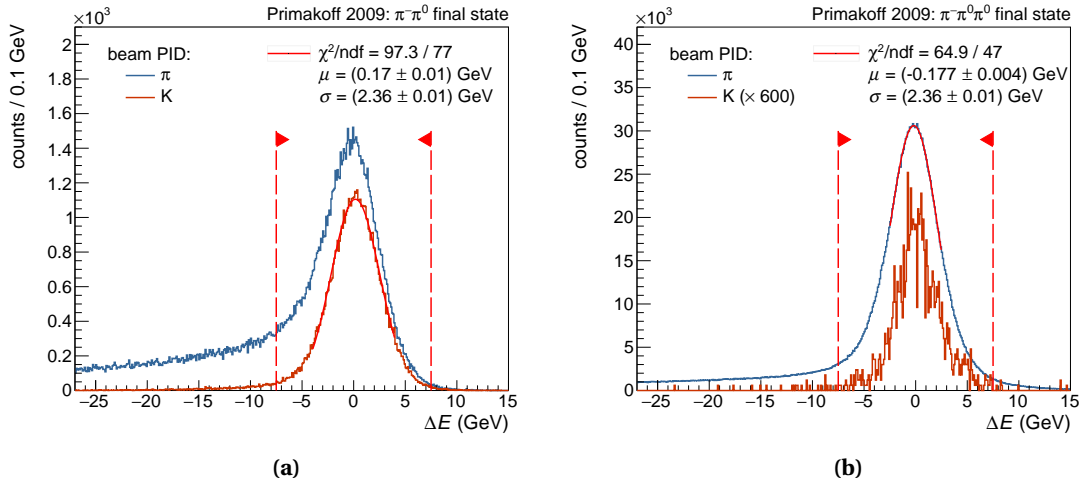


Fig. 5.18 Exclusivity distribution of (a) $\pi^-\gamma^{(*)} \rightarrow \pi^-\pi^0$, $K^- \rightarrow \pi^-\pi^0$, and (b) $\pi^- + \text{Ni} \rightarrow \pi^-\pi^0\pi^0 + \text{Ni}$, $K^- \rightarrow \pi^-\pi^0\pi^0$ events. The kaon samples are shown in red, the pion samples in blue. The $K^- \rightarrow \pi^-\pi^0\pi^0$ sample has been scaled by a factor 600 to be in the same order of magnitude as the $\pi^- + \text{Ni} \rightarrow \pi^-\pi^0\pi^0 + \text{Ni}$ sample. The selected ranges are indicated by the red dashed lines.

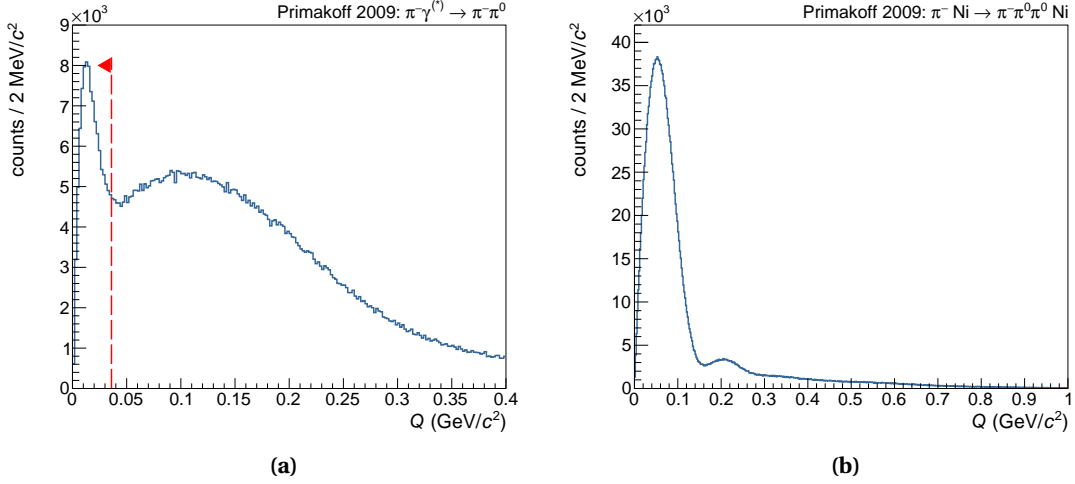


Fig. 5.19 Momentum transfer distribution in (a) $\pi^- \gamma^{(*)} \rightarrow \pi^- \pi^0$ and (b) events. Note the different x -axis range. In (a), we can clearly see two different contributions: the Primakoff peak at very small Q and at $Q \approx 0.1 \text{ GeV}/c^2$ a background contribution. In (b), we see the first diffractive minimum at $Q \approx 0.16 \text{ GeV}/c^2$.

transfer Q . Primakoff events are characterized by very small momentum transfers (see Section 2.2). We can clearly identify the Primakoff contribution and a background contribution in Fig. 5.19a which shows selected $\pi^- \gamma^{(*)} \rightarrow \pi^- \pi^0$ events. To enrich Primakoff events in this event sample, we require

$$Q \leq 36 \text{ MeV}/c^2 \quad (5.27)$$

as indicated by the red dashed line. We cut on the same Q range for the kaon decays.

The $\pi^- + \text{Ni} \rightarrow \pi^- \pi^0 \pi^0 + \text{Ni}$ event sample is dominated by diffractive production and features therefore a shallower Q -distribution. Again, we are interested in potential leakage of this channel into the $\pi^- \gamma^{(*)} \rightarrow \pi^- \pi^0$ Primakoff sample. Even events at high Q in $\pi^- + \text{Ni} \rightarrow \pi^- \pi^0 \pi^0 + \text{Ni}$ might leak to low Q in $\pi^- \gamma^{(*)} \rightarrow \pi^- \pi^0$, when one π^0 is lost in the final state. We therefore choose the maximum range in Q , which is limited by the pseudodata, which we generated up to $Q = 1 \text{ GeV}/c$ (see Chapter 6).

We can further clean the sample by requiring that the pions in the final states form the K^- -mass. Fig. 5.20 shows the distributions for the two- and three-body decay. For both decays, we require

$$460 \text{ MeV}/c^2 \leq \sqrt{s} \leq 530 \text{ MeV}/c^2 \quad (5.28)$$

The $\pi^- \gamma^{(*)} \rightarrow \pi^- \pi^0$ event selection suffers from a background contribution stemming from $\pi^- \gamma^{(*)} \rightarrow \pi^- \gamma$ events. Being also produced via the Primakoff effect, these events feature the same narrow Weizsäcker-Williams Q^2 -dependence and pass the exclusivity cut. When a low-energy shower, caused e.g. by noise in a calorimeter, is combined to the correct π^0 -mass, the event is very likely to also pass all other cuts. To minimize the impact of $\pi\gamma$ background, we require that

$$\Delta E_{\pi\gamma} = E_{\pi^-} + E_{\gamma_1} - E_{\text{beam}} < 15 \text{ GeV} \quad (5.29)$$

with E_{γ_1} being the energy of the highest-energetic photon in the event. This reduces the combinatorial background under the π^0 peak in the $m_{\gamma\gamma}$ -distribution.

5.3. EVENT SELECTION

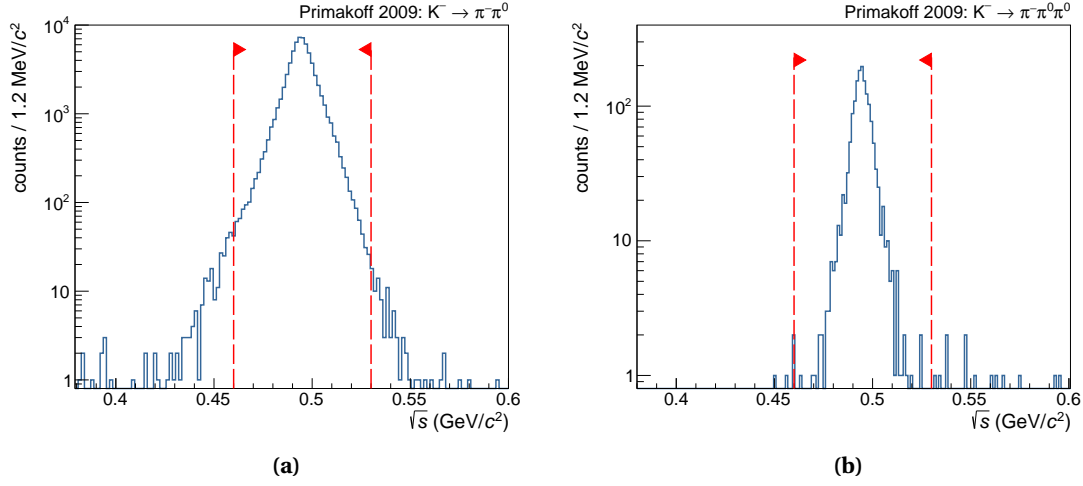


Fig. 5.20 Invariant mass distribution of the final state for (a) $K^- \rightarrow \pi^- \pi^0$ and (b) $K^- \rightarrow \pi^- \pi^0 \pi^0$ decays. The selected ranges in \sqrt{s} are indicated by the red dashed lines.

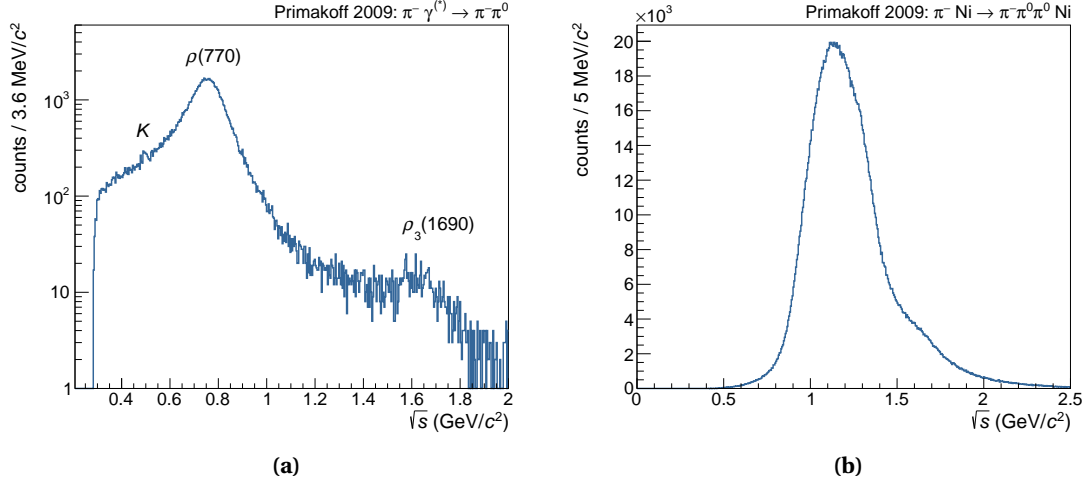


Fig. 5.21 Invariant mass distribution of the final state for (a) $\pi^- \gamma^{(*)} \rightarrow \pi^- \pi^0$ and (b) $\pi^- + \text{Ni} \rightarrow \pi^- \pi^0 \pi^0 + \text{Ni}$ events.

Fig. 5.21 shows the invariant mass distributions of the pion interactions in the nickel target. In Fig. 5.21a, we can identify the $\rho(770)$, as expected and explained in Section 2.3.2. We can also see a contamination of our event sample with free kaon decays, $K^- \rightarrow \pi^- \pi^0$ due to imperfection of the CEDARs. At $\sqrt{s} = m_{\pi^- \pi^0} \approx 1650 \text{ MeV}/c^2$, we can identify another resonance, which has been investigated in Ref. [46] and can be identified as the $\rho_3(1690)$. Fig. 5.21b shows the same features as in Ref. [63]. More kinematic distributions for the different channels can be found in Appendix B.

5.3.3 Overview of event sample sizes in the Primakoff 2009 data set

Figs. 5.22 and 5.23 summarize the different selection criteria which are applied for the four final states of interest. Fig. 5.22 shows the event numbers for pion interactions with nickel

nuclei, for which we identified our beam particle as pion and applied a cut on the z -position of the interaction inside the 4 mm nickel target disk. After the preselection of events, we are left with 33 million events. Out of these, the COMPASS 2009 data set offers ~ 2 million events which can be identified as $\pi^- + \text{Ni} \rightarrow \pi^- \pi^0 \pi^0 + \text{Ni}$ and $\sim 100,000$, which can be identified as $\pi^- \gamma^{(*)} \rightarrow \pi^- \pi^0$. So, despite the lower acceptance for the $\pi^- \pi^0 \pi^0$ final state, COMPASS has recorded an order of magnitude more $\pi^- + \text{Ni} \rightarrow \pi^- \pi^0 \pi^0 + \text{Ni}$ events than $\pi^- \gamma^{(*)} \rightarrow \pi^- \pi^0$ events. We can explain this by the much higher cross section for $\pi^- + \text{Ni} \rightarrow \pi^- \pi^0 \pi^0 + \text{Ni}$ events, since this final state can be produced diffractively. Due to the dominant cross section for diffractive production via Pomeron exchange, the $\pi^- + \text{Ni} \rightarrow \pi^- \pi^0 \pi^0 + \text{Ni}$ event sample is very clean.

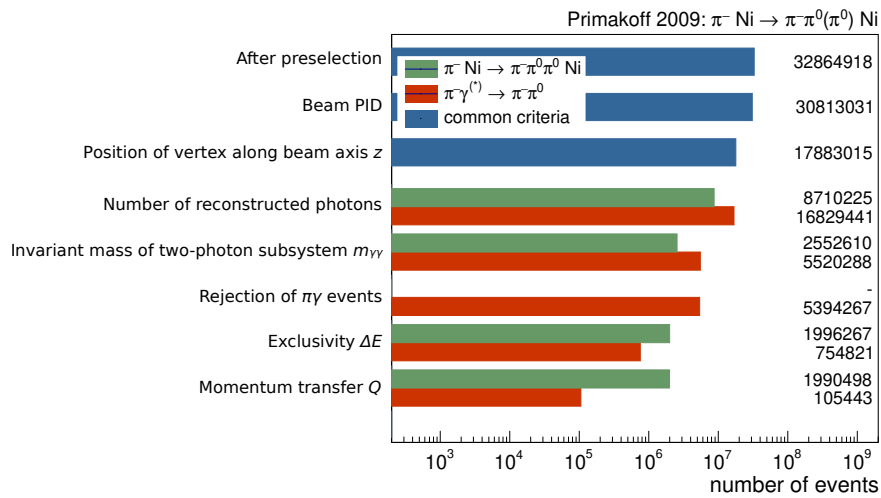


Fig. 5.22 Number of selected events after applying each cut for the selection of $\pi^- \gamma^{(*)} \rightarrow \pi^- \pi^0$ and $\pi^- + \text{Ni} \rightarrow \pi^- \pi^0 \pi^0 + \text{Ni}$ events. The details of each cut are explained in the text. The rejection of $\pi\gamma$ events is only applied to $\pi^- \gamma^{(*)} \rightarrow \pi^- \pi^0$ events.

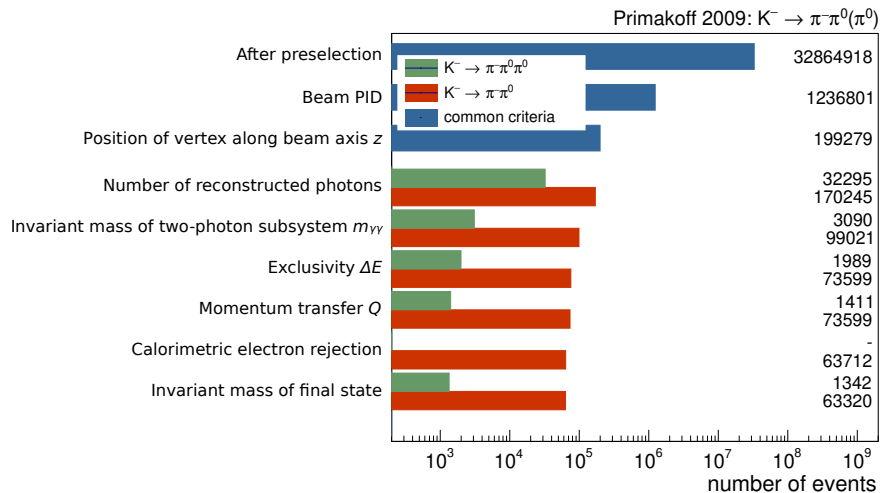


Fig. 5.23 Number of selected events after applying each cut for the selection of $K^- \rightarrow \pi^- \pi^0$ and $K^- \rightarrow \pi^- \pi^0 \pi^0$ events. The details of each cut are explained in the text. The calorimetric electron rejection to suppress background from K_{e3} events is only applied to $K^- \rightarrow \pi^- \pi^0$ events.

Fig. 5.23 shows the event numbers for the kaon decays, for which we identified the beam particle as kaon and applied a cut on the z position of the decay, outside any high-density material. The selected sample sizes reflect the beam composition. For the kaons, we lose a lot of events already after the beam PID. The branching ratio $\text{BR}(K^- \rightarrow \pi^- \pi^0 \pi^0) \approx 2\%$ is a factor ten smaller than $\text{BR}(K^- \rightarrow \pi^- \pi^0) \approx 20\%$. Together with a lower acceptance for two π^0 s in the final state, we identified only 1300 $K^- \rightarrow \pi^- \pi^0 \pi^0$ decays in the Primakoff 2009 data set. In contrast to that, we have 63,000 $K^- \rightarrow \pi^- \pi^0$ decays.

Chapter 6

Generation of pseudodata by Monte-Carlo simulation

The measured distributions are influenced by the spectrometer's acceptance and resolution. For measuring the absolute cross section determining $F_{3\pi}$, the acceptance needs to be known precisely. And for the tiny Q values of Primakoff reactions, resolution effects play an important role. To study these effects, a Monte-Carlo simulation is needed.

To obtain a reconstructed pseudodata sample including acceptance and resolution effects, one has to process a sample of generated events, e.g. $\pi^- + \text{Ni} \rightarrow \pi^- \pi^0(\pi^0) + \text{Ni}$ or $K^- \rightarrow \pi^- \pi^0(\pi^0)$, through a Monte Carlo simulation of the COMPASS spectrometer setup as realistic as possible. The propagation of the particles through the 2009 spectrometer geometry must include stochastic processes like multiple scattering or pair conversion and are implemented in the COMGEANT framework [119] based on the GEANT3 (GEometry ANd Tracking) software [120]. After the particles are propagated and the energy deposit in each mass element has been determined, the detector response is simulated within the same software framework responsible for real event reconstruction, called CORAL (COMpass Reconstruction AnaLysis software package) [106]. Subsequently, the same event reconstruction algorithms, e.g. for track fitting and shower fitting, are applied as they were applied for real data. So within the COMPASS software framework, both the reconstruction of pseudodata and the reconstruction of real data is done in CORAL ensuring a similar treatment.

The dominant contributions to the acceptance and resolution of the desired final states are

1. the amount of material between the interaction point and the calorimeter, which determines the photon-loss probability predominantly due to pair conversion,
2. the calorimetric trigger which requires a minimum energy of the π^0 ,
3. and the resolution of ECAL2. Compared to precise tracking detectors, the spatial and energy resolution of the calorimeter is large and the resolution of final states involving π^0 s is hence dominated by the calorimeter resolution.

The Monte Carlo simulation of the COMPASS setup with hadron beams is described in Section 10 of Ref. [82]. In the following, we will focus on aspects of the treatment of pseudodata that are relevant or specific for this work.

6.1 Material description

It is a difficult task to verify the material description of a simulation tool which should correspond to the real material distribution in the COMPASS spectrometer. The number of reconstructed interaction vertices, which is in principle a good indication for material, depends on the exact transverse and angular distributions of particle trajectories, which is difficult to reproduce in simulation. Moreover, the vertex reconstruction efficiency drops significantly with increasing distance to the target region. Downstream of the first dipole magnet SM1, the low vertex reconstruction efficiency prevents any comparison between simulation and the real data.

Still, we checked the material description of COMGEANT by comparing it to the material description of another simulation framework called TGEANT [121]. Since the material descriptions were developed independently, the comparison provides at least a consistency check. We found deviations in the order of 10% radiation length, in particular at the RICH detector [122]. However, the significant differences, which were found, pointed rather to a wrong description in TGEANT, when comparing it to the real detectors.

A correct material description is in particular important when looking at multiple final states with a different number of photons. The amount of material between interaction point and ECAL2 determines the photon loss probability P_{conv} due to pair conversion. Final states with four photons, e.g. $\pi^- + \text{Ni} \rightarrow \pi^- \pi^0 \pi^0 + \text{Ni}$ or $K^- \rightarrow \pi^- \pi^0 \pi^0$ are therefore more sensitive to the material description, with a total probability of accepting four photons $P_{\text{acc}}^{4\gamma} \propto (1 - P_{\text{conv}})^4$, than our desired final states with two photons, $\pi^- \gamma^{(*)} \rightarrow \pi^- \pi^0$ and $K^- \rightarrow \pi^- \pi^0$, for which $P_{\text{acc}}^{2\gamma} \propto (1 - P_{\text{conv}})^2$. A wrong material description in the simulation can therefore explain potential differences when comparing the relative yields of $\pi^- \pi^0$ and $\pi^- \pi^0 \pi^0$ final states. An inconsistent material description may therefore explain the differences between the two values for the luminosity from $K^- \rightarrow \pi^- \pi^0$ and $K^- \rightarrow \pi^- \pi^0 \pi^0$ decays, see Chapter 7.

6.2 ECAL calibration

CORAL reconstructs the simulated photon energies systematically wrong by about +1%. The effect can be seen in Fig. 5.4b when looking at disjoint clusters with a distance of $d_{\gamma\gamma} > 16$ cm. To account for that, various options have been investigated: as it was done in previous works, e.g. in Refs. [46, 63, 91], we tried to describe the correlation between reconstructed photon energy E_γ and the true photon energy \tilde{E}_γ . However, as can be seen in Fig. 5.4, a simple energy-dependent correction does not account for the more complex effects that appear for overlapping clusters. The needed correction depends also on the spatial distribution and

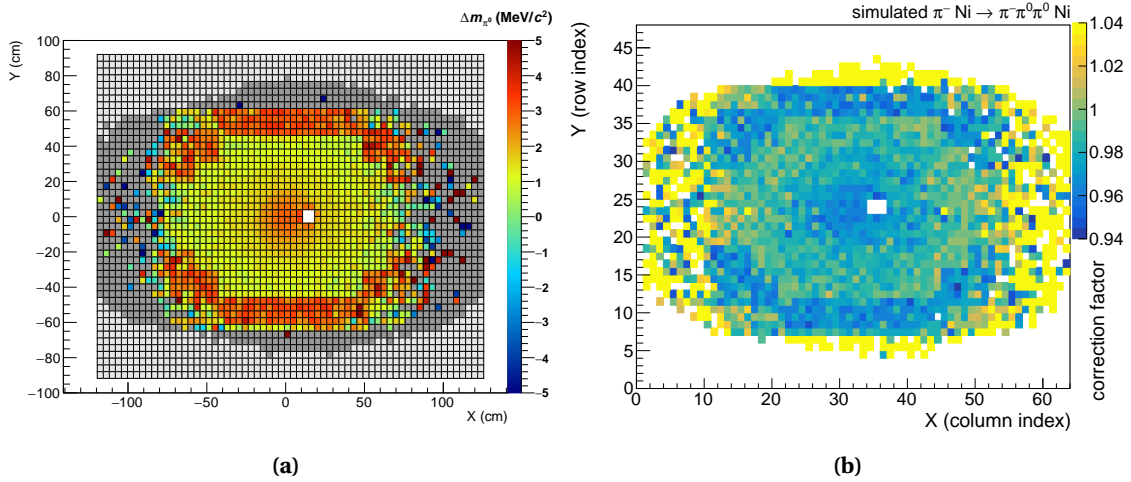


Fig. 6.1 π^0 -calibration of simulated data: in (a): difference of the peak position in the reconstructed $m_{\gamma\gamma}$ invariant mass spectrum compared to the nominal π^0 -mass for each cell individually. Figure provided by [113]. in (b): correction factor for the energy calibration of ECAL2 for each cell with sufficiently high number of hits in simulation. The correction factor was averaged over the energy range from $2\text{ GeV} < E_{\text{cell}} < 80\text{ GeV}$.

overlap probability of the photon showers. Since $\pi^- \gamma^{(*)} \rightarrow \pi^- \pi^0$, $\pi^- + \text{Ni} \rightarrow \pi^- \pi^0 \pi^0 + \text{Ni}$, $K^- \rightarrow \pi^- \pi^0$, and $K^- \rightarrow \pi^- \pi^0 \pi^0$ events have different energy and spatial distributions of the photons, it is not possible to find a simple energy-dependent correlation which manages to correct all channels at once. A way to account for the mentioned effects and reproduce the same inaccuracies as they are probably also present in real data, is to also apply a π^0 -calibration of the pseudodata on a per-cell level, analog to the real data.

For the ECAL π^0 -calibration in real data, there is no event selection applied. Any pair of reconstructed photons, which can be found in the data set, is used for the per-cell calibration. Due to the high cross-section for diffractive processes (see Section 2.1.3), the real data set is dominated by $\pi^- + \text{Ni} \rightarrow \pi^- \pi^0 \pi^0 + \text{Ni}$ events. We hence developed the per-cell π^0 calibration [113] on the generated $\pi^- + \text{Ni} \rightarrow \pi^- \pi^0 \pi^0 + \text{Ni}$ pseudodata set in order to be as close as possible to the energy and spatial distributions of the photons in the real data set.

Fig. 6.1a shows the deviation of the reconstructed π^0 -peak in the $m_{\gamma\gamma}$ mass distribution from the nominal π^0 -mass. The transition from shashlik- to radiation-hardened lead glass modules is prominently seen as a systematic jump to about 5 MeV deviation. Further away of the nominal beam axis, the calorimeter was not sufficiently illuminated to perform an energy-dependent per-cell π^0 calibration. Towards the center, in straight prolongation of the beam axis from the target position (slightly left of the hole), where most of the photons hit the calorimeter, the reconstructed π^0 -mass is too high by almost 4 MeV/c². The effect weakens when we leave the center of ECAL2 and reach the edge of the shashlik part. Since in simulation, all shashlik blocks are exactly the same, the effect can only be caused by properties of the showers. The striking difference is the occupancy of the calorimeter. While many photons hit the ECAL center, the occupancy towards the edges is significantly lower. We therefore have a high overlap probability in the center, whereas showers in the outer shashlik part or even further outside practically do not overlap. This leads to the observed behavior of Fig. 5.4b of a biased position and energy reconstruction, when the two photons enter the calorimeter

close to each other. To replicate the reconstruction of real data and its inaccuracies when two photons overlap, is hence to apply the π^0 calibration also on simulated data.

Fig. 6.1b shows the correction factor for ECAL2 cells, which is applied to shift the π^0 -mass peak to its nominal position. The energy-dependent parameters for each cell of the applied calibration can be found in Ref. [78]. Only cells, which have had a sufficient amount of hits in the pseudodata set, such that a π^0 -calibration could be performed, are shown. The correction factor for each cell is dependent on the deposited energy. Fig. 6.1b shows the correction factor for each cell averaged over an energy range from 2 GeV to 80 GeV. Each cell, which is not shown in Fig. 6.1 has a correction factor set to one.

6.3 ECAL resolution

The resolution of the spectrometer for final states with neutral particles is dominated by the calorimetric measurement of photons in the final state. Among all detector resolutions, a correct description of the resolution of ECAL2 in simulation is hence of high priority.

In simulation, the energy is smeared on cell level. The energy resolution of a cell depends on the photon energy E_γ and its energy dependence can be parametrized by [123]

$$\frac{\sigma_{E,\text{cal}}}{E_\gamma} = \sqrt{\frac{a^2}{E_\gamma} + b^2 + \frac{c^2}{E_\gamma^2}} \quad (6.1)$$

with a , b , and c being cell-type and material specific parameters. The stochastic term a represents statistical fluctuations, the systematic term b is mainly driven by calibration uncertainties. The COMGEANT framework makes the potentially oversimplified assumption that these parameters are the same for lead glass, radiation-hardened lead glass, and shashlik cells: $a = 0.065 \text{ GeV}^{\frac{1}{2}}$, $b = 0.020$, and $c = 0.000 \text{ GeV}$.

When looking at the width of the π^0 peak in the $m_{\gamma\gamma}$ distribution, we can eliminate effects from detectors other than the calorimeter and study the calorimeter resolution exclusively. Fig. 6.2 shows a channel with one π^0 and a channel with two π^0 s for comparison. We chose to show $K^- \rightarrow \pi^- \pi^0$ instead of $\pi^- \gamma^{(*)} \rightarrow \pi^- \pi^0$ events in Fig. 6.2a due to its low background contamination. Fig. 6.2b shows $\pi^- + \text{Ni} \rightarrow \pi^- \pi^0 \pi^0 + \text{Ni}$ events due to its high statistics. As can be seen, the simulation does not accurately reproduce the width of the π^0 -peak. It is too narrow in simulation.

Table 6.1 summarizes results of fits to the distributions in Fig. 6.2. We observe the general trend, that the resolution of the calorimeter is worse for lower-energetic clusters and therefore, worse for $\pi^- \pi^0 \pi^0$ compared to $\pi^- \pi^0$ final states. While the agreement between simulation and data for $\pi^- \gamma^{(*)} \rightarrow \pi^- \pi^0$ is just within 1σ and hence still acceptable, the simulation does not reproduce the $\pi^- + \text{Ni} \rightarrow \pi^- \pi^0 \pi^0 + \text{Ni}$ events accurately. One of the differences between the two reactions is the different photon energies. In the kaon decays, the photon energies are in average higher than in the diffractive scattering events. Potentially, the energy dependence of the calorimeter resolution is not correctly reproduced and deviates especially

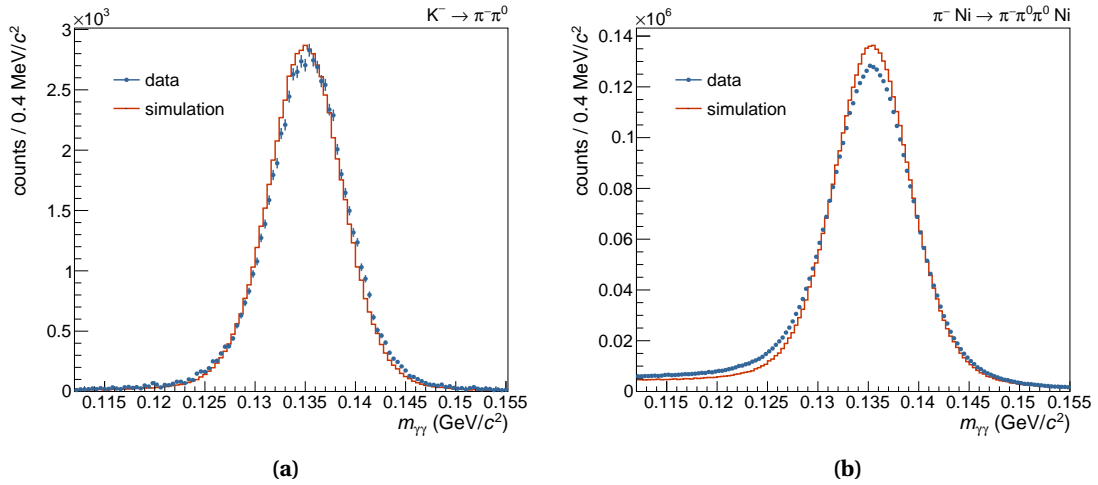


Fig. 6.2 Two-photon invariant mass distribution of data (blue) in comparison to simulation (red) as measured in ECAL2 for (a) $K^- \rightarrow \pi^- \pi^0$ and (b) $\pi^- + \text{Ni} \rightarrow \pi^- \pi^0 \pi^0 + \text{Ni}$ events.

Table 6.1 Position m_{π^0} and width σ_{π^0} of the π^0 -peak for final states with one and two π^0 (s). The parameters have been determined from fits to the histograms in Fig. 6.2 with a Gaussian and a second-order polynomial.

	data	simulation
$m_{\pi^0} (\pi^- \pi^0)$	$(135.26 \pm 0.01) \text{ MeV}/c^2$	$(135.010 \pm 0.005) \text{ MeV}/c^2$
$\sigma_{\pi^0} (\pi^- \pi^0)$	$(3.8 \pm 0.1) \text{ MeV}/c^2$	$(3.7 \pm 0.1) \text{ MeV}/c^2$
$m_{\pi^0} (\pi^- \pi^0 \pi^0)$	$(135.294 \pm 0.003) \text{ MeV}/c^2$	$(135.364 \pm 0.003) \text{ MeV}/c^2$
$\sigma_{\pi^0} (\pi^- \pi^0 \pi^0)$	$(4.08 \pm 0.05) \text{ MeV}/c^2$	$(3.88 \pm 0.07) \text{ MeV}/c^2$

for lower energies. But also the spatial distribution for showers is different for the two reactions. The $\pi^- + \text{Ni} \rightarrow \pi^- \pi^0 \pi^0 + \text{Ni}$ events illuminate the calorimeter also further away from the center, such that we have a higher fraction of showers in the lead glass modules. The author of Ref. [63] has shown, that the resolution of lead glass and radiation-hardened lead glass modules differs significantly from the resolution of the shashlik modules. Probably, the implementation of the per-cell energy resolution according to Eq. (6.1) requires parameters, which are adapted to different module types. A better simulation of the ECAL2 energy resolution is in any case desirable.

We use the π^0 mass according to Eq. (5.12) to kinematically constrain our events and improve the Q -resolution. A too optimistic calorimeter energy-resolution in simulation influences only indirectly the resolution in Q . But it still leads to an overestimated Q -resolution. Fig. 6.3 shows the comparison of the data to simulation for $K^- \rightarrow \pi^- \pi^0$ decays, which in reality have $Q = 0 \text{ GeV}/c$. The distribution is dominated by resolution effects. Indeed, we observe that the simulation produces a peak, which is slightly too sharp. All in all, we still have a good agreement of the data with simulation.

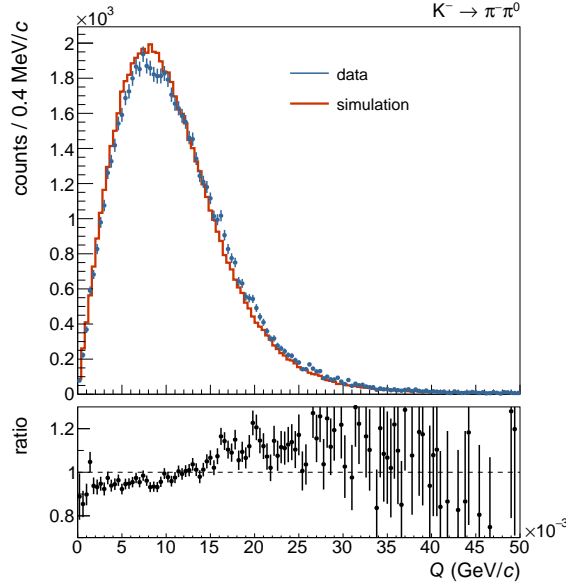


Fig. 6.3 Comparison of the Q -resolution in simulation (red) compared to the data (blue) in $K^- \rightarrow \pi^- \pi^0$ decays. The lower plot shows the ratio of bin counts data/simulation. The correction/smearing (see Section 6.4) of the beam energy in simulation has already been applied for the shown distribution.

6.4 Simulation of the beam

To propagate the particles of the reaction of interest through the COMPASS geometry, one has to transform the event kinematics, which are usually generated in the center-of-momentum system, to the laboratory system and place the interaction vertex inside the desired volume. To simulate the correct energy distribution, direction spread of the events, and reproduce a realistic spatial distribution, it is mandatory to take beam parameters from real data. The beam parameter space is five-dimensional: the spatial distribution of beam trajectories in the plane perpendicular to the nominal beam direction ($x_{\text{beam}}, y_{\text{beam}}$) at a specific z -position, the inclinations ($p_x/p_z, p_y/p_z$) at the same z -position, and the beam momentum or energy E_{beam} . We take measured beam trajectories from the Primakoff 2009 data set to obtain realistic distributions for ($x_{\text{beam}}, y_{\text{beam}}$) and ($p_x/p_z, p_y/p_z$). Ideally, the simulated data set should be one order of magnitude bigger than the real data set. We therefore use all recorded events in the 2009 data set, in particular also the events triggered by the beam trigger (see Section 3.3.3 and Table 3.2).

The beam energy directly influences the energetic balance ΔE . And a correct replication of the ΔE distribution is important as we use it to kinematically constrain our events according to Eq. (5.12). Being heavily influenced by the kinematic constraints, the distribution in Q is hence very sensitive to ΔE and finally E_{beam} . In the data, we use the correlation of the four-dimensional space ($x_{\text{beam}}, y_{\text{beam}}, p_x/p_z, p_y/p_z$) to narrow down the measured exclusivity distribution. The simulation should take these correlations into account.

E_{beam} is not directly measured, since the beam momentum station (BMS) is not used for hadron beams (see Section 3.2). In principle, there are two possibilities to assign a momen-

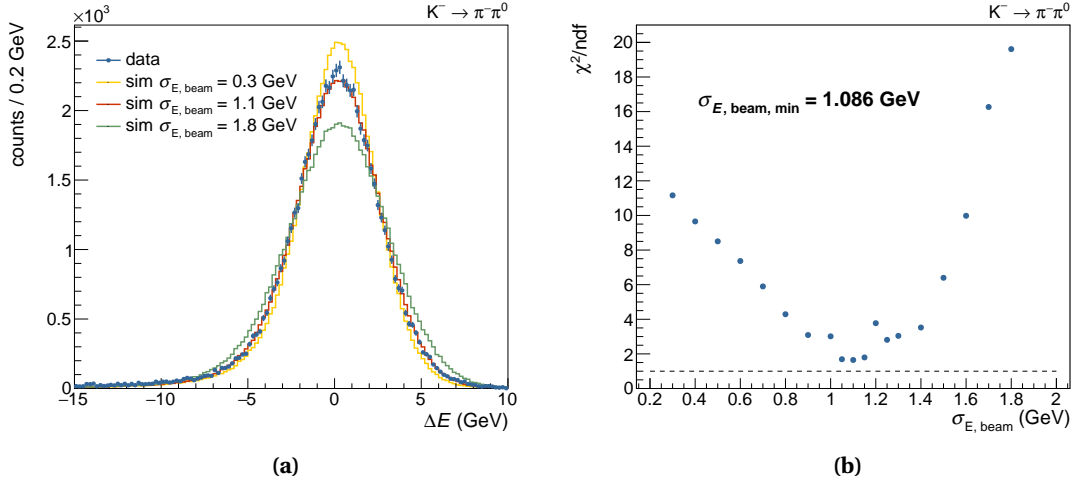


Fig. 6.4 Impact on the beam momentum determination in simulation. In (a): comparison of the measured exclusivity distribution in data compared to simulations with different values of $\sigma_{E, \text{beam}}$. In (b): the reduced χ^2 of the simulation to the data as a function of $\sigma_{E, \text{beam}}$. The function has minimum at $\sigma_{E, \text{beam}, \text{min}}$.

tum to the beam trajectories based on real data: the first is to determine it from the measured final state or secondly to calculate it from the beam energy polynomial of Eq. (3.4). Taking the momentum distribution from the measured final state has the disadvantage that the resolution of the detector has to be determined. The resolution has to be taken out of the obtained distribution before plugging it back into the simulation. Otherwise, we account twice for it. More severe is the fact, that each particle in the final state needs to be measured and its momentum or energy needs to be determined which drastically limits the number of beam trajectories, to which we can assign a momentum.

The beam energy from the polynomial of Eq. (3.4), also comes with a complication: different from what the polynomial suggests, there is no strict functional relation between $(x_{\text{beam}}, y_{\text{beam}}, p_x/p_z, p_y/p_z)$ and E_{beam} but only a correlation. We therefore have to account for the width of this correlation by smearing the functional relation with a Gaussian distribution. The width of the Gaussian distribution $\sigma_{E, \text{beam}}$ can be determined empirically by comparing the exclusivity distributions of simulation and data. This is best done in $K^- \rightarrow \pi^- \pi^0$ reactions, since the selected event set is clean and they should appear at $\Delta E = 0$ GeV.

Fig. 6.4a shows the simulated exclusivity of $K^- \rightarrow \pi^- \pi^0$ events for different widths $\sigma_{E, \text{beam}}$ of the correlation between true beam energy and the result of the polynomial. We determine the best $\sigma_{E, \text{beam}}$ by scanning through different values and evaluating the χ^2/ndf compared to the data. The result of the scan can be seen in Fig. 6.4b. Interpolating gives a minimum $\chi^2/\text{ndf} = 1.64$ at

$$\sigma_{E, \text{beam}, \text{min}} \approx 1.086 \text{ GeV} \quad (6.2)$$

Considering that the ECAL energy resolution is not exactly described by simulation, see Section 6.3, we should keep in mind, that the value of Eq. (6.2) might not be precise as well. A worse energy resolution leads to a broader exclusivity peak and hence, less smearing is necessary to reproduce the width of the distribution in the data. Anyway, we will smear the result of the beam polynomial of Eq. (3.4) with a Gaussian distribution according to Eq. (6.2).

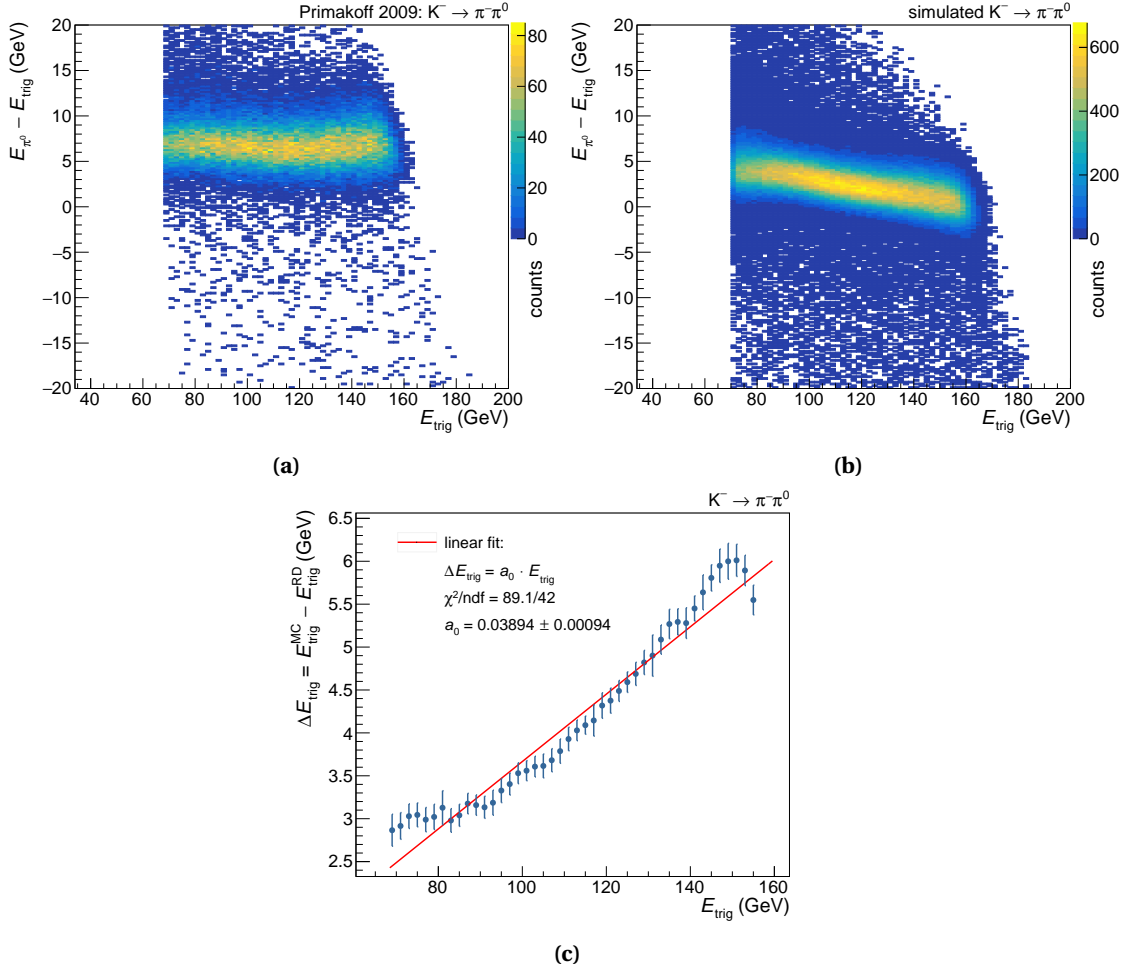


Fig. 6.5 Correlation between energy deposit in the trigger region E_{trig} and energy of the π^0 in $K^- \rightarrow \pi^- \pi^0$ decays. In (a) and (b): $E_{\pi^-} - E_{\text{trig}}$ for real data and in simulation. In (c): difference of the mean values of (a) and (b), determined by fitting a Gaussian distribution in slices of E_{trig} . The red line is a linear fit.

6.5 Trigger simulation

In the event selection, we perform a cut on the deposited energy in the trigger region, see Section 5.1. The cut prevents a possibly unfeasible modelling of the trigger efficiency in an energy range $E_{\text{trig}} < 68$ GeV, where the trigger efficiency can not be approximated linearly, see Fig. 3.7. Still, we have to make sure that the simulation reproduces correctly the amount of energy deposit in the trigger region. A way to verify the simulation, is to compare the energy deposit in the trigger region with the energy of a neutral pion. To do so, we need a channel with one π^0 in the final state. Again, we consider $K^- \rightarrow \pi^- \pi^0$ decays, since this channel is very practically background free in real data.

Fig. 6.5 shows the correlation between the reconstructed energy of the π^0 in the final state, E_{π^0} , for real data (a) and simulated data (b). As can be seen, the average deposited energy in the trigger region is always smaller than the reconstructed E_{π^0} . This can be explained by threshold

effects of the ECAL2 modules and the missing π^0 -calibration, which is not yet applied when summing up the energy deposits for the trigger decision. In real data (RD), E_{π^0} is constantly around 6 GeV smaller than E_{trig} , whereas in simulation (MC), the difference varies from 4 GeV at low E_{trig} to almost 0 GeV at high E_{trig} .

Fig. 6.5 shows the difference of the mean values of the upper two distributions, determined by fitting a Gaussian distribution in slices of E_{trig} . Assuming that E_{π^0} is the same for simulation and real data, this difference can only be explained by a difference $\Delta E_{\text{trig}} = E_{\text{trig}}^{\text{MC}} - E_{\text{trig}}^{\text{RD}}$. For the purpose of correcting E_{trig} to first order, we can find a scaling factor by fitting it linearly:

$$\begin{aligned} \Delta E_{\text{trig}} &= E_{\text{trig}}^{\text{MC}} - E_{\text{trig}}^{\text{RD}} = a_0 \cdot E_{\text{trig}} \\ \Rightarrow E_{\text{trig}}^{\text{RD}} &\approx (1 - a_0) \cdot E_{\text{trig}}^{\text{MC}} \end{aligned} \quad (6.3)$$

with $a_0 = 0.03894$ determined from the fit. Despite the various approximations, the correction of Eq. (6.3) performs well in correcting the observed deviations and in describing the kinematic distributions of the channels of interest, as can be seen in Appendix B.

6.6 Q-dependencies

The presented analysis is very sensitive to the Q -distribution of the data. It is hence important to simulate the correct Q -dependence. In case of $\pi^- \gamma^{(*)} \rightarrow \pi^- \pi^0$ events, we know the dependence from theory: it is given by the Weizsäcker-Williams approximation of Eq. (2.23). Since the distribution is peaking at very small values of Q , the observed shape is dominated by resolution effects. With the correct description of resolution effects in Monte-Carlo simulation, we can directly reproduce the expected Q -distribution of $\pi^- \gamma^{(*)} \rightarrow \pi^- \pi^0$ events. The resolution in Q has been investigated in Section 5.2.3 and has been verified in Section 6.3. Fig. 6.6 shows the distribution of momentum transfer Q in simulated $\pi^- \gamma^{(*)} \rightarrow \pi^- \pi^0$ events. The input to

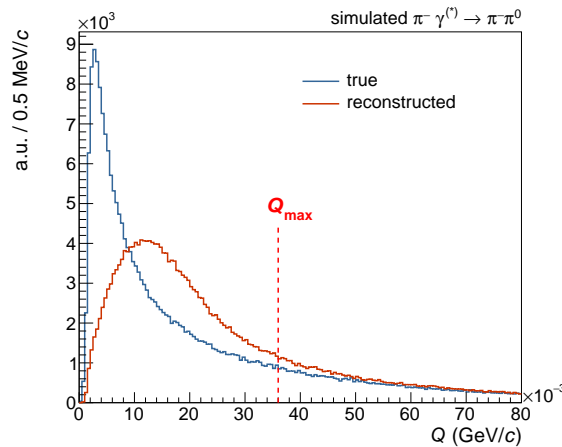


Fig. 6.6 Comparison of the true Q -dependence of the cross-section given by the Weizsäcker-Williams approximation (blue) and the reconstructed distribution (red) in simulated $\pi^- \gamma^{(*)} \rightarrow \pi^- \pi^0$ events. The achieved resolution in the range of ~ 12 MeV/ c is about a factor 4 larger than the true peak structure. The red dashed line indicates Q_{max} up to which the Q -integration is performed.

the simulation is distributed according to Eq. (2.23) and shown in blue. The reconstructed output after propagating the particles through the COMPASS spectrometer is shown in red. It becomes clear, that the resolution-limiting effects of the apparatus must be understood well, when the Q -integrated cross section up to $Q_{\max} = 36 \text{ MeV}/c$ shall be determined with precision.

For $\pi^- + \text{Ni} \rightarrow \pi^- \pi^0 \pi^0 + \text{Ni}$ events, we do not have a model to describe the Q -dependence. Instead, we have to determine an empirical shape from real data distribution. We have learned from Eq. (2.15), that the dependence on Q^2 for small Q^2 can be described by an exponential decay. Indeed, when looking at the distribution of $\pi^- + \text{Ni} \rightarrow \pi^- \pi^0 \pi^0 + \text{Ni}$ events, as it is done in Fig. 6.7, we can identify an exponential dependence for small Q^2 , which is valid approximately up to the first diffractive minimum at $Q_{\text{diffmin}}^2 = 0.026 \text{ GeV}^2/c^2$. Fig. 6.7b shows a zoom into the range of small Q^2 .

Above $Q_{\text{incoherent}}^2 = 0.2 \text{ GeV}^2/c^2$, we observe also an exponential dependence but with much shallower slope. Incoherent scattering of the pion on the nickel nucleus, i.e. when the pion doesn't "see" the whole nucleus, but single nucleons, is the usual explanation of the observed shallow Q^2 -dependence at these high values. Between Q_{diffmin}^2 and $Q_{\text{incoherent}}^2$, the dependence features the first diffractive minimum and a series of shoulders and dips.

We therefore split the entire Q^2 range into three parts: low Q^2 from $0 \text{ GeV}^2/c^2$ to Q_{diffmin}^2 , medium Q^2 from Q_{diffmin}^2 to $Q_{\text{incoherent}}^2$, and high Q^2 above $Q_{\text{incoherent}}^2$. Figs. 6.7b to 6.7d show the corresponding Q^2 -ranges. We fit the observed distribution in the high- Q^2 range, with an exponential, in the intermediate Q^2 -range with a Chebyshev polynomial, and at low- Q^2 , with the sum of two exponentials, where the parameters of one of the two are the same as for the low- Q^2 range:

$$f(Q^2) = \begin{cases} A \cdot \exp(-a \cdot Q^2) & \text{for } Q^2 > Q_{\text{incoherent}}^2 \\ \sum_{i=0}^8 p_i \cdot T_i(Q^2) & \text{for } Q_{\text{diffmin}}^2 < Q^2 \leq Q_{\text{incoherent}}^2 \\ B \cdot \exp(-a \cdot Q^2) + \exp(-b \cdot Q^2) & \text{for } Q^2 \leq Q_{\text{diffmin}}^2 \end{cases} \quad (6.4)$$

with T_i being the Chebyshev polynomials of the first kind, a , b , p_i fit parameters, and A , B scale parameters which have to be determined in a way, that the function is continuous. The fit parameters depend on $m_{3\pi}$. To account for the mass-dependence, we split the data set into $40 \text{ MeV}/c^2$ mass bins from $420 \text{ MeV}/c^2$ to $2.5 \text{ GeV}/c^2$, extracted the parameters and generated pseudodata in each mass bin independently. The extracted parameters can be found in Ref. [78]. Fig. 6.7 shows the integration over all mass bins after applying a weighted model to the data.

The distributions necessarily contain the detector resolution effect when extracting the Q^2 -dependence empirically from data. We accounted for the detector resolution, by increasing the exponential slope at low Q^2 , which is around $200 \text{ GeV}^{-2} c^2$, by $12 \text{ GeV}^{-2} c^2$ before plugging the events back into the Monte-Carlo simulation. This leads to a satisfactory replication of the observed Q^2 -dependence at low Q^2 as can be seen in Fig. 6.7b. Still, Fig. 6.7 shows effects of the detector resolution: dips are filled in the simulated pseudodata and shoulders are less pronounced.

All in all, the Q^2 -distribution is quite well reproduced for the important region of small Q . The

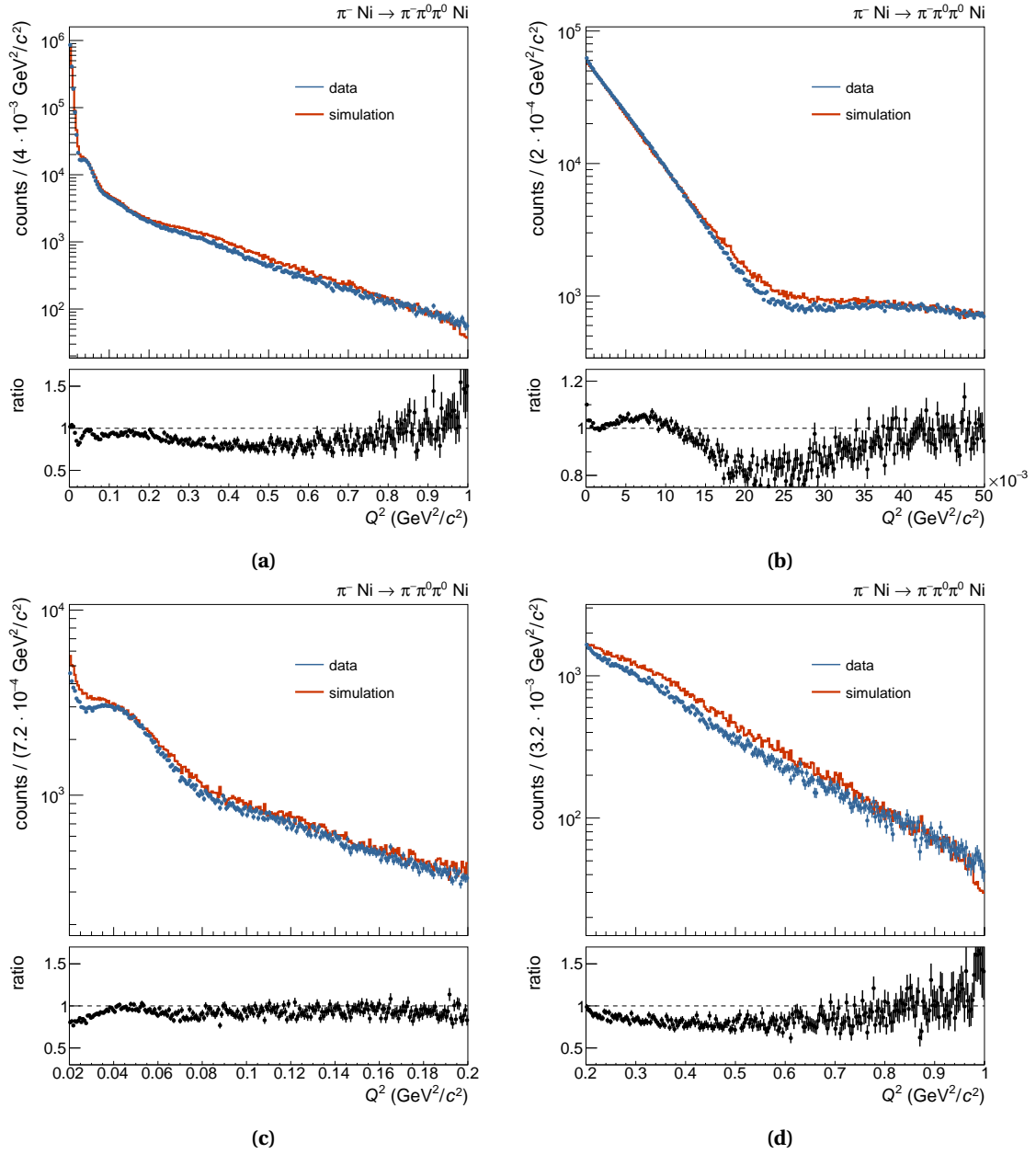


Fig. 6.7 The observed distribution of momentum transfer Q^2 of $\pi^- + \text{Ni} \rightarrow \pi^- \pi^0 \pi^0 + \text{Ni}$ events (blue) in comparison to simulation (red). The figure shows different ranges in Q (a)-(d). The lower plots show the ratios data/simulation.

$m_{3\pi}$ -dependence is implemented and the whole Q^2 -range is covered. The generated pseudo-data sample shows many improved characteristics compared to the simulation of Ref. [63]. Its biggest shortcoming is that the Weizsäcker-Williams shape, which appear in the very first bins in the Q^2 -spectra is not correctly reproduced. Events at very low Q have the highest probability to leak again to low Q when one π^0 is lost.

Chapter 7

Determination of the integrated luminosity via free kaon decays

The measurement of an absolute cross section requires to determine the luminosity integrated over the time of the data taking period. For our fixed-target geometry, the integrated luminosity depends on properties of both, the incoming beam and the target:

$$\hat{L} := \int_t L dt = \int_t dt \Phi_\pi \rho_{\text{target}} l = N_\pi \frac{\rho_{\text{target}} l}{A_r \cdot N_A} \quad (7.1)$$

where $\Phi_\pi = \frac{dN_\pi}{dt}$ represents the flux of incoming beam pions, ρ_{target} is the density of nickel (the target material), l is the thickness of the nickel target, A_r the standard atomic weight of nickel, and N_A the avogadro constant. To calculate \hat{L} , we need therefore to determine the effective number of incoming pions (N_π) during the data-taking period.

At the Serpukhov experiment on $F_{3\pi}$ by Antipov *et al.* [39], the number of beam particles was measured by a scintillation counter. Also, the COMPASS spectrometer provides counting detectors for incoming beam particles. However, at the beam intensities of the COMPASS experiment, we must account for trigger and DAQ dead times, which arise due to the finite amount of time required to process the data of one event and prepare for the next. Not every beam pion could therefore effectively trigger the acquisition of an event. The effective number of pions N_π can be calculated via

$$N_\pi = N'_\pi \cdot \bar{\epsilon}_{\text{DAQ}} = \int_t dt \Phi_\pi \cdot \epsilon_{\text{DAQ}}(t) \quad (7.2)$$

from the actually counted number of pions N'_π and the average probability to record the particle $\bar{\epsilon}_{\text{DAQ}}$. Determining $\bar{\epsilon}_{\text{DAQ}}$ with the desired accuracy of $\mathcal{O}(1\%)$ is challenging at COMPASS because the DAQ and trigger dead times strongly depend on beam intensity and average event size.

An elegant way to overcome this possible limitation is to use the kaon fraction in the negative hadron beam. The kaon decays are recorded in the same data set and hence are affected by

DAQ and trigger dead times in exactly the same way as pions. The effective integrated kaon flux $\int_t dt \Phi_K \epsilon_{\text{DAQ}}(t) = N_K = N'_K \cdot \bar{\epsilon}_{\text{DAQ}}$ can be determined from the number of detected and identified kaon decays $N_{K \rightarrow X}$ into final state X by

$$N_K = \frac{N_{K \rightarrow X}}{\Gamma_X/\Gamma_{\text{tot}} \cdot \left(1 - e^{-\frac{L}{\gamma c \tau}}\right) \cdot \eta_X \cdot \epsilon_K} \quad (7.3)$$

with $\Gamma_X/\Gamma_{\text{tot}}$ being the branching ratio into the considered final state X , $\gamma c \tau$ the mean distance, which kaons travel in the laboratory frame before they decay, L the length of the decay volume, η the acceptance of the spectrometer for final state X determined by simulation, and ϵ_K the CEDAR tag efficiency of Eq. (3.3). Potential decay volumes have to be free of material. As already mentioned in Section 5.3.2, we chose two decay volumes directly upstream and downstream of the target. The target area between beam telescope and first planes of tracking detectors offers high-quality vertex reconstruction capability. Fig. 7.1 illustrates length and position of the two decay volumes.

Knowing the true ratio of kaons and pions R_{beam} in the beam, we can relate the effective kaon flux to the effective pion flux via

$$N_\pi = \frac{N_K \cdot \epsilon_\pi}{R_{\text{beam}}} \quad (7.4)$$

with ϵ_π being the CEDAR efficiency for detecting pions from Eq. (3.3). The approximation that the ratio is constant over the length of our decay volumes is sufficiently good. Since lifetime τ and branching ratios $\Gamma_i/\Gamma_{\text{tot}}$ of the charged kaon are known to a sub-percent level [18] and R_{beam} is known with a precision of around 2%, see Eq. (3.1) [82], the effective luminosity can be determined with sufficient accuracy.

Using free kaon decays to determine the luminosity comes with more advantages: effects from e.g. pile-up events or the beam description, which are independent of the particle species but might influence the acceptance, are effectively taken into account: even if not considered correctly in simulation, the effects will cancel as long as it is done in the same way in simulation of kaon decays and of pion interactions. Moreover, if taking the $K^- \rightarrow \pi^- \pi^0$ decay

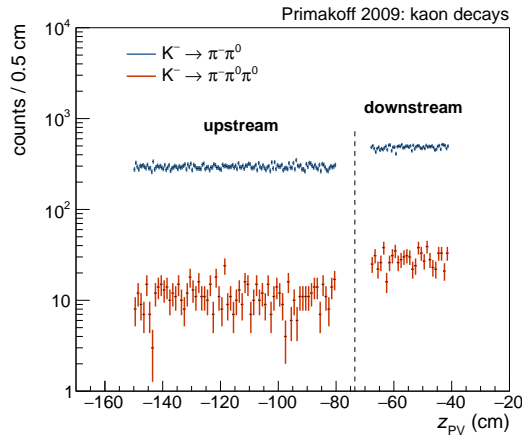


Fig. 7.1 Detected kaon decays up- and downstream of the target. The target position is indicated by a dashed line. $K^- \rightarrow \pi^- \pi^0$ decays are shown in blue, $K^- \rightarrow \pi^- \pi^0 \pi^0$ decays are shown in red.

Table 7.1 Kaon decay channels and their branching ratios $\Gamma_i/\Gamma_{\text{tot}}$ as listed in Ref. [18].

decay channel	$\Gamma_i/\Gamma_{\text{tot}}$	comment
$K^- \rightarrow \mu^- \bar{\nu}_\mu$	$(63.56 \pm 0.11)\%$	Negligible energy deposit in ECAL2
$K^- \rightarrow \pi^- \pi^0 (K_{2\pi})$	$(20.67 \pm 0.08)\%$	Similar systematics as $\pi^- \gamma^{(*)} \rightarrow \pi^- \pi^0$
$K^- \rightarrow \pi^- \pi^- \pi^+$	$(5.583 \pm 0.024)\%$	Negligible energy deposit in ECAL2
$K^- \rightarrow e^- \pi^0 \bar{\nu}_e (K_{e3})$	$(5.07 \pm 0.08)\%$	Missing energy, not exclusive
$K^- \rightarrow \mu^- \pi^0 \bar{\nu}_\mu (K_{\mu3})$	$(3.352 \pm 0.033)\%$	Missing energy, not exclusive
$K^- \rightarrow \pi^- \pi^0 \pi^0 (K_{3\pi})$	$(1.760 \pm 0.023)\%$	Used to determine π/K -ratio of beam
$K^- \rightarrow \mu^- \bar{\nu}_\mu \gamma$	$(0.62 \pm 0.08)\%$	Not exclusive, no π^0 -peak in $m_{\gamma\gamma}$
others	$< 10^{-4}$	No significant background contribution.

channel, which is the same final state as our $\pi^- \gamma^{(*)} \rightarrow \pi^- \pi^0$ events, other systematic effects, which might be introduced by an incorrect simulation, such as e.g. an inaccurate material description, are at least partly compensated.

7.1 Overview of charged-kaon decays

Being the lightest meson with strangeness, the kaon can only decay via the weak interaction leading to comparatively long lifetimes. The mean lifetime [18] and average mean decay length in the laboratory frame for a charged kaon at COMPASS beam energy is given by

$$\begin{aligned} \tau &= (1.238 \pm 0.002) \cdot 10^{-8} \text{ s} \\ \gamma c \tau &= \frac{\bar{E}_{\text{beam}}}{m_{K^-} \cdot c^2} \cdot c \tau \approx (1435 \pm 7) \text{ m} \end{aligned} \quad (7.5)$$

where $\bar{E}_{\text{beam}} = (191 \pm 1) \text{ GeV}$.

The PDG lists many possible decay modes [18]. Table 8.1 summarizes all kaon decay channels with a branching ratio $\Gamma_i/\Gamma_{\text{tot}} > 10^{-4}$. The preferred decay is the leptonic two-body decay to $\mu^- \bar{\nu}_\mu$ with a branching ratio of 64%. The $K^- \rightarrow e^- \bar{\nu}_e$ decay is helicity suppressed and has only a branching fraction of around $1.6 \cdot 10^{-5}$, despite the in principle larger phase space.

We can measure and select kaon decays into a particular channel only if this channel has a sufficiently high branching ratio. In Section 5.3.3, we have selected ~ 1300 $K^- \rightarrow \pi^- \pi^0 \pi^0$ decays, which have a branching ratio of 1.8%. Any decay with a significantly smaller branching ratio will hence not contribute a measurable quantity of events. The decay $K^- \rightarrow \mu^- \bar{\nu}_\mu \gamma$ is the last decay channel, which could contribute. Its, by a factor of three, lower branching ratio might partly be compensated by its presumably higher acceptance, since it has only one photon in the final state. However, we lack the selection criteria of exclusivity due to the unobserved neutrino. It is hence difficult to distinguish from background.

In general, decay channels with neutrinos in the final state, which appear to be non-exclusive, are harder to select and separate from background. Attempts to determine a value for the

integrated luminosity \hat{L} from the semi-leptonic decays $K_{\mu 3}$ and $K_{e 3}$ did not give a consistent picture over the whole phase space. This represents non-understood background processes. We therefore consider these channels only as potential source of background to other channels.

Since the data during the 2009 Primakoff run are taken mainly with the Primakoff trigger (see Section 3.3.3), the decay must deposit enough energy in ECAL2 to trigger the acquisition of the event. Charged muons and pions deposit only a small fraction of their energy in ECAL2 and hence do not trigger the DAQ, such that the $K^- \rightarrow \mu^- \bar{\nu}_\mu$ and $K^- \rightarrow \pi^- \pi^- \pi^+$ decay channels are not recorded. We are left with two channels, from which we can determine a value for the effective integrated luminosity:

$$\begin{aligned} K^- &\rightarrow \pi^- \pi^0 (K_{2\pi}) \\ K^- &\rightarrow \pi^- \pi^0 \pi^0 (K_{3\pi}) \end{aligned} \quad (7.6)$$

The following decay channels are considered for potential background contributions:

$$\begin{aligned} K^- &\rightarrow e^- \pi^0 \bar{\nu}_e (K_{e3}) \\ K^- &\rightarrow \mu^- \pi^0 \bar{\nu}_\mu (K_{\mu 3}) \end{aligned} \quad (7.7)$$

As we will see later, the background contributions of the mentioned processes are very small, due to an effective suppression by the applied event selection. The misidentification probability for $K^- \rightarrow \mu^- \bar{\nu}_\mu \gamma$ to $K^- \rightarrow \pi^- \pi^0$ can safely be assumed to be even smaller than the corresponding probability for $K_{\mu 3}$ events and hence negligible.

7.2 Simulation of kaon decays

A good description of charged kaon decays in simulation is essential to determine the acceptance ϵ_X for final state X in Eq. (7.3). This comprises a correct description of the kinematics, but also specific challenges that come with the simulation of free particle decays along the beam line. It turned out to be necessary to generate kaon decays in a very large z -range from $z_{K,\min} = -300$ cm to $z_{K,\max} = 400$ cm. The large range covers far more than the target area and the selected z_{pV} -range in Section 5.3.2. It stretches over the magnetic field of the first dipole magnet (SM1). Decays inside the magnetic field of SM1 can be misidentified as kaon decays in the vicinity of the target with a small scattering angle: if the actual decay in the field happens in the bending plane of the magnet, the reconstruction algorithm will interpret it as deflection by SM1, bridge the trajectory segments up- and downstream of SM1, assign a wrong momentum to the new trajectory and reconstruct a vertex close to the target. It is hence important to cover this range also in simulation.

7.2.1 Kinematics of hadronic K^- -decays

The two-body decay of the $K_{2\pi}$ channel is well-defined by giving $|p_{\pi^-}|$ and θ_{π^-} in the laboratory frame. The two quantities are shown in Fig. 7.2 illustrating the quality of the simulation. More kinematic distributions can be found in Appendix B.2.

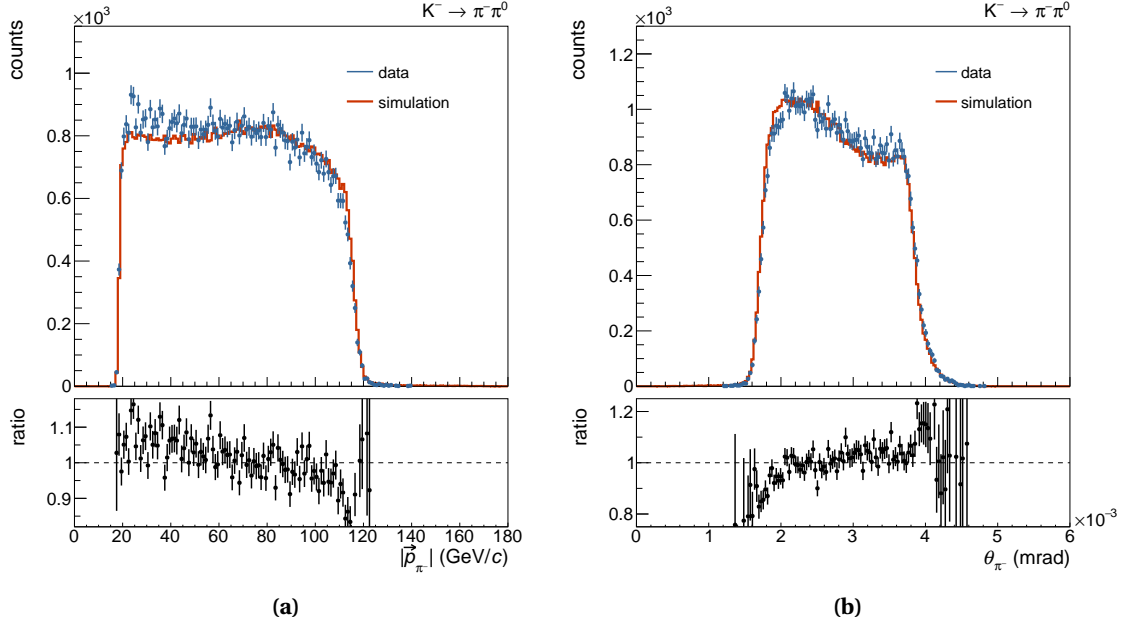


Fig. 7.2 Kinematic distributions of selected $K_{2\pi}$ decays in the laboratory frame in comparison to simulated $K_{2\pi}$ decays: in (a): the reconstructed momentum of the π^- and in (b): the angle θ of the π^- w.r.t the beam trajectory.

The three-body kinematics of the $K_{3\pi}$ is more involved. The Dalitz plot and hence the phase space of the $K^\pm \rightarrow \pi^\pm \pi^0 \pi^0$ decay is not uniformly populated. As introduced in the 1960ies by Weinberg [124], the square of the matrix element $|\mathcal{M}|^2$, which describes this Dalitz plot distribution, can be parametrized by a series expansion:

$$\frac{d|\mathcal{M}|^2}{dX dY} \propto 1 + gY + hY^2 + kX^2 + \dots \quad (7.8)$$

with

$$\begin{aligned} X &= (s_2 - s_1)/m_{\pi^\pm}^2 \\ Y &= (s_3 - s_0)/m_{\pi^\pm}^2 \end{aligned} \quad (7.9)$$

where m_{π^\pm} has been introduced to make the coefficients g , h , and k dimensionless, and $s_i = (p_K - p_i)^2$, $i = 1, 2, 3$; $s_0 = (m_{K^\pm}^2 + 2m_{\pi^0}^2 + m_{\pi^\pm}^2)/3$. p_1 and p_2 are the four-momenta of the neutral pions, p_3 the one of the charged pion. We take the values for the parameters from the PDG [18]:

$$\begin{aligned} g &= 0.626 \pm 0.007 \\ h &= 0.052 \pm 0.008 \\ k &= 0.0054 \pm 0.0035 \end{aligned} \quad (7.10)$$

In 2006, the NA48 experiment at the CERN SPS observed a cusp-like anomaly in the $m_{\pi^0\pi^0}$ invariant mass distribution [125], which alters the Dalitz plot and requires a different empirical parametrization [126]. However, the effects of the cusp on the population of the phase space are very small and negligible for our desired accuracy.

7.2. SIMULATION OF KAON DECAYS

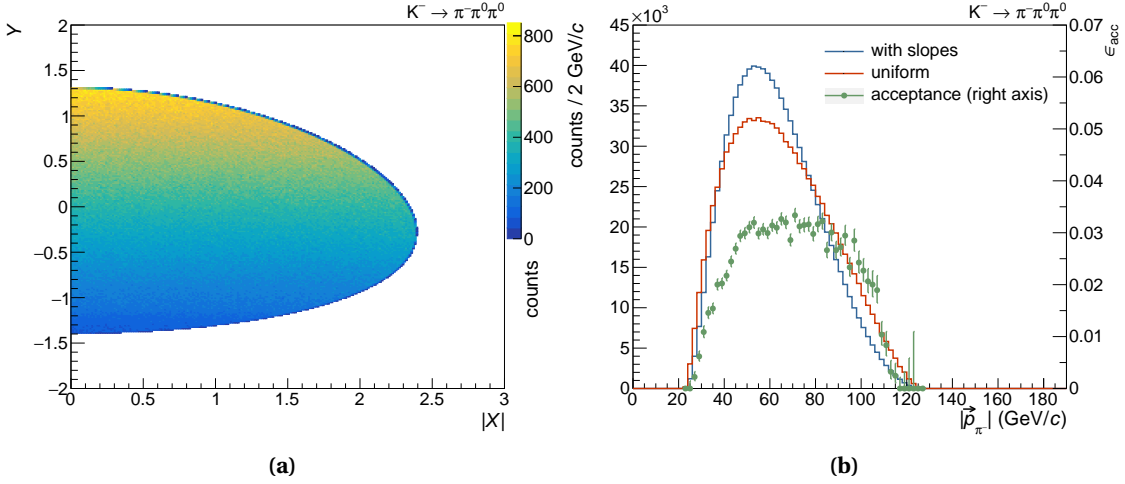


Fig. 7.3 In (a): population of the phase space in $K^- \rightarrow \pi^- \pi^0 \pi^0$ decays according to the parametrization of Eq. (7.8). In (b): difference in the distribution of p_{π^-} in $K^- \rightarrow \pi^- \pi^0 \pi^0$ decays with (blue) and without (red) Dalitz plot slopes.

Fig. 7.3a illustrates the population of the phase space according to the parametrization of Eq. (7.8). As can be seen in Fig. 7.3b, the population of the Dalitz plot has a large impact on the momentum distribution of the π^- in the final state. Considering the slopes, we have more events at smaller $|\vec{p}_{\pi^-}|$, i.e. in a corner of the phase space with higher acceptance.

The simulated pseudodata matches nicely the observed distributions, as it is shown in Fig. 7.4. More kinematic distributions can be found in Appendix B.3.

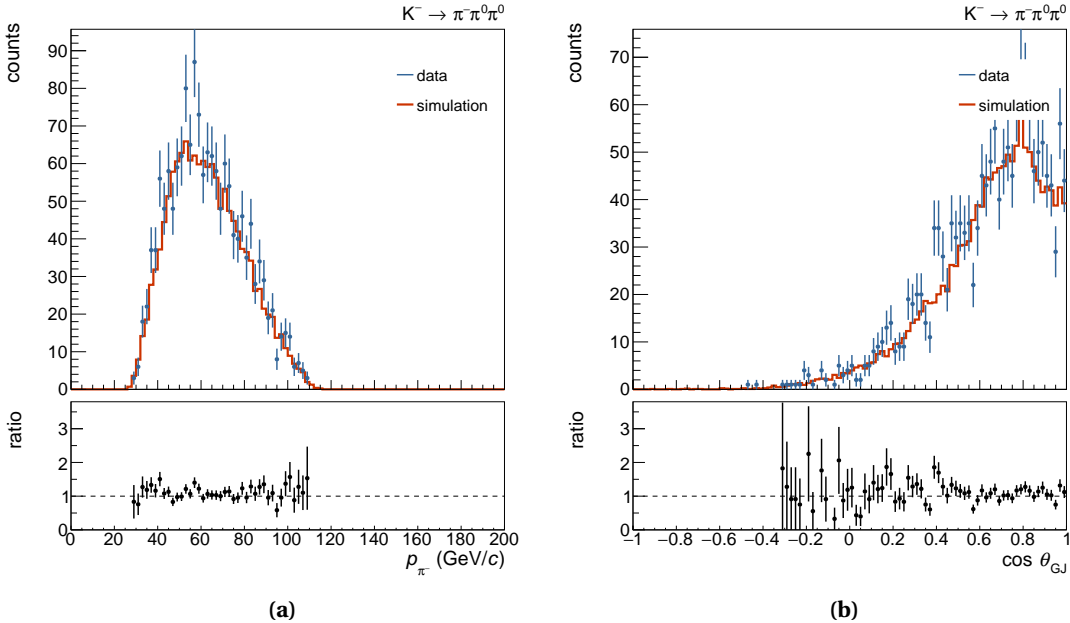


Fig. 7.4 Kinematic distributions of the $K^- \rightarrow \pi^- \pi^0 \pi^0$ decay in comparison to simulation. In (a): momentum distribution of the π^- . In (b): Polar angle distribution of the π^- in the Gottfried-Jackson rest frame. The lower plots show the ratio data/simulation.

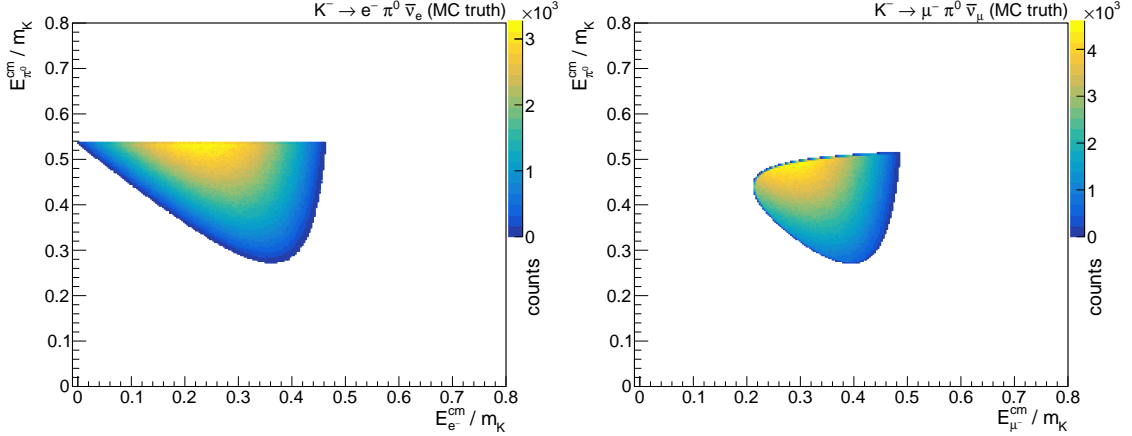


Fig. 7.5 Population of the phase space according to Eq. (7.11) from Ref. [127] for (a) K_{e3} and (b) $K_{\mu3}$ decays

7.2.2 Kinematics of semileptonic K^- -decays

Also the phase space of the two semileptonic decay channels of Eq. (7.7), K_{e3} and $K_{\mu3}$, is not flat. To correctly and quantitatively predict the background which we expect from these channels, we have to accurately model the decay kinematics. We take the parametrization of the population density of the general K_{l3} phase space from Ref. [127]. The population density ρ is a function of E_l^{cm} and $E_{\pi^0}^{\text{cm}}$ and describes the dependence of the partial decay width $\frac{d^2\Gamma(K_{l3}^-)}{dE_l^{\text{cm}} \cdot dE_{\pi^0}^{\text{cm}}}$. It can be parametrized by:

$$\frac{d^2\Gamma(K_{l3}^-)}{dE_l^{\text{cm}} \cdot dE_{\pi^0}^{\text{cm}}} = \rho(E_l^{\text{cm}}, E_{\pi^0}^{\text{cm}}) = N(A_1|f_+(t)|^2 + A_2f_+(t)f_-(t) + A_3|f_-(t)|^2) \quad (7.11)$$

where E_l^{cm} and $E_{\pi^0}^{\text{cm}}$ are the lepton and pion energies in the kaon rest frame (cm); t is the 4-momentum transfer to the leptonic system:

$$t = (p_K - p_\pi)^2 \quad (7.12)$$

N is a numerical factor; $f_-(t) = (f_0(t) - f_+(t))(m_K^2 - m_{\pi^0}^2)/t$; m_K and m_{π^0} are the charged kaon and neutral pion mass according to [18]. The kinematic factors are:

$$\begin{aligned} A_1 &= m_K (2E_l^{\text{cm}} E_\nu^{\text{cm}} - m_K (E_{\pi^0}^{\text{cm},\text{max}} - E_{\pi^0}^{\text{cm}})) + m_l^2 ((E_{\pi^0}^{\text{cm},\text{max}} - E_{\pi^0}^{\text{cm}})/4 - E_\nu^{\text{cm}}) \\ A_2 &= m_l^2 (E_\nu^{\text{cm}} - (E_{\pi^0}^{\text{cm},\text{max}} - E_{\pi^0}^{\text{cm}})/2) \\ A_3 &= m_l^2 (E_{\pi^0}^{\text{cm},\text{max}} - E_{\pi^0}^{\text{cm}})/4 \end{aligned} \quad (7.13)$$

Here $E_{\pi^0}^{\text{cm},\text{max}} = (m_K^2 + m_{\pi^0}^2 - m_l^2)/2m_K$, m_l is the charged lepton mass, and $E_\nu^{\text{cm}} = m_K - E_l^{\text{cm}} - E_{\pi^0}^{\text{cm}}$ is the neutrino energy in the kaon rest frame.

The form factors $f_+(t)$ and $f_0(t)$ can be approximated by a Taylor expansion in the variable

Table 7.2 Acceptances $\epsilon_{i \rightarrow X}$ for kaon decays up- and downstream of the target as determined from simulation. i is indicated in the columns, X in the rows. Numerical values are give only for the $\epsilon_{i \rightarrow X}$ which are not less than one order of magnitude smaller than the biggest uncertainty. For certain probabilities, we could give only upper limits with the given amount of simulated pseudodata.

$\eta_{i \rightarrow X}$ (%)	2π	3π	$e3$	$\mu3$
2π upstream	11.40 ± 0.02	$< 5 \cdot 10^{-4}$	$\sim \mathcal{O}(10^{-3})$	0.012 ± 0.004
2π downstream	19.03 ± 0.04	$< 1 \cdot 10^{-3}$	0.018 ± 0.006	0.03 ± 0.01
3π upstream	$< 6 \cdot 10^{-5}$	2.79 ± 0.03	$\sim \mathcal{O}(10^{-3})$	$< 10^{-3}$
3π downstream	$< 2 \cdot 10^{-4}$	7.03 ± 0.08	$< 2 \cdot 10^{-3}$	$< 4 \cdot 10^{-3}$

$t/m_{\pi^+}^2$:

$$f_+(t) = 1 + \lambda'_+ \frac{t}{m_{\pi^+}^2} + \lambda''_+ \left(\frac{t}{m_{\pi^+}^2} \right)^2 \quad (7.14)$$

$$f_0(t) = 1 + \lambda_0 \frac{t}{m_{\pi^+}^2}$$

The values λ'_+ , λ''_+ , and λ_0 have to be extracted from experiment. We take the most recent values by the NA48/2 collaboration, published in Ref. [127]:

$$\begin{aligned} \lambda'_+ &= (24.27 \pm 2.88 \pm 2.89) \cdot 10^{-3} \\ \lambda''_+ &= (1.83 \pm 1.05 \pm 1.09) \cdot 10^{-3} \\ \lambda_0 &= (14.20 \pm 1.14 \pm 1.07) \cdot 10^{-3} \end{aligned} \quad (7.15)$$

The phase space density, which was generated according to Eqs. (7.11) to (7.15) can be seen in Fig. 7.5. The phase space is spanned by the energy of the two measured particles of the three-body decay, the lepton and the π^0 .

7.3 Determination of the effective integrated luminosity

We learn from Eqs. (7.3) and (7.4), how we determine the effective number of pions N_π from the number of detected kaons $N_{K \rightarrow X}$ into final state X in the 2009 Primakoff data set. Considering leakage from one decay channel to the other, we must modify Eq. (7.3) by adding additional terms describing not only the acceptance, but also the leakage probability $\eta_{i \rightarrow X}$, that final state i is identified as X :

$$N_{K \rightarrow X} = N_K \cdot \epsilon_K \cdot \left(1 - \exp^{-\frac{L}{\gamma c \tau}} \right) \sum_i \eta_{i \rightarrow X} \frac{\Gamma_i}{\Gamma_{\text{tot}}} \quad (7.16)$$

with $X = 2\pi, 3\pi$ and $i = 2\pi, 3\pi, e3, \mu3$. It is hence indispensable to determine the $\eta_{i \rightarrow X}$.

The $\eta_{i \rightarrow X}$ are to be determined from simulation. Given that all kinematic distributions are correctly described in all dimensions, we can simplify the problem to one dimension and define $\eta_{i \rightarrow X}$ as the ratio of number of events, which pass all cuts of the event selection for state X , to the number of events, which have actually been simulated of channel i and which

have been generated inside our decay volume. Our decay volume is five-dimensional given by the beam parameters ($x_{\text{beam}}, y_{\text{beam}}, p_x/p_z, p_y/p_z$) and z_{PV} . The volume, in which events are generated should be larger than the actual decay volume to account for edge effects, when the decay was in reality outside the volume, but reconstructed inside. Especially in z , the generated range should cover much more than the actual selected range, since the resolution is comparatively bad, and we have the reconstruction effects mentioned in Section 7.2.

Table 7.2 shows the $\eta_{i \rightarrow X}$ determined from simulation. None of the other decays forms a significant background contribution to the $K_{3\pi}$ -decay. However, the semileptonic kaon decays have a probability to form a background contribution to the $K_{2\pi}$ -decays, which is in the same order of magnitude as the statistical uncertainty on $\eta_{2\pi \rightarrow 2\pi}$. In combination with the smaller branching ratio, they have only a small impact on the luminosity. Their contribution is around 30% of the statistical uncertainty on the leading term. Contributions from other channels, in particular $K^- \rightarrow \mu^- \bar{\nu}_\mu \gamma$ with the next highest branching ratio, can hence be neglected due to even smaller branching ratios and smaller $\eta_{i \rightarrow X}$.

On a last remark: $\eta_{e3 \rightarrow 2\pi}$ is in the same order of magnitude or even smaller than $\eta_{\mu3 \rightarrow 2\pi}$. This is achieved by the calorimetric particle identification, which is described in Section 5.3.2. The electron suppression hence performs at the same level or even better than the muon suppression.

From the data in Table 7.2, we can determine the effective integrated luminosity according to Eqs. (7.4) and (7.16). We do this for up- and downstream decay volumes and for each decay channel separately. The result can be seen in Fig. 7.6. We calculated the weighted means of up- and downstream decay volumes for $K_{2\pi}$ and $K_{3\pi}$ decays, which are also shown in Fig. 7.6. The weighted results are:

$$\begin{aligned} \hat{L}_{\text{eff}}(K_{2\pi}) &= (5.87 \pm 0.09) \text{ nb}^{-1} \\ \hat{L}_{\text{eff}}(K_{3\pi}) &= (5.48 \pm 0.17) \text{ nb}^{-1} \end{aligned} \quad (7.17)$$

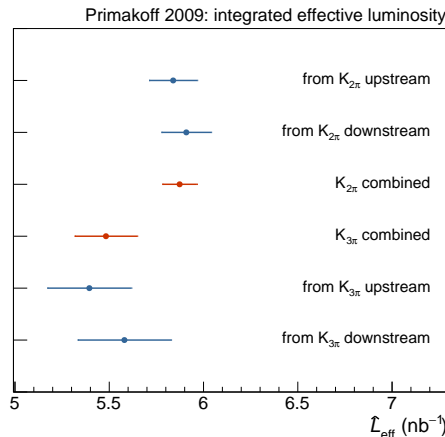


Fig. 7.6 Values for the effective integrated luminosity $\int dt L \cdot \epsilon_{\text{DAQ}}(t)$ of the 2009 Primakoff run. The values were obtained from two different decay channels $K^- \rightarrow \pi^- \pi^0$ and $K^- \rightarrow \pi^- \pi^0 \pi^0$ and two different decay volumes up- and downstream of the target (see Section 5.3.2).

The values do not match within their 1-sigma uncertainties. The discrepancy between the two channels amounts to

$$\hat{L}_{\text{eff}}(K_{3\pi}) - \hat{L}_{\text{eff}}(K_{2\pi}) = 0.39 \text{ nb}^{-1} \approx 2.3\sigma \quad (7.18)$$

It is hence unlikely that the observed difference is due to statistical fluctuations, but rather of systematic nature. Because we assume, that the systematic uncertainties of the $K_{2\pi}$ decay are very similar to $\pi^- \gamma^{(*)} \rightarrow \pi^- \pi^0$ events, we will take the value of $\hat{L}_{\text{eff}}(2\pi)$ and account for the difference to $\hat{L}_{\text{eff}}(K_{3\pi})$ in the systematic uncertainties.

7.4 Systematic uncertainties

There are various sources of systematic uncertainties for the luminosity. The CEDAR tag efficiencies, see Eq. (3.3), and the ratio of kaon to pion in the beam R_{beam} , see Eq. (3.1), are subject to an explicit systematic uncertainty. Also manufacturing accuracy and material properties of the target are subject to systematic uncertainties. The limiting factor here is certainly the precision of the 4.2 mm thickness of the target disk.

Other systematic uncertainties, such as the impact of the ECAL resolution in simulation or cut choices, are more difficult to quantify. Studies, how variations of these parameters influence the final result, can give a good estimate on the magnitude of the respective systematic uncertainties. However, many of these effects are represented in the independent measurements of the luminosity from $K_{2\pi}$ and $K_{3\pi}$ decays. These decays vary in the energy distribution of the photons, have different cut thresholds in many dimensions, different kinematic constraining procedures (see Section 5.2.3), and illuminate ECAL2 differently.

The two independent values for the luminosity from $K_{2\pi}$ and $K_{3\pi}$ in Eq. (7.17) provide an estimate on the systematic uncertainty. To deduce a value for the systematic uncertainty, we follow the approach in Ref. [128]: since the statistical σ_i and systematic s uncertainties on a given measurement $\hat{L}_{\text{eff}}(i)$ are uncorrelated, the total uncertainty is $\sqrt{\sigma_i^2 + s^2}$. The expected difference in the two measurements becomes $\sqrt{(\sigma_{2\pi}^2 + s^2) + (\sigma_{3\pi}^2 + s^2)}$. If we set this equal to the observed difference, we obtain an estimate for the systematic uncertainty

$$s = \sqrt{\frac{1}{2} \left((\hat{L}_{\text{eff}}(2\pi) - \hat{L}_{\text{eff}}(3\pi))^2 - (\sigma_{2\pi}^2 + \sigma_{3\pi}^2) \right)} \approx 0.34 \text{ nb}^{-1} \quad (7.19)$$

Due to statistical fluctuations, $|\hat{L}_{\text{eff}}(2\pi) - \hat{L}_{\text{eff}}(3\pi)|$ could be smaller than $\sigma_{2\pi}^2 + \sigma_{3\pi}^2$. In that case, one would conclude that there is no evidence for systematic effects and set our estimate to zero. The approach results in a small bias for small s , but is well applicable in our case.

Table 7.3 lists and quadratically adds all contributions to the systematic uncertainty on the final result:

$$\hat{L}_{\text{eff}} = (5.87(\pm 0.09)_{\text{stat}}(\pm 0.35)_{\text{syst}}) \text{ nb}^{-1} \quad (7.20)$$

The value has large systematic uncertainties, which are dominated by the two different values from $K_{2\pi}$ and $K_{3\pi}$ decays. It is, however, one of the advantages of measuring the luminosity via

Table 7.3 Sources of systematic uncertainties on the luminosity value.

source	systematic uncertainty
R_{beam}	1.1%
CEDAR efficiency ϵ_{π}	1.0%
CEDAR efficiency ϵ_K	0.1%
target properties	$\sim 1\%$
others (from difference in $K_{2\pi}$ and $K_{3\pi}$)	5.8%
total	6.1%

free kaon decays that $\pi^- \gamma^{(*)} \rightarrow \pi^- \pi^0$ events have similar systematics compared to $K^- \rightarrow \pi^- \pi^0$ decays. Many effects should therefore cancel. We probably overestimate the systematic uncertainties in Eq. (7.20). In finalizing this analysis, they can probably be lowered, by thorough checks and meaningful variations of cut thresholds and ECAL resolution in simulation and study the impacts not only on the value for the luminosity, but in combination with the result on $F_{3\pi}$ and $\Gamma_{\rho \rightarrow \pi\gamma}$.

Chapter 8

Extracting values for $F_{3\pi}$ and the radiative width of the $\rho(770)$

In Chapter 2, we have learned, how we can extract a value for $F_{3\pi}$ and $\Gamma_{\rho \rightarrow \pi\gamma}$ by measuring the cross section for $\pi^- \gamma^{(*)} \rightarrow \pi^- \pi^0$ as a function of $\sqrt{s} = m_{\pi^- \pi^0}$. The needed pion-photon collisions are realized in Primakoff reactions, where the photon is provided by the Coulomb field of nuclei in the nickel target. In a first step, we have to determine the number of Primakoff events in the data set and separate them from background processes. We will see, that the main background contribution is due to diffractive $\pi^- + \text{Ni} \rightarrow \pi^- \pi^0 \pi^0 + \text{Ni}$ events, in which one π^0 is lost. Beyond, we will list all considered background processes and assess the significance of their contribution.

Once this is done, we have to account for the acceptance, which is determined from simulation and normalize the observed cross section to the photon flux in the nuclear Coulomb field according to the equivalent-photon approximation of Eq. (2.23). Taking this into account, we can fit the observed cross section to the dispersive model and determine $F_{3\pi}$ and $\Gamma_{\rho \rightarrow \pi\gamma}$.

8.1 Considered background contributions

We will start with listing considered background processes and assess their contribution in the data set. The dominant background stems from $\pi^- \text{Ni} \rightarrow \pi^- \pi^0 \pi^0 \text{Ni}$ reactions as well as the inelastic scattering off the nickel nucleus and will be discussed in the next section.

8.1.1 Kaon decays

One class of background arises from kaon decays. The free kaon decays occur practically uniformly distributed over z in the target area. Some decays will hence pass our Primakoff event selection cut on the position of the vertex to be inside (or at least close to) the target.

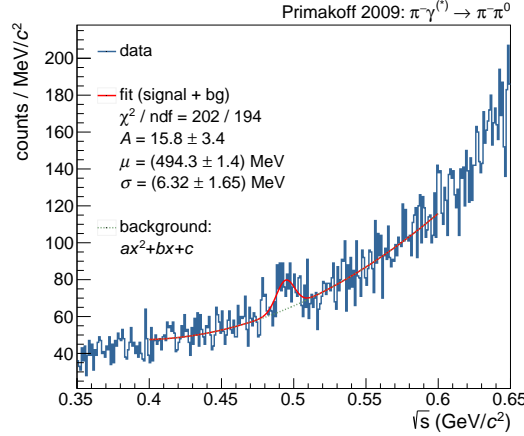


Fig. 8.1 \sqrt{s} distribution of selected $\pi^- \gamma^{(*)} \rightarrow \pi^- \pi^0$ events around m_{K^-} . It features an excess of events at $\sqrt{s} = m_{K^-} \approx 500 \text{ MeV}/c^2$ due to a background contribution from $K_{2\pi}$ decays. We fitted the distribution from $400 \text{ MeV}/c^2$ to $600 \text{ MeV}/c^2$ with a Gaussian distribution on top of a parabola to determine the number background events stemming from $K_{2\pi}$ decays.

We identified all relevant kaon decay channels in Chapter 7, which are $K^- \rightarrow X$ with

$$X = \begin{cases} 2\pi & (\pi^- \pi^0) \\ 3\pi & (\pi^- \pi^0 \pi^0) \\ e3 & (e^- \pi^0 \bar{\nu}_e) \\ \mu3 & (\mu^- \pi^0 \bar{\nu}_\mu) \end{cases} \quad (8.1)$$

and generated a pseudodata set for each of the relevant channels. From this pseudodata set, we can determine the probability η_X for a kaon decay to be misidentified as $\pi^- \gamma^{(*)} \rightarrow \pi^- \pi^0$ event. The CEDAR detectors are not included in the simulation, such that we can not include the efficiency of the beam particle identification into η_X . We can however estimate the number of background events from the $K_{2\pi}$ channel, since they appear at $\sqrt{s} = m_{K^-} = 494 \text{ MeV}/c^2$. The shape of the kaon peak is well described by a Gaussian distribution. Fig. 8.1 shows the \sqrt{s} distribution of selected $\pi^- \gamma^{(*)} \rightarrow \pi^- \pi^0$ events around m_{K^-} . It features an excess of events at $\sqrt{s} = m_{K^-} \approx 500 \text{ MeV}/c^2$ which can be fitted with a Gaussian distribution on top of a parabola to account for the smooth underlying nearby distribution. From this fit, we estimated the number of background events from $K_{2\pi}$ decays and predicted the number of events stemming from the other decay channels by normalizing to $K_{2\pi}$ decays and taking into account the different $\Gamma_X/\Gamma_{\text{tot}}$ and η_X . Table 8.1 summarizes the results of this consideration.

As can be seen, η_{e3} and $\eta_{3\pi}$ are two orders of magnitude smaller than $\eta_{2\pi}$, because the corresponding events do not pass the exclusivity cut. $\eta_{\mu3}$ is another order of magnitude smaller due to the efficient muon identification of the COMPASS spectrometer. In combination with the smaller branching ratios, the contribution to the background from K_{e3} , $K_{\mu3}$, and $K_{3\pi}$ decays is negligible. The only remaining significant contribution arises from $K_{2\pi}$ decays. We will account for this contribution by neglecting data close to $m_K \approx 500 \text{ MeV}/c^2$ in the final cross section.

Table 8.1 Relevant kaon decay channels (see Chapter 7), their branching ratios, the probability to be misidentified as $\pi^-\gamma^{(*)} \rightarrow \pi^-\pi^0$ events determined by simulation (without the CEDAR particle identification), and the estimated number of background events for each channel. The number of events from $K_{2\pi}$ decays was estimated from the fit in Fig. 8.1.

K^- decay channel	$\Gamma_X/\Gamma_{\text{tot}}$	η_X (from simulation)	# events
$K_{2\pi}(\pi^-\pi^0)$	$(20.67 \pm 0.08)\%$	$(2.34 \pm 0.02) \cdot 10^{-3}$	224 ± 26
K_{e3}	$(5.07 \pm 0.08)\%$	$(3.26 \pm 0.18) \cdot 10^{-5}$	0.76 ± 0.08
$K_{\mu3}$	$(3.352 \pm 0.033)\%$	$(3.30 \pm 0.67) \cdot 10^{-6}$	0.051 ± 0.006
$K_{3\pi}(\pi^-\pi^0\pi^0)$	$(1.760 \pm 0.023)\%$	$(1.13 \pm 0.11) \cdot 10^{-5}$	0.092 ± 0.011

8.1.2 Kaon interactions

In contrast to the pions, the kaons are no eigenstate of the G -parity operator. The $K^-\pi^0$ final state can hence be produced diffractively. This enhances the cross section with respect to a production purely in Primakoff reactions, and it is a priori not clear, that the amount of background from the $K^- + \text{Ni} \rightarrow K^-\pi^0 + \text{Ni}$ can be neglected.

The COMPASS spectrometer offers a RICH (Ring Imaging Cherenkov) detector for particle identification in the final state by means of which $K^-\pi^0$ could be distinguished from $\pi^-\pi^0$ final states. However, the RICH offers a high separation power only for particle momenta up to $|\vec{p}_R| \approx 30 \text{ GeV}/c$ [118]. A final state particle identification would hence come at the expense of a drastic cut in the final state phase space and loss of statistics.

In this context, we need to quantify the order of magnitude of background from kaon interactions $K^- + \text{Ni} \rightarrow K^-\pi^0 + \text{Ni}$. For this purpose, we plot the invariant mass distribution of the pion sample with the assumption that the charged particle is a kaon. The $m_{K^-\pi^0}$ distribution is dominated by the $K^*(892)$, see Ref. [129]. The $K^*(892)$ is a relatively narrow resonance $\Gamma_{\text{tot}} \approx 50 \text{ MeV}/c^2$ at $m_{K^*} = 892 \text{ MeV}/c^2$ [18]. If there was a non-negligible background contribution in the pion sample, the $K^*(892)$ should be visible when we plot the $m_{\pi^-\pi^0}$ distribution

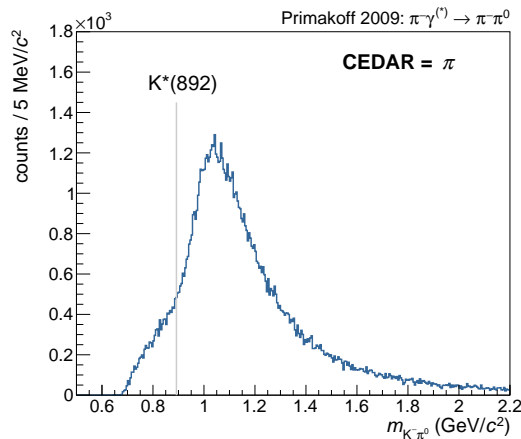


Fig. 8.2 Distribution of \sqrt{s} of selected $\pi^-\gamma^{(*)} \rightarrow \pi^-\pi^0$ events under the assumption that the charged particle in final state is a kaon. The light gray line indicates the nominal mass of the $K^*(892)$.

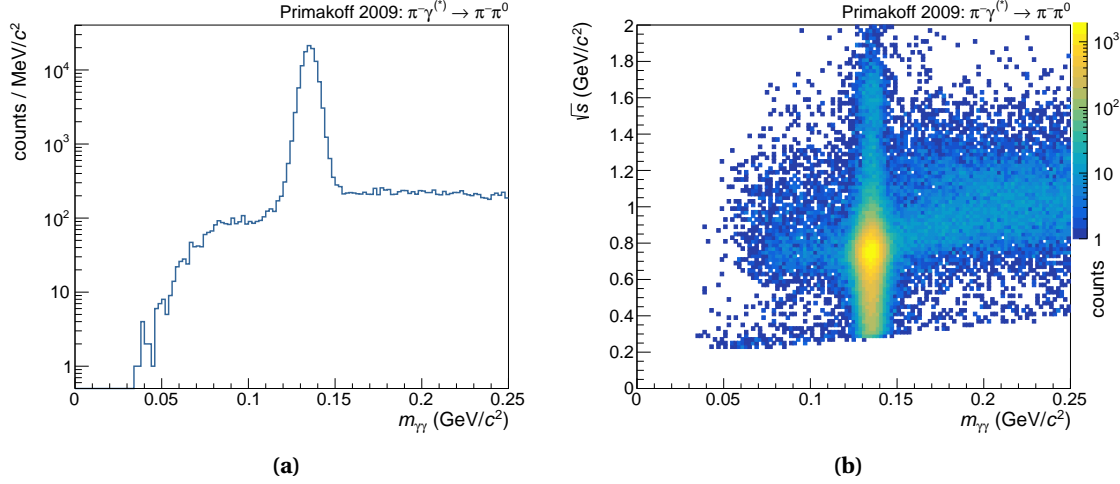


Fig. 8.3 In (a): invariant mass $m_{\gamma\gamma}$ of the two-photon system in the final state of $\pi^-\gamma^{(*)} \rightarrow \pi^-\pi^0$ events. The π^0 -peak sits on a pedestal formed by two photons which do not form a π^0 . In (b): the two-dimensional correlation between $m_{\gamma\gamma}$ and \sqrt{s} .

with the K^- -mass assumption. Fig. 8.2 shows the described mass distribution. The $\rho(770)$ peak, which we see in the usual $m_{\pi^-\pi^0}$ mass distribution, is shifted to a higher mass value of $\sim 1.05 \text{ MeV}/c^2$ under this assumption. At the $K^*(892)$ mass, indicated with a light gray line, the distribution shows no peculiar structure. This points to the correctness of the assumption, that the amount of background from kaon interactions inside the nickel target is negligible. We can hence do without a final state PID by the RICH detector.

8.1.3 Non- π^0 events

Fig. 8.3 shows the two-photon invariant mass distribution of $\pi^-\gamma^{(*)} \rightarrow \pi^-\pi^0$ events. As can be seen in logarithmic scale, the π^0 -peak sits on a background of $\gamma\gamma$ -masses, which do not form a π^0 . This background needs to be addressed. There are different hypothetical background contributions, which can lead to a broad distribution in $m_{\gamma\gamma}$:

- Primakoff Compton reactions $\pi^-\gamma^{(*)} \rightarrow \pi^-\gamma$, in which the cluster of the photon is artificially split, i.e. two photons close to each other are reconstructed instead of one. This process should however be independent of \sqrt{s} . Fig. 8.3b shows, that the background correlates strongly with \sqrt{s} . We can conclude, that this background, if existent, is very small.
- Double bremsstrahlung events $\pi^-\gamma \rightarrow \pi^-\gamma\gamma$, in which the pion in the final state emits two photons. The cross section of this process has been calculated by Kaiser and Friedrich in Ref. [67] as a function of $\eta = m_\gamma/(\sqrt{s} - m_\pi)$. Fig. 8.4 shows the result of the calculation. We can see the infrared divergence for $\eta \rightarrow 0$. Due to minimum photon energy of $E_{\gamma,\min} = 2 \text{ GeV}$ and minimum distance between two clusters of $d_{\gamma\gamma,\min} \sim 5 \text{ cm}$, the experiment imposes a minimum η . From Fig. 8.3a, we can determine the experimental limits. We can not reconstruct $m_{\gamma\gamma} < 0.05 \text{ GeV}/c^2$. This leads to a $\eta_{\min} \approx 0.3$

at threshold, where the cross section for double bremsstrahlung events has already dropped to $\sim 2 \cdot 10^{-2} \mu\text{b}$. Experimentally, the minimal η decreases with increasing \sqrt{s} , such that the cross section for double bremsstrahlung events should be highest in the upper left corner of Fig. 8.3b. However, we do not see any events in this region. We must conclude, that our experimental minimal η prevents us from recording double bremsstrahlung events.

- Combinatorial background from $\pi^- + \text{Ni} \rightarrow \pi^- \pi^0 \pi^0 + \text{Ni}$ events, in which we loose/neglect one (low-energetic) photon of each π^0 , since we combine the two most-energetic photons (see Section 5.2) when reconstructing the $\pi^- \pi^0$ final state. If the lost/neglected photons are rather low-energetic, the event still passes exclusivity conditions and the changed kinematics might also lie at the selected small momentum transfers. Studying this effect in simulated pseudodata, when the $\pi^- + \text{Ni} \rightarrow \pi^- \pi^0 \pi^0 + \text{Ni}$ are misinterpreted as $\pi^- \gamma^{(*)} \rightarrow \pi^- \pi^0$ and pass all two-pion cuts, leads to Fig. 8.5b. The distribution features the exact same characteristics as the main background contribution in Fig. 8.3b. The almost horizontal structure at around $\sqrt{s} = 0.8 \text{ GeV}/c^2$ can hence be attributed to the leakage from 3π . Since we treat and subtract this background separately (see Section 8.2.2), we must not subtract it here!
- The distribution of Fig. 8.3b shows a background contribution at very small \sqrt{s} , close to the kinematic threshold and at small $m_{\gamma\gamma}$, below the π^0 -mass, which can not be attributed to the combinatorial background from $\pi^- + \text{Ni} \rightarrow \pi^- \pi^0 \pi^0 + \text{Ni}$ events. To clarify the origin of this contribution, we release the cut on Q and look at the $m_{\gamma\gamma}$ -distribution at low $\sqrt{s} < 0.4 \text{ GeV}/c^2$, as it is done in Fig. 8.5a. The distribution shows a discrete structure for $m_{\gamma\gamma} < m_{\pi^0}$ with bumps instead of a smooth behavior. Such structures are known in COMPASS and discussed in Ref. [130]. They can be attributed to π^0 production in hadronic interactions downstream of the target inside the spectrometer. Wrongly assuming that the π^0 originated at the target, will lead to a too small angle between the two photons and, according to Eq. (5.6), to a too small mass. Each of the bumps can be connected to a material concentration in detector groups in the spectrometer. What we see in terms of low- \sqrt{s} , low- $m_{\gamma\gamma}$ background are remains of these structures, which do not significantly leak into the signal region, when the cut on q_T is applied.

To sum it up: the major background contribution could be attributed to combinatorial background from $\pi^- + \text{Ni} \rightarrow \pi^- \pi^0 \pi^0 + \text{Ni}$ reactions. The remaining background from π^0 -decays inside the spectrometer is not as dangerous, since it occurs at specific $m_{\gamma\gamma}$ and does not significantly leak into the signal region. Double-bremsstrahlung events and background from the Primakoff Compton reaction could be excluded. To not account for 3π -leakage twice, we should refrain from any background subtraction in e.g. sideband analysis based on $m_{\gamma\gamma}$.

8.2 Background subtraction

In Section 2.1.3, we have learned that diffractive processes have a large cross section. The direct diffractive production of $\pi^- \pi^0$ final state is forbidden by G -parity conservation. Still,

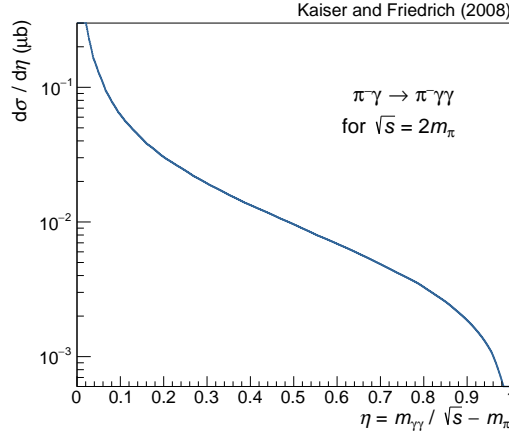


Fig. 8.4 Two-photon mass spectrum for the reaction $\pi^- \gamma \rightarrow \pi^- \gamma \gamma$ as a function of the variable η . Taken from Ref. [67]

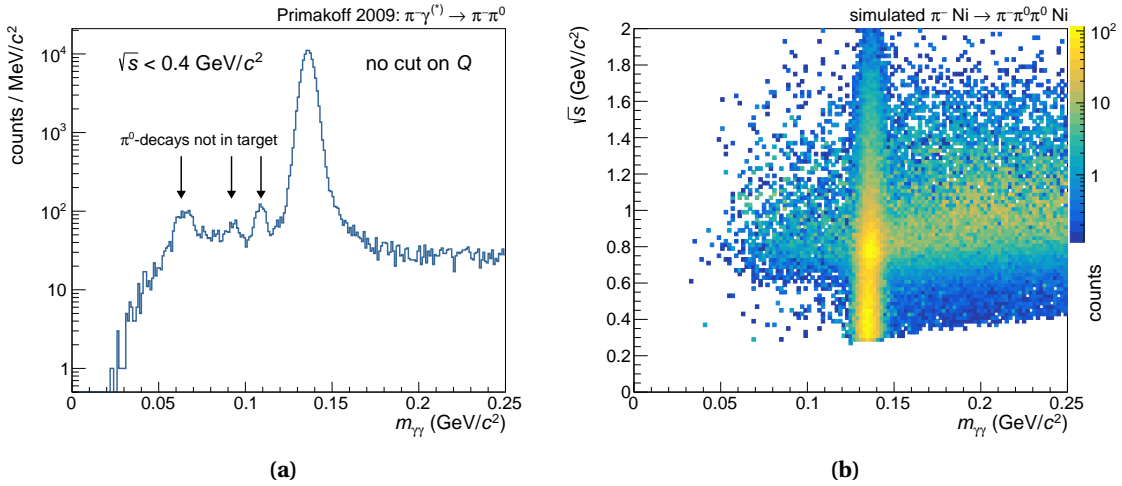


Fig. 8.5 In (a): Invariant mass of the two-photon system in $\pi^- \gamma^{(*)} \rightarrow \pi^- \pi^0$ events without cut on Q at small \sqrt{s} . Below the π^0 -peak, we observe structures that can be attributed to π^0 decays in material downstream in the spectrometer. In (b): the two-dimensional correlation between $m_{\gamma\gamma}$ and \sqrt{s} in simulated $\pi^- + \text{Ni} \rightarrow \pi^- \pi^0 \pi^0 + \text{Ni}$ events.

we expect a significant leakage from diffractive $\pi^- + \text{Ni} \rightarrow \pi^- \pi^0 \pi^0 + \text{Ni}$ events to the $\pi^- \gamma^{(*)} \rightarrow \pi^- \pi^0$ event sample. When one of the two π^0 s in the final state is very low-energetic, the event still passes exclusivity and q_T selection criteria.

To disentangle the leakage from Primakoff events, we make use of the fact, that the two processes have a different dependence on the momentum transfer Q . As shown in Fig. 6.6, we are dominated by resolution effects at low Q . The loss of one π^0 leads to another statistical effect on the Q distribution of diffractive $\pi^- \pi^0 \pi^0$ events leaking into $\pi^- \pi^0$ final state. Our approach is therefore to study the leakage with Monte-Carlo simulation.

8.2.1 Evaluation of the $\pi^- + \text{Ni} \rightarrow \pi^- \pi^0 \pi^0 + \text{Ni}$ model

It is essential to have a $\pi^- + \text{Ni} \rightarrow \pi^- \pi^0 \pi^0 + \text{Ni}$ pseudodata sample, which is correctly distributed in all relevant dimensions, to study the leakage from $\pi^- + \text{Ni} \rightarrow \pi^- \pi^0 \pi^0 + \text{Ni}$ events to $\pi^- \gamma^{(*)} \rightarrow \pi^- \pi^0$. A simple pseudodata set uniformly filling the three-pion phase space and neglecting the existing resonances will not lead to an accurate leakage prediction. The model needs to incorporate the largest contributions from a partial-wave analysis to accurately reproduce the observed angular and invariant mass distributions. In a partial-wave analysis, the experimentally observed distribution of intensity $\mathcal{I}(m_f, Q^2, \tau)$, which depends on m_f of the final state, the transferred momentum Q , and a set of independent kinematic variables τ is expanded in a basis of partial waves ψ_i , which also interfere. The intensity is described by the coherent sum:

$$\mathcal{I}(m_{3\pi}, Q^2, \tau) = \left| \sum_i \psi_i(m_{3\pi}, Q^2, \tau) \right| \quad (8.2)$$

For details about the partial-wave analysis method, cf. Ref. [59]. For a given three-particle final state the invariant mass m_f and five independent kinematic variables are needed to fully describe the reaction.

For the purpose of background prediction from the $\pi^- + \text{Ni} \rightarrow \pi^- \pi^0 \pi^0 + \text{Ni}$ sample into our $\pi^- \gamma^{(*)} \rightarrow \pi^- \pi^0$ event sample, the details of the single partial waves are of minor importance. What matters, is that the sample weighted according to the model reproduces the experimentally observed kinematic distributions with sufficient accuracy. In the following, we show the polar and azimuthal angle of the $\pi^- \pi^0$ subsystem in the Gottfried-Jackson frame and the angles of the π^- in the helicity frame. Together with the invariant masses $m_{\pi^- \pi^0 \pi^0}$ and $m_{\pi^- \pi^0}$ this uniquely defines the kinematics of the event.

We used the model developed in Ref. [63] as starting point. A refined event selection for the $\pi^- + \text{Ni} \rightarrow \pi^- \pi^0 \pi^0 + \text{Ni}$ final state (see Section 5.3.2), a corrected pseudodata set (see Chapter 6), and a more elaborate partial-wave set [131] lead to a more precise prediction of the expected three-pion leakage.

Dealing with large wave sets, a global fit, which accounts for all angular, mass, and Q^2 -dependencies at once, is technically impossible. Therefore, the analysis is commonly performed in bins of the momentum transfer Q . Our model for $\pi^- + \text{Ni} \rightarrow \pi^- \pi^0 \pi^0 + \text{Ni}$ events was developed in three different Q^2 -bins to account for waves, which contribute only in a limited Q^2 -range. The first bin ranges from 0 to $2 \cdot 10^{-3} \text{ GeV}^2/c^2$ covering the Primakoff region and enabling waves which describe photon exchange. These waves sit only at low Q due to their Weizsäcker-Williams dependence. The second bin covers the Q^2 -range up to the first diffractive minimum at $0.0126 \text{ GeV}^2/c^2$. The third bin covers the remaining range up to $1 \text{ GeV}^2/c^2$. One of the shortcomings of the current simulated sample is that we assumed the nickel mass for the recoil particle. But at high Q^2 , the probability of incoherent, quasi-elastic scattering, i.e. the scattering on single nucleons is non-negligible.

The presented model proved to be very robust against variations of the discussed binning, which is an indication for an appropriate selection of waves. A drawback in the presented model is that the correct Weizsäcker-Williams shape of the photon-exchange is not taken into

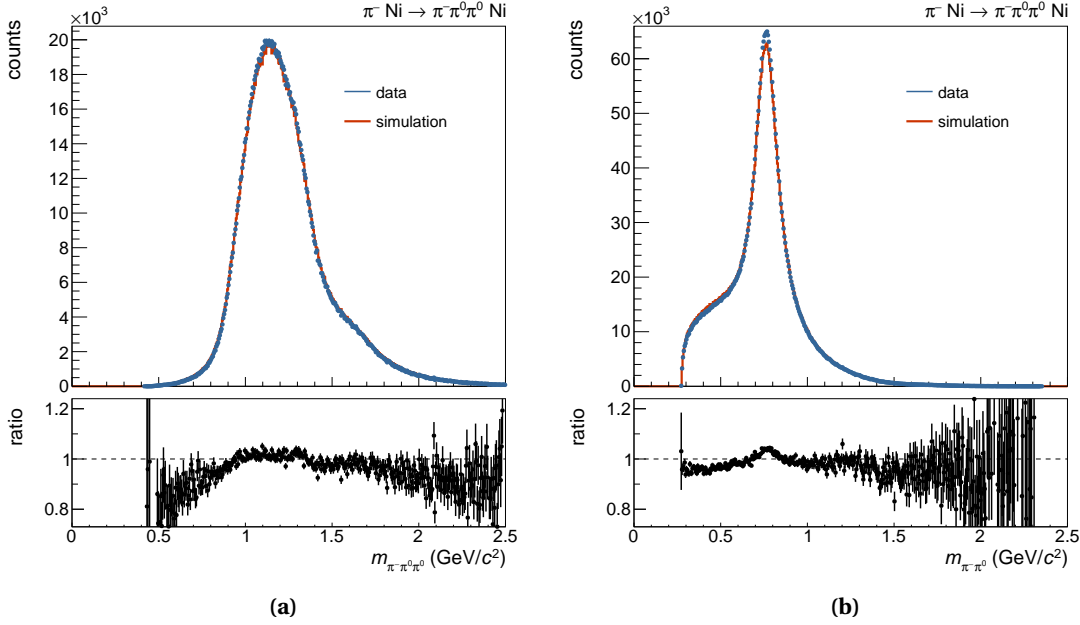


Fig. 8.6 Invariant mass of the final state (a) and of the $\pi^-\pi^0$ subsystem (b) in $\pi^- + \text{Ni} \rightarrow \pi^-\pi^0\pi^0 + \text{Ni}$ reactions (blue) compared to simulation (red). The spectrum in (a) is dominated by the $a_1(1260)$. Other resonances like the $a_2(1320)$ and the $\pi_2(1670)$ can be identified by eye. The spectrum of the $\pi^-\pi^0$ subsystem is dominated by the $\rho(770)$. The lower plots show the ratio data/simulation.

account. These events might have a higher probability to leak into $\pi^-\pi^0$ final state, since they appear already in the three-pion final state at low q_T . For a future publication, the explicit Q^2 -shape of the Coulomb interaction could be taken into account.

The presented model was developed by D. Ryabchikov [131]. It is based on the region of the phase space, to which we are experimentally sensitive. Using the angular information, it can be extrapolated to the corners of the phase space, in which the experiment has no acceptance. The minimal energy to reconstruct a photon of 2 GeV and the covered solid angle of ECAL2 impose experimentally a minimum energy for the π^0 in the laboratory frame. We can assume, that the model accurately describes this important corner for the specific case of leakage prediction into $\pi^-\gamma^{(*)} \rightarrow \pi^-\pi^0$ despite the low spectrometer acceptance in this corner.

To evaluate the model, we compare the pseudodata set with the 2009 Primakoff data. Fig. 8.6 shows the final state invariant mass in (a) and the invariant mass of the $\pi^-\pi^0$ subsystem in (b). The spectrum is dominated by a broad peak with its maximum at around $m_{3\pi} = 1.25 \text{ GeV}/c^2$. This corresponds to the $a_1(1260)$. The shoulder on the right side of this peak points to a contribution of the radiatively produced $a_2(1320)$. Going further to even higher masses, a small enhancement can be observed. The position of this enhancement is roughly at the mass of the $\pi_2(1670)$. Indeed, in the partial-wave analysis the contribution of these resonances have been confirmed, and they form the largest intensities. The $m_{\pi^-\pi^0}$ -spectrum is dominated by the $\rho(770)$.

The shapes around the prominent resonances are correctly reproduced by simulation. However, we see deviations between data and simulation up to 20% at small masses of $m_{\pi^-\pi^0}$.

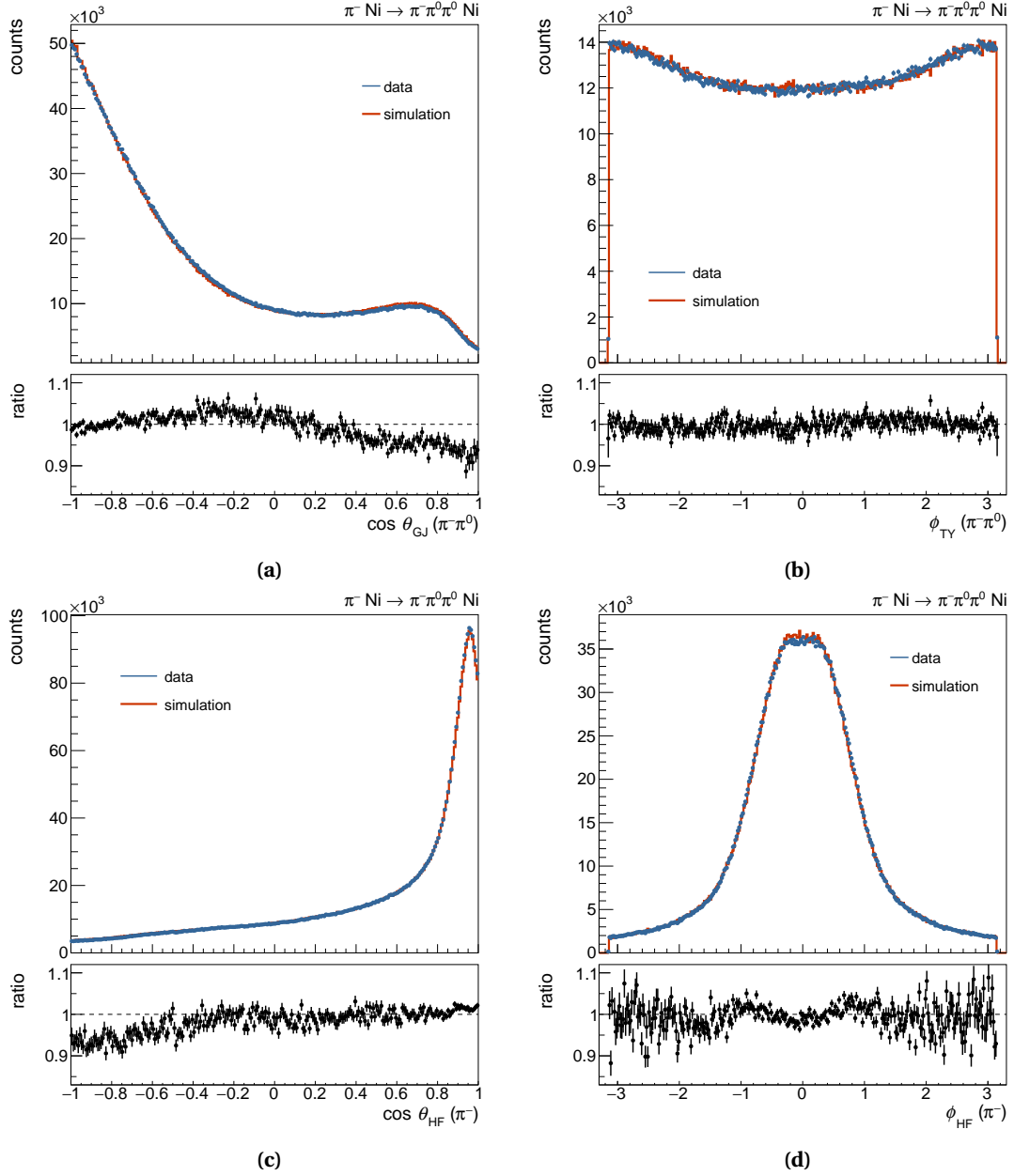


Fig. 8.7 Angular distributions in the Gottfried-Jackson frame (a and b) for the $\pi^- \pi^0$ subsystem and in the helicity frame (c and d) for the π^- in $\pi^- + \text{Ni} \rightarrow \pi^- \pi^0 \pi^0 + \text{Ni}$ reactions (blue) in comparison to simulation (red). The lower plots show the ratio data/simulation.

These deviations can in parts be attributed to $K_{3\pi}$ -decays, which appear at the kaon mass of $m_K \approx 500 \text{ MeV}/c^2$. But certainly, these deviations should be understood even better.

The differences express themselves also in angular distributions, which are shown in Fig. 8.7. Especially in the polar angle Figs. 8.7a and 8.7c, deviations between data and simulation become apparent. Despite room for improvement, the model shows satisfactory properties in regions where the bulk of events is located. Deviations from the experimental distributions

in the most populated regions of phase space are only on the 1%-level. The model is significantly improved compared to previous partial-wave analysis, e.g. in Ref. [63]. More kinematic distributions can be found in Appendix B.1.

8.2.2 Determination of the number of elastic Primakoff events

When applying the event selection of $\pi^- \gamma^{(*)} \rightarrow \pi^- \pi^0$ events for the $\pi^- + \text{Ni} \rightarrow \pi^- \pi^0 \pi^0 + \text{Ni}$ pseudodata sample, we receive the predicted shape of leakage of $\pi^- \pi^0 \pi^0$ -events into our $\pi^- \gamma^{(*)} \rightarrow \pi^- \pi^0$ event sample. Since we have correctly simulated the three-pion sample, we get the prediction in every kinematic variable. To disentangle signal and background, we look at the momentum transfer distribution, as it is show in Fig. 8.8. Indeed, the spectrum features a component peaking between 0.1 and 0.2 GeV/c which resembles the shape of the leakage prediction.

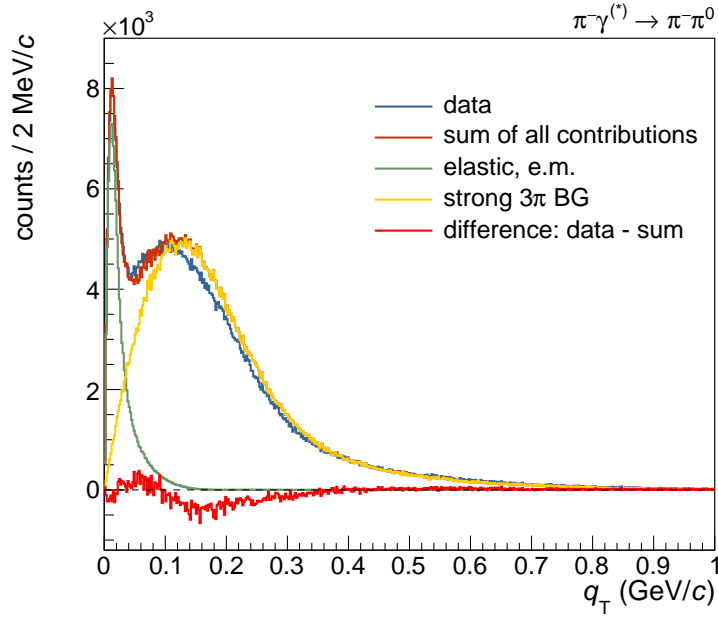
However, it becomes clear from Fig. 8.8a, that the spectrum cannot be described by only the two components. Inelastic scattering processes, in which the nucleus gets excited by photon exchange, are not only a possible explanation, but are even expected. When we include a contribution, in which we excite the nucleus in the giant dipole resonance and assume the Goldhaber-Teller model [132] for the corresponding form factor, we end up with the spectrum shown in Fig. 8.8b. The contribution of an E1, e.g. the giant dipole resonance, is shown in magenta. The sum of all contributions describes almost perfectly the observed spectrum. To sum it up: due to the quality of the $\pi^- + \text{Ni} \rightarrow \pi^- \pi^0 \pi^0 + \text{Ni}$ simulation, we can trust the predicted shape of the leakage and resolve an additional contribution, which in terms of intensity lies an order of magnitude below the other two contributions.

Additional information to determine the amount of signal events, comes from angular distributions. Fig. 8.9 applies the same relative intensity of each contribution as in Fig. 8.8b. The result matches well with the experimentally observed distribution. Small deviations at small polar angles $\cos \theta_{\text{GJ}}$ may hint to a slightly wrong acceptance in this corner of phase space. In ϕ_{TY} , we see excellent agreement, given that the acceptance and resolution effects of the three- and the two-pion final state plus the partial-wave model contribute in a non-trivial manner. Trusting the smeared $\sin^2 \phi_{\text{TY}}$ -dependence from simulation, we can estimate the number of signal events very precisely, as long as we assume that all other background is flat in ϕ_{TY} .

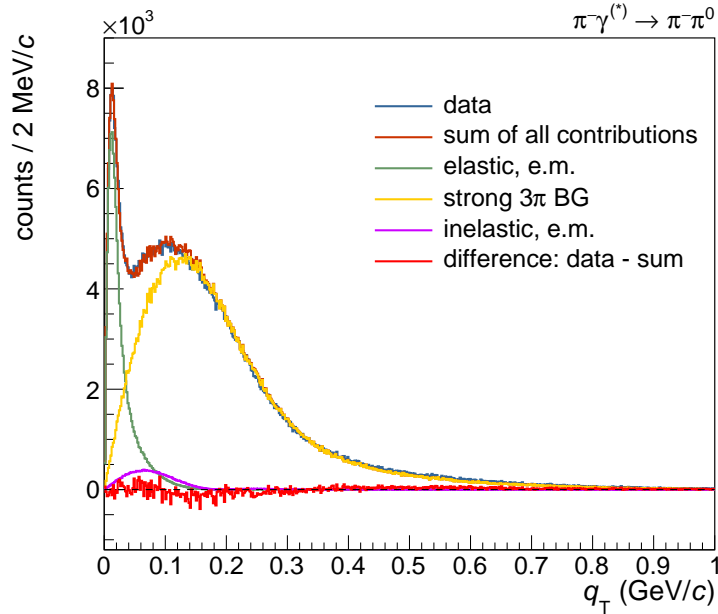
Another advantage of subtracting background based on ϕ_{TY} is that the signal shape can be parametrized. The signal shape is well described by

$$\sigma(\phi_{\text{TY}}) = A \cdot \left(1 + b \cdot \sin^2 \phi_{\text{TY}} + c \cdot \sin^2 \left(\frac{\phi_{\text{TY}}}{\pi} \right) \right) \quad (8.3)$$

with $b = 0.594 \pm 0.012$ and $c = 0.070 \pm 0.010$ determined from a fit to $\pi^- \gamma^{(*)} \rightarrow \pi^- \pi^0$ simulated pseudodata, as shown in Fig. 8.10a. Fig. 8.10b illustrates the high quality of the parametrization. We assume, that the parametrization does not depend on \sqrt{s} . In simulation, the ϕ_{TY} dependence was compatible with Eq. (8.3) over the whole tested range from $\sqrt{s} = 0.3 \text{ GeV}/c^2$ to $1.2 \text{ GeV}/c^2$.



(a)



(b)

Fig. 8.8 Description of the q_T -spectrum with different background components in the selected $\pi^-\gamma^{(*)} \rightarrow \pi^-\pi^0$ sample. The components were scaled to maximize the agreement with the observed spectrum. In (a): description of the spectrum with only two components, the leakage of $\pi^- + \text{Ni} \rightarrow \pi^-\pi^0\pi^0 + \text{Ni}$ determined from simulation and the elastic Coulomb scattering (signal). The bright red curve shows the difference between the sum of both components. Clearly, the observed distribution can not be described with only two components. In (b): a component stemming from inelastic scattering by exciting an E1, e.g. the giant dipole resonance of the nickel nucleus, is added. The fit describes the whole distribution nicely. The difference is compatible with zero.

8.2. BACKGROUND SUBTRACTION

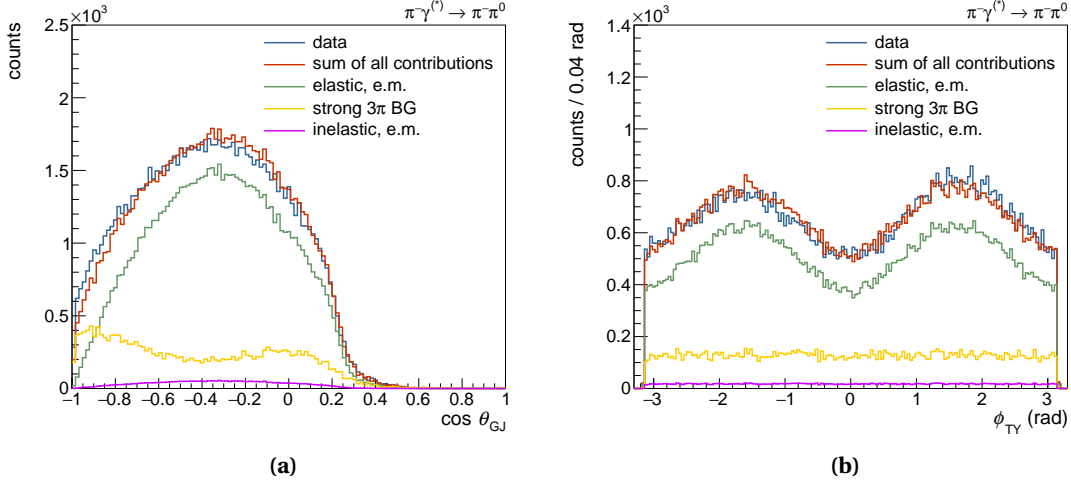


Fig. 8.9 Angular distributions of the reconstructed π^- in the Gottfried-Jackson frame for selected $\pi^- \gamma^{(*)} \rightarrow \pi^- \pi^0$ events. We took the same intensity for the different background contributions as in Fig. 8.8b. Note, that we applied $q_T < 36 \text{ MeV}/c$. We assumed a uniform dependence on ϕ_{TY} for inelastic electromagnetic contribution. If indeed caused by the giant dipole resonance, the additional degree of freedom of the oscillation will lead to a uniform contribution. For the polar angle of the inelastic contribution, we assumed the same dependence as for the elastic Coulomb scattering.

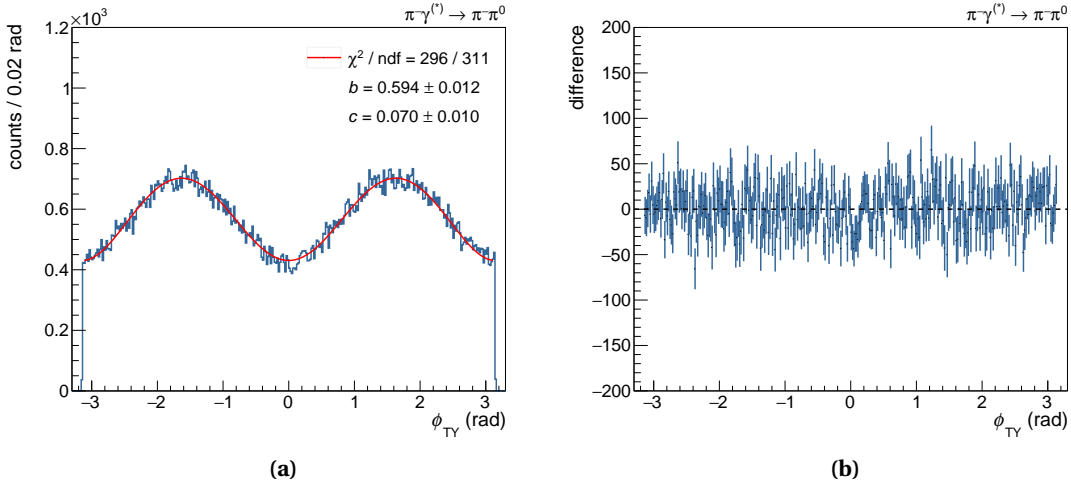


Fig. 8.10 Parametrization of the resolved ϕ_{TY} -dependence of the Primakoff signal. The distribution in (a) is obtained from simulation. The red curve shows a fit of the empirically obtained Eq. (8.3) to it. (b) shows the difference between the distribution and the fit. It is compatible with zero within the uncertainties. The parametrization is suited.

The parametrization allows us to determine the number of elastically scattered Primakoff events in small bins of \sqrt{s} . We choose a bin size of $20 \text{ MeV}/c^2$ according to the curvatures of the cross section and the available statistics. By a fit of the observed ϕ_{TY} -distribution in each \sqrt{s} -bin according to Eq. (8.3) added to a flat background contribution, we can determine the number of elastically scattered Primakoff events. Examples for selected fits in certain mass bins can be found in Appendix B.4. Fig. 8.11 shows the result of the corresponding fits in each mass bin.

The approach assumes all background to be flat in ϕ_{TY} . This is however not true at $\sqrt{s} \approx m_K = 500 \text{ MeV}/c^2$. We have seen in Section 8.1.1, that we have expected background from $K_{2\pi}$ -decays in this region. This background is not flat in ϕ_{TY} , as can be seen in Appendix B.2 in Fig. B.2h. We therefore can not trust the determined number of signal events at $\sqrt{s} \approx 500 \text{ MeV}/c^2$. The corresponding bins in Fig. 8.11 are indicated in red and will be neglected from now on.

As illustrated in Section 2.1.3, also ω - and π -exchange form potential background processes. As π -exchange is flat in ϕ_{TY} , it is correctly subtracted. ω -exchange however, features the same $\sin^2 \phi_{\text{TY}}$ -dependence as γ -exchange. An approach to disentangle ω -exchange from Primakoff processes is to exploit the characteristic Q -dependence. Fig. 8.8b illustrates however, that there is practically no additional significant contribution needed to describe the spectrum. This is an indication, that ω -exchange is negligible. A proper investigation of ω -exchange as background remains to be done.

8.3 Correcting for experimental acceptance

The acceptance of the experiment has to be determined from simulation. For $\pi^- \gamma^{(*)} \rightarrow \pi^- \pi^0$ events, the COMPASS spectrometer has an acceptance of $\sim 8\%$. Fig. 8.12 shows the acceptance as a function of the three independent variables describing our $\pi^- \gamma^{(*)} \rightarrow \pi^- \pi^0$ reaction. As expected, the acceptance does not show any dependence on ϕ_{TY} . Fig. 8.12b illustrates the limited experimental resolution for ϕ_{TY} at the small q_T -values. True $\tilde{\phi}_{\text{TY}}$ and reconstructed ϕ_{TY} are only weakly correlated. The \sin^2 -dependence appears to be very smeared. Experimentally, we observe the dependence of Eq. (8.3).

The acceptance in $\cos \theta_{\text{GJ}}$ is mainly driven by the trigger. A minimum energy deposit in the central region of ECAL2 means that the π^0 has to have a minimum energy in the lab frame. When the π^0 goes in backwards direction in the GJ-frame, i.e. high $\cos \theta_{\text{GJ}}$ for the π^- , it has too

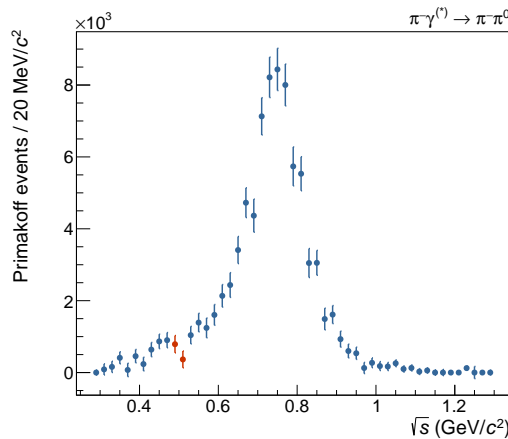


Fig. 8.11 Number of elastically scattered Primakoff events as determined from a fit to ϕ_{TY} . The points at $\sqrt{s} = m_K = 500 \text{ MeV}/c^2$ are drawn in red.

8.3. CORRECTING FOR EXPERIMENTAL ACCEPTANCE

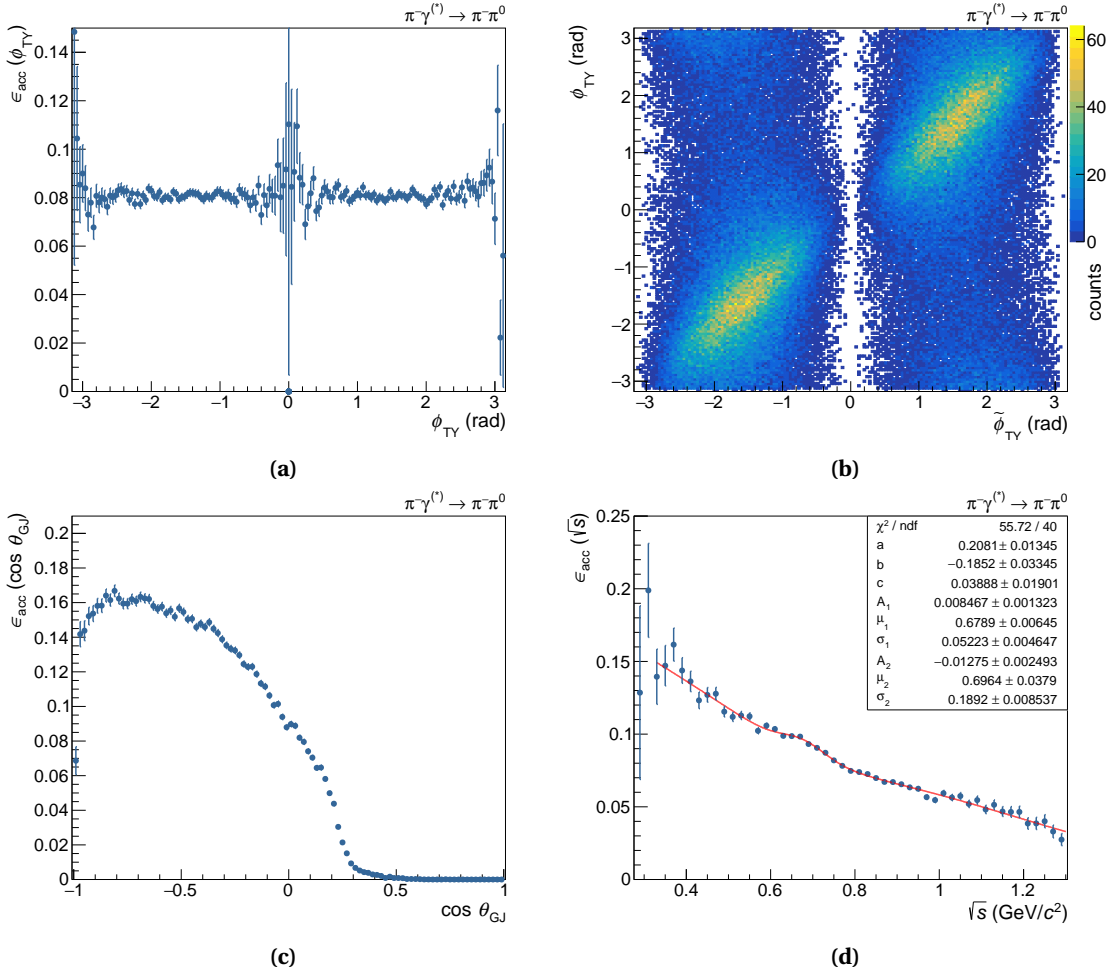


Fig. 8.12 Acceptances for $\pi^- \gamma^{(*)} \rightarrow \pi^- \pi^0$ events as a function of (a) ϕ_{TY} , (c) $\cos \theta_{\text{GJ}}$, and (d) \sqrt{s} . In (b): correlation plot between generated $\tilde{\phi}_{\text{TY}}$ and reconstructed ϕ_{TY} .

little energy when boosted into the lab frame to trigger the acquisition of the event. Hence, the acceptance drops for positive $\cos \theta_{\text{GJ}}$ of the π^- . At $\cos \theta_{\text{GJ}}(\pi^-) > 0.3$, the acceptance has practically reached zero.

Looking at Fig. 8.12d, we see that the acceptance also drops with increasing \sqrt{s} . This is a consequence of bigger angles between final state π^- and π^0 in the lab frame for higher \sqrt{s} . This in turn leads to a more peripheral illumination of the calorimeter. The central trigger part, is hit less often leading to a smaller acceptance.

To obtain an acceptance-corrected spectrum in \sqrt{s} and minimize effects of statistical fluctuations, we parametrized $\epsilon_{\text{acc}}(\sqrt{s})$. We account for the overall curvature by fitting a parabola to describe the large scale shape. The wiggles at $\sqrt{s} = m_\rho \approx 775 \text{ MeV}c^2$ are no statistical fluctuations but can be explained by bin-migration effects. From the peak of the ρ -resonance, events can end up slightly left and right of it due to resolution effects. This leads to an apparent high acceptance left and right of the peak and a dip at exactly m_ρ . To account for the wiggles,

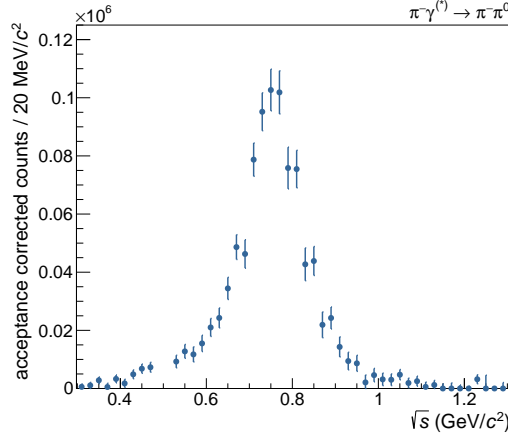


Fig. 8.13 Acceptance corrected number of Primakoff events.

we added two Gaussians to the polynomial of order two:

$$\epsilon_{\text{acc}}(\sqrt{s}) = ax^2 + bx + c + A_1 \cdot e^{\left(\frac{x-\mu_1}{\sigma_1}\right)^2} + A_2 \cdot e^{\left(\frac{x-\mu_2}{\sigma_2}\right)^2} \quad (8.4)$$

with the parameters $a, b, c, A_1, \mu_1, \sigma_1, A_2, \mu_2,$ and σ_2 as shown in Fig. 8.12d. Fig. 8.13 shows the number of Primakoff events corrected with Eq. (8.4).

8.4 Normalization to the photon flux

The Weizsäcker-Williams or equivalent-photon approximation of Eq. (2.23) factorizes the differential cross-section into two terms: one term describes the photon density $f(s, Q^2)$ around the nucleus as a function of s and Q^2 . The other term describes the actual interaction between a real photon and the beam pion $\sigma_{\pi\gamma \rightarrow \pi\pi}$. This cross-section can be expressed as function of s , when the integration over t (or $\cos \theta$ respectively) is carried out. The differential cross-section of Eq. (2.23) can then be written as

$$\frac{d\sigma^{\text{EPA}}}{ds dQ^2} = f(s, Q^2) \cdot \sigma_{\pi\gamma \rightarrow \pi\pi}(s) \quad (8.5)$$

with the photon flux factor

$$f(s, Q^2) = \frac{Z^2 \alpha}{\pi(s - m_\pi^2)} \cdot F^2(Q^2) \cdot \frac{Q^2 - Q_{\text{min}}^2(s)}{Q^4} \quad (8.6)$$

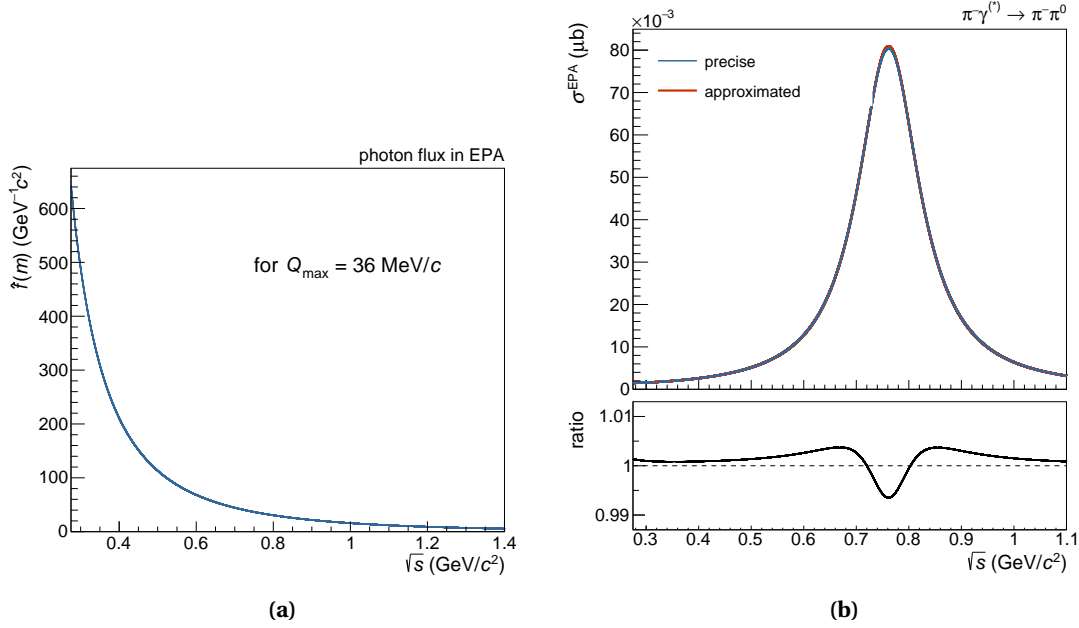


Fig. 8.14 In (a): photon flux according to Eq. (8.8) as a function of \sqrt{s} . In (b): comparison of precisely determined and approximated $\sigma^{\text{EPA}}(\sqrt{s})$ for Breit-Wigner distributions. The lower plot shows the ratio precise/approximated.

The total cross section in a $\sqrt{s} =: m'$ bin with the bin center at m and a width of Δm is hence given by

$$\begin{aligned}
 \sigma_{\Delta m}^{\text{EPA}}(m) &= \int_{\Delta m} 2m' \cdot \sigma_{\pi\gamma \rightarrow \pi\pi}(m') \int_{Q_{\min}^2(m')}^{Q_{\max}^2} f(m', Q^2) dQ^2 dm' \\
 &= \Delta m \cdot \sigma_{\pi\gamma \rightarrow \pi\pi}(m) \cdot 2m \int_{Q_{\min}^2(m)}^{Q_{\max}^2} f(m, Q^2) dQ^2 \\
 &= \Delta m \cdot \sigma_{\pi\gamma \rightarrow \pi\pi}(m) \cdot \hat{f}(m)
 \end{aligned} \tag{8.7}$$

with

$$\hat{f}(m) = 2m \cdot \int_{Q_{\min}^2(m)}^{Q_{\max}^2} f(m, Q^2) dQ^2 \tag{8.8}$$

being the Q -integrated flux factor. It is shown in Fig. 8.14a for our event selection, where we accepted events up to $Q_{\max} = 36 \text{ MeV}/c$. Due to its divergent term at $s = m_{\pi}^2$, it features a strong dependence on \sqrt{s} , and at the kinematic threshold of $s = 4m_{\pi}^2$, it still leads to large corrections.

We assumed for the calculation Eq. (8.7), that the bin width is small compared to the curvature in m' of $f(m', Q^2)$ and $\sigma_{\pi\gamma \rightarrow \pi\pi}(m')$. Instead of integrating, we can then evaluate the functions

in the bin center and multiply with the bin width. The approximation is good for bin widths of $\Delta m \sim 20 \text{ MeV}/c^2$. The error introduced by the approximation is largest at the point with highest curvature, i.e. at the peak of the ρ -resonance. For $\Delta m = 20 \text{ MeV}/c^2$ it is still around 0.5% as can be seen in Fig. 8.14b. To be able to show measurements of $\sigma_{\pi\gamma \rightarrow \pi\pi}(s)$, one should correct for the difference. But the correction is small compared the statistical uncertainties introduced by the measurement. In the following, we neglect these corrections.

8.5 Fitting the dispersive model

Having corrected for the photon flux, we can convert the number of events to a cross section using the value for the luminosity of Eq. (7.20). The result can be seen in Fig. 8.15. As discussed in details in Section 2.4.2, we can fit the dispersive model of Eq. (2.75) to the measured cross section data. First, we notice, that the χ^2 -fit is able to describe the shape very well. The reduced is $\chi^2/\text{ndf} = 0.88$. This hints to a consistent treatment of statistical uncertainties on single data points.

The fit yields values for the two subtraction constants $C_2^{(1)}$ and $C_2^{(2)}$ as given in Fig. 8.15. Using Eq. (2.80), we can calculate a value for $F_{3\pi}$ from the two subtraction constants. Similarly, we use Eqs. (2.81) to (2.85) to extract a value for the radiative width of the $\rho(770)$:

$$\begin{aligned} F_{3\pi} &= (8.58 \pm 0.18) \text{ GeV}^{-3} \\ \Gamma_{\rho \rightarrow \pi\gamma} &= (65.6 \pm 1.0) \text{ keV} \end{aligned} \tag{8.9}$$

where the given uncertainties are purely statistical.

For an estimate on the systematic uncertainties stemming from the luminosity measurement, we vary the luminosity within its systematic uncertainties ($\pm 6\%$) and extract a value for $F_{3\pi}$ and $\Gamma_{\rho \rightarrow \pi\gamma}$. For decreased luminosity, we obtain $F_{3\pi} = 8.83 \text{ GeV}^{-3}$ and $\Gamma_{\rho \rightarrow \pi\gamma} = 69.6 \text{ keV}$. For increased luminosity, we obtain $F_{3\pi} = 8.31 \text{ GeV}^{-3}$ and $\Gamma_{\rho \rightarrow \pi\gamma} = 61.7 \text{ keV}$. This leads to:

$$\begin{aligned} F_{3\pi} &= \left(8.58 (\pm 0.18)_{\text{stat}} \left(\begin{smallmatrix} +0.25 \\ -0.27 \end{smallmatrix} \right)_{\text{syst,lumi}} \right) \text{ GeV}^{-3} \\ \Gamma_{\rho \rightarrow \pi\gamma} &= \left(65.6 (\pm 1.0)_{\text{stat}} \left(\begin{smallmatrix} +4.0 \\ -3.9 \end{smallmatrix} \right)_{\text{syst,lumi}} \right) \text{ keV} \end{aligned} \tag{8.10}$$

The result is dominated by systematic uncertainties, considering only systematic uncertainties of the luminosity determination. We chose a very conservative approach resulting in, most probably, overestimating these systematics. We have not exploited the fact, that the systematic uncertainties of the $K_{2\pi}$ -decay are similar to our measured $\pi^- \gamma^{(*)} \rightarrow \pi^- \pi^0$ channel. Careful variations of all important parameters in the event selection and in the simulation, may lead to a more realistic estimate.

A proper discussion of additional systematic effects will follow in Chapter 9.

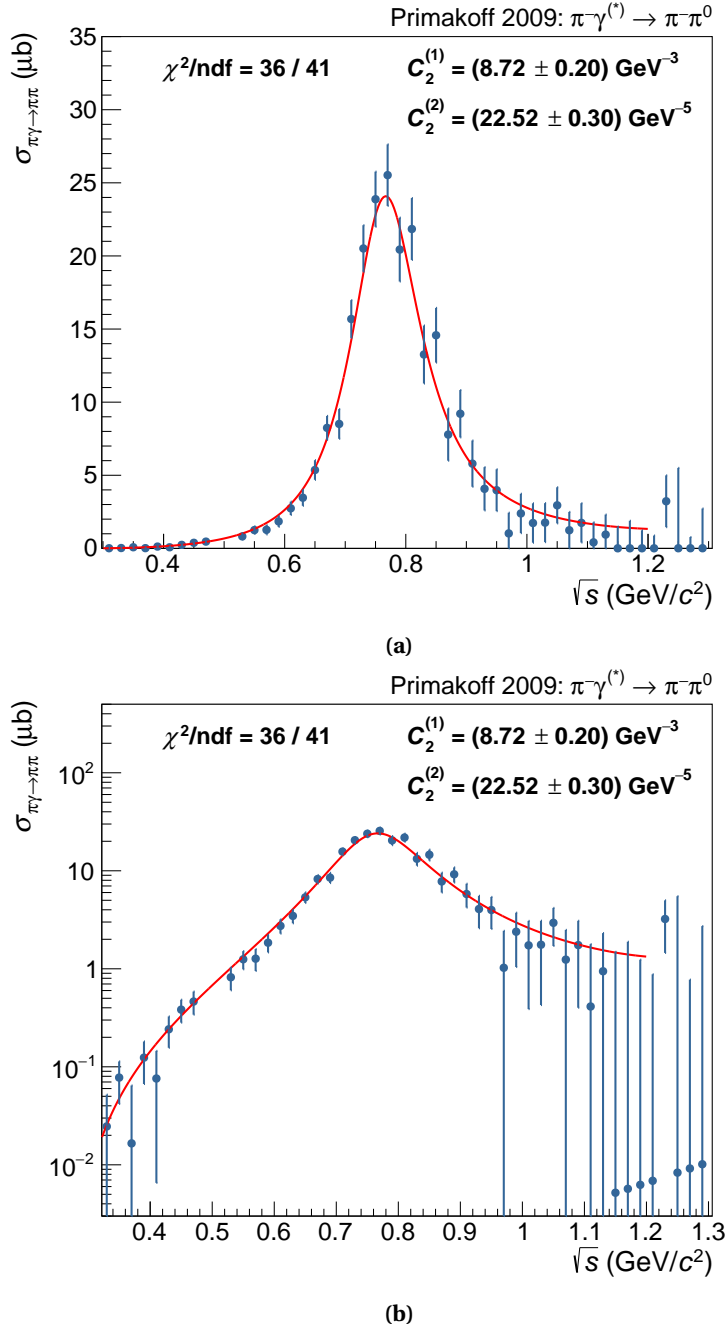


Fig. 8.15 Fit of the dispersive model to the measured cross section $\sigma_{\pi\gamma \rightarrow \pi\pi}$ in (a) linear and (b) logarithmic scale.

8.6 Summary and open issues

The analysis presented in Chapters 5 to 8 consists of many steps. During the journey, we mentioned shortcomings and potential improvements, which could help to improve the accuracy of the result. We will shortly summarize, where room for improvement still exists and compile a list of issues, which need to be addressed.

- The Q -dependence of the simulated $\pi^- + \text{Ni} \rightarrow \pi^- \pi^0 \pi^0 + \text{Ni}$ events deviates from the experimentally observed one, as can be seen in Fig. 6.7. Resampling from the existing pseudodata sample, might be a relatively simple approach to get a better description without regenerating the simulated events.
- A general problem of the leakage prediction of $\pi^- + \text{Ni} \rightarrow \pi^- \pi^0 \pi^0 + \text{Ni}$ events into the $\pi^- \gamma^{(*)} \rightarrow \pi^- \pi^0$ sample is the incorrect Q -dependence of Coulomb interaction. In the partial-wave analysis, the chiral wave accounts for photon exchange. However, in the 3π pseudodata set, these events have the shallow diffractive Q -dependence and thus the probability to leak into very small q_t for these events might be underestimated. Common partial-wave analysis are performed in bins of Q^2 and do not allow for individual Q -dependencies of different waves. However, a relatively simple approach would be to use a simulated Weizsäcker-Williams $\pi^- \pi^0 \pi^0$ sample weighted with the intensity of the chiral wave predicted by ordinary partial-wave analysis.
- The presented acceptance correction in Section 8.3 disregards statistical and systematic effects introduced by the correction. Bootstrapping approaches provide a robust possibility to quantify statistical uncertainties.
- In Section 8.4, we use an approximation in order to show and fit $\sigma_{\pi\gamma \rightarrow \pi\pi}$ directly instead of σ^{EPA} . It is beneficial to publish $\sigma_{\pi\gamma \rightarrow \pi\pi}$, because it is the quantity, which is usually predicted by theory. Corrections, which arise due to the approximation need to be addressed.

Chapter 9

Discussion of the result and outlook

The result of Eq. (8.10) is in terms of the statistical uncertainty in disagreement with the theory prediction of Eq. (1.33) by 6.7σ . In this chapter, we will explain, where this discrepancy may come from and give a proper estimate on the systematic uncertainty. The latter is currently dominated by the background model. We will explain the differences in the analysis to previous published values, elaborate on the most probable reason for the discrepancy, and use it to estimate the current state of the systematic uncertainty. The COMPASS Primakoff data set has more physics to offer than only the presented analysis on $F_{3\pi}$ and $\Gamma_{\rho \rightarrow \pi\gamma}$. We will conclude with an outlook, what other physics hides in the COMPASS Primakoff data set.

9.1 Comparison to previous results and systematic uncertainties

The COMPASS collaboration has already released [108] and published results of this analysis in Refs. [133, 134, 135]. Primed variables will denote these previously published values. The values were obtained by fitting the dispersive model to a \sqrt{s} -spectrum with much coarser binning, see Fig. 9.1. The published values, based on this fit, are:

$$\begin{aligned} F'_{3\pi} &= (10.3(\pm 0.1)_{\text{stat}}(\pm 0.6)_{\text{syst}}) \text{ GeV}^{-3} \\ \Gamma'_{\rho \rightarrow \pi\gamma} &= (76(\pm 1)_{\text{stat}}(\overset{+10}{-8})_{\text{syst}}) \text{ keV} \end{aligned} \quad (9.1)$$

They disagree with Eq. (8.10), but are in agreement with the theory prediction. In trying to find and explain the origin of the big discrepancy to the values presented in this thesis, we notice that already the luminosity is assumed differently:

$$\hat{L}'_{\text{eff}} = (5.21(\pm 0.04)_{\text{stat}}(\pm 0.48)_{\text{syst}}) \text{ nb}^{-1} \quad (9.2)$$

Similar to the presented analysis, we used $K_{2\pi}$ and $K_{3\pi}$ -decays to determine the luminosity. However, CEDAR efficiencies were previously not considered. Taking the efficiencies into account, leads to a factor $\frac{\epsilon_{\pi}}{\epsilon_K} \approx 1.13$, such that the values for the effective, integrated luminosity agree within 0.2σ :

$$\hat{L}_{\text{eff}} = (5.87 \pm 0.09) \text{ nb}^{-1} = 0.2\sigma \cdot \frac{\epsilon_{\pi}}{\epsilon_K} \hat{L}'_{\text{eff}} \quad (9.3)$$

The remaining very small difference can be attributed to statistical fluctuations due to differences in the event selection.

The wrong luminosity impacts directly the obtained results for $F'_{3\pi}$ and $\Gamma'_{\rho \rightarrow \pi\gamma}$. Applying the updated luminosity values and redoing the fit, as shown in Fig. 9.1b, yields:

$$\begin{aligned} F'_{3\pi} &= (9.6(\pm 0.1)_{\text{stat}}(\pm 0.6)_{\text{syst}}) \text{ GeV}^{-3} \\ \Gamma'_{\rho \rightarrow \pi\gamma} &= (66(\pm 1)_{\text{stat}}(\overset{+9}{-7})_{\text{syst}}) \text{ keV} \end{aligned} \quad (9.4)$$

While $\Gamma'_{\rho \rightarrow \pi\gamma}$ is now significantly lower and agrees within the uncertainty to the value presented in this analysis, we still observe a discrepancy in the values of $F_{3\pi}$.

$F_{3\pi}$ is very sensitive to the shape of the distribution particularly at the kinematic threshold. We may hence suspect the origin of the discrepancy in e.g. a wrong background subtraction, since this can impact the shape significantly. Indeed, the main difference in the two analysis is the way how background was subtracted. Instead of determining the number of Primakoff events from ϕ_{TY} , we previously looked at Q^2 -distributions in bins of \sqrt{s} as shown in Fig. 9.2.

Determining the number of Primakoff events from ϕ_{TY} , we assumed that the shape does not depend on \sqrt{s} . This assumption might be not exactly fulfilled. Since we obtained the parametrization of the shape integrated over \sqrt{s} , it is mainly determined by events at $\sqrt{s} = m_\rho$, where most of the events are located. We can hence assume, that underneath the ρ -peak, we subtracted background correctly. As a consequence, $\Gamma_{\rho \rightarrow \pi\gamma}$ and $\Gamma'_{\rho \rightarrow \pi\gamma}$ agree. Further away from the peak, closer to the threshold, our assumed shape of the signal in ϕ_{TY} might be less adequate. We underestimate the number of Primakoff events, leading to a smaller $F_{3\pi}$.

Estimating the number of Primakoff events from Q^2 -distributions comes also with disadvantages: The systematic uncertainties, which are introduced by choosing the fit range arbitrarily,

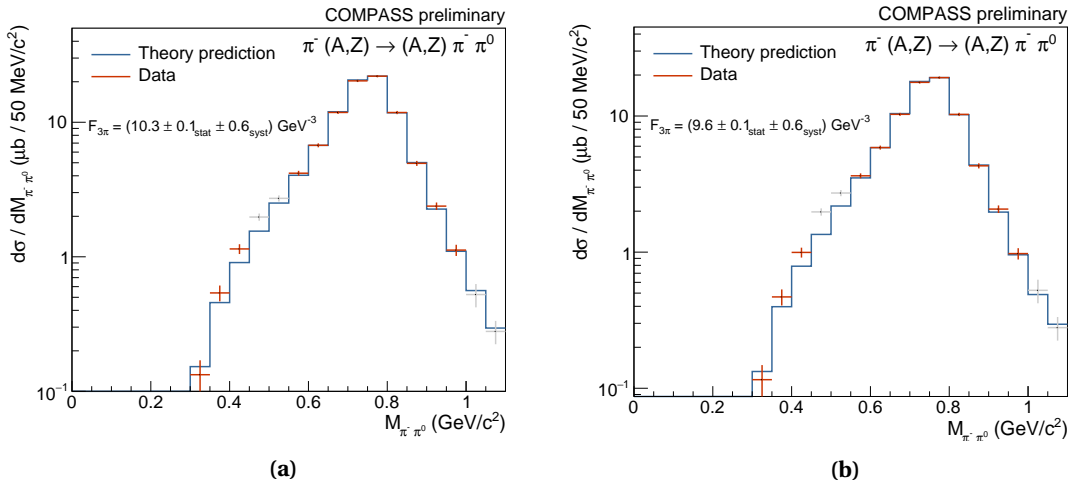


Fig. 9.1 Background subtracted and acceptance corrected number of events, multiplied with the effective, integrated luminosity. The values are not normalized to the photon flux, nor corrected to the bin size. Data is shown in red, the fit in blue. (a) was published in Ref. [133] and shows the obtained values with a luminosity of $\hat{L}_{\text{eff}} = 5.21 \text{ keV}$. For (b), we applied a different luminosity of $\hat{L}_{\text{eff}} = 5.87 \text{ keV}$ taking into account CEDAR efficiencies.

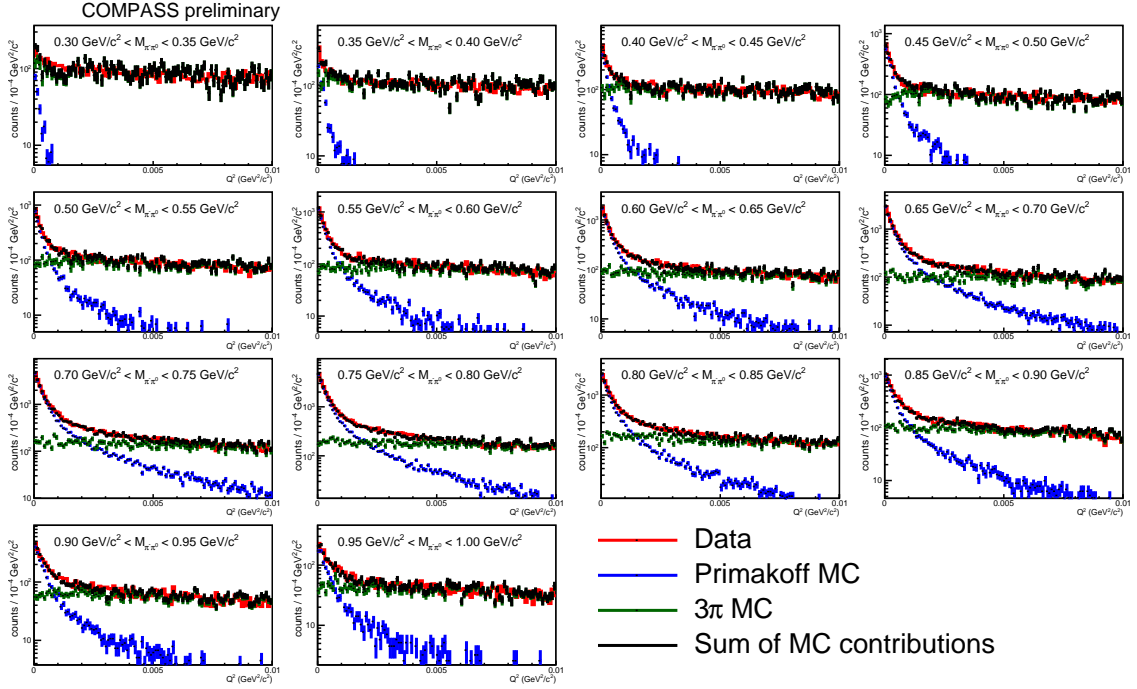


Fig. 9.2 Fitting the observed Q^2 -distributions (red) in \sqrt{s} -bins with the sum (black) of Primakoff (blue) and 3π background (green). The shapes of the contributions were obtained from Monte-Carlo simulation (MC). (Published in Ref. [133])

as it was done with $Q_{\max} = 0.01 \text{ GeV}^2/c^2$ in Fig. 9.2, are large and not correctly reflected in Eq. (9.4). Especially close to the kinematic threshold, additional background contributions e.g. from inelastic scattering events, in which the nucleus gets excited, might contribute and decrease the number of Primakoff events. It was shown in Fig. 8.8, that such contributions are necessary to properly describe the observed Q^2 -shape.

All in all, the two different approaches provide a possibility to estimate the present systematic uncertainties due to background subtraction. Following the approach of Eq. (7.19), we get for the systematic uncertainty $s_{F_{3\pi}}$ on $F_{3\pi}$

$$s_{F_{3\pi}} = \sqrt{\frac{1}{2} \left((F_{3\pi} - F'_{3\pi})^2 - (\sigma^2 + \sigma'^2) \right) + s_{\text{lumi}}^2} = 1.21 \text{ GeV}^{-3} \quad (9.5)$$

and for the final result, we take the weighted average:

$$F_{3\pi} = (9.24 (\pm 0.21)_{\text{stat}} (\pm 0.83)_{\text{sys}}) \text{ GeV}^{-3} \quad (9.6)$$

where we have quadratically added the systematic uncertainty of Eq. (8.10) to the one of Eq. (9.5).

The large magnitude of the systematic uncertainty illustrates the need for a still better background model. Ideas of additional contributions like quasi-elastic scattering on the nucleus, ω - or π -exchange exist and need to be implemented and tested. Another approach is to study in detail the $\phi_{\text{T}Y}$ -dependence of the signal contribution in simulation. An increased $\pi^- \gamma^{(*)} \rightarrow$

$\pi^-\pi^0$ pseudodata set will give more information. Assuming that other background is flat in ϕ_{TY} , this will facilitate a background subtraction without separation of single contributions.

9.2 Conclusion and outlook

The result presented in this thesis is not yet final. Despite its preliminary character, we have illustrated the potential of the analysis to extract a value for $F_{3\pi}$ with an uncertainty $< 4\%$. Statistical uncertainties are already on a 2% level. As many other high-precision measurements, we are limited by systematic uncertainties. Two main contributions to the systematic uncertainty have been identified in this thesis: the uncertainty on the luminosity value and the uncertainty due to background subtraction.

To reduce uncertainties on the luminosity, two approaches seem feasible. The preferred approach is to correct material description and calorimeter resolution in simulation in order to get the two values from $K_{2\pi}$ and $K_{3\pi}$ decays into agreement or at least reduce the discrepancy. The second approach is to quantify to which extent systematic effects in $K_{2\pi}$ decays cancel due to their similarity to effects in $\pi^-\gamma^{(*)} \rightarrow \pi^-\pi^0$ events.

The situation on the background model is currently less clear. A robust and well-understood model is necessary to reliably determine the number of Primakoff events. Ideas on additional background contributions stemming from inelastic scattering on target nuclei, e.g. exciting the giant dipole resonance, have been introduced and, to some extent, formalized in Section 2.2.3. Due to the described improvements in the quality of simulated data, and the achieved agreement between simulation and data, we are now capable of disentangling different contributions. Especially the reanalysis of $\pi^- + \text{Ni} \rightarrow \pi^-\pi^0\pi^0 + \text{Ni}$ data and producing better pseudodata with proper shapes in Q , will help to determine the background model. However, this work has just started.

9.3 Radiative width of the $\rho_3(1690)$

The COMPASS Primakoff data set offers a wealth of interesting physics to discover. A signal, which already became apparent in Section 5.3.2, is the peak at $m_{\pi\pi} = 1.7 \text{ GeV} \cdot c^2$. In Ref. [46], a first partial-wave analysis indicated an f -wave nature of the peak. The only known spin $J = 3$ particle in this mass range is the $\rho_3(1690)$. Since the peak is visible at low Q (the Primakoff even selection was applied in Fig. 9.3) and vanishes at higher Q , it is very likely that the signal is produced via photon exchange indicating a non-vanishing radiative coupling of the ρ_3 -resonance.

The amount of data in the Primakoff 2009 data set in this mass region is sparse, as can be seen in Fig. 9.3a, and may be a limiting factor on the precision of a measurement of the radiative coupling of the ρ_3 . COMPASS has recorded another set of Primakoff data in 2012. Within the context of this thesis, we performed an event selection on the 2012 data set in Refs. [107, 136] and confirmed a roughly four-times higher number of recorded Primakoff events.

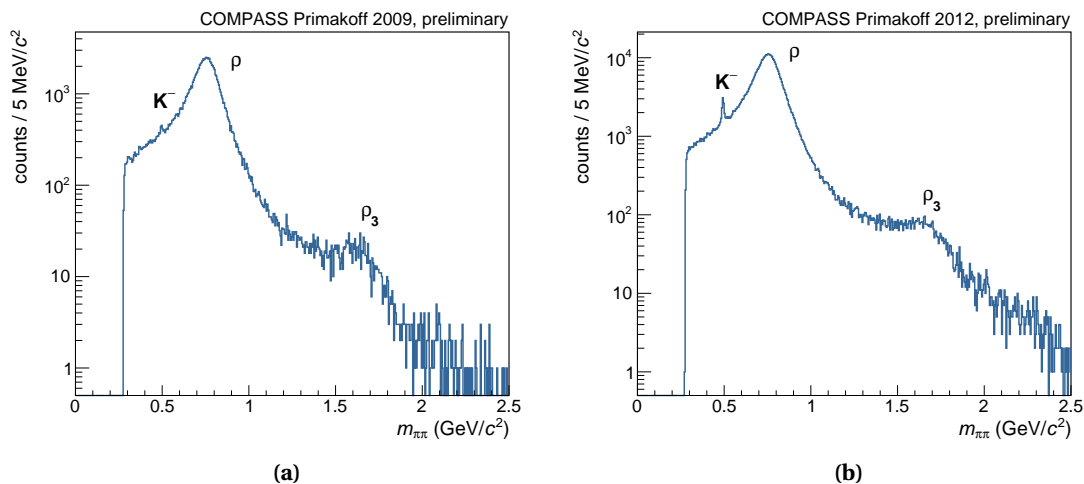


Fig. 9.3 Invariant mass distribution of the final state for selected $\pi^- \gamma^{(*)} \rightarrow \pi^- \pi^0$ events in the (a) 2009 and (b) 2012 Primakoff data set.

To use the 2012 data, development of a high-quality Monte-Carlo simulation is necessary. In particular the calorimeter simulation of the current simulation framework is qualitatively insufficient. Ongoing efforts to improve the TGeant [121] framework show promising improvements and might soon lead to equally good simulation results.

9.4 Analysis of $\pi^- \gamma^{(*)} \rightarrow \pi^- \pi^0 \pi^0$ cross section

The cross section for chiral production via Coulomb interaction of the three-pion final state shows a \sqrt{s} -dependence, which is predicted by low-energy theorems. ChPT adds higher-order corrections to the tree-level prediction. These corrections contribute less in the charged-

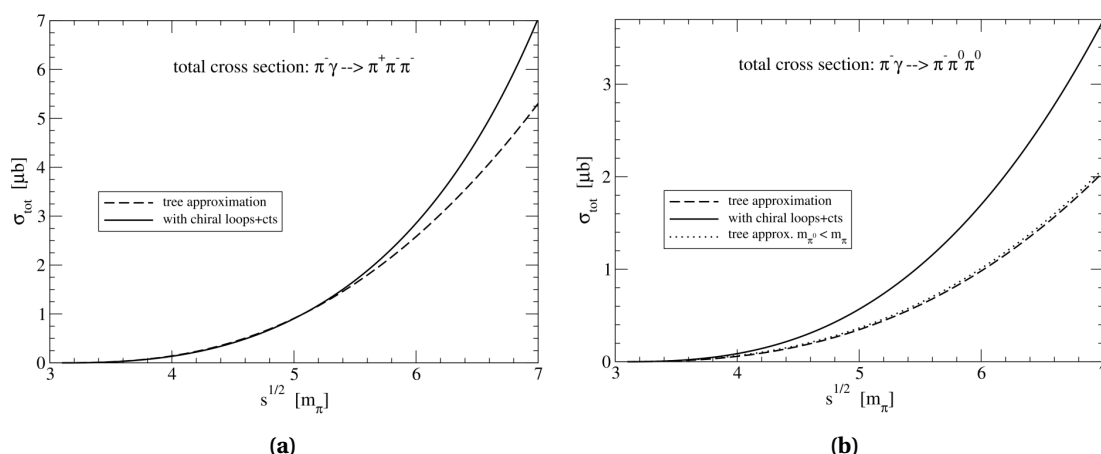


Fig. 9.4 ChPT prediction of the total cross section for (a) $\pi\gamma \rightarrow \pi^- \pi^+ \pi^-$ and (b) $\pi\gamma \rightarrow \pi^- \pi^0 \pi^0$ events. The leading order (dashed) and next-to-leading order (solid) calculations are shown. The dotted line shows isospin breaking effects. Taken from Ref. [67].

pion final states than they do in the $\pi^- \pi^0 \pi^0$ final state, as can be seen in Fig. 9.4. For this reason the $\pi^- \gamma \rightarrow \pi^- \pi^0 \pi^0$ cross section provides a unique opportunity to verify, that low-energy dynamic of QCD is correctly described by ChPT.

For the accurate description of background from $\pi^- + \text{Ni} \rightarrow \pi^- \pi^0 \pi^0 + \text{Ni}$ to $\pi^- \gamma^{(*)} \rightarrow \pi^- \pi^0$ events, we developed a partial-wave model of the $\pi^- \pi^- \pi^0$ final state in $\Delta\sqrt{s} = 40 \text{ MeV}/c^2$ mass bins. The model includes the chiral wave. A measurement of the $\pi^- \gamma^{(*)} \rightarrow \pi^- \pi^0 \pi^0$ cross section requires only converting the intensity of the chiral wave in each \sqrt{s} -bin to a cross section. Given the sufficient precision of the measurement, COMPASS can contribute to a validation of ChPT and improve values for the six LECs, which appear in these higher-order calculations.

Appendix A

Equations, transformations, and conventions

A.1 Gell-Mann matrices

The standard form of the Gell-Mann $SU(3)$ matrices representing flavor or color degrees of freedom:

$$\begin{aligned}\lambda_1 &= \begin{pmatrix} 0 & 1 & 0 \\ 1 & 0 & 0 \\ 0 & 0 & 0 \end{pmatrix}, & \lambda_2 &= \begin{pmatrix} 0 & -i & 0 \\ i & 0 & 0 \\ 0 & 0 & 0 \end{pmatrix}, \\ \lambda_3 &= \begin{pmatrix} 1 & 0 & 0 \\ 0 & -1 & 0 \\ 0 & 0 & 0 \end{pmatrix}, & \lambda_4 &= \begin{pmatrix} 0 & 0 & 1 \\ 0 & 0 & 0 \\ 1 & 0 & 0 \end{pmatrix}, \\ \lambda_5 &= \begin{pmatrix} 0 & 0 & -i \\ 0 & 0 & 0 \\ i & 0 & 0 \end{pmatrix}, & \lambda_6 &= \begin{pmatrix} 0 & 0 & 0 \\ 0 & 0 & 1 \\ 0 & 1 & 0 \end{pmatrix}, \\ \lambda_7 &= \begin{pmatrix} 0 & 0 & 0 \\ 0 & 0 & -i \\ 0 & i & 0 \end{pmatrix}, & \lambda_8 &= \frac{1}{\sqrt{3}} \begin{pmatrix} 1 & 0 & 0 \\ 0 & 1 & 0 \\ 0 & 0 & -2 \end{pmatrix}\end{aligned}\tag{A.1}$$

They satisfy the commutation relation $[\lambda_a, \lambda_b] = i \sum_{c=1}^{N_c^2-1} f_{abc} \lambda^c$ with the totally antisymmetric $SU(3)$ structure constant f_{abc} .

A.2 Dirac matrices

Here, the standard representation of the Dirac matrices is given:

$$\gamma^\mu = (\gamma^0, \vec{\gamma}) \quad \gamma^0 = \gamma_0 = \begin{pmatrix} \mathbb{1} & 0 \\ 0 & -\mathbb{1} \end{pmatrix} \quad \vec{\gamma} = \begin{pmatrix} 0 & \vec{\sigma} \\ -\vec{\sigma} & 0 \end{pmatrix} \quad (\text{A.2})$$

with the 2×2 unit matrix $\mathbb{1}$ and the Pauli spin matrices

$$\vec{\sigma} = (\sigma_x, \sigma_y, \sigma_z), \quad (\text{A.3})$$

$$\sigma_x = \begin{pmatrix} 0 & 1 \\ 1 & 0 \end{pmatrix}, \quad \sigma_y = \begin{pmatrix} 0 & -i \\ i & 0 \end{pmatrix}, \quad \sigma_z = \begin{pmatrix} 1 & 0 \\ 0 & -1 \end{pmatrix}$$

The Dirac matrices satisfy the anticommutator relation $\{\gamma^\mu, \gamma^\nu\} = 2g^{\mu\nu}$ with the metric tensor

$$g^{\mu\nu} = \begin{pmatrix} 1 & 0 & 0 & 0 \\ 0 & -1 & 0 & 0 \\ 0 & 0 & -1 & 0 \\ 0 & 0 & 0 & -1 \end{pmatrix} \quad (\text{A.4})$$

One important combination of γ matrices is

$$\gamma^5 = i\gamma^0\gamma^1\gamma^2\gamma^3 = \gamma_5 = \begin{pmatrix} 0 & \mathbb{1} \\ \mathbb{1} & 0 \end{pmatrix} \quad (\text{A.5})$$

A.3 Lorentz transformation of the electromagnetic field of a point charge

This section is a summary of the corresponding paragraphs of Ref. [66] and we will therefore follow the notation and conventions used there. For a general Lorentz transformation from a system K to a system K' moving with velocity \vec{v} relative to K , the transformation of an electromagnetic field can be written

$$\vec{E}' = \gamma(\vec{E} + \vec{\beta} \times \vec{B}) - \frac{\gamma^2}{\gamma+1} \vec{\beta}(\vec{\beta} \cdot \vec{E}) \quad (\text{A.6})$$

$$\vec{B}' = \gamma(\vec{B} - \vec{\beta} \times \vec{E}) - \frac{\gamma^2}{\gamma+1} \vec{\beta}(\vec{\beta} \cdot \vec{B})$$

with $\vec{\beta} = \frac{\vec{v}}{c}$ and $\gamma = \frac{1}{\sqrt{1-\beta^2}}$ being the Lorentz factor.

For the specific Lorentz transformation for a boost along the x_1 -axis with speed $c\beta$ from the unprimed to the primed system, the explicit equations of the field according to Eq. (A.6) are:

$$\begin{aligned} E'_1 &= E_1 & B'_1 &= B_1 \\ E'_2 &= \gamma(E_2 - \beta B_3) & B'_2 &= \gamma(B_2 - \beta E_3) \\ E'_3 &= \gamma(E_3 - \beta B_2) & B'_3 &= \gamma(B_3 - \beta E_2) \end{aligned} \quad (\text{A.7})$$

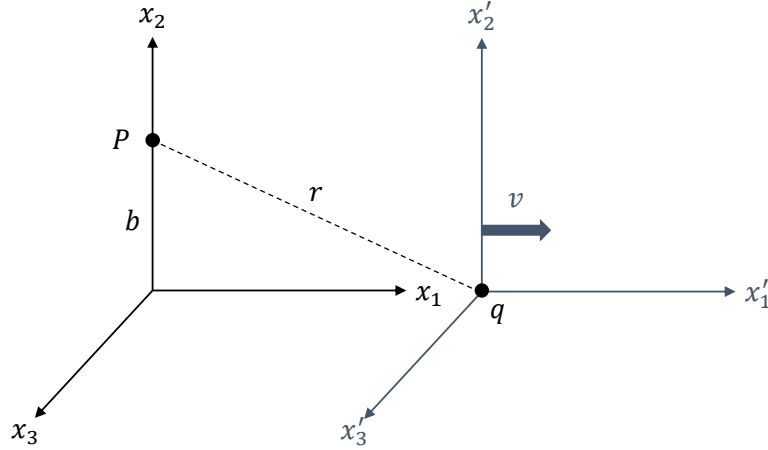


Fig. A.1 Particle of charge q moving at constant velocity \vec{v} passes an observation point P at impact parameter b . The observer is at rest in system K and the charge is at rest in system K' .

with the subscripts 1, 2, and 3 indicating ordinary Cartesian spatial components.

To illustrate, how the electromagnetic field of an ultra-relativistic charged particle transforms, we consider following example: an observer in system K sees a point charge q which moves at a constant velocity \vec{v} in a straight line. The charge is at rest in the system K' . We suppose, that the charge moves in positive x_1 direction and that its closest distance to the observer at point P is the impact parameter b . Fig. A.1 shows an appropriate choice of coordinate systems. At $t = t' = 0$ the origins of the two systems coincide and the point charge q is at its closest distance to the observer P . The fields are to be evaluated in point P . In the primed system K' , P has the coordinates $x'_1 = -vt'$, $x'_2 = b$, $x'_3 = 0$, and is a distance $r' = \sqrt{b^2 + (vt')^2}$ away from q . Hence, the electric and magnetic fields at the observation P in the system K' are:

$$\begin{aligned} E'_1 &= -\frac{qv t'}{r'^3} & B'_1 &= 0 \\ E'_2 &= \frac{qb}{r'^3} & B'_2 &= 0 \\ E'_3 &= 0 & B'_3 &= 0 \end{aligned} \quad (\text{A.8})$$

What we are actually interested in, is the electromagnetic field of the point charge at point P in the system K where the observer is at rest. We will need to express r' in terms of coordinates of K . Since $x_1 = 0$ for P in K , we just have to transform the time $t' = \gamma[t - (v/c^2)x_1] = \gamma t$. This leads to following non-vanishing field components in K :

$$\begin{aligned} E'_1 &= -\frac{q\gamma v t}{(b^2 + \gamma^2 v^2 t^2)^{3/2}} \\ E'_2 &= \frac{qb}{(b^2 + \gamma^2 v^2 t^2)^{3/2}} \end{aligned} \quad (\text{A.9})$$

Then, applying the inverse transformation of Eq. (A.8), we find the transformed fields in the

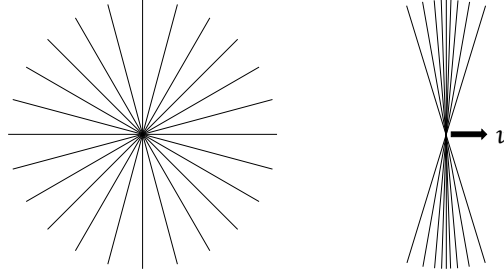


Fig. A.2 Lines of electric force for a point charge at rest (left) and in motion for $\gamma \simeq 3$ (right). The figure was adapted from [66].

system K :

$$\begin{aligned}
 E_1 &= E'_1 = -\frac{q\gamma v t}{(b^2 + \gamma^2 v^2 t^2)^{3/2}} \\
 E_2 &= \gamma E'_2 = \frac{\gamma q b}{(b^2 + \gamma^2 v^2 t^2)^{3/2}} \\
 B_3 &= \gamma \beta E'_2 = \beta E_2
 \end{aligned}
 \tag{A.10}$$

with all other components vanishing.

We are now examining the ultra-relativistic limit, when $\beta \rightarrow 1$ and $\gamma \gg 1$, since this case applies to scattering processes in a Coulomb field. The electromagnetic field is Lorentz contracted as illustrated in Fig. A.2. Hence, the observer is exposed to the field only for a very short amount of time (around $t = 0$ when the charge is in the distance b):

$$\Delta t \sim \frac{b}{\gamma v}
 \tag{A.11}$$

The longitudinal component of the electric field (E_1) varies rapidly from positive to negative with negative t to positive t and has zero time integral. In the ultra-relativistic limit, the observer will not realize this component if the detecting apparatus has any inertia. Consequently, the observer will see only the transverse components. At P , the observer sees mutually perpendicular transverse electric and magnetic fields of equal amplitude ($E_2 = B_3$) as depicted in Fig. A.3. This property is indistinguishable from the fields of a pulse of plane

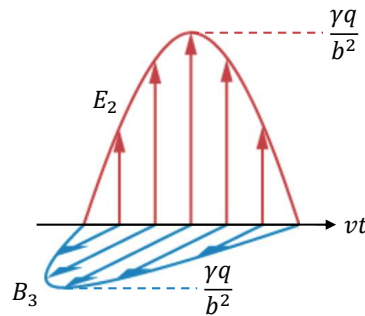


Fig. A.3 Fields of a in x_1 -direction uniformly moving particle at the observation point P as a function of time. The shape of the function is an approximation and does not correspond to the functions obtained in Eq. (A.10).

polarized radiation propagating in x_1 direction. It is this similarity that motivates the method of virtual quanta or equivalent photon approximation as developed by von Weizsäcker and Williams [68, 69]. They correlated the effects of the collision of the Coulomb “plane” of an ultra-relativistic charge with some system with the corresponding effects produced by the interaction of radiation (quasi-real photons) with the same system.

A.4 Derivation of angular dependencies of $\pi^- \gamma \rightarrow \pi^- \pi^0$

The matrix element for the process in Eq. (2.42) is given by Eq. (2.48). Due to four-momentum conservation, we have:

$$p_1^\mu = p_2^\mu + p_0^\mu - q^\mu \quad (\text{A.12})$$

and we realize that we can express the matrix element by any three of the four involved four-momenta, since terms containing the same four-vector twice equal zero due to the properties of the Levi-Civita tensor:

$$\begin{aligned} \mathcal{M}(s, t, u) &= i \epsilon_{\mu\nu\alpha\beta} \epsilon^\mu p_1^\nu p_2^\alpha p_0^\beta \mathcal{F}(s, t, u) \\ &= -i \epsilon_{\mu\nu\alpha\beta} \epsilon^\mu q^\nu p_2^\alpha p_0^\beta \mathcal{F}(s, t, u) \end{aligned} \quad (\text{A.13})$$

In the GJ-frame, the spatial components of the four-vectors are given by:

$$\begin{aligned} \vec{q} &= -q \begin{pmatrix} 0 \\ 0 \\ 1 \end{pmatrix} & \vec{\epsilon}_1 &= \begin{pmatrix} 1 \\ 0 \\ 0 \end{pmatrix} & \vec{\epsilon}_2 &= \begin{pmatrix} 0 \\ 1 \\ 0 \end{pmatrix} \\ \vec{p}_0 &= -p' \begin{pmatrix} \sin \theta \cos \phi \\ \sin \theta \sin \phi \\ \cos \theta \end{pmatrix} & \vec{p}_2 &= p' \begin{pmatrix} \sin \theta \cos \phi \\ \sin \theta \sin \phi \\ \cos \theta \end{pmatrix} \end{aligned} \quad (\text{A.14})$$

Averaging over the two possible transverse polarization vectors and realizing that only permutations with either $\alpha = 0$ or $\beta = 0$ are non-vanishing ($\vec{p}_0 \parallel \vec{p}_2$), we have

$$\begin{aligned} \frac{1}{2} \sum_{\text{pol}} |\mathcal{M}_{\text{fi}}|^2 &= \frac{1}{2} \sum_{k=1,2} |\epsilon_{\mu\nu\alpha\beta} \epsilon_k^\mu q^\nu p_2^\alpha p_0^\beta|^2 |\mathcal{F}(s, t, u)|^2 \\ &= \frac{1}{2} \sum_{k=1,2} |\epsilon_{\mu\nu 0 \beta} \epsilon_k^\mu q^\nu p_2^0 p_0^\beta + \epsilon_{\mu\nu \alpha 0} \epsilon_k^\mu q^\nu p_2^\alpha p_0^0|^2 |\mathcal{F}(s, t, u)|^2 \\ &= \frac{1}{2} \sum_{k=1,2} |p_2^0 \vec{p}_0 \cdot (\vec{\epsilon}_k \times \vec{q}) - p_0^0 \vec{p}_2 \cdot (\vec{\epsilon}_k \times \vec{q})|^2 |\mathcal{F}(s, t, u)|^2 \\ &= \frac{1}{2} \left(\underbrace{|2E' q p' \sin \theta \sin \phi|^2}_{k=1} + \underbrace{|2E' q p' \sin \theta \cos \phi|^2}_{k=2} \right) |\mathcal{F}(s, t, u)|^2 \\ &= E'^2 q^2 (s - 4m_\pi^2) \sin^2 \theta (\sin^2 \phi + \cos^2 \phi) |\mathcal{F}(s, t, u)|^2 \\ &= \frac{1}{32} (s - m_\pi^2)^2 (s - 4m_\pi^2) (1 - \cos^2 \theta) |\mathcal{F}(s, t, u)|^2 \end{aligned} \quad (\text{A.15})$$

with $p_2^0 = p_0^0 \equiv E'$. As indicated in Eq. (A.15), the term with $\sin^2 \phi$ -dependence stems from $\vec{\epsilon}_1$ and those with $\cos^2 \phi$ -dependence from $\vec{\epsilon}_2$. Due to the averaging over the two transverse polarization vectors, we lose the ϕ -dependence: for a real photon, there is no privileged azimuthal angle. However, we know from the discussion in App. A.3 that the photon is polarized if it is a Primakoff photon. The production plane acts as a reference plane in azimuthal direction and the polarization vector of a quasi-real Primakoff photon lies in this plane. We are left with only $\vec{\epsilon}_1$. The overall process will hence exhibit a $\sin^2 \phi$ -dependence.

A.5 Twice subtracted dispersion relation

We derive the exact formula for the twice-subtracted dispersion relation of Eq. (2.67). We start with inserting the identity

$$\begin{aligned}
\frac{1}{s'-s} &= \frac{1}{s'-s} - \frac{1}{s'-s_0} - \frac{s-s_0}{(s'-s_0)(s'-s_1)} + \frac{1}{s'-s_0} + \frac{s-s_0}{(s'-s_0)(s'-s_1)} \\
&= \frac{s'-s_0}{(s'-s)(s'-s_0)} - \frac{s'-s}{(s'-s)(s'-s_0)} - \frac{s-s_0}{(s'-s_0)(s'-s_1)} + \frac{1}{s'-s_0} + \frac{s-s_0}{(s'-s_0)(s'-s_1)} \\
&= \frac{(s-s_0)(s'-s_1)}{(s'-s)(s'-s_0)(s'-s_1)} - \frac{(s'-s)(s-s_0)}{(s'-s)(s'-s_0)(s'-s_1)} + \frac{1}{s'-s_0} + \frac{s-s_0}{(s'-s_0)(s'-s_1)} \\
&= \frac{(s-s_0)(s-s_1)}{(s'-s)(s'-s_0)(s'-s_1)} + \frac{(s'-s_1)+(s-s_0)}{(s'-s_0)(s'-s_1)} \\
&= \frac{(s-s_0)(s-s_1)}{(s'-s)(s'-s_0)(s'-s_1)} + \frac{s'-s_1-s_0}{(s'-s_0)(s'-s_1)} + \frac{s}{(s'-s_0)(s'-s_1)}
\end{aligned} \tag{A.16}$$

into Eq. (2.67) which leads to the twice subtracted dispersion relation

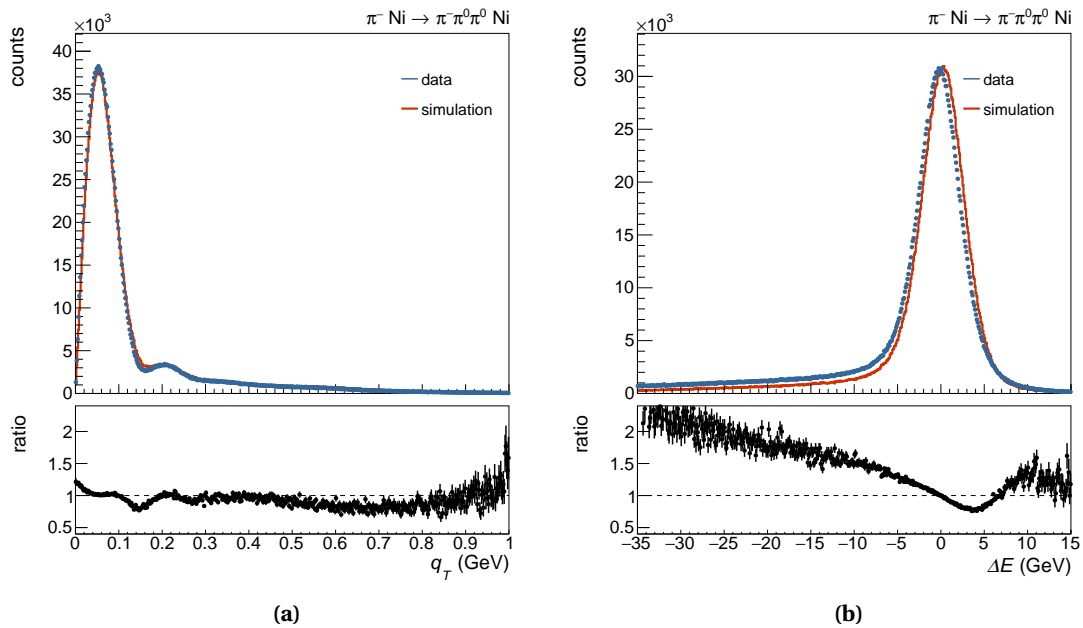
$$\begin{aligned}
f(s) &= \frac{1}{\pi} \underbrace{\int_{s_{\text{thr}}}^{\infty} \frac{(s'-s_0-s_1) \text{Im}f(s')}{(s'-s_0)(s'-s_1)} ds'}_{C_2^{(1)}} + s \cdot \frac{1}{\pi} \underbrace{\int_{s_{\text{thr}}}^{\infty} \frac{\text{Im}f(s')}{(s'-s_0)(s'-s_1)} ds'}_{C_2^{(2)}} + \frac{(s-s_0)(s-s_1)}{\pi} \int_{s_{\text{thr}}}^{\infty} \frac{\text{Im}f(s')}{(s'-s)(s'-s_0)(s'-s_1)} ds' \\
&= C_2^{(1)} + C_2^{(2)} \cdot s + \frac{(s-s_0)(s-s_1)}{\pi} \int_{s_{\text{thr}}}^{\infty} \frac{\text{Im}f(s')}{(s'-s)(s'-s_0)(s'-s_1)} ds'
\end{aligned} \tag{A.17}$$

Appendix B

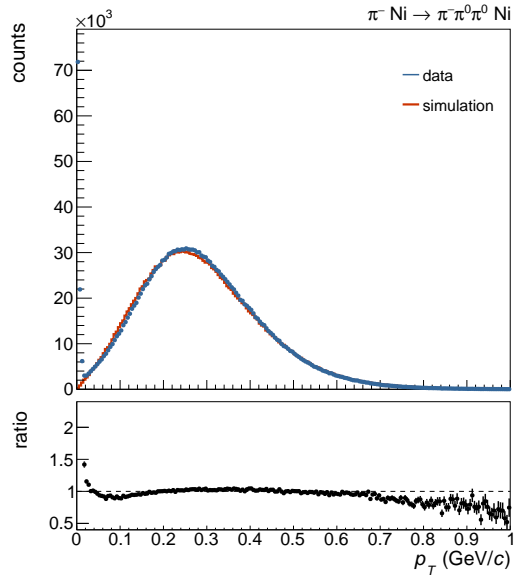
Kinematic distributions

B.1 Kinematic distributions of the selected $\pi^- + \text{Ni} \rightarrow \pi^- \pi^0 \pi^0 + \text{Ni}$ events and comparison to simulation

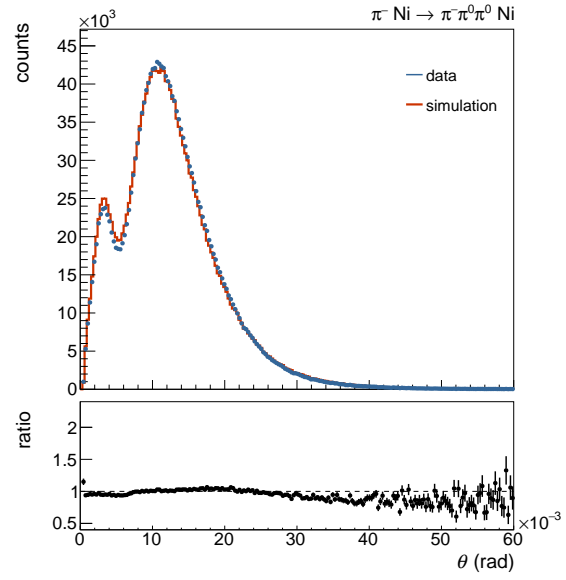
Fig. B.1 shows important kinematic distributions of the selected $\pi^- + \text{Ni} \rightarrow \pi^- \pi^0 \pi^0 + \text{Ni}$ event sample. All in all, we have achieved satisfactory agreement between the selected event sample from real data and simulated $\pi^- + \text{Ni} \rightarrow \pi^- \pi^0 \pi^0 + \text{Ni}$ events. There are however variables, for which the deviations are bigger than in others. For example the exclusivity peak, which is shown in Fig. B.1b, is shifted and significantly sharper in simulated data than in real data. It might be partly due to a slightly different calorimeter resolution, as can be seen in Fig. B.1i.



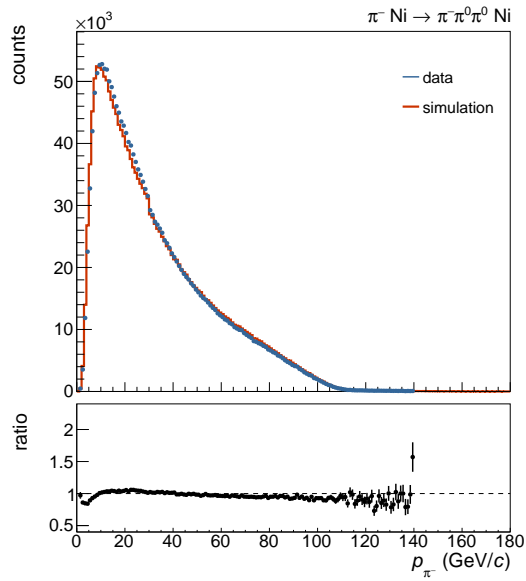
B.1. KINEMATIC DISTRIBUTIONS OF THE SELECTED $\pi^- + \text{Ni} \rightarrow \pi^- \pi^0 \pi^0 + \text{Ni}$ EVENTS AND COMPARISON TO SIMULATION



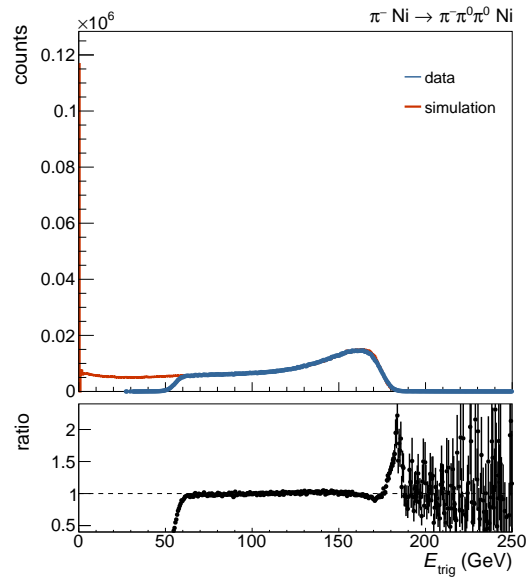
(c)



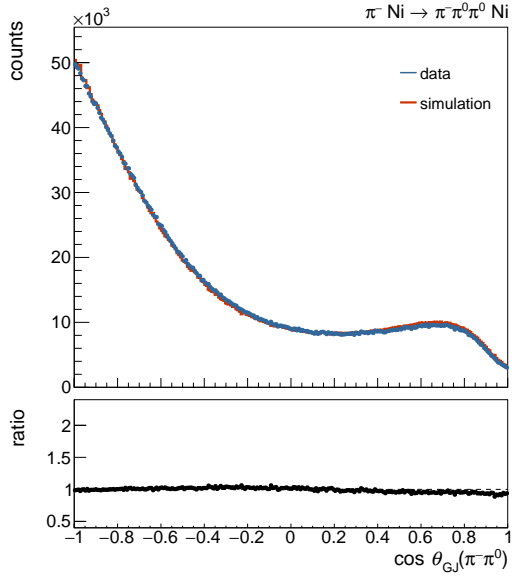
(d)



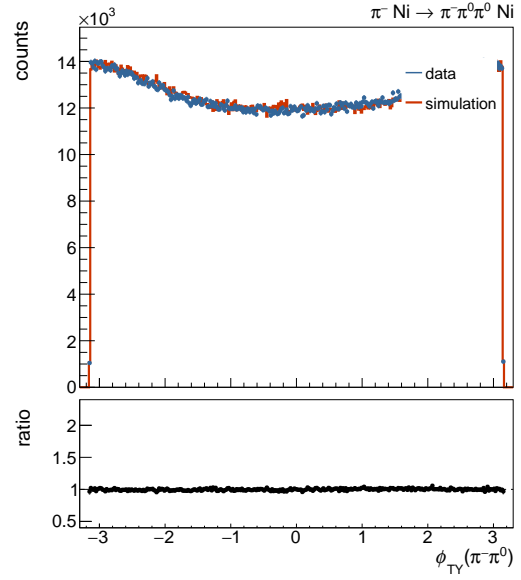
(e)



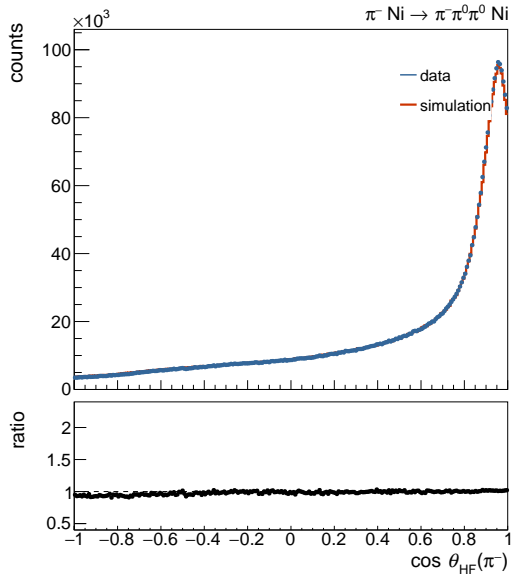
(f)



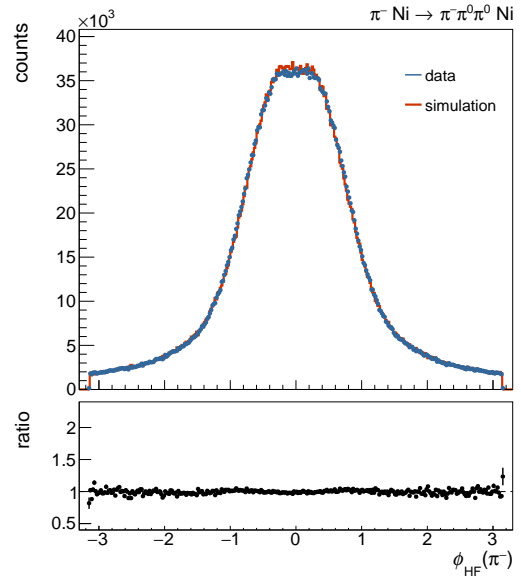
(g)



(h)



(i)



(j)

B.1. KINEMATIC DISTRIBUTIONS OF THE SELECTED $\pi^- + \text{Ni} \rightarrow \pi^- \pi^0 \pi^0 + \text{Ni}$ EVENTS AND COMPARISON TO SIMULATION

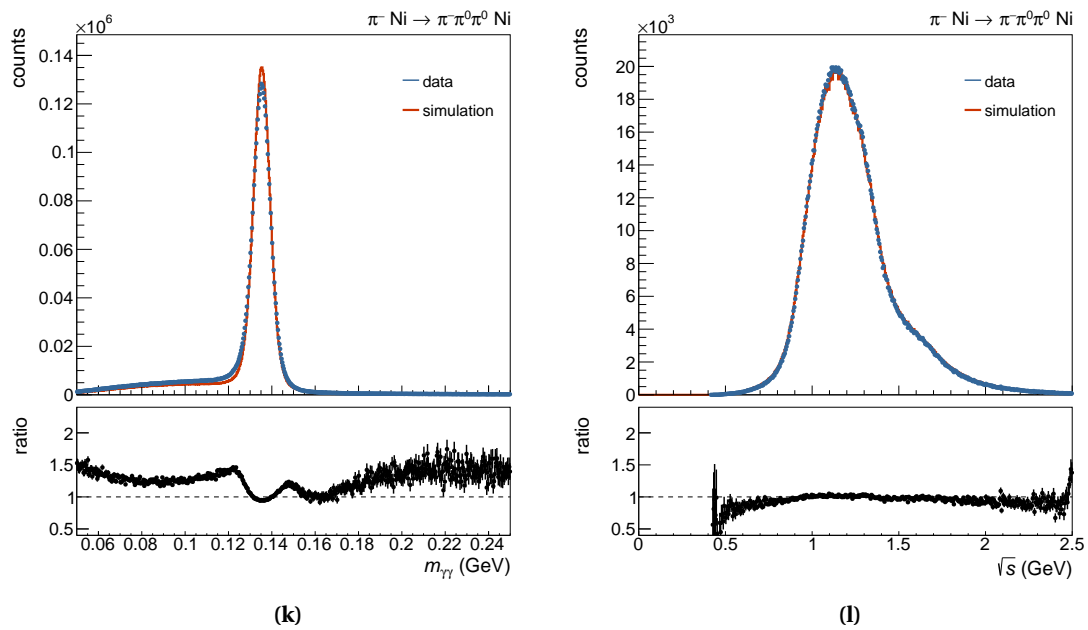
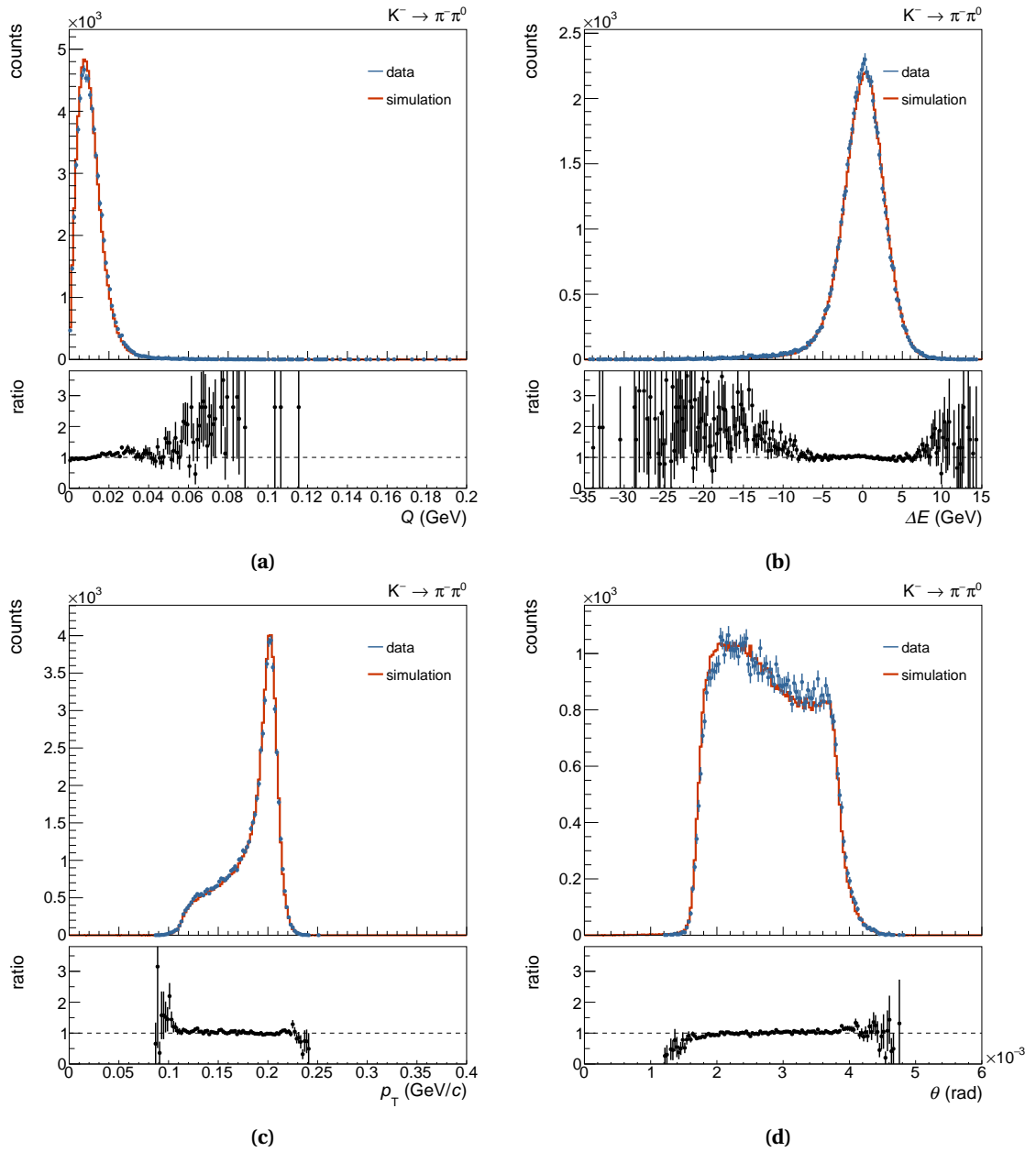


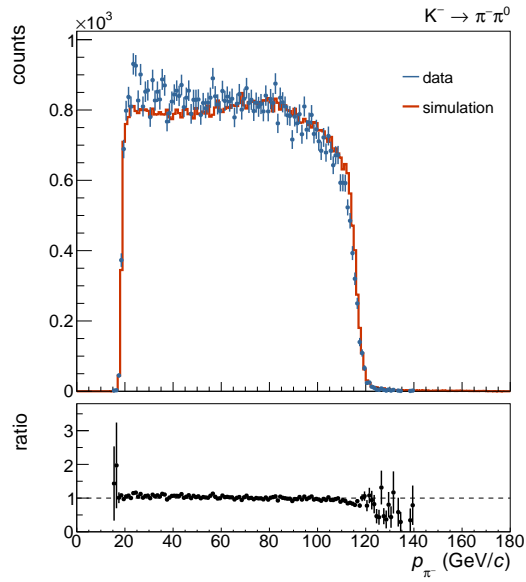
Fig. B.1 Selected kinematic distributions of $\pi^- + \text{Ni} \rightarrow \pi^- \pi^0 \pi^0 + \text{Ni}$ events. The data (blue) are compared to simulation (red). The lower plots illustrate the ratio data/simulation. All cuts of the presented event selection in Chapter 5 are applied, except cuts on variables that are shown.

B.2 Kinematic distributions of the selected $K^- \rightarrow \pi^- \pi^0$ events and comparison to simulation

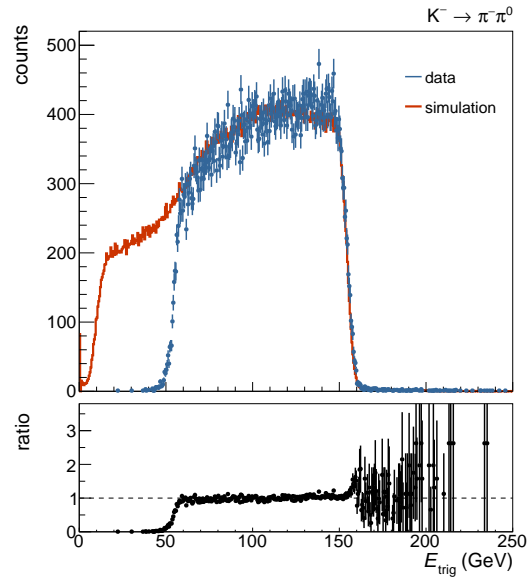
Fig. B.2 shows important kinematic distributions of the selected $K^- \rightarrow \pi^- \pi^0$ event sample. We have achieved very good agreement between the selected event sample from real data and simulation.



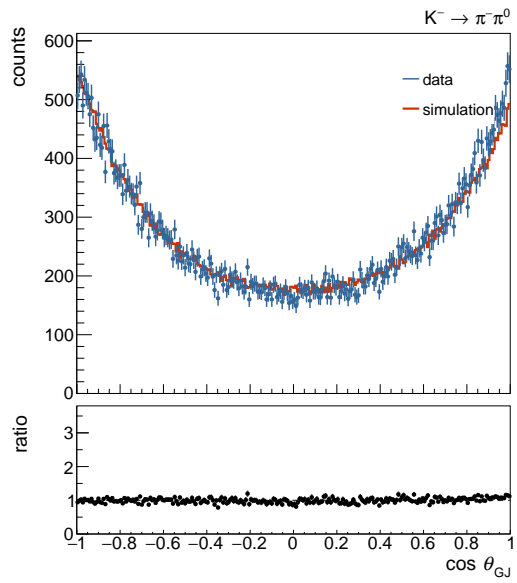
B.2. KINEMATIC DISTRIBUTIONS OF THE SELECTED $K^- \rightarrow \pi^- \pi^0$ EVENTS AND COMPARISON TO SIMULATION



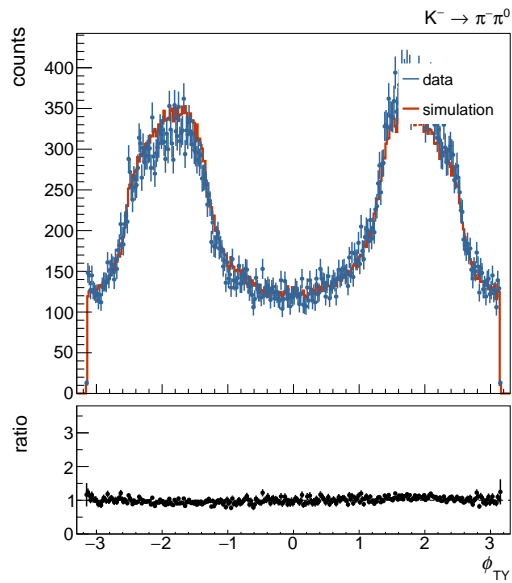
(e)



(f)



(g)



(h)

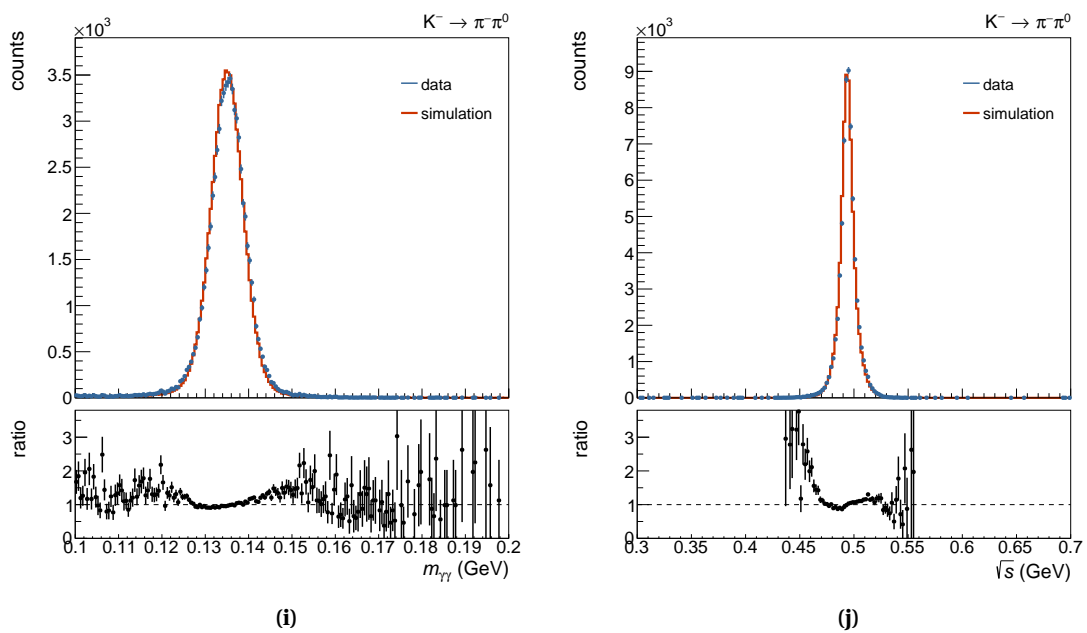
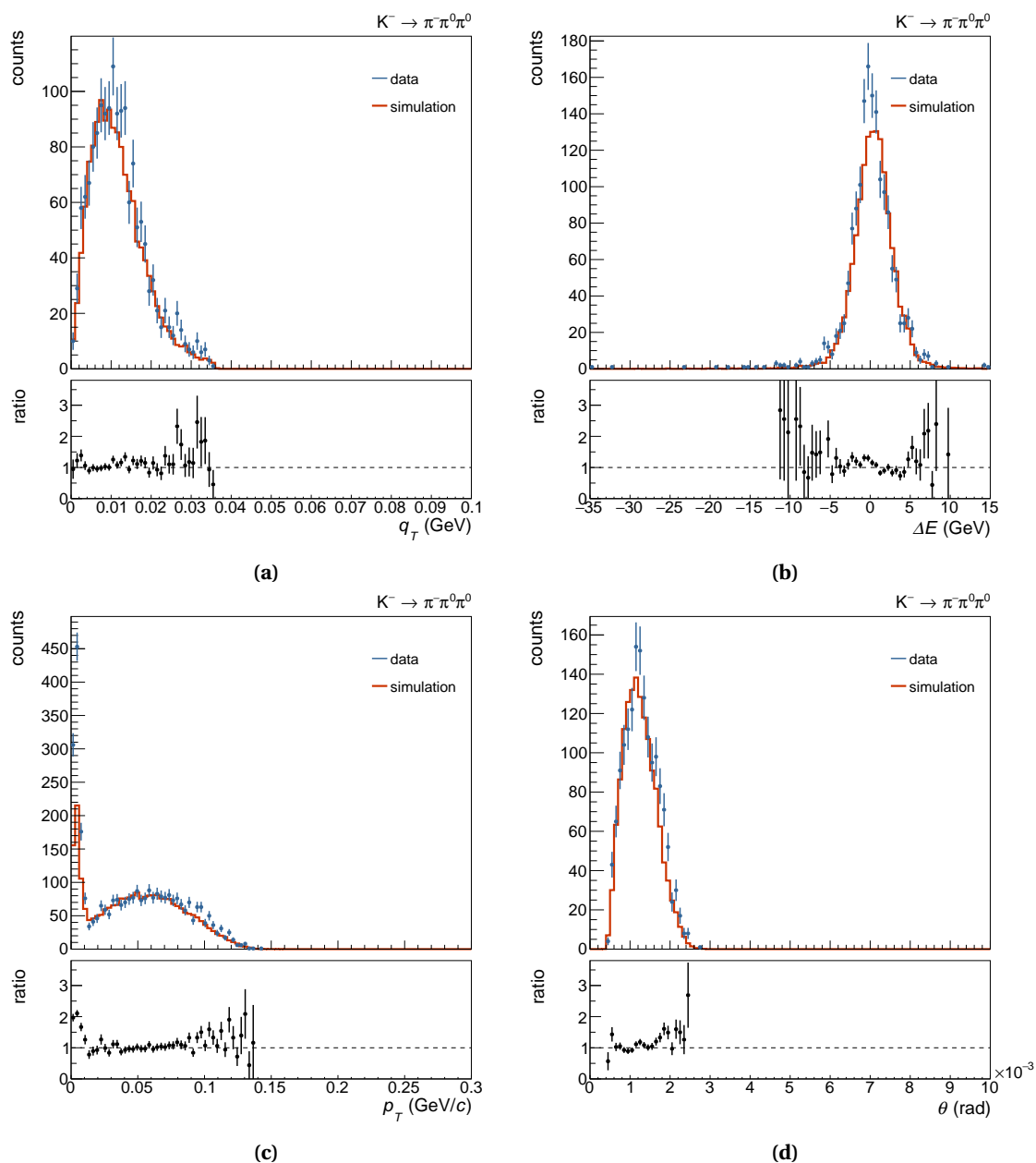
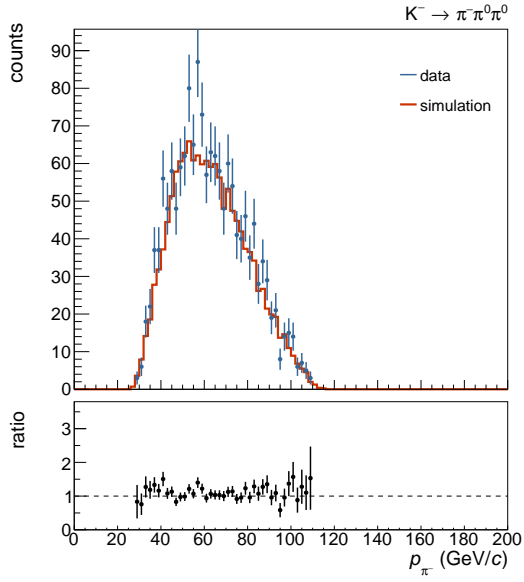


Fig. B.2 Selected kinematic distributions of $K^- \rightarrow \pi^- \pi^0$ events from real data (blue) in comparison with simulated pseudodata (red). The lower plots illustrate the ratio data/simulation. All cuts of the presented event selection in Chapter 5 are applied, except cuts on variables that are shown.

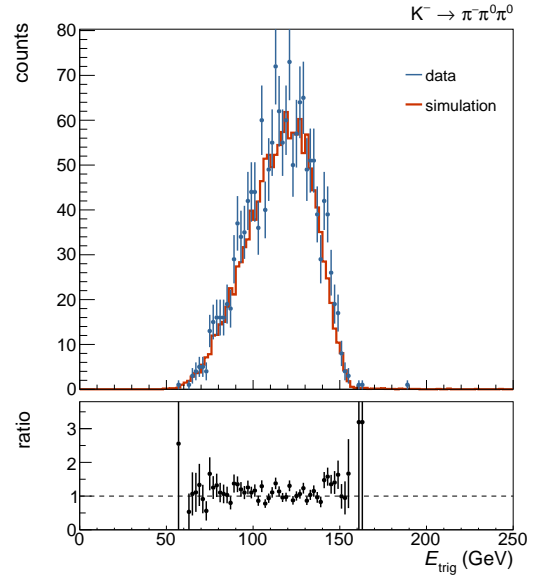
B.3 Kinematic distributions of the selected $K^- \rightarrow \pi^- \pi^0 \pi^0$ events and comparison to simulation

Fig. B.3 shows important kinematic distributions of the selected $K^- \rightarrow \pi^- \pi^0 \pi^0$ event sample. We have achieved very good agreement between the selected event sample from real data and simulation.

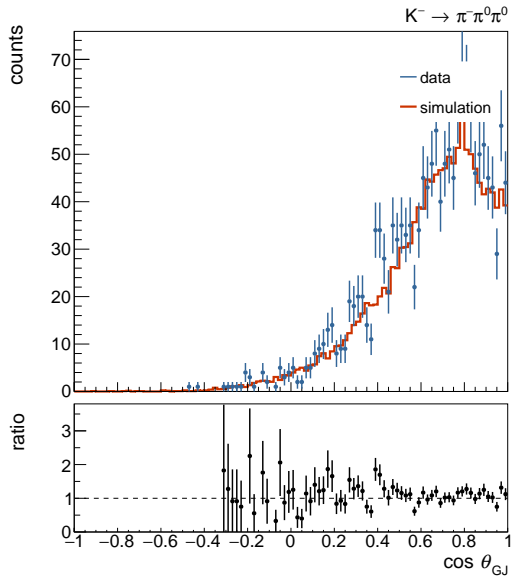




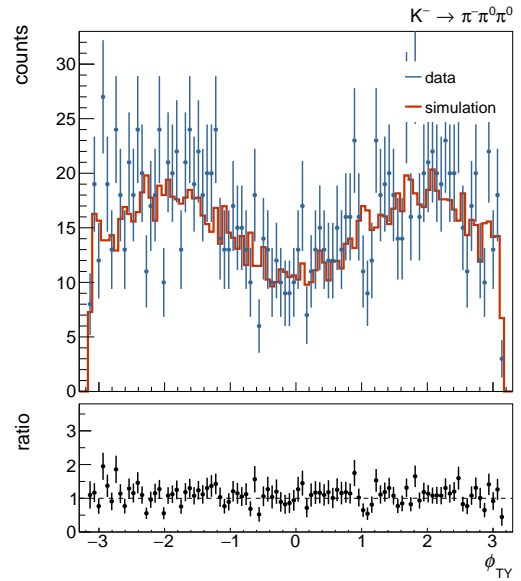
(e)



(f)



(g)



(h)

B.3. KINEMATIC DISTRIBUTIONS OF THE SELECTED $K^- \rightarrow \pi^- \pi^0 \pi^0$ EVENTS AND COMPARISON TO SIMULATION

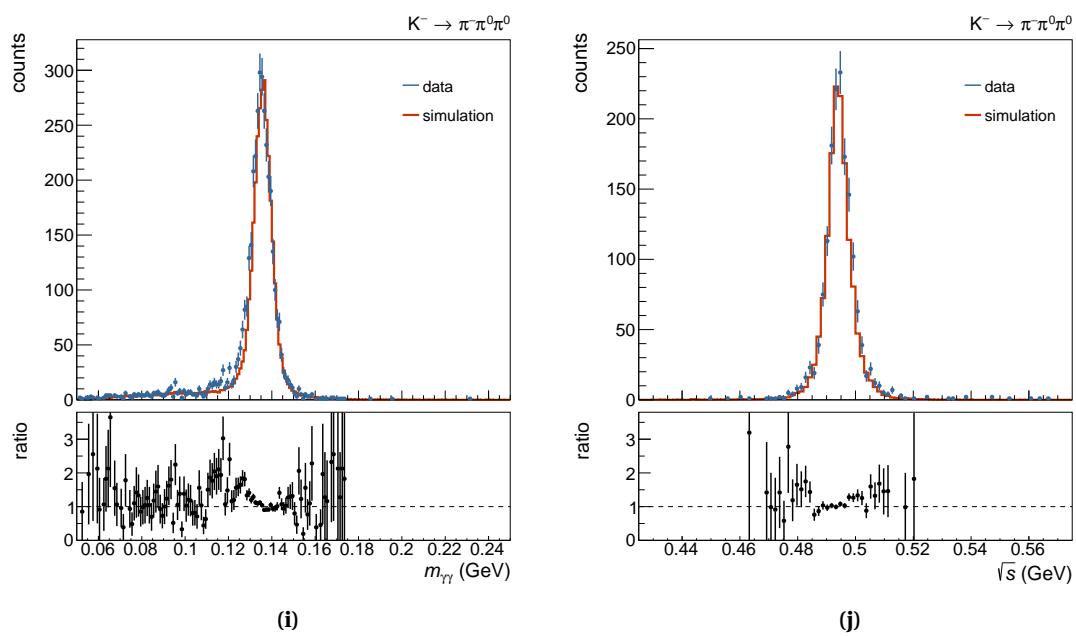


Fig. B.3 Selected kinematic distributions of $K^- \rightarrow \pi^- \pi^0$ events from real data (blue) in comparison with simulated pseudodata (red). The lower plots illustrate the ratio data/simulation. All cuts of the presented event selection in Chapter 5 are applied, except cuts on variables that are shown.

B.4 ϕ_{TY} distributions in selected $\pi^- \gamma^{(*)} \rightarrow \pi^- \pi^0$ events

Fig. B.4 shows exemplarily four out of the 50 ϕ_{TY} -distributions in selected $\pi^- \gamma^{(*)} \rightarrow \pi^- \pi^0$ events, which we obtain in bins of \sqrt{s} . We chose \sqrt{s} bins distributed over the whole spectrum, which represent important points. Fig. B.4a shows the first bin directly above threshold. We expect only very few signal events there, which leads to only a small modulation in ϕ_{TY} . Fig. B.4b shows the distribution around the kaon mass, where we expect additional background from $K_{2\pi}$ -decays. Since this background is not flat in ϕ_{TY} (see Appendix B.2), we have to exclude these bins from the final result. We cannot trust the number of signal events around $\sqrt{s} \approx m_K$ to which we add a flat background contribution.

Apart from this region, we can determine the number of elastically scattered Primakoff events, by a fit according to Eq. (8.3).

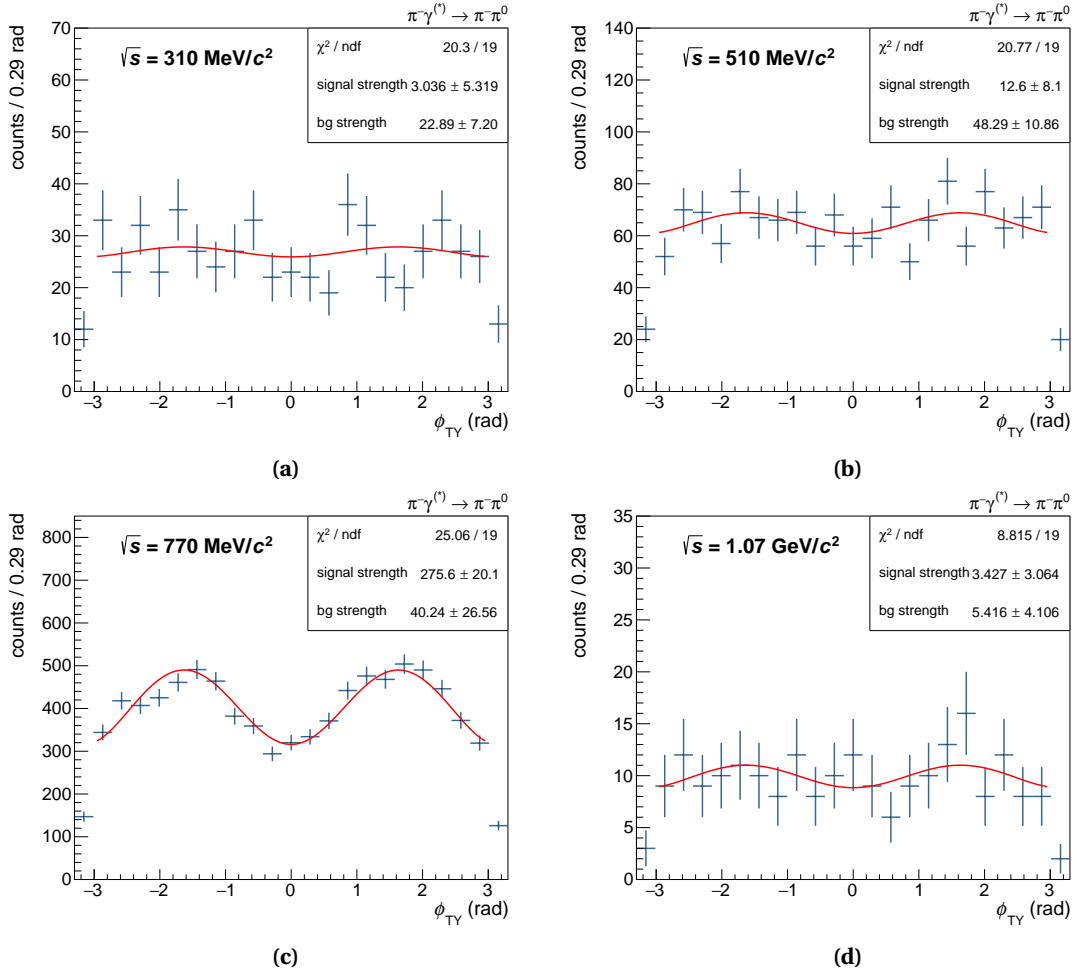


Fig. B.4 Four examples of fits to the experimental ϕ_{TY} distribution in selected $\pi^- \gamma^{(*)} \rightarrow \pi^- \pi^0$ events. (a) shows the first bin, directly above threshold. (b) shows the distribution at $\sqrt{s} \approx m_K$, (c) at $\sqrt{s} \approx m_\rho$, and (d) in a region, where we are dominated by background. The red curves show a fit according to Eq. (8.3) plus a flat background. From the relative strength to each other, we can calculate the number of signal events.

Appendix C

Register description of crosspoint switch firmware

The following list describes all IPBus registers, which are available on the FPGA. To understand the abbreviations of pin names, please consult the datasheet of the VSC3144 chip.

- **IPBus address 0x0: “version”**
Read permission only. Verification of firmware version tag.
- **IPBus address 0x1: “ctrl”**
 - (0) enable power for VSC3144
 - (1) reset signal for FPGA
 - (2) reset signal for VSC3144
- **IPBus address 0x2: “setup”**
 - (0) INITB on switch 0x280
 - (1) CONFIG on switch 0x280
 - (2) INITB softctrl
 - (21 → 11) readval0 address
- **IPBus address 0x3: “config”**
 - (0) Software INITB on switch 0x281
 - (1) Software CONFIG on switch 0x281
 - (2) User INITB on switch 0x281
 - (3) Switchstate store on switch 0x281
 - (4) Staging readback on switch 0x281
 - (5) Address striping on switch 0x281

– (21 → 11) readval1 adresse

- **IPBus adresse 0x4: “port connections”**

Set all port connections here. Any output can be connected to any input port

– (10 → 0) input port

– (21 → 11) output port

- **IPBus adresse 0x5: “register read 1”**

Read permission only. After a latency of $< 10\mu\text{s}$, the content of the switch register specified in readval0 address is displayed here.

- **IPBus adresse 0x6: “register read 2”**

Read permission only. After a latency of $< 10\mu\text{s}$, the content of the switch register specified in readval1 address is displayed here.

- **IPBus adresse 0x7: “temperature sensor”**

Read permission only. The temperature sensor and alarm register sets the on-board temperature sensing and alarm threshold functions. The VSC3144 has circuitry that detects the approximate temperature of the die and flags temperatures exceeding a user-selected, preset range. The temperature sensor register allows you to read the die temperature sensor value (an uncalibrated, approximate temperature) and set a temperature threshold at which to assert an alarm. It is a 4-bit value, which can be translated to temperature using the datasheet of the VSC3144.

– (3 → 0) alarm threshold

– (7 → 4) die temperature

List of Figures

1.1	World data on α_s as a function of the energy scale Q	5
1.2	Masses and widths of the light mesons	9
1.3	Tree-level diagrams of anomalous processes which proceed dominantly via the Wess-Zumino-Witten term	13
1.4	π^0 -lifetime measurements in comparison to the theory prediction	15
1.5	Distribution of the events in reaction (1.34) over s as measured by Antipov <i>et al.</i>	17
1.6	$\Gamma(\rho^\pm \rightarrow \pi^\pm \gamma)$, the radiative width of the $\rho(770)$	20
2.1	Definition of the Gottfried-Jackson (GJ) and helicity (HF) reference frames	23
2.2	Production of an n -body final state X via diffraction or photon exchange of a pion beam on a target nucleon/nucleus N	24
2.3	Photo-production of a π^0	26
2.4	Kinematics for a fixed-target, Primakoff process into final state X in the laboratory frame	27
2.5	Shown in (a): Q dependence of the cross section in the Weizsäcker-Williams equivalent photon approximation. Shown in (b): direction of the momentum transfer	29
2.6	Kinematics of reaction $\pi^- \gamma^{(*)} \rightarrow \pi^- \pi^0$ in the center-of-momentum frame	33
2.7	Kinematics of reaction $\pi^- + \text{Ni} \rightarrow \pi^- \pi^0 + \text{Ni}$ in the center-of-momentum frame depicted in a three-dimensional view	34
2.8	Tree-level diagram for coherent $\rho(770)$ -production and total cross sections for the reaction $\pi \gamma \rightarrow \pi^- \pi^0$ with and without a model for the ρ -meson	36

2.9	Tree-level graph for the dominant contribution to electromagnetic corrections to $\pi^- \gamma \rightarrow \pi^- \pi^0$ and lowest-order amplitude $f^{(0)}(s, \cos \theta_{\text{GJ}})$ including radiative corrections as a function of s for various values of θ_{GJ}	38
2.10	Contours for the Cauchy integral formula for the calculation of $f(s)$	39
2.11	Basis functions $\mathcal{F}_2^{(i)}$ for $\gamma \pi \rightarrow \pi \pi$	41
3.1	Schematic view of the COMPASS setup for measurements with hadron beams	46
3.2	Basic principle of the CEDAR detector	47
3.3	Schematic view of the target holder used for measurements with nuclear targets	49
3.4	Distribution of primary vertices in the target area and acceptance of kaon decays over the Ni target	50
3.5	Structure of ECAL2	51
3.6	Arrangement of trigger elements in the spectrometer	52
3.7	Efficiency of the ECAL2 trigger as a function of the energy	53
3.8	Data Handling Card (DHC) mounted on a VME carrier card	55
3.9	Setup and network topology of the iFDAQ in the years 2014 to 2019	56
3.10	Communication diagram of the different processes which form the support software of the iFDAQ	57
4.1	Event builder architectures	60
4.2	Possibility to scale data throughput of a hardware event builder	61
4.3	Multi-fiber push on (MPO) connector and harness fiber	62
4.4	Layout of the custom-designed PCB for the crosspoint switch	62
4.5	Front and back view of the chassis for the crosspoint switch	63
4.6	Block diagram of the functionality of the crosspoint switch	64
4.7	Configuration tools and graphical user interfaces for editing the involved database tables	66
4.8	Schematic working principle of configuration of the crosspoint switch	67
4.9	Distributions provided by the GUI of the beam monitoring	69

5.1	Efficiency of the muon identification system	74
5.2	Position and inclination of the beam for selected $\pi^- \gamma^{(*)} \rightarrow \pi^- \pi^0$ events	75
5.3	Number of selected events after applying each cut of the preselection	76
5.4	Distances of photons hitting ECAL2 and their reconstruction biases	78
5.5	Applying the intra-cell position dependent calibration for the Shashlik modules	80
5.6	Position and width of the reconstructed π^0 -mass peak with (a) and without (b) the intra-cell position dependent calibration	81
5.7	Time and energy distribution of reconstructed photons	82
5.8	Distance of reconstructed showers in the x/y-plane of ECAL2 \vec{x}_γ to (a) the scattered pion \vec{x}_{π^-} and (b) to other showers $\vec{x}_{\gamma'}$ vs shower energy E_γ	82
5.9	Number of reconstructed photons for $\pi^- \gamma^{(*)} \rightarrow \pi^- \pi^0$ and $\pi^- + \text{Ni} \rightarrow \pi^- \pi^0 \pi^0 + \text{Ni}$ events	83
5.10	Applying kinematic constraints: \sqrt{s} -resolution in $K^- \rightarrow \pi^- \pi^0$ and $K^- \rightarrow \pi^- \pi^0 \pi^0$ decays	84
5.11	Applying kinematic constraints: Q^2 -resolution in $K^- \rightarrow \pi^- \pi^0$ and $K^- \rightarrow \pi^- \pi^0 \pi^0$ decays	85
5.12	Slope of t' -distribution for different values of the calorimeter position	87
5.13	Distribution of events along the beam axis (z_{PV}) versus the scattering angle θ	88
5.14	Deposited energy of the charged track in ECAL2 vs its momentum in $K^- \rightarrow e^- \pi^0 \bar{\nu}_e$ and $K^- \rightarrow \pi^- \pi^0$ decays	89
5.15	Top view of the COMPASS spectrometer with the two dipole magnets SM1 and SM2 and the electromagnetic calorimeter of the SAS ECAL2	90
5.16	Position of photons x_γ in the bending plane of the magnets to the straight extrapolation x_1 of the charged track	91
5.17	Invariant mass spectrum of the $\gamma\gamma$ subsystem	92
5.18	Exclusivity distribution of $\pi^- \gamma^{(*)} \rightarrow \pi^- \pi^0$, $K^- \rightarrow \pi^- \pi^0$, $\pi^- + \text{Ni} \rightarrow \pi^- \pi^0 \pi^0 + \text{Ni}$, and $K^- \rightarrow \pi^- \pi^0 \pi^0$ events	92
5.19	Momentum transfer distribution in $\pi^- \gamma^{(*)} \rightarrow \pi^- \pi^0$ and events	93
5.20	Invariant mass distribution of the final state for $K^- \rightarrow \pi^- \pi^0$ and $K^- \rightarrow \pi^- \pi^0 \pi^0$ decays	94

5.21	Invariant mass distribution of the final state for $\pi^- \gamma^{(*)} \rightarrow \pi^- \pi^0$ and $\pi^- + \text{Ni} \rightarrow \pi^- \pi^0 \pi^0 + \text{Ni}$ events	94
5.22	Number of selected events after applying each cut for the selection of $\pi^- \gamma^{(*)} \rightarrow \pi^- \pi^0$ and $\pi^- + \text{Ni} \rightarrow \pi^- \pi^0 \pi^0 + \text{Ni}$ events	95
5.23	Number of selected events after applying each cut for the selection of $K^- \rightarrow \pi^- \pi^0$ and $K^- \rightarrow \pi^- \pi^0 \pi^0$ events	95
6.1	π^0 -calibration of simulated data	99
6.2	Two-photon invariant mass distribution of data in comparison to simulation as measured in ECAL2 for $K^- \rightarrow \pi^- \pi^0$ and $\pi^- + \text{Ni} \rightarrow \pi^- \pi^0 \pi^0 + \text{Ni}$ events	101
6.4	Impact on the beam momentum determination in simulation	103
6.5	Correlation between energy deposit in the trigger region and energy of the π^0 in $K^- \rightarrow \pi^- \pi^0$ decays	104
6.6	Comparison of the true Q -dependence of the cross-section given by the Weizsäcker-Williams approximation (blue) and the reconstructed distribution (red)	105
6.7	The observed distribution of momentum transfer Q^2 of $\pi^- + \text{Ni} \rightarrow \pi^- \pi^0 \pi^0 + \text{Ni}$ events in comparison to simulation	107
7.1	Detected kaon decays up- and downstream of the target	110
7.2	Kinematic distributions of selected $K_{2\pi}$ decays in the laboratory frame in comparison to simulation	113
7.3	Population of the phase space in $K^- \rightarrow \pi^- \pi^0 \pi^0$ decays and difference in the distribution of p_{π^-} in $K^- \rightarrow \pi^- \pi^0 \pi^0$ decays with and without Dalitz plot slopes	114
7.4	Kinematic distributions of the $K^- \rightarrow \pi^- \pi^0 \pi^0$ decay in comparison to simulation	114
7.5	Population of the phase space for K_{e3} and $K_{\mu3}$ decays	115
8.1	\sqrt{s} distribution of selected $\pi^- \gamma^{(*)} \rightarrow \pi^- \pi^0$ events around m_{K^-}	122
8.2	Distribution of \sqrt{s} of selected $\pi^- \gamma^{(*)} \rightarrow \pi^- \pi^0$ events under the assumption that the charged particle in final state is a kaon	123
8.3	Invariant mass of the two-photon system of $\pi^- \gamma^{(*)} \rightarrow \pi^- \pi^0$ events and two-dimensional correlation between $m_{\gamma\gamma}$ and \sqrt{s}	124
8.4	Two-photon mass spectrum for the reaction $\pi^- \gamma \rightarrow \pi^- \gamma\gamma$	126

8.5	Invariant mass of the two-photon system in $\pi^-\gamma^{(*)} \rightarrow \pi^-\pi^0$ events without cut on Q at small \sqrt{s} and two-dimensional correlation between $m_{\gamma\gamma}$ and \sqrt{s} for simulated $\pi^- + \text{Ni} \rightarrow \pi^-\pi^0\pi^0 + \text{Ni}$ events	126
8.6	Invariant mass of the final state and of the $\pi^-\pi^0$ subsystem in $\pi^- + \text{Ni} \rightarrow \pi^-\pi^0\pi^0 + \text{Ni}$ reactions	128
8.7	Angular distributions in the Gottfried-Jackson frame and in the helicity frame in $\pi^- + \text{Ni} \rightarrow \pi^-\pi^0\pi^0 + \text{Ni}$ reactions	129
8.8	Description of the q_T -spectrum with different background components in the selected $\pi^-\gamma^{(*)} \rightarrow \pi^-\pi^0$ sample	131
8.9	Angular distributions of the reconstructed π^- in the Gottfried-Jackson frame for selected $\pi^-\gamma^{(*)} \rightarrow \pi^-\pi^0$ events	132
8.10	Parametrization of the resolved ϕ_{TY} -dependence of the Primakoff signal	132
8.11	Number of elastically scattered Primakoff events as determined from a fit to ϕ_{TY}	133
8.12	Acceptances for $\pi^-\gamma^{(*)} \rightarrow \pi^-\pi^0$ events as a function of $\cos\theta_{\text{GJ}}$, ϕ_{TY} , and \sqrt{s}	134
8.13	Acceptance corrected number of Primakoff events	135
8.14	Photon flux as a function of \sqrt{s} and comparison of precisely determined and approximated σ^{EPA}	136
8.15	Fit of the dispersive model to the measured cross section $\sigma_{\pi\gamma \rightarrow \pi\pi}$	138
9.3	Invariant mass distribution of the final state for selected $\pi^-\gamma^{(*)} \rightarrow \pi^-\pi^0$ events in 2009 and 2012 Primakoff data set	145
9.4	ChPT prediction of the total cross section for $\pi\gamma \rightarrow \pi^-\pi^-\pi^+$ and $\pi\gamma \rightarrow \pi^-\pi^0\pi^0$ events	145
A.1	Particle of charge q moving at constant velocity \vec{v} passes an observation point P at impact parameter b	149
A.2	Lines of electric force for a point charge at rest (left) and in motion for $\gamma \simeq 3$ (right)	150
A.3	Fields of a in x_1 -direction uniformly moving particle at the observation point P as a function of time	150
B.1	Selected kinematic distributions of $\pi^- + \text{Ni} \rightarrow \pi^-\pi^0\pi^0 + \text{Ni}$ events in comparison to simulation	156
B.2	Selected kinematic distributions of $K^- \rightarrow \pi^-\pi^0$ events in comparison to simulation	159

B.3 Selected kinematic distributions of $K^- \rightarrow \pi^- \pi^0$ events in comparison to simulation 162

B.4 Four examples of fits to the experimental ϕ_{TY} distribution in selected $\pi^- \gamma^{(*)} \rightarrow \pi^- \pi^0$ events 163

List of Tables

1.1	Examples of anomalous processes as described by the WZW term	13
2.1	Dependencies of the total cross section on selected experimental parameters for different scattering processes	25
3.1	Overview of target disks used during the Primakoff run 2009	50
3.2	Overview of target disks used during the Primakoff run 2009	53
5.1	Parameters of the cut on beam position and inclination	76
5.2	Parameters of cubic cell response function	80
5.3	Resolutions in \sqrt{s} and Q^2 for $\pi^-\pi^0$ and $\pi^-\pi^0\pi^0$ final states for different π^0 constraining procedures	86
6.1	Position and width of the π^0 -peak for final states with one and two π^0 (s)	101
7.1	Kaon decay channels and their branching ratios $\Gamma_i/\Gamma_{\text{tot}}$ as listed in Ref. [18].	111
7.2	Acceptances for kaon decays	116
7.3	Sources of systematic uncertainties on the luminosity value	119
8.1	Relevant kaon decay channels, their branching ratios, the probability to be misidentified as $\pi^-\gamma^{(*)} \rightarrow \pi^-\pi^0$ events, and the estimated number of background events	123

Bibliography

- [1] D. P. Aguillard *et al.*, “Measurement of the positive muon anomalous magnetic moment to 0.20 ppm,” 2023. *cited in (document) (p. 1)*
- [2] M. Riordan, “The Discovery of Quarks,” *Science* **256** (1992) 1287–1293. *cited in 1.1 (p. 3)*
- [3] P. A. Zyla *et al.*, [Particle Data Group], “Review of Particle Physics - Plots of Cross Sections and Related Quantities,” *PTEP* **2020** (2020) 696–712. 083C01. *cited in 1.1 (p. 4)*
- [4] V. V. Ezhela, S. B. Lugovsky, and O. V. Zenin, “Hadronic part of the muon $g - 2$ estimated on the $\sigma_{tot}^{2003}(e^+e^- \rightarrow hadrons)$ evaluated data compilation,” [arXiv:hep-ph/0312114](https://arxiv.org/abs/hep-ph/0312114). *cited in 1.1 (p. 4)*
- [5] N. Brambilla, S. Eidelman, P. Foka, *et al.*, “QCD and strongly coupled gauge theories: challenges and perspectives,” *The European Physical Journal C* **74** (2014) . <http://dx.doi.org/10.1140/epjc/s10052-014-2981-5>. *cited in 1.1 (p. 5), 1.1.1 (p. 6), 1.1.2 (p. 10), 1.2 (p. 11)*
- [6] P. A. Zyla *et al.*, [Particle Data Group], “Review of Particle Physics - Quantum Chromodynamics,” *PTEP* **2020** (2020) 153–179. 083C01. *cited in 1.1 (p. 5), 1.1 (p. 6)*
- [7] H. D. Politzer, “Reliable Perturbative Results for Strong Interactions?,” *Phys. Rev. Lett.* **30** (1973) 1346–1349. <https://link.aps.org/doi/10.1103/PhysRevLett.30.1346>. *cited in 1.1 (p. 6)*
- [8] D. J. Gross and F. Wilczek, “Ultraviolet Behavior of Non-Abelian Gauge Theories,” *Phys. Rev. Lett.* **30** (1973) 1343–1346. <https://link.aps.org/doi/10.1103/PhysRevLett.30.1343>. *cited in 1.1 (p. 6)*
- [9] G. S. Bali, H. Neff, T. Düssel, T. Lippert, and K. Schilling, “Observation of string breaking in QCD,” *Phys. Rev. D* **71** (2005) . <http://dx.doi.org/10.1103/PhysRevD.71.114513>. *cited in 1.1.1 (p. 6)*
- [10] W. Heisenberg, “Über den Bau der Atomkerne,” *Z. Physik* **77** (1932) 1–11. <https://doi.org/10.1007/BF01342433>. *cited in 1.1.1 (p. 6)*
- [11] M. Gell-Mann, “The eightfold way: A theory of strong interaction symmetry,” (1961) . <https://www.osti.gov/biblio/4008239>. *cited in 1.1.1 (p. 6)*

- [12] Y. Ne'eman, "Derivation of strong interactions from a gauge invariance," *Nucl. Phys.* **26** (1961) 222–229. *cited in 1.1.1 (p. 6)*
- [13] T. Horn and C. D. Roberts, "The pion: an enigma within the Standard Model," *Journal of Physics G: Nuclear and Particle Physics* **43** (2016) 073001. <http://dx.doi.org/10.1088/0954-3899/43/7/073001>. *cited in 1.1.2 (p. 7)*
- [14] Y. Nambu, "Quasi-particles and gauge invariance in the theory of superconductivity," *Phys. Rev.* **117** (1960) 648–663. <https://link.aps.org/doi/10.1103/PhysRev.117.648>. *cited in 1.1.2 (p. 7)*
- [15] J. Goldstone, A. Salam, and S. Weinberg, "Broken symmetries," *Phys. Rev.* **127** (1962) 965–970. <https://link.aps.org/doi/10.1103/PhysRev.127.965>. *cited in 1.1.2 (p. 7), 1.1.2 (p. 10)*
- [16] P. A. Zyla *et al.*, [Particle Data Group], "Review of Particle Physics - Quark Summary Table," *PTEP* **2020** (2020) 37. 083C01. *cited in 1.1.2 (p. 8)*
- [17] P. A. Zyla *et al.*, [Particle Data Group], "Review of Particle Physics - Quark model," *PTEP* **2020** (2020) 37. 083C01. *cited in 1.2 (p. 9)*
- [18] P. A. Zyla *et al.*, [Particle Data Group], "Review of Particle Physics - Meson Summary Table," *PTEP* **2020** (2020) 37. 083C01. *cited in 1.2 (p. 9), 1.2 (p. 11), 1.4 (p. 15), 1.4 (p. 18), 1.6 (p. 20), 2.3.2 (p. 36), 5.2.3 (p. 86), 5.3.1 (p. 87), 7 (p. 110), 7.1 (p. 111), 7.1 (p. 111), 7.2.1 (p. 113), 7.2.2 (p. 115), 8.1.2 (p. 123), C (p. 173)*
- [19] M. Faber and R. Höllwieser, "Chiral symmetry breaking on the lattice," *Prog. Part. Nucl. Phys.* **97** (2017) 312–355, arXiv:1908.09740 [hep-lat]. *cited in 1.1.2 (p. 9)*
- [20] S. Weinberg, "Phenomenological lagrangians," *Physica A* **96** (1979) 327–340. <https://www.sciencedirect.com/science/article/pii/0378437179902231>. *cited in 1.1.2 (p. 10), 1.1.2 (p. 10)*
- [21] S. Weinberg, "Dynamical approach to current algebra," *Phys. Rev. Lett.* **18** (1967) 188–191. <https://link.aps.org/doi/10.1103/PhysRevLett.18.188>. *cited in 1.1.2 (p. 10)*
- [22] J. Gasser and H. Leutwyler, "Chiral perturbation theory to one loop," *Annals of Physics* **158** (1984) 142–210. <https://www.sciencedirect.com/science/article/pii/0003491684902422>. *cited in 1.1.2 (p. 10)*
- [23] J. Gasser and H. Leutwyler, "Chiral perturbation theory: Expansions in the mass of the strange quark," *Nuclear Physics B* **250** (1985) 465–516. <https://www.sciencedirect.com/science/article/pii/0550321385904924>. *cited in 1.1.2 (p. 10)*
- [24] H. Leutwyler, "On the foundations of chiral perturbation theory," *Annals of Physics* **235** (Oct, 1994) 165–203. <http://dx.doi.org/10.1006/aphy.1994.1094>. *cited in 1.1.2 (p. 10)*

-
- [25] G. Ecker and U.-G. Meissner, “What is a low-energy theorem?,” *Comments Nucl. Part. Phys.* **21** (1995) 347–367, arXiv:hep-ph/9409442. *cited in 1.1.2 (p. 10)*
- [26] H. Atherton *et al.*, “Direct measurement of the lifetime of the neutral pion,” *Physics Letters B* **158** (1985) 81–84. <https://www.sciencedirect.com/science/article/pii/0370269385907440>.
cited in 1.2 (p. 11), 1.4 (p. 15), 1.3.1 (p. 15)
- [27] J. S. Bell and R. Jackiw, “A PCAC puzzle: $\pi^0 \rightarrow \gamma\gamma$ in the σ -model,” *Il Nuovo Cimento A (1965-1970)* **60** (1969) 47–61. *cited in 1.2 (p. 11), 1.4 (p. 15)*
- [28] S. L. Adler, “Axial-vector vertex in spinor electrodynamics,” *Phys. Rev.* **177** (1969) 2426–2438.
<https://link.aps.org/doi/10.1103/PhysRev.177.2426>. *cited in 1.2 (p. 11), 1.4 (p. 15)*
- [29] P. A. Zyla *et al.*, [Particle Data Group], “Review of Particle Physics - Leptonic decays of charged pseudoscalar mesons,” *PTEP* **2020** (2020) . 083C01. *cited in 1.2 (p. 11)*
- [30] J. Wess and B. Zumino, “Consequences of anomalous ward identities,” *Physics Letters B* **37** no. 1, (1971) 95–97. <https://www.sciencedirect.com/science/article/pii/037026937190582X>.
cited in 1.2 (p. 13)
- [31] E. Witten, “Global aspects of current algebra,” *Nuclear Physics B* **223** no. 2, (1983) 422–432. <https://www.sciencedirect.com/science/article/pii/0550321383900639>.
cited in 1.2 (p. 13)
- [32] A. M. Bernstein and B. R. Holstein, “Neutral pion lifetime measurements and the QCD chiral anomaly,” *Rev. Mod. Phys.* **85** (2013) 49–77.
<https://link.aps.org/doi/10.1103/RevModPhys.85.49>. *cited in 1.2 (p. 13), 1.3.1 (p. 15)*
- [33] O. Bär and U.-J. Wiese, “Can one see the number of colors?,” *Nuclear Physics B* **609** no. 1, (2001) 225–246. <https://www.sciencedirect.com/science/article/pii/S0550321301002887>.
cited in 1.2 (p. 14)
- [34] I. Larin *et al.*, [The PrimEx Collaboration], “Precision measurement of the neutral pion lifetime,” *Science* **368** (2020) 505–509. *cited in 1.4 (p. 15), 1.3.1 (p. 15), 2.2.1 (p. 26)*
- [35] M. Bychkov *et al.*, “New precise measurement of the pion weak form factors in $\pi^+ \rightarrow e^+ \nu\gamma$ decay,” *Phys. Rev. Lett.* **103** (2009) 051802.
<https://link.aps.org/doi/10.1103/PhysRevLett.103.051802>.
cited in 1.4 (p. 15), 1.3.1 (p. 16)
- [36] D. A. Williams *et al.*, [The Crystal Ball Collaboration], “Measurement of $\pi^0\pi^0$ production in two-photon collisions,” *Phys. Rev. D* **41** (1990) 3324–3335.
<https://link.aps.org/doi/10.1103/PhysRevD.41.3324>. *cited in 1.4 (p. 15), 1.3.1 (p. 15)*
-

- [37] A. Browman *et al.*, “Decay width of the neutral π meson,” *Phys. Rev. Lett.* **33** (1974) 1400–1403. <https://link.aps.org/doi/10.1103/PhysRevLett.33.1400>.
cited in 1.4 (p. 15), 1.3.1 (p. 15)
- [38] K. Kampf and B. Moussallam, “Chiral expansions of the π^0 lifetime,” *Phys. Rev. D* **79** (2009) 076005.
<https://link.aps.org/doi/10.1103/PhysRevD.79.076005>. *cited in 1.4 (p. 15), 1.3.1 (p. 16)*
- [39] Y. M. Antipov *et al.*, “Investigation of the chiral anomaly $\gamma \rightarrow 3\pi$ in pion pair production by pion in the nuclear coulomb field,” *Phys. Rev. D* **36** (1987) 21–29.
<https://link.aps.org/doi/10.1103/PhysRevD.36.21>. *cited in 1.3.2 (p. 16), 1.5 (p. 17), 2.3.2 (p. 36), 7 (p. 109)*
- [40] L. Ametller, M. Knecht, and P. Talavera, “Electromagnetic corrections to $\gamma\pi^\pm \rightarrow \pi^0\pi^\pm$,” *Phys. Rev. D* **64** (Oct, 2001) 094009.
<https://link.aps.org/doi/10.1103/PhysRevD.64.094009>.
cited in 1.3.2 (p. 17), 2.9 (p. 38), 2.3.3 (p. 38), 2.3.3 (p. 38)
- [41] J. Bijnens, A. Bramon, and F. Cornet, “Three-pseudoscalar photon interactions in chiral perturbation theory,” *Physics Letters B* **237** no. 3, (1990) 488–494. <https://www.sciencedirect.com/science/article/pii/037026939091212T>.
cited in 1.3.2 (p. 17), 2.3.3 (p. 37), 2.3.3 (p. 37), 2.4.3 (p. 43)
- [42] T. Hannah, “The anomalous process $\gamma\pi \rightarrow \pi\pi$ to two loops,” *Nuclear Physics B* **593** no. 3, (2001) 577–595. <https://www.sciencedirect.com/science/article/pii/S0550321300006416>.
cited in 1.3.2 (p. 17), 2.3.1 (p. 35), 2.3.1 (p. 35), 2.3.3 (p. 37), 2.4 (p. 39), 2.4.3 (p. 43)
- [43] Giller I., Ocherashvili A., Ebertshäuser T., Moinester M. A., and Scherer S., “A new determination of the $\gamma\pi \rightarrow \pi\pi$ anomalous amplitude via $\pi e^- \rightarrow \pi^- e^- \pi^0$ data,” *The European Physical Journal A - Hadrons and Nuclei* **25** no. 2, (2005) 229–240.
cited in 1.3.2 (p. 17), 1.3.2 (p. 18), 2.3.2 (p. 36)
- [44] S. Amendolia *et al.*, “First measurement of the reaction $\pi^- e \rightarrow \pi^- \pi^0 e$,” *Physics Letters B* **155** no. 5, (1985) 457–460. <https://www.sciencedirect.com/science/article/pii/037026938591603X>.
cited in 1.3.2 (p. 17), 1.3.2 (p. 18)
- [45] J. M. Friedrich, “Chiral Dynamics in Pion-Photon Reactions: Habilitation,” Sep, 2012. <https://cds.cern.ch/record/1566653>. Presented 2012. *cited in 1.3.2 (p. 18), 2.2 (p. 26), 2.2.2 (p. 27), 2.2.2 (p. 28), 2.2.2 (p. 28), 2.6 (p. 33)*
- [46] J. Seyfried, “Determination of the Chiral Anomaly and Studies on the Pion Polarizability in Pion-Nickel Reactions from COMPASS at CERN,” Master’s thesis, Technical University of Munich, Germany, 2017. *cited in 1.3.2 (p. 18), 3.4 (p. 54), 5.3.2 (p. 94), 6.2 (p. 98), 9.3 (p. 144)*

-
- [47] P. J. O'Donnell, "Radiative decays of mesons," *Rev. Mod. Phys.* **53** (Oct, 1981) 673–685.
<https://link.aps.org/doi/10.1103/RevModPhys.53.673>.
cited in 1.4.1 (p. 18), 1.40 (p. 18), 1.4.2 (p. 20)
- [48] C. Becchi and G. Morpurgo, "Test of the nonrelativistic quark model for "elementary" particles: Radiative decays of vector mesons," *Phys. Rev.* **140** (Nov, 1965) B687–B690.
<https://link.aps.org/doi/10.1103/PhysRev.140.B687>. *cited in 1.40 (p. 18)*
- [49] N. Barik, P. C. Dash, and A. R. Panda, "Radiative decay of mesons in an independent-quark potential model," *Phys. Rev. D* **46** (Nov, 1992) 3856–3861.
<https://link.aps.org/doi/10.1103/PhysRevD.46.3856>. *cited in 1.40 (p. 18)*
- [50] B. J. Owen, W. Kamleh, D. B. Leinweber, M. S. Mahbub, and B. J. Menadue, "Transition of $\rho \rightarrow \pi\gamma$ in lattice qcd," *Phys. Rev. D* **92** (Aug, 2015) 034513.
<https://link.aps.org/doi/10.1103/PhysRevD.92.034513>.
cited in 1.4.1 (p. 19)
- [51] C. Alexandrou, L. Leskovec, S. Meinel, J. Negele, S. Paul, M. Petschlies, A. Pochinsky, G. Rendon, and S. Syritsyn, " $\pi\gamma \rightarrow \pi\pi$ transition and the ρ radiative decay width from lattice qcd," *Phys. Rev. D* **98** (Oct, 2018) 074502.
<https://link.aps.org/doi/10.1103/PhysRevD.98.074502>.
cited in 1.4.1 (p. 19)
- [52] C. Alexandrou, L. Leskovec, S. Meinel, J. Negele, S. Paul, M. Petschlies, A. Pochinsky, G. Rendon, and S. Syritsyn, "Erratum: $\pi\gamma \rightarrow \pi\pi$ transition and the ρ radiative decay width from lattice qcd [phys. rev. d 98, 074502 (2018)]," *Phys. Rev. D* **105** (Jan, 2022) 019902.
<https://link.aps.org/doi/10.1103/PhysRevD.105.019902>.
cited in 1.4.1 (p. 19)
- [53] B. Abi *et al.*, [Muon $g - 2$ Collaboration], "Measurement of the positive muon anomalous magnetic moment to 0.46 ppm," *Phys. Rev. Lett.* **126** (Apr, 2021) 141801.
<https://link.aps.org/doi/10.1103/PhysRevLett.126.141801>.
cited in 1.4.1 (p. 19)
- [54] T. Aoyama *et al.*, "The anomalous magnetic moment of the muon in the standard model," *Physics Reports* **887** (2020) 1–166. <https://www.sciencedirect.com/science/article/pii/S0370157320302556>. The anomalous magnetic moment of the muon in the Standard Model. *cited in 1.4.1 (p. 19)*
- [55] L. Capraro *et al.*, "The ρ Radiative Decay Width: A Measurement at 200-GeV," *Nucl. Phys. B* **288** (1987) 659. *cited in 1.6 (p. 20), 2.3.2 (p. 37)*
- [56] J. Huston *et al.*, "Measurement of the resonance parameters and radiative width of the ρ^+ ," *Phys. Rev. D* **33** (Jun, 1986) 3199–3202.
<https://link.aps.org/doi/10.1103/PhysRevD.33.3199>. *cited in 1.6 (p. 20), 1.4.2 (p. 20), 2.3.2 (p. 37)*
- [57] T. Jensen *et al.*, "Radiative decay width of the ρ^- meson," *Phys. Rev. D* **27** (Jan, 1983) 26–46.
-

- <https://link.aps.org/doi/10.1103/PhysRevD.27.26>. *cited in 1.6 (p. 20), 1.4.2 (p. 20), 2.3.2 (p. 37)*
- [58] B. Gobbi *et al.*, “Production of ρ^- in the nuclear coulomb field,” *Phys. Rev. Lett.* **33** (Dec, 1974) 1450–1453.
<https://link.aps.org/doi/10.1103/PhysRevLett.33.1450>.
cited in 1.6 (p. 20), 1.4.2 (p. 20)
- [59] B. Ketzer, B. Grube, and D. Ryabchikov, “Light-meson spectroscopy with COMPASS,” *Progress Particle and Nuclear Physics* **113** (2020) . 103755. *cited in 2.1.3 (p. 24), 2.1.3 (p. 24), 2.4 (p. 39), 2.4.4 (p. 43), 8.2.1 (p. 127)*
- [60] T. Regge, “Introduction to complex orbital momenta,” *Il Nuovo Cimento* **14** (1959) 951–976. *cited in 2.1.3 (p. 24)*
- [61] R. G. Newton, *The complex j-plane - complex angular momentum in nonrelativistic quantum scattering theory*. 1964. *cited in 2.1.3 (p. 24)*
- [62] V. De Alfaro and T. Regge, *Potential scattering*. 1965. *cited in 2.1.3 (p. 24)*
- [63] M. Krämer, “Evaluation and Optimization of a Digital Calorimetric Trigger and Analysis of Pion-Photon-Interactions in $\pi^-Ni \rightarrow \pi^- \pi^0 \pi^0 Ni$ Reactions at COMPASS at CERN,” PhD thesis, Technische Universität München, 2017. *cited in 2.1.3 (p. 25), 3.3.2 (p. 51), 3.4 (p. 54), 5.1 (p. 75), 5.2 (p. 80), 5.2.3 (p. 85), 5.3.2 (p. 94), 6.2 (p. 98), 6.3 (p. 101), 6.6 (p. 107), 8.2.1 (p. 127), 8.2.1 (p. 130)*
- [64] R. T. Deck, “Kinematical interpretation of the first $\pi - p$ resonance,” *Phys. Rev. Lett.* **13** (Aug, 1964) 169–173.
<https://link.aps.org/doi/10.1103/PhysRevLett.13.169>.
cited in 2.1.3 (p. 25)
- [65] H. Primakoff, “Photo-production of neutral mesons in nuclear electric fields and the mean life of the neutral meson,” *Phys. Rev.* **81** (Mar, 1951) 899–899.
<https://link.aps.org/doi/10.1103/PhysRev.81.899>. *cited in 2.2.1 (p. 26)*
- [66] J. D. Jackson, *Classical electrodynamics; 2nd ed.* Wiley, New York, NY, 1975.
<https://cds.cern.ch/record/100964>. *cited in 2.2.1 (p. 26), A.3 (p. 148), A.2 (p. 150)*
- [67] Kaiser N. and Friedrich J. M., “Cross-sections for low-energy $\pi^- \gamma$ reactions,” *The European Physical Journal A* **36** no. 2, (2008) 181–188. *cited in 2.2.2 (p. 27), 2.8 (p. 36), 2.3.2 (p. 36), 8.1.3 (p. 124), 8.4 (p. 126), 9.4 (p. 145)*
- [68] C. F. V. Weizsäcker, “Ausstrahlung bei Stößen sehr schneller Elektronen,” *Zeitschrift für Physik* **88** no. 9-10, (Sept., 1934) 612–625. *cited in 2.2.3 (p. 28), A.3 (p. 151)*
- [69] E. J. Williams, “Nature of the high energy particles of penetrating radiation and status of ionization and radiation formulae,” *Phys. Rev.* **45** (May, 1934) 729–730.
<https://link.aps.org/doi/10.1103/PhysRev.45.729>. *cited in 2.2.3 (p. 28), A.3 (p. 151)*

- [70] B. Povh, K. Rith, C. Scholz, F. Zetsche, and W. Rodejohann, *Particles and Nuclei - An Introduction to the Physical Concepts*. Springer, Berlin, 2015. *cited in 2.2.3 (p. 29)*
- [71] E. F. S. de Cruz *et al.*, “Electron-scattering form factors for the giant dipole resonance,” *Journal of Physics G: Nuclear and Particle Physics* **21** no. 7, (Jul, 1995) 973. <https://dx.doi.org/10.1088/0954-3899/21/7/009>. *cited in 2.2.4 (p. 32)*
- [72] M. Hoferichter, B. Kubis, and D. Sakkas, “Extracting the chiral anomaly from $\gamma\pi \rightarrow \pi\pi$,” *Phys. Rev. D* **86** (Dec, 2012) 116009. <https://link.aps.org/doi/10.1103/PhysRevD.86.116009>. *cited in 2.3 (p. 33), 2.3.1 (p. 35), 2.3.2 (p. 37), 2.4 (p. 39), 2.4.2 (p. 41), 2.4.2 (p. 42), 2.4.3 (p. 43), 2.4.3 (p. 43)*
- [73] N. Kaiser. Personal communication. *cited in 2.3 (p. 33)*
- [74] R. J. Eden, P. V. Landshoff, D. I. Olive, and J. C. Polkinghorne, *The Analytic S-Matrix*. Cambridge University Press, New York, 1966. *cited in 2.4 (p. 39)*
- [75] M. Hoferichter, B. Kubis, F. Niecknig, and S. P. Schneider, “Dispersive analysis of the pion transition form factor,” *The European Physical Journal C* **74** no. 3180, (2014) 1434–6052. *cited in 2.4.2 (p. 41)*
- [76] M. Hoferichter, B. Kubis, and M. Zanke, “Radiative resonance couplings in $\gamma\pi \rightarrow \pi\pi$,” *Phys. Rev. D* **96** (Dec, 2017) 114016. <https://link.aps.org/doi/10.1103/PhysRevD.96.114016>. *cited in 2.11 (p. 41), 2.4.2 (p. 41), 2.4.2 (p. 42), 2.4.3 (p. 43), 2.4.4 (p. 44), 2.4.4 (p. 44), 2.4.4 (p. 44)*
- [77] M. Hoferichter and B. Kubis. Personal communication, 2014. *cited in 2.11 (p. 41)*
- [78] D. Ecker, “COMPASS wiki.” https://twiki.cern.ch/twiki/bin/view/Compass/HadronAnalysis/Primakoff_pi-pi0, 2023. [Online; accessed 5-May-2023]. *cited in 2.4.2 (p. 42), 6.2 (p. 100), 6.6 (p. 106)*
- [79] R. García-Martín, R. Kamiński, J. R. Peláez, and J. R. de Elvira, “Precise determination of the $f_0(600)$ and $f_0(980)$ pole parameters from a dispersive data analysis,” *Phys. Rev. Lett.* **107** (Aug, 2011) 072001. <https://link.aps.org/doi/10.1103/PhysRevLett.107.072001>. *cited in 2.4.4 (p. 44)*
- [80] P. Abbon *et al.*, “The COMPASS experiment at CERN,” *Nuclear Instruments and Methods in Physics Research Section A: Accelerators, Spectrometers, Detectors and Associated Equipment* **577** no. 3, (2007) 455–518. <https://www.sciencedirect.com/science/article/pii/S0168900207005001>. *cited in 3.1 (p. 45), 3.1 (p. 46), 3.1 (p. 46), 3.3.3 (p. 52)*
- [81] F. Gautheron *et al.*, [COMPASS], “COMPASS-II Proposal,” *cited in 3.1 (p. 45), 3.1 (p. 46)*
- [82] P. Abbon *et al.*, [COMPASS Collaboration], “The COMPASS Setup for Physics with Hadron Beams,” *Nucl. Instrum. Methods Phys. Res., A* **779** (Sep, 2014) 69–115. 47 p, [arXiv:1410.1797](https://arxiv.org/abs/1410.1797). <https://cds.cern.ch/record/1950827>. *cited in 3.1 (p. 46), 3.1 (p. 46), 3.2 (p. 47), 3.2 (p. 48), 3.3 (p. 49), 3.3 (p. 49), 3.3.2 (p. 51), 3.5 (p. 51), 3.6 (p. 52), 3.3.3 (p. 52), 3.7 (p. 53), 5.1 (p. 73), 6 (p. 98), 7 (p. 110)*

- [83] M. Krämer, J. M. Friedrich, and S. Huber, “Measurement of the hadron beam composition for the 2009 primakoff measurement,” *COMPASS note 2016-6* (2016) .
<https://wwwcompass.cern.ch/compass/notes/2016-6/2016-6.pdf>.
cited in 3.2 (p. 47)
- [84] C. Bovet *et al.*, “The CEDAR (Cerenkov Differential Counters with Achromatic Ring Focus) Project,” *IEEE Transactions on Nuclear Science* **25** no. 1, (1978)
572–576. *cited in 3.2 (p. 47), 3.2 (p. 48), 5.3.1 (p. 87)*
- [85] J. M. Friedrich, “CEDAR performance 2009,” *COMPASS note 2010-15* (2010) .
<https://wwwcompass.cern.ch/compass/notes/2010-15/2010-15.pdf>.
cited in 3.2 (p. 48), 3.2 (p. 48)
- [86] J. M. Friedrich and M. Krämer, “Reconstruction of the pion beam energy from beam optics,” *COMPASS note 2012-2* (2012) .
<https://wwwcompass.cern.ch/compass/notes/2012-2/2012-2.pdf>.
cited in 3.2 (p. 48), 3.2 (p. 49), 5.1 (p. 75)
- [87] S. Uhl, “Photon Reconstruction and Partial-Wave Analysis of Three-Body Final States with Neutral Particles at COMPASS,” PhD thesis, Technische Universität München, 2016.
cited in 3.3.2 (p. 51), 5.2.1 (p. 78), 4 (p. 79)
- [88] C. Bernet *et al.*, “The compass trigger system for muon scattering,” *Nuclear Instruments and Methods in Physics Research Section A: Accelerators, Spectrometers, Detectors and Associated Equipment* **550** no. 1, (2005) 217–240. <https://www.sciencedirect.com/science/article/pii/S0168900205012568>.
cited in 3.3.3 (p. 52)
- [89] C. Adolph *et al.*, [COMPASS Collaboration], “Measurement of the charged-pion polarizability,” *Phys. Rev. Lett.* **114** (Feb, 2015) 062002.
<https://link.aps.org/doi/10.1103/PhysRevLett.114.062002>.
cited in 3.8 (p. 54), 3.4 (p. 54)
- [90] C. Adolph *et al.*, [COMPASS Collaboration], “First measurement of chiral dynamics in $\pi^- \gamma \rightarrow \pi^- \pi^- \pi^+$,” *Phys. Rev. Lett.* **108** (May, 2012) 192001.
<https://link.aps.org/doi/10.1103/PhysRevLett.108.192001>.
cited in 3.8 (p. 54), 3.4 (p. 54)
- [91] S. Huber, “Upgrade of the COMPASS calorimetric trigger and determination of the charged-pion polarisability,” PhD thesis, Technische Universität München, 2017.
cited in 3.4 (p. 54), 5.1 (p. 73), 5 (p. 80), 5.2.2 (p. 83), 5.3.1 (p. 88), 6.2 (p. 98)
- [92] PICMG (PCI Industrial Computer Manufacturers Group), “AdvancedTCA Overview.” Online.
<https://www.picmg.org/openstandards/advancedtca/>. *cited in 3.5.1 (p. 55)*
- [93] D. Steffen *et al.*, “Overview and future developments of the fpga-based daq of compass,” *Journal of Instrumentation* **11** no. 02, (Feb, 2016) C02025.
<https://dx.doi.org/10.1088/1748-0221/11/02/C02025>. *cited in 3.5.1 (p. 55)*

-
- [94] H. C. van der Bij *et al.*, “S-LINK, a data link interface specification for the LHC era,” 1997. hs1.web.cern.ch/HSI/s-link/introduc/rt97.ps. *cited in 3.5.1 (p. 55)*
- [95] S. Huber *et al.*, “Intelligence Elements and Performance of the FPGA-based DAQ of the COMPASS Experiment,” *PoS TWEPP-17* (2018) 127. *cited in 3.5.1 (p. 56)*
- [96] B. Grube, “A Trigger Control System for COMPASS and A Measurement of the Transverse Polarization of Λ and Ξ Hyperons from Quasi-real Photo-Production,” PhD thesis, Technische Universität München, 2006. *cited in 3.5.1 (p. 56)*
- [97] C. G. Larrea, K. Harder, D. Newbold, D. Sankey, A. Rose, A. Thea, and T. Williams, “IPbus: a flexible Ethernet-based control system for xTCA hardware,” *Journal of Instrumentation* **10** no. 02, (Feb, 2015) C02019. <https://dx.doi.org/10.1088/1748-0221/10/02/C02019>. *cited in 3.5.1 (p. 56)*
- [98] M. Bodlak *et al.*, “Development of new data acquisition system for COMPASS experiment,” *Nucl. Part. Phys. Proc.* **273-275** (2016) 976–981. *cited in 3.10 (p. 57)*
- [99] O. Šubrt, “Algorithms for processing of large data sets using distributed architectures and load balancing,” PhD thesis, Czech Technical University in Prague, 2020. *cited in 3.5.2 (p. 58)*
- [100] C. Michalski, “Entwicklung eines Echtzeit-Strahlprofil-monitoring-Systems für das COMPASS-II Experiment,” Master’s thesis, Albert-Ludwigs-universität Freiburg, Germany, 2013. *cited in 4 (p. 59), 4.2 (p. 67), 4.2 (p. 68)*
- [101] [ATLAS], W. Vazques *et al.*, “The ATLAS Data Acquisition System in LHC Run 2,” 2017. <https://dx.doi.org/10.1088/1742-6596/898/3/032017>. *cited in 4.1 (p. 60)*
- [102] [CMS], G. Badaro *et al.*, “The Phase-2 Upgrade of the CMS Data Acquisition,” tech. rep., CERN, Geneva, 2021. <https://cds.cern.ch/record/2797509>. *cited in 4.1 (p. 60)*
- [103] S. Teknoloji, “FAQ.” <https://www.samm.com/mpo-mtp-frequently-asked-questions>, 2023. [Online; accessed 7-August-2023]. *cited in 4.3 (p. 62)*
- [104] S. Bartknecht *et al.*, “Development and performance verification of the gandalf high-resolution transient recorder system,” *IEEE Transactions on Nuclear Science* **58** no. 4, (2011) 1456–1459. *cited in 4.2 (p. 68)*
- [105] “ANSI/VITA 41.0-2006,” tech. rep., VXS VMEbus Switched Serial Standard, 2006. *cited in 4.2 (p. 68)*
- [106] COMPASS collaboration, “CORAL.” <https://gitlab.cern.ch/compass/coral>, 2019. [Online; accessed 2-May-2022]. *cited in 5 (p. 71), 6 (p. 97)*
- [107] N.-H. Kang, D. Ecker, and A. Maltsev, “Event selection of the Primakoff reaction $\pi^- \text{Ni} \rightarrow \pi^- \pi^0 \text{Ni}$ for the 2012 dataset and comparison with 2009 dataset,” *COMPASS release note 2022-02* (2022). https://wwwcompass.cern.ch/compass/results/2022/february_evtsel_Primakoff/Primakoff_pimpi0_evtSel_COMPASS_release_note.pdf. *cited in 5 (p. 72), 9.3 (p. 144)*
-

- [108] A. Maltsev, D. Ecker, and D. Ryabchikov, “Measurement of $F_{3\pi}$ constant from 2009 Primakoff data,” *COMPASS release note 2022-08* (2022) .
https://wwwcompass.cern.ch/compass/results/2022/august_Primakoff_F3pi_2009/Primakoff_release_note.pdf. *cited in 5 (p. 72), 5 (p. 81), 5.2.4 (p. 86), 5.2.4 (p. 87), 9.1 (p. 141)*
- [109] P. A. Zyla *et al.*, [Particle Data Group], “Review of Particle Physics - Passage of Particles Through Matter,” *PTEP* **2020** (2020) 696–712. 083C01. *cited in 5.1 (p. 74)*
- [110] A. A. Lednev, “Shower separation program for ecal2,” *COMPASS note 2009-7* (2009) .
<https://wwwcompass.cern.ch/compass/notes/2007-10/2007-10.pdf>. *cited in 5.2.1 (p. 78)*
- [111] A. Lednev, “Electron shower transverse profile measurement,” *Nuclear Instruments and Methods in Physics Research Section A: Accelerators, Spectrometers, Detectors and Associated Equipment* **366** no. 2, (1995) 292–297. <https://www.sciencedirect.com/science/article/pii/0168900295007172>. *cited in 5.2.1 (p. 78), 5.2.2 (p. 82)*
- [112] S. Aumiller, “Neural Networks for Photon Reconstruction in Electromagnetic Calorimeters for the COMPASS and AMBER experiments.” Bachelor thesis — to be published. *cited in 5.2.1 (p. 79)*
- [113] S. Gerassimov. Personal communication. *cited in 3 (p. 79), 6.1 (p. 99), 6.2 (p. 99)*
- [114] T. Nagel, “Measurement of the charged pion polarizability at COMPASS,” PhD thesis, TU München, 2012. *cited in 5 (p. 80)*
- [115] D. Scheck, “Kalibrierung eines elektromagnetischen Kalorimeters für Messungen der Pionstruktur.” Bachelor thesis, 2019. *cited in 5 (p. 80)*
- [116] T. Schlüter, “A code for kinematic fitting with constraints from intermediate particle masses,” *COMPASS note 2007-10* (2007) .
<https://wwwcompass.cern.ch/compass/notes/2009-7/2009-7.pdf>. *cited in 5.2.3 (p. 84)*
- [117] D. Ryabchikov, “Kinematic fitting.” Personal communication, 2023. *cited in 5.2.3 (p. 85), 5.2.3 (p. 86)*
- [118] S. Wallner, “Exploring the Strange-Meson Spectrum with COMPASS in the Reaction $K^- + p \rightarrow K^- \pi^- \pi^+ + p$,” PhD thesis, Technische Universität München, 2022. *cited in 5.3.1 (p. 89), 8.1.2 (p. 123)*
- [119] COMPASS collaboration, “COMGEANT.”
<https://gitlab.cern.ch/compass/comgeant>, 2019. [Online; accessed 2-May-2022]. *cited in 6 (p. 97)*
- [120] R. Brun, F. Bruyant, M. Maire, A. C. McPherson, and P. Zancarini, “GEANT3,” *cited in 6 (p. 97)*

-
- [121] Szameitat, Tobias, “New Geant4-based Monte Carlo Software for the COMPASS-II Experiment at CERN,” PhD thesis, Albert-Ludwigs-Universität Freiburg, 2016. *cited in 6.1 (p. 98), 9.3 (p. 145)*
- [122] S. Aumiller, “Primakoff geometries at COMPASS - TGEANT vs. COMGEANT.” Online. https://indico.cern.ch/event/1265090/contributions/5372808/attachments/2634026/4556285/RICH_material_distribution_COMGEANT_vs_TGEANT.pdf. *cited in 6.1 (p. 98)*
- [123] P. A. Zyla *et al.*, [Particle Data Group], “Review of Particle Physics - Particle Detectors at Accelerators,” *PTEP* **2020** (2020) 551–588. 083C01. *cited in 6.3 (p. 100)*
- [124] S. Weinberg, “New test for $\Delta i = \frac{1}{2}$ in K^+ decay,” *Phys. Rev. Lett.* **4** (Jan, 1960) 87–89. <https://link.aps.org/doi/10.1103/PhysRevLett.4.87>. *cited in 7.2.1 (p. 113)*
- [125] J. Batley *et al.*, [NA48/2], “Observation of a cusp-like structure in the $\pi^0\pi^0$ invariant mass distribution from $k^\pm \rightarrow \pi^\pm\pi^0\pi^0$ decay,” *Physics Letters B* **633** no. 2-3, (Feb, 2006) 173–182. *cited in 7.2.1 (p. 113)*
- [126] J. Batley *et al.*, [NA48/2], “Empirical parameterization of the $k^\pm \rightarrow \pi^\pm\pi^0\pi^0$ decay dalitz plot,” *Physics Letters B* **686** no. 2-3, (Mar, 2010) 101–108. *cited in 7.2.1 (p. 113)*
- [127] J. R. Batley *et al.*, [NA48/2], “Measurement of the form factors of charged kaon semileptonic decays,” *JHEP* **10** (2018) 150, arXiv:1808.09041 [hep-ex]. *cited in 7.5 (p. 115), 7.2.2 (p. 115), 7.2.2 (p. 116)*
- [128] L. Lyons, “On estimating systematic errors,” *cited in 7.4 (p. 118)*
- [129] J. Beckers, “Search for Light-Meson Resonances in Diffractively Produced $K^-K^+\pi^-$, $K_S^0\pi^-$, and $K_S^0K^-$ Final States Measured at COMPASS.” Master thesis, 2021. *cited in 8.1.2 (p. 123)*
- [130] J. Bernhard, J. M. Friedrich, T. Schlüter, and K. Schönning, “Comment on “Material Evidence of a 38 MeV Boson”,” 2012. *cited in 8.1.3 (p. 125)*
- [131] D. Ryabchikov, “Partial-wave analysis of $\pi^-Ni \rightarrow \pi^-\pi^0\pi^0Ni$ reactions.” Personal communication, 2023. *cited in 8.2.1 (p. 127), 8.2.1 (p. 128)*
- [132] T. J. deForest and J. D. Walecka, “Electron scattering and nuclear structure,” *Advances Phys.* **15** no. 57, (1, 1966) . <https://www.osti.gov/biblio/4525917>. *cited in 8.2.2 (p. 130)*
- [133] J. Friedrich, [COMPASS], “Chiral symmetry breaking: Current experimental status and prospects,” *EPJ Web Conf.* **282** (2023) 01007. *cited in 9.1 (p. 141), 9.1 (p. 142), 9.2 (p. 143)*
- [134] [COMPASS], D. Ecker, “Testing the chiral anomaly and measuring the radiative width of the $\rho(770)$ at COMPASS,” International Workshop on Hadron Structure and Spectroscopy, 2022. https://indico.cern.ch/event/1121975/contributions/5016505/attachments/2499239/4293016/Ecker_20220830.pdf. *cited in 9.1 (p. 141)*
-

- [135] [COMPASS], D. Ecker and A. Maltsev, “Testing Predictions of the Chiral Anomaly in Primakoff Reactions at COMPASS,” HADRON2023, 2023.
https://agenda.infn.it/event/33110/contributions/197449/attachments/106516/150064/Ecker_20230608_v3.pdf. *cited in 9.1 (p. 141)*
- [136] N.-H. Kang, “Primakoff analysis $\pi^- \text{Ni} \rightarrow \pi^- \pi^0 \text{Ni}$ with 2012 data from COMPASS at CERN,” Master’s thesis, Technical University of Munich, Germany, 2022. *cited in 9.3 (p. 144)*

Acknowledgements

Spending a lot of time in the mountains, I frequently find myself in intimidating situations, some of which might seemingly be life-threatening. But writing my doctoral thesis on experimental particle physics is by far the most challenging, frightening, and courageous project I have ever faced. Despite requiring a very different skill set, mountaineering and research in particle physics have common principles: the bigger the project, the more you should think step-by-step and the more daring the undertaking, the more important the company. I can call myself very lucky with the people who accompanied me on this expedition.

First, I want to thank Prof. Stephan Paul for giving me the financial support, the freedom, and the possibility to work on this interesting topic. Generations of PhD students have benefited from the amount of trust he puts into them, and I am more than happy to be one of them. A big thank you and special shout-out to Jan Friedrich, for the endless patience in discussing kinematics, nuclear excitations, and other backgrounds late in the evening after a full day of work missing subway after subway. I honestly admire the pictures you have in mind, when talking about particles. This makes seemingly boring mathematical formulations so much more alive. I hope, I can maintain this approach towards physics, always trying to understand what actually is behind.

All the nice physics results of COMPASS would not have been possible without Igor Konorov. He keeps the experiment running against all odds. I was impressed by his dedication and the time, which he is gladly providing, to contribute to successful data taking. Thank you for instructing me during the hardware work of this thesis. If I can at least partly maintain the analytic approach of debugging electronics, I am more than happy.

To Dima and Andrii, who have contributed a lot to the analysis. I appreciated all the discussion about physics and I learned a lot from you. Dima, your enthusiasm and excitement in “humps” and “bumps” of physical distributions, made the analysis possible so far. I am very optimistic that together, we finish the analysis and publish soon!

To all the colleagues and former colleagues at E18 and at CERN. You made me feel welcomed, and you provided a fun working environment. Always giving advice and trying to help where help was needed. More than once, basically every day, I relied on your stock of chocolate, beer, or cereal bars depending on the occasion. I enjoyed the interesting discussions with you during the coffee and lunch breaks at CERN and in Munich. Without your good company, I would not have made it through all these years.

To all my friends in Allgäu, Grenoble, Geneva, Munich, etc. With your help, I managed to sustain a somewhat healthy balance between work and leisure time. I am extremely grateful for all the fun moments in the Alps, for the fun evenings in the house in Sergy or in Munich, for dinners and parties, for boozy reunions after a long time. All of this makes me forget physics for a couple of hours. I hope our friendship will continue!

Dear mom and dad, well I don't even know where to start. I would be nothing without you. Words do not come close to how grateful I am for a family like this. To my little sister and my beautiful goddaughter, whose journey will soon begin: I love you and I hope that the strong bond between us will stay forever, even though we are living far apart from each other!

To Moni, the beautiful girl, whom I got to know shortly before starting my PhD. The girl who stayed with me, first as girlfriend, later as wife. Our relationship, which survived the years I spent in Geneva, means the world to me. She had to endure not only my forgetfulness, when my thoughts circulated around physics instead of e.g. taking the correct junction while driving, but also my long working hours, when times were not easy. You are, what makes me happy and content. You are giving a meaning to all of this. I love you!